Optical and luminescence properties of noble metal nanoparticles

by

K. L. Dimuthu M. Weerawardene

B.S., University of Colombo, 2011

AN ABSTRACT OF A DISSERTATION

submitted in partial fulfillment of the requirements for the degree

DOCTOR OF PHILOSOPHY

Department of Chemistry
College of Arts and Sciences

KANSAS STATE UNIVERSITY
Manhattan, Kansas

2017

Abstract

The remarkable optical and luminescence properties of noble metal nanoparticles (with diameters < 2 nm) attract researchers due to potential applications in biomedicine, photocatalysis, and optoelectronics. Extensive experimental investigations on luminescence properties of thiolate-protected gold and silver nanoclusters during the past decade have failed to unravel their exact photoluminescence mechanism. Herein, density functional and time-dependent density functional theory (DFT and TDDFT) calculations are performed to elucidate electronic-level details of several such systems upon photoexcitation. Multiple excited states are found to be involved in photoemission from $Au_{25}(SR)_{18}^-$ nanoclusters, and their energies agree well with experimental emission energies. The Au_{13} core-based excitations arising due to electrons excited from superatom P orbitals into the lowest two superatom D orbitals are responsible for all of these states. The large Stokes shift is attributed to significant geometrical and electronic structure changes in the excited state. The origin of photoluminescence of $Ag_{25}(SR)_{18}^-$ nanoclusters is analogous to their gold counterparts and heteroatom doping of each cluster with silver and gold correspondingly does not affect their luminescence mechanism. Other systems have been examined in this work to determine how widespread these observations are. We observe a very small Stokes shift for $Au_{38}(SH)_{24}$ that correlates with a relatively rigid structure with small bond length changes in its Au_{23} core and a large Stokes shift for $Au_{22}(SH)_{18}$ with a large degree of structural flexibility in its Au_7 core. This suggests a relationship between the Stokes shift of gold−thiolate nanoparticles and their structural flexibility upon photoexcitation.

The effect of ligands on the geometric structure and optical properties of the $Au_{20}(SR)_{16}$ nanocluster is explored. Comparison of the relative stability and optical absorption spectra suggests that this system prefers the $[Au_7(Au_8SR_8)(Au_3SR_4)(AuSR_2)_2]$ structure regardless of whether aliphatic or aromatic ligands are employed.

The real-time (RT) TDDFT method is rapidly gaining prominence as an alternative approach to capture optical properties of molecular systems. A systematic benchmark study is performed to demonstrate the consistency of linear-response (LR) and RT-TDDFT methods for calculating the optical absorption spectra of a variety of bare gold and silver nanoparticles with different sizes and shapes.

Optical and luminescence properties of noble metal nanoparticles

by

K. L. Dimuthu M. Weerawardene

B.S., University of Colombo, 2011

A DISSERTATION

submitted in partial fulfillment of the requirements for the degree

DOCTOR OF PHILOSOPHY

Department of Chemistry
College of Arts and Sciences

KANSAS STATE UNIVERSITY
Manhattan, Kansas

2017

Approved by:

Major Professor
Christine M. Aikens

Copyright

Abstract

The remarkable optical and luminescence properties of noble metal nanoparticles (with diameters < 2 nm) attract researchers due to potential applications in biomedicine, photocatalysis, and optoelectronics. Extensive experimental investigations on luminescence properties of thiolate-protected gold and silver nanoclusters during the past decade have failed to unravel their exact photoluminescence mechanism. Herein, density functional and time-dependent density functional theory (DFT and TDDFT) calculations are performed to elucidate electronic-level details of several such systems upon photoexcitation. Multiple excited states are found to be involved in photoemission from $Au_{25}(SR)_{18}^-$ nanoclusters, and their energies agree well with experimental emission energies. The Au_{13} core-based excitations arising due to electrons excited from superatom P orbitals into the lowest two superatom D orbitals are responsible for all of these states. The large Stokes shift is attributed to significant geometrical and electronic structure changes in the excited state. The origin of photoluminescence of $Ag_{25}(SR)_{18}^-$ nanoclusters is analogous to their gold counterparts and heteroatom doping of each cluster with silver and gold correspondingly does not affect their luminescence mechanism. Other systems have been examined in this work to determine how widespread these observations are. We observe a very small Stokes shift for $Au_{38}(SH)_{24}$ that correlates with a relatively rigid structure with small bond length changes in its Au_{23} core and a large Stokes shift for $Au_{22}(SH)_{18}$ with a large degree of structural flexibility in its Au_7 core. This suggests a relationship between the Stokes shift of gold−thiolate nanoparticles and their structural flexibility upon photoexcitation.

The effect of ligands on the geometric structure and optical properties of the $Au_{20}(SR)_{16}$ nanocluster is explored. Comparison of the relative stability and optical absorption spectra suggests that this system prefers the $[Au_7(Au_8SR_8)(Au_3SR_4)(AuSR_2)_2]$ structure regardless of whether aliphatic or aromatic ligands are employed.

The real-time (RT) TDDFT method is rapidly gaining prominence as an alternative approach to capture optical properties of molecular systems. A systematic benchmark study is performed to demonstrate the consistency of linear-response (LR) and RT-TDDFT methods for calculating the optical absorption spectra of a variety of bare gold and silver nanoparticles with different sizes and shapes.

Table of Contents

List of Figures

List of Tables

Acknowledgements

First and foremost, I would like to thank my advisor Professor Christine Aikens, for her guidance and support throughout the past five years. Your kindness, patience, motivation, and advices encouraged me to pursue my graduate research well at Kansas State University. I would also like to acknowledge my supervisory committee members: Professor Paul Smith, Professor Bin Liu, Professor Emily McLaurin, and Professor Dale Schinstock.

I would like to express my gratitude towards all the present and past Aikens' group members for their support and sharing their research experiences with me. I enjoyed working with you all.

I would like to acknowledge Professor Dhammike Dissanayake, Professor Samantha Weerasinghe, and all the other professors at University of Colombo for sharing their knowledge and paving the way for me to follow my dreams.

I want to acknowledge my parents and my two sisters with all my heart for their love and courage that strengthens me every day. My gratitude is extended to all my friends here in Manhattan and back in Sri Lanka as well.

Finally, I would like to thank my husband, Kushan for being there with me through it all.

Dedication

To my parents and my two sisters.

To my husband Kushan.

Chapter 1 - Introduction

Historically, noble metals such as gold and silver have been valued for their beauty and rarity. They are inert and resistive to degradation under environmental conditions. However, when the size of these systems is decreased to the nanometer size regime (10^{-9} m) they exhibit extraordinary physicochemical properties. The use of gold and silver nanoparticles for coloration of glass, ceramic, and pottery dates back to ancient times, although it was then unknown that the material was indeed small particles in the nanoscale. The most interesting size range of noble metal nanoparticles is from about a dozen to a few hundred atoms which is equivalent to the subnanometer to ~2 nm range. The size of these systems leads to quantum effects that result in discrete energy levels, multiple absorption bands, enhanced photoluminescence, and improved catalytic activity, enabling a wide variety of fundamental and technological applications in e.g., catalysis,[1, 2] energy conversion and storage,[3, 4] sensing,[5-7] and biomedicine.[5, 8, 9]

1.1 Ligand protected noble metal nanoparticles

The absorption spectra of monolayer-protected clusters (MPCs) can be used to identify particular nanoparticle stoichiometries. Understanding of the correlation between geometric structure and optical properties of MPCs advanced significantly with the first crystal structure determination of a thiolate-stabilized nanoparticle in 2007 for $Au_{102}(SR)_{44}$[10] and subsequent identification of the total structure of $Au_{25}(SR)_{18}{}^{-}$.[11, 12] Both geometries suggested that in general, thiolate-protected noble metal nanoparticles have a common structural picture, which consist of a highly symmetric metallic core protected by metal-thiolate oligomeric units or "staple motifs". The Au_{102} cluster can be accurately described as having a decahedral Au_{79} core protected with 19 (RS-Au-SR) monomeric staples and 2 (RS-Au-SR-Au-SR) dimeric staple motifs, whereas the icosahedral Au_{13} core is protected by 6 dimeric staple motifs in the Au_{25} nanocluster. These compositions agree with a "divide and protect" structure motif predicted previously, where bonding in thiolate protected gold clusters, $Au_M(SR)_X$ is understood as $Au_{M-X}(AuSR)_X$.[13]

The thermodynamic stability and the chemical nature of MPCs can be predicted in part using the "superatom electronic theory".[14] The theory has been most widely used for gas-phase clusters.[15] The "superatomic orbitals" for approximately spherical particles are the solution to the Schrödinger equation for a spherically symmetric well potential.[16] The aufbau rule for

delocalized superatomic orbitals is $1S^2| 1P^6| 1D^{10}| 2S^2 1F^{14}| 2P^6 1G^{18}| 2D^{10} 3S^2 1H^{22}|\ldots$ wherein S-P-D-F-G-H- denote the angular momentum character of the orbitals.[17, 18] Many metal clusters can be formulated as $(L_s \bullet A_N X_M)^z$, where X represents one-electron withdrawing or localizing ligands and L represents ligands that coordinate to the core surface by dative bonds and do not withdraw electrons from the core metal atoms A. The number of superatomic electrons is given by,

$$n^* = N n_A - M - z$$

where N is the number of metal atoms, n_A is the atomic valence ($n_A = 1$ for both gold and silver), M gives the number of one-electron withdrawing or localizing ligands, and z is the total charge on the cluster. The L_s weak ligands may complete the steric protection of the core surface. When the electron count n^* corresponds to a superatomic shell closing "magic number" (similar to a noble-gas-like configuration) such as 2, 8, 18, 34, 58, 92, etc., the cluster achieves special electronic stability.[17, 18] Geometric shell closings can also stabilize metal nanoclusters. It has been suggested that geometric shell closure dominates the stability of Au_{144} and larger thiolate-protected gold nanoclusters[19-22] while Au_{102} and smaller clusters are stabilized via electronic shell fillings.[12, 23]

1.2 Optical properties of noble metal nanoparticles

Gold and silver nanoparticles in the 10-100 nm size regime display fascinating optical properties that can be characterized by a strong absorption peak in the visible-IR region of the optical absorption spectrum.[24-27] This phenomenon is called the surface plasmon resonance (SPR), which is the collective oscillation of conduction electrons in the presence of an electric field.[28] In 1908, Gustov Mie solved Maxwell's equations for light interaction with a single gold nanoparticle to explain plasmonic properties of gold nanoparticles.[29] However, classical electromagnetic theory does not account for quantum effects of smaller nanoparticles. Gold and silver nanoclusters with a core diameter less than 2 nm demonstrate molecular properties and discrete absorption spectra[30, 31] and warrant the necessity of quantum mechanical calculations to elucidate their optical properties.

1.2.1 Optical properties of thiolate protected gold and silver nanoclusters

The optical absorption spectra of smaller gold-thiolate nanoclusters consist of multiple peaks due to quantum confinement effects. Each nanocluster has an essentially unique spectrum that can be used as a 'fingerprint' to identify the stoichiometry of the system.

1.2.1.1 $Au_{25}(SR)_{18}$ nanocluster

Due to its unique properties and remarkable stability, the $Au_{25}(SR)_{18}^-$ nanocluster has been extensively investigated both experimentally and theoretically. It exhibits a high resistance to decomposition[32] and core etching.[33] The $Au_{25}(SR)_{18}$ cluster is stable regardless of the charge state of -1, 0, +1,[34] and has been crystallographically resolved for each charge state.[11, 12, 35, 36] The optical absorption spectrum and highest occupied molecular orbital – lowest unoccupied molecular orbital (HOMO-LUMO) gap of $Au_{25}(SR)_{18}^-$ appears not to be significantly affected by the thiolate ligand (R) nature.[34, 37] The structure of the $Au_{25}(SR)_{18}^-$ cluster consists of a nearly icosahedral Au_{13} core surrounded by six V-shaped -SR-Au-SR-Au-RS- (dimeric staple) motifs in an approximately icosahedral arrangement as shown in Figure 1.1.[11, 12, 38] The UV-vis spectrum of $Au_{25}(SH)_{18}^-$ exhibits multiple molecular-like transitions with well-defined bands at 1.8, 2.75, and 3.1 eV.[12]
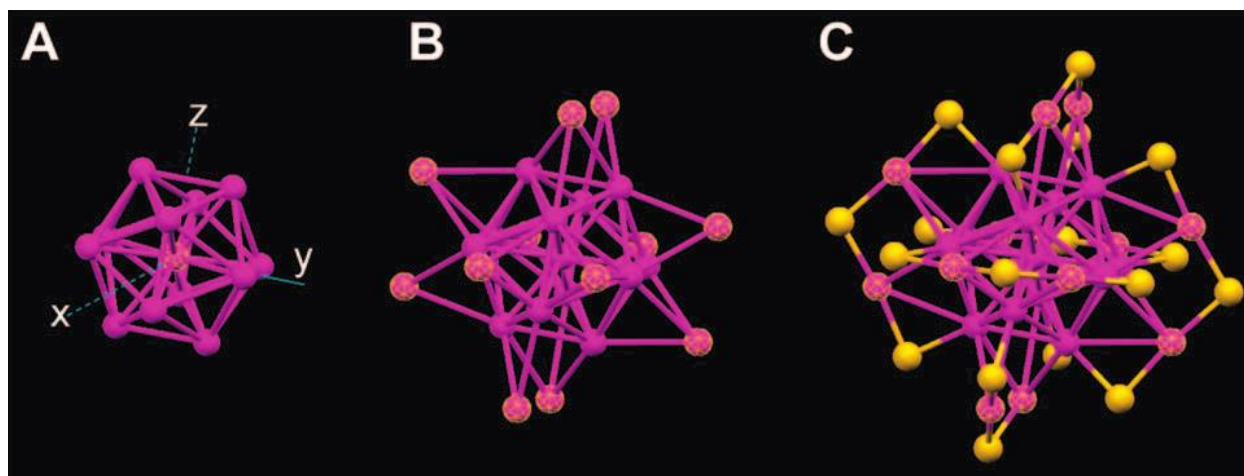
Figure 1.1 Crystal Structure of $Au_{25}(SR)_{18}$- cluster (A) the icosahedral Au_{13} core (B) Au_{13} core with exterior 12 gold atoms (C) Au_{25} cluster protected by 18 thiolate ligands (for clarity R groups are omitted, magenta-Au; yellow-S) (Reprinted with permission from *J. Am. Chem. Soc.* 2008, *130*, 5883-5885. Copyright 2008 American Chemical Society)

In order to correlate the cluster structure and optical properties of $Au_{25}(SR)_{18}^-$ system, time-dependent density functional theory (TDDFT) calculations were performed using $Au_{25}(SH)_{18}^-$ as a model, where the R groups were substituted with H atoms.[12] Figure 1.2A shows Kohn-Sham (KS) molecular orbital energies and atomic orbital contributions and Figure 1.2B shows the theoretical absorption spectrum, where a, b, and c label the peaks corresponding to experimental absorption bands. In the electronic structure of $Au_{25}(SH)_{18}^-$ the HOMO, LUMO, LUMO+1 and LUMO+2 orbitals constitute the *sp*-band, which are mainly composed of 6*sp* atomic orbitals of gold whereas HOMO-1 through HOMO-5 are constructed from 5*d* atomic orbitals of gold and hence constitute the *d*-band. The projected density of states and the Kohn-Sham orbitals of the system show that the HOMO is a triply degenerate superatom P orbital, the LUMO and LUMO+1 are two-fold and three-fold degenerate sets of D orbitals, respectively, and the LUMO+2 represents a 2S orbital.[12, 38] The first absorption peak arises primarily from the HOMO → LUMO transition, which is essentially an intraband transition (*sp*→*sp*); the second peak is formed from a combination of HOMO → LUMO+1, HOMO → LUMO+2, and HOMO-2 → LUMO transitions, which are both interband (*d*→*sp*) and intraband transitions; and the third peak is generated primarily from the HOMO-5 → LUMO interband transition.[12]
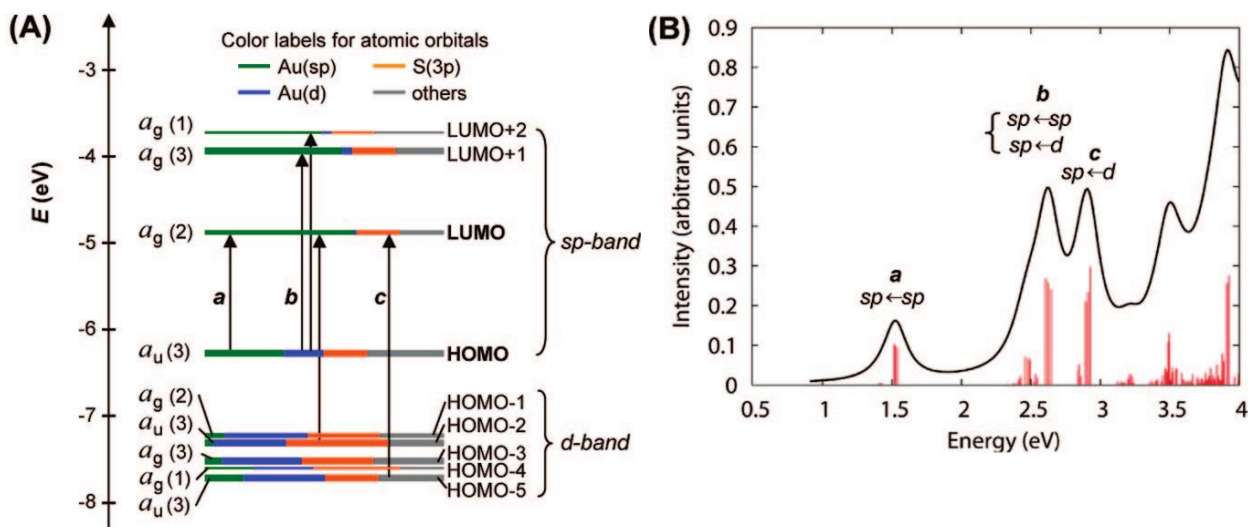
Figure 1.2 (A) Kohn-Sham orbital energy level diagram for a model compound $Au_{25}(SH)_{18}^-$ (B) The theoretical absorption spectrum of $Au_{25}(SH)_{18}^-$. (Reprinted with permission from *J. Am. Chem. Soc.* 2008, *130*, 5883-5885. Copyright 2008 American Chemical Society)

The ligand effect on the optical absorption spectrum of $Au_{25}(SR)_{18}^-$ nanoparticle has been explored. Aikens has shown that replacing the R groups in $Au_{25}(SR)_{18}^-$ with R = H, CH_3, and CH_2CH_3 changes the first absorption peak by less than 0.1 eV whereas the second peak shifts to about 0.15 eV energy lower for R = CH_3, and CH_2CH_3 compared to R = H.[39] Guo and Murray experimentally investigated para-substituted phenyl groups in the $Au_{25}(SCH_2CH_2Ph)_{18}^-$ nanoparticle.[37] They observed similar optical absorption spectra with slight deviations of the second and third peaks to higher energy with respect to R=CH_2CH_2Ph. Aikens performed DFT calculations on $Au_{25}(SPhX)_{18}^-$ (X = H, F, Cl, Br, CH_3, OCH_3) systems and observed a splitting of the P_z superatomic orbital away from P_x and P_y, which leads to a double peak for the first main peak in the absorption spectrum.[40] Para substituents mostly did not affect the absorption spectra although ~0.1 eV changes were evident in the third peak. Other theoretical investigations by Tlahuice-Flores have shown an increase in the distortion of the $Au_{25}S_{18}$ framework in the order of X = H, Cl, NO_2, and CO_2H para substituents.[41] The more distorted structures exhibited significantly reduced HOMO-LUMO gaps, which in turn affected the optical absorption spectra. Akola et al.[42] published the TDDFT spectra of the full $Au_{25}(SCH_2CH_2Ph)_{18}^-$ MPC and the model $Au_{25}(SCH_3)_{18}^-$ system, which is somewhat red-shifted with respect to that of the full MPC. The first peak of the absorption spectrum in the full MPC had the characteristic 'double-peak' shape with a prominent shoulder that is well-known for experimental $Au_{25}(SR)_{18}^-$ compounds, whereas the methyl complex exhibited a single peak. They attributed the change in peak shape to symmetry-breaking of the P orbitals induced by the longer ligands. However, Jiang et al.[43] observed a double peak even for methyl-thiolated Au_{25} system when spin orbit coupling (SOC) was included in TDDFT calculations.

Aikens has shown that the inclusion of a continuum solvent during the TDDFT calculations affects the absorption spectrum of a $Au_{25}(SH)_{18}^-$ nanoparticle slightly.[39] Moreover, it has been observed that a triple-zeta basis set red-shifts the spectrum ~0.1 eV compared to a double-zeta basis set. A comparison of several GGA and asymptotically-corrected functionals (LB94, SAOP) for $Au_{25}(SH)_{18}^-$ showed that the first excitation peak calculated using GGA functionals lies about 0.1 eV lower in energy than peak energies calculated with LB94 or SAOP. The theoretical spectra of the neutral and cationic $Au_{25}(SR)_{18}$ systems have also been reported.[44] An increased splitting has been observed in superatomic P orbitals when the charge of the cluster is increased from -1 to +1 (Figure 1.3).[44, 45] All charge states have shown a double peak structure

for the excitations involving $1a_u \rightarrow a_g$ transitions.[44] Recently, Tofanelli et al.[36] published the experimental absorption spectra at all three charge states that agree well with the previous theoretical spectra. Furthermore, the evolution of the structures with the oxidation state was described using the Jahn-Teller effect.
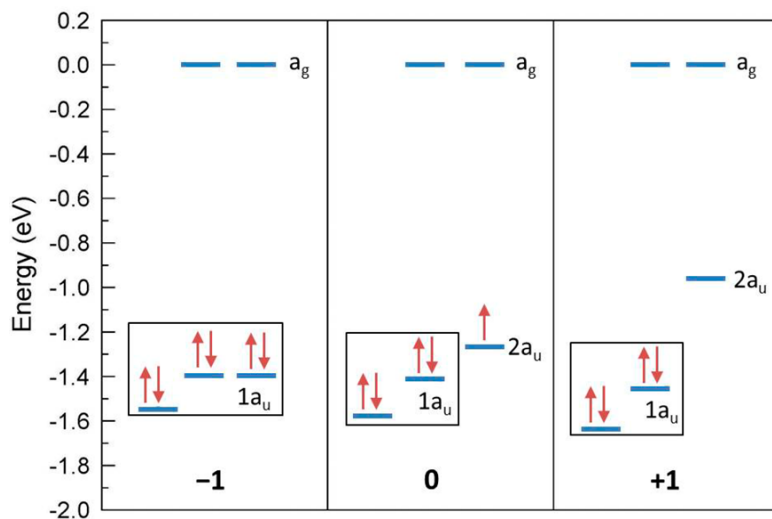
Figure 1.3 Orbital diagrams in Au$_{25}$(SR)$_{18}^z$ (z=-1, 0, +1) (Reprinted with permission from *J. Am. Chem. Soc.* 2013, *135*, 15585-15594. Copyright 2013 American Chemical Society)

1.2.1.2 Other gold thiolate nanoclusters

Theoretical optical absorption spectra obtained with TDDFT calculations have been widely used to predict geometric structures of gold thiolate nanoclusters. One of the earliest predicted geometries is the D_3 isomer of Au$_{38}$(SR)$_{24}$, whose TDDFT absorption spectrum was found to be in good agreement with experiment.[46] This isomer was subsequently confirmed experimentally.[23] The frontier orbitals of Au$_{38}$(SR)$_{24}$ near the HOMO-LUMO gap arise primarily from Au($6sp$) atomic orbitals and are delocalized throughout the core of the system. However, due to the elongated geometry of the nanoparticle, these orbitals have approximate cylindrical symmetry such as Σ, Π, Δ, etc. The first three peaks in the optical absorption spectrum (up to 1.72 eV) were found to arise from intraband transitions.[23] The fourth peak (1.89-2.01 eV) was determined to arise mainly from transitions out of the oligomeric ligand-based d-band into the sp-based orbitals.

Pei et al.[48] predicted 3 isomers containing an edge-fused bitetrahedral Au_8 core protected with 4 $[Au_3(SR)_4]$ "trimeric" staple motifs for $Au_{20}(SR)_{16}$,[47] where theoretical spectra agreed qualitatively well with the experimental optical absorption spectrum of $Au_{20}(SCH_2CH_2Ph)_{16}$. However, a recent crystal structure determination of $Au_{20}(TBBT)_{16}$ revealed that the geometric structure possesses a unique bitetrahedral Au_7 core with a surrounding octameric ring $[Au_8(SR)_8]$, one trimeric and two monomeric staple motifs.[49] To answer the question whether or not the structure of this system exhibits any dependence on the type of ligand, Weerawardene and Aikens performed DFT and TDDFT calculations and predicted that both aliphatic and aromatic ligands will have the same structure, with a bitetrahedral Au_7 core.[50] A large number of theoretical studies have been carried out to validate predicted geometries for known compositions with no crystal structure information, by comparing the experimental spectra with TDDFT spectra.[51-56] For example, two DFT investigations have predicted the geometric structure of highly luminescent $Au_{22}(SR)_{18}$ nanocluster differently.[57, 58] However, the theoretical optical absorption spectrum calculated by Zeng and coworkers for a structure containing an Au_7 kernel surrounded by a unique $[Au_6(SR)_6]$ ring type motif and three $Au_3(SR)_4$ staples is in better agreement with the experimental absorption spectrum.[57] Moreover, optical absorption spectra of gold thiolate nanoclusters with known crystal structures have also been extensively investigated using TDDFT to understand the origin of their optical properties as well as to draw structure property relationships.[59-65]

1.2.1.3 Silver thiolate nanoclusters

The total structure determination of $Au_{25}(SR)_{18}^-$ initiated the investigation of its silver analog. Aikens performed TDDFT calculations to study optical and electronic properties of $Ag_{25}(SH)_{18}^-$.[66] The approximately triply degenerate HOMO, doubly degenerate LUMO, and triply degenerate LUMO+1 orbitals were observed similar to $Au_{25}(SH)_{18}^-$. At the SAOP/TZP level of theory, the HOMO→LUMO transition of $Ag_{25}(SH)_{18}^-$ was calculated to lie at 1.64 eV. Unlike the gold counterpart, the strong second peak at 2.33 eV was predicted to arise from the HOMO→LUMO+1 transition. Although the HOMO-LUMO gaps are similar for gold and silver systems, the splitting between the LUMO and LUMO+1 is ~0.3 eV smaller for $Ag_{25}(SH)_{18}^-$, which causes the second peak to originate from the HOMO→LUMO+1 transition. Notably, this

"golden silver" nanoparticle was synthesized and characterized later and the experimental UV-vis spectrum agreed well with the calculated spectrum.[67]

The structural formula of the first thiolate protected silver nanocluster was identified to be $Ag_{44}(SR)_{30}^{4-}$.[68] The x-ray crystal structure of this nanoparticle was solved by two groups independently who found that it consists of an inner icosahedral core of 12 atoms surrounded by a 20-atom decahedral outer core, which is capped with six $Ag_2(SR)_5$ motifs.[69, 70] This cluster has 18 delocalized electrons, so that the HOMO is a 1D superatomic orbital, the LUMO is a 2S orbital, and the LUMO+1 is a 1F orbital.[70] The two lowest-energy transitions were found to arise mainly from 1D→1F type transitions and the higher energy peaks arise from ligand-based orbitals.

$Ag_{31}(SG)_{19}$ and $Ag_{15}(SG)_{11}$ nanoparticles have also been investigated using both experiment and theory.[71] The stoichiometries were suggested using mass spectrometry and DFT calculations that predicted the 15-atom cluster to consist of a Ag_8 core protected by 1 trimeric, 1 dimeric, and 2 monomeric staple motifs, whereas the 31-atom cluster possesses a Ag_{21} core covered by 1 dimeric and 8 monomeric staple motifs. Experimental and theoretical spectra were found to agree well for both clusters.

1.2.2 Bare clusters

Larger gold and silver nanoparticles show a sharp and distinct optical response in the visible region due to plasmonic properties. The number of plasmonic modes as well as their frequencies and widths are determined by the shape, size, and dielectric environment of the nanoparticle.[72] During the past few years, different synthetic approaches have been used to successfully synthesize various gold and silver nanoparticles including nanorods,[73] nanobars,[74] nanowires,[75, 76] cubes,[77-80] triangular prisms,[81, 82] octahedra,[77, 79] truncated octahedra,[77, 79] cuboctahedra,[77, 79] and icosahedra.[80] Several groups have experimentally studied the size and shape dependence of the optical properties of gold and silver nanoparticles.[77, 83, 84]

Recently, many theoretical investigations that employ TDDFT have been reported for gold and silver nanoparticles with various sizes and shapes.[72, 85-94] Linear-response (LR) TDDFT has been used to explore optical properties of tetrahedral Ag_n ($n \leq 120$) particles,[91] silver and gold nanorod clusters (Ag_n, Au_n, $n = 12$-120)[85, 91], larger systems,[92, 93] as well as charged Au_6^{4+}, Au_{44}^{4+}, and Au_{146}^{2+} systems.[93] The real-time (RT) TDDFT approach has also been employed in

studying SPR emergence in pentagonal gold nanorods,[88, 94] icosahedral 147-atom gold and silver nanoparticles,[94] the absorption spectra of magic numbered Au_{13}, and Au_{55} clusters,[95] and Au_n nanoclusters (n = 54, 146, 308, 560, 922, 1414).[96]

1.3 Luminescence properties of noble metal nanoparticles

Luminescent metal nanoparticles are gaining ground as a new class of metal nanostructures. Their ultrafine size, good biocompatibility, and high stability have drawn increasing research interest during the past decade to replace semiconductor quantum dots and organic dyes in a wide range of applications including bio-imaging, sensing, and cancer therapy.[97-103] However, luminescence properties of noble metal nanoparticles are much less well-understood than their optical absorption properties.

1.3.1 Luminescence properties of thiolate protected gold and silver nanoparticles

In 2000, Whetten and coworkers studied the photoluminescence from gold nanocrystals that consist of 1.1 and 1.7 nm gold cores (about 38 and 145 atoms respectively) surrounded by a passivating layer of dodecanethiol molecules.[104] A novel near-infrared (1.1 – 1.6 μm) emission was observed with an estimated quantum yield of (4.4 ± 1.5) × 10^{-5} for the larger nanoparticle. This photoluminescence was assigned to *sp* to *sp*-like transitions, analogous to intraband transitions in bulk gold. Subsequently, visible wavelength fluorescence (700 – 800 nm) was reported for four water soluble monolayer-protected gold nanoparticles with a core diameter < 2 nm, and it was attributed to *d-sp* interband transitions.[105] Later, Murray and coworkers suggested that photoluminescence arises from surface states related to ligands rather than core-based transitions, since five gold nanoparticles having core sizes in the range of 11-201 atoms were found to emit over the same range of energies (0.9 – 1.8 eV) when excited at 451 nm.[106] Increased quantum yields ranging from 1 × 10^{-3} to 7 × 10^{-4} were observed for a group of glutathione protected gold nanoclusters having 18-39 core atoms that emit around 1.6 – 1.8 eV with a maximum Stokes shift of 0.4 eV.[32, 107] They suggested that emission occurs from vibrationally relaxed states of the first electronically excited state.

The primary focus of photoluminescence studies has been on the $Au_{25}(SR)_{18}^-$ system even before its crystal structure was determined. Extensive experimental investigations have

been performed to identify temperature, ligand, and charge state dependence of emission as well as to understand the photoluminescence mechanism of the 25-atom gold nanocluster. The earliest studies by Link et al.[108] and Murray and coworkers[109] reported two emission bands that indicated radiative recombination between the ground state and two excited states. Link et al.[108] used two models to explain the origin of the luminescence peaks around 1.15 and 1.5 eV. In the "solid state" model (Figure 1.4A) the two peaks were attributed to intraband and interband transitions whereas in the "molecular" model (Figure 1.4B) these were attributed to phosphorescence and fluorescence. Later, the emission peaks at 1.38 and 1.2 eV observed for the $Au_{25}(SR)_{18}$ (R = CH_2CH_2Ph) nanocluster were assigned to relaxed luminescence across the HOMO-LUMO gap and to sub-bandgap energy luminescence respectively.[109]

(A)

(B)
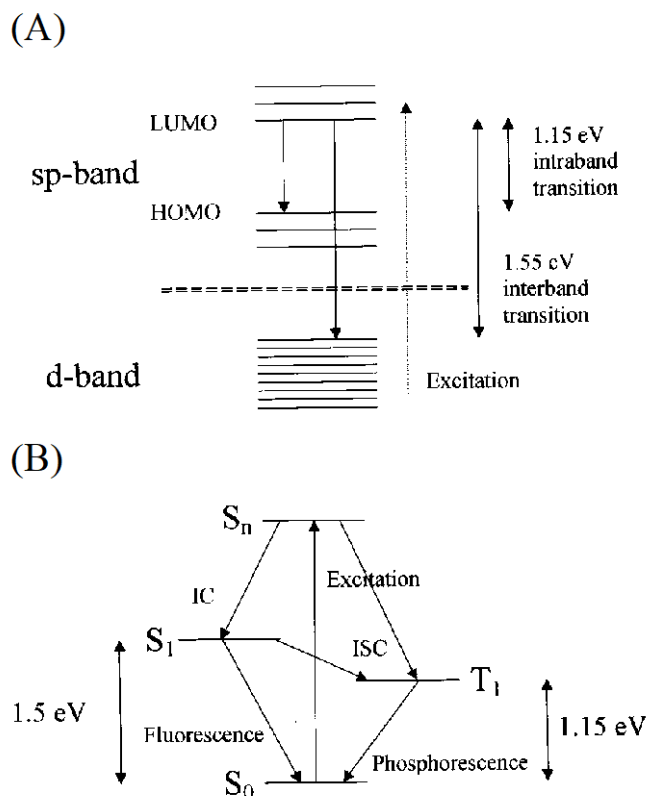
Figure 1.4 (A) Solid-state model and (B) Molecular model to explain the origin of the two luminescence bands (Reprinted with permission from *J. Phys. Chem. B* 2002, *106*, 3410-3415. Copyright 2002 American Chemical Society)

The ligand effect on the photoluminescence of the Au_{25} nanocluster has been explored. For glutathione protected Au_{25}, Pradeep and coworkers did not observe significant changes to the

luminescence peak lying around 1.7 – 1.8 eV upon ligand exchange.[110, 111] Therefore, the observed emission was attributed to electronic transitions associated with the gold core. Ramakrishna, Goodson, and coworkers also predicted that luminescence arises out of the Au_{25} core states since the growth time constants are independent of the passivating ligand.[112] However, the ligand-dependent decay of luminescence was attributed to the relaxation of Au_{25} core states to semi-ring states. Wang et al.[113] reported that increasing the number of polar ligands on the nanocluster linearly increases the luminescence intensity of the near-infrared peak. Furthermore, Wu and Jin observed that the ligand's ability to donate electron density to the metal core via the S-Au bond in $Au_{25}(SR)_{18}^-$ can enhance the fluorescence quantum yield.[114] They suggested that the photoluminescence mechanism is a ligand to metal nanoparticle core charge transfer (LMNCT). It has also been demonstrated that the higher electropositivity of the metal core enhances the fluorescence signal's intensity.

The temperature dependence of the emission of the Au_{25} nanocluster has also been investigated. The emission energy of the $Au_{25}(SG)_{18}$ did not change in the temperature range of 80 – 300 K, suggesting that there are no major geometric changes in the system affecting its electronic structure.[111] However, it was observed that the intensity of the fluorescence decreases with decreasing temperature implying that the non-radiative vibrational relaxation channel becomes prominent. Recently Knappenberger and co-workers showed that the luminescence intensity of a neutral phenylethanethiolate-stabilized Au_{25} nanoparticle increased with increasing temperature from 4.5 to 50 K but decreased as the temperature was further increased from 50 to 200 K.[115]

Other experimental studies have been carried out to investigate the photoluminescence properties of the monolayer protected Au_{38} nanoparticle as well. The emission of the hexanethiolate protected system was studied in the 4-300 K temperature regime.[116] At low temperatures, four emission bands were observed in the energy range of 0.97 – 1.47 eV. The energies and intensities of these peaks did not change significantly as a function of temperature. The lowest energy peak at 0.98 eV was attributed to the HOMO–LUMO transition and higher energy peaks at 1.15, 1.26, and 1.46 eV were attributed to transitions from higher excited states within the core. Recently, Knappenberger and coworkers also studied temperature-dependent photoluminescence of $Au_{38}(SC_{12}H_{25})_{24}$ in the temperature range of 4.5 – 200 K.[115] No significant change in emission intensities was observed in the 4.5 – 50 K temperature range, similar to the

previous study. However, in the 50 – 200 K temperature range, the intensities decreased while the peaks red-shifted. In the same temperature range, two emission bands were observed at 1.58 and 1.74 eV.

Recently, strongly luminescent $Au_{22}(SG)_{18}$ nanoclusters were synthesized, which emit in the visible/NIR region around 665 nm with a Stokes shift of 145 nm.[57] The microsecond-scale luminescence lifetime was attributed to possible long motifs on the cluster surface. Lee and coworkers rigidified the gold shell of this cluster using tetraoctylammonium cations to obtain an increased QY of 60%.[117] Combined time-resolved and temperature-dependent luminescence techniques suggested that the origin of luminescence is a ligand-to-metal–metal charge transfer state of the gold shell, which is a high QY triplet state in frozen media.

Luminescence properties of thiolate protected silver nanoclusters have not been studied as much as their gold counterparts. In 2010, Wang and coworkers reported a tetracationic cluster, $[Ag_{62}S_{13}(S^tBu)_{32}]^{4+}$, that displays intense red emission in both the solid state and solution at room temperature with a quantum yield of 0.014.[118] They tentatively assigned this red emission as originating from an excited state relating to charge transfer from S $3p$ to Ag $5s$ perturbed by $Ag(I)\cdots Ag(I)$ interactions. In 2015, the experimental emission curves of $[Ag_{25}(SR)_{18}]^-$ and $Ag_{29}(BDT)_{12}(TPP)_4$ (BDT, 1,3-benzenedithiol; TPP, triphenylphosphine) nanoclusters were reported,[67, 119] but no insight into the origin of their emission was described. More recently, Liu et al.[120] studied the crystal and solution photoluminescence of a series of center-doped $MAg_{24}(SR)_{18}$ (M = Ag/Pd/Pt/Au) nanoclusters. The crystal photoluminescence intensities followed a sequence of $PdAg_{24}(SR)_{18} < Ag_{25}(SR)_{18} < PtAg_{24}(SR)_{18} < AuAg_{24}(SR)_{18}$ that suggested a core-atom-directing charge transfer from the ligands to the metal kernels. It was further revealed that the solvent plays an important role in the photoluminescence intensity rather than the emission wavelength of Ag_{25} and doped systems.

1.4 Objectives and overview of the thesis

Photoluminescence of metal nanoparticles has drawn increasing research interest during the past decade due to their potential applications in biomedicine, photocatalysis, and optoelectronics. Despite the extensive experimental investigations performed on thiolate protected noble metal nanoparticles, the origin and underlying mechanism of photoluminescence in these systems still remain unclear. A main objective of this thesis is to unravel the origin of

photoluminescence and obtain atomistic details of the changes that occur upon photoexcitation for several thiolate-protected gold and silver nanoparticles. A secondary objective is to understand how the optical properties of the thiolate protected 20-atom gold cluster vary with aliphatic and aromatic ligands. The final objective of this thesis is to compare the optical absorption spectra calculated for a wide variety of bare gold and silver nanoclusters that differ in size and shape using two different approaches of time-dependent density functional theory (TDDFT): linear response (LR) TDDFT and real-time (RT) TDDFT.

Chapter 2 details the theory and computational methods used in this research. Chapter 3 (Weerawardene, K. L. D. M.; Aikens, C. M., *J. Am. Chem. Soc.* **2016**, *138*, 11202-11210) gives insights into the photoluminescence origin of $Au_{25}(SR)_{18}^-$ nanoparticles and discusses the ligand effects. In Chapter 4 (Weerawardene, K. L. D. M.; Guidez, E. B.; Aikens, C. M., *J. Phys. Chem. C* **2017**, *121*, 15416-15423), luminescence properties of $Au_{38}(SR)_{24}$ and $Au_{22}(SR)_{18}$ nanoparticles are described using TDDFT methods. Chapter 5 details theoretical investigations of the photoluminescence origin of thiolate-protected silver and doped silver nanoparticles. In Chapter 6 (Weerawardene, K. L. D. M.; Aikens, C. M., *J. Phys. Chem. C* **2016**, *120*, 8354-8363), the effects of aliphatic and aromatic ligands on the structure and optical absorption of $Au_{20}(SR)_{16}$ nanocluster are analyzed. Chapter 7 compares the optical absorption spectra calculated for bare gold and silver nanoclusters that differ in size and shape using LR and RT-TDDFT.

1.5 References

1.   Sun, Y., Conversion of Ag Nanowires to AgCl Nanowires Decorated with Au Nanoparticles and Their Photocatalytic Activity. *J. Phys. Chem. C* **2010**, *114*, 2127-2133.
2.   Rashid, M. H.; Bhattacharjee, R. R.; Kotal, A.; Mandal, T. K., Synthesis of Spongy Gold Nanocrystals with Pronounced Catalytic Activities. *Langmuir* **2006**, *22*, 7141-7143.
3.   Chen, Y.-S.; Choi, H.; Kamat, P. V., Metal-Cluster-Sensitized Solar Cells. A New Class of Thiolated Gold Sensitizers Delivering Efficiency Greater Than 2%. *J. Am. Chem. Soc.* **2013**, *135*, 8822-8825.
4.   Hirakawa, T.; Kamat, P. V., Photoinduced Electron Storage and Surface Plasmon Modulation in $Ag@TiO_2$ Clusters. *Langmuir* **2004**, *20*, 5645-5647.
5.   Jiang, S.; Win, K. Y.; Liu, S.; Teng, C. P.; Zheng, Y.; Han, M.-Y., Surface-Functionalized Nanoparticles for Biosensing and Imaging-Guided Therapeutics. *Nanoscale* **2013**, *5*, 3127-3148.
6.   Mahmoud, M. A.; El-Sayed, M. A., Different Plasmon Sensing Behavior of Silver and Gold Nanorods. *J. Phys. Chem. Lett.* **2013**, *4*, 1541-1545.
7.   Saha, K.; Agasti, S. S.; Kim, C.; Li, X.; Rotello, V. M., Gold Nanoparticles in Chemical and Biological Sensing. *Chem. Rev.* **2012**, *112*, 2739-2779.

8.　　Arvizo, R. R.; Bhattacharyya, S.; Kudgus, R. A.; Giri, K.; Bhattacharya, R.; Mukherjee, P., Intrinsic Therapeutic Applications of Noble Metal Nanoparticles: Past, Present and Future. *Chem. Soc. Rev.* **2012**, *41*, 2943-2970.

9.　　Zhou, W.; Gao, X.; Liu, D.; Chen, X., Gold Nanoparticles for In Vitro Diagnostics. *Chem. Rev.* **2015**, *115*, 10575-10636.

10.　　Jadzinsky, P. D.; Calero, G.; Ackerson, C. J.; Bushnell, D. A.; Kornberg, R. D., Structure of a Thiol Monolayer-Protected Gold Nanoparticle at 1.1 Å Resolution. *Science* **2007**, *318*, 430-433.

11.　　Heaven, M. W.; Dass, A.; White, P. S.; Holt, K. M.; Murray, R. W., Crystal Structure of the Gold Nanoparticle $[N(C_8H_{17})_4][Au_{25}(SCH_2CH_2Ph)_{18}]$. *J. Am. Chem. Soc.* **2008**, *130*, 3754-3755.

12.　　Zhu, M.; Aikens, C. M.; Hollander, F. J.; Schatz, G. C.; Jin, R., Correlating the Crystal Structure of A Thiol-Protected Au_{25} Cluster and Optical Properties. *J. Am. Chem. Soc.* **2008**, *130*, 5883-5885.

13.　　Häkkinen, H.; Walter, M.; Grönbeck, H., Divide and Protect: Capping Gold Nanoclusters with Molecular Gold−Thiolate Rings. *J. Phys. Chem. B* **2006**, *110*, 9927-9931.

14.　　Khanna, S. N.; Jena, P., Assembling Crystals from Clusters. *Phys. Rev. Lett.* **1992**, *69*, 1664-1667.

15.　　Castleman, A. W., From Elements to Clusters: The Periodic Table Revisited. *J. Phys. Chem. Lett.* **2011**, *2*, 1062-1069.

16.　　de Heer, W. A., The Physics of Simple Metal Clusters: Experimental Aspects and Simple Models. *Rev. Mod. Phys.* **1993**, *65*, 611-676.

17.　　Walter, M.; Akola, J.; Lopez-Acevedo, O.; Jadzinsky, P. D.; Calero, G.; Ackerson, C. J.; Whetten, R. L.; Grönbeck, H.; Häkkinen, H., A Unified View of Ligand-Protected Gold Clusters as Superatom Complexes. *Proc. Natl. Acad. Sci. U.S.A.* **2008**, *105*, 9157-9162.

18.　　Hakkinen, H., Atomic and Electronic Structure of Gold Clusters: Understanding Flakes, Cages and Superatoms from Simple Concepts. *Chem. Soc. Rev.* **2008**, *37*, 1847-1859.

19.　　Lopez-Acevedo, O.; Akola, J.; Whetten, R. L.; Grönbeck, H.; Häkkinen, H., Structure and Bonding in the Ubiquitous Icosahedral Metallic Gold Cluster $Au_{144}(SR)_{60}$. *J. Phys. Chem. C* **2009**, *113*, 5035-5038.

20.　　Dass, A., Faradaurate Nanomolecules: A Superstable Plasmonic 76.3 kDa Cluster. *J. Am. Chem. Soc.* **2011**, *133*, 19259-19261.

21.　　Qian, H.; Zhu, Y.; Jin, R., Atomically Precise Gold Nanocrystal Molecules with Surface Plasmon Resonance. *Proc. Natl. Acad. Sci. U.S.A.* **2012**, *109*, 696-700.

22.　　Wong, O. A.; Heinecke, C. L.; Simone, A. R.; Whetten, R. L.; Ackerson, C. J., Ligand Symmetry-Equivalence on Thiolate Protected Gold Nanoclusters Determined by NMR Spectroscopy. *Nanoscale* **2012**, *4*, 4099-4102.

23.　　Lopez-Acevedo, O.; Tsunoyama, H.; Tsukuda, T.; Häkkinen, H.; Aikens, C. M., Chirality and Electronic Structure of the Thiolate-Protected Au_{38} Nanocluster. *J. Am. Chem. Soc.* **2010**, *132*, 8210-8218.

24.　　Halas, N. J.; Lal, S.; Chang, W.-S.; Link, S.; Nordlander, P., Plasmons in Strongly Coupled Metallic Nanostructures. *Chem. Rev.* **2011**, *111*, 3913-3961.

25.　　Chen, H.; Shao, L.; Li, Q.; Wang, J., Gold nanorods and their plasmonic properties. *Chem. Soc. Rev.* **2013**, *42*, 2679-2724.

26.　　Vincenzo, A.; Roberto, P.; Marco, F.; Onofrio, M. M.; Maria Antonia, I., Surface plasmon resonance in gold nanoparticles: a review. *J. Phys.: Condens. Matter* **2017**, *29*, 203002.

27.	Yang, H.; Wang, Y.; Chen, X.; Zhao, X.; Gu, L.; Huang, H.; Yan, J.; Xu, C.; Li, G.; Wu, J.; Edwards, A. J.; Dittrich, B.; Tang, Z.; Wang, D.; Lehtovaara, L.; Häkkinen, H.; Zheng, N., Plasmonic twinned silver nanoparticles with molecular precision. *Nat. Commun.* **2016**, *7*, 12809.

28.	Willets, K. A.; Duyne, R. P. V., Localized Surface Plasmon Resonance Spectroscopy and Sensing. *Annu. Rev. Phys. Chem.* **2007**, *58*, 267-297.

29.	Mie, G., Beiträge zur Optik trüber Medien, speziell kolloidaler Metallösungen. *Ann. Phys.* **1908**, *330*, 377-445.

30.	Harbich, W.; Fedrigo, S.; Buttet, J., The Optical Absorption Spectra of Small Silver Clusters (n=5–11) Embedded in Argon Matrices. *Chem. Phys. Lett.* **1992**, *195*, 613-617.

31.	Harb, M.; Rabilloud, F.; Simon, D.; Rydlo, A.; Lecoultre, S.; Conus, F.; Rodrigues, V.; Félix, C., Optical absorption of small silver clusters: Ag_n, (n=4–22). *J. Chem. Phys.* **2008**, *129*, 194108.

32.	Negishi, Y.; Nobusada, K.; Tsukuda, T., Glutathione-Protected Gold Clusters Revisited: Bridging the Gap between Gold(I)−Thiolate Complexes and Thiolate-Protected Gold Nanocrystals. *J. Am. Chem. Soc.* **2005**, *127*, 5261-5270.

33.	Shichibu, Y.; Negishi, Y.; Tsukuda, T.; Teranishi, T., Large-Scale Synthesis of Thiolated Au_{25} Clusters via Ligand Exchange Reactions of Phosphine-Stabilized Au_{11} Clusters. *J. Am. Chem. Soc.* **2005**, *127*, 13464-13465.

34.	Negishi, Y.; Chaki, N. K.; Shichibu, Y.; Whetten, R. L.; Tsukuda, T., Origin of Magic Stability of Thiolated Gold Clusters: A Case Study on $Au_{25}(SC_6H_{13})_{18}$. *J. Am. Chem. Soc* **2007**, *129*, 11322-11323.

35.	Zhu, M.; Eckenhoff, W. T.; Pintauer, T.; Jin, R., Conversion of Anionic $[Au_{25}(SCH_2CH_2Ph)_{18}]^-$ Cluster to Charge Neutral Cluster via Air Oxidation. *J. Phys. Chem. C* **2008**, *112*, 14221-14224.

36.	Tofanelli, M. A.; Salorinne, K.; Ni, T. W.; Malola, S.; Newell, B.; Phillips, B.; Hakkinen, H.; Ackerson, C. J., Jahn-Teller effects in $Au_{25}(SR)_{18}$. *Chem. Sci.* **2016**, *7*, 1882-1890.

37.	Guo, R.; Murray, R. W., Substituent Effects on Redox Potentials and Optical Gap Energies of Molecule-like $Au_{38}(SPhX)_{24}$ Nanoparticles. *J. Am. Chem. Soc.* **2005**, *127*, 12140-12143.

38.	Akola, J.; Walter, M.; Whetten, R. L.; Häkkinen, H.; Grönbeck, H., On the Structure of Thiolate-Protected Au_{25}. *J. Am. Chem. Soc.* **2008**, *130*, 3756-3757.

39.	Aikens, C. M., Effects of Core Distances, Solvent, Ligand, and Level of Theory on the TDDFT Optical Absorption Spectrum of the Thiolate-Protected Au_{25} Nanoparticle. *J. Phys. Chem. A* **2009**, *113*, 10811-10817.

40.	Aikens, C. M., Geometric and Electronic Structure of $Au_{25}(SPhX)_{18}-$ (X = H, F, Cl, Br, CH_3, and OCH_3). *J. Phys. Chem. Lett.* **2010**, *1*, 2594-2599.

41.	Tlahuice-Flores, A.; Whetten, R. L.; Jose-Yacaman, M., Ligand Effects on the Structure and the Electronic Optical Properties of Anionic $Au_{25}(SR)_{18}$ Clusters. *J. Phys. Chem. C* **2013**, *117*, 20867-20875.

42.	Akola, J.; Kacprzak, K. A.; Lopez-Acevedo, O.; Walter, M.; Grönbeck, H.; Häkkinen, H., Thiolate-Protected Au_{25} Superatoms as Building Blocks: Dimers and Crystals. *J. Phys. Chem. C* **2010**, *114*, 15986-15994.

43.	Jiang, D.-e.; Kühn, M.; Tang, Q.; Weigend, F., Superatomic Orbitals under Spin–Orbit Coupling. *J. Phys. Chem. Lett.* **2014**, *5*, 3286-3289.

44. Antonello, S.; Perera, N. V.; Ruzzi, M.; Gascón, J. A.; Maran, F., Interplay of Charge State, Lability, and Magnetism in the Molecule-like $Au_{25}(SR)_{18}$ Cluster. *J. Am. Chem. Soc.* **2013**, *135*, 15585-15594.

45. Zhu, M.; Aikens, C. M.; Hendrich, M. P.; Gupta, R.; Qian, H.; Schatz, G. C.; Jin, R., Reversible Switching of Magnetism in Thiolate-Protected Au_{25} Superatoms. *J. Am. Chem. Soc.* **2009**, *131*, 2490-2492.

46. Pei, Y.; Gao, Y.; Zeng, X. C., Structural Prediction of Thiolate-Protected Au_{38}: A Face-Fused Bi-icosahedral Au Core. *J. Am. Chem. Soc.* **2008**, *130*, 7830-7832.

47. Pei, Y.; Gao, Y.; Shao, N.; Zeng, X. C., Thiolate-Protected $Au_{20}(SR)_{16}$ Cluster: Prolate Au_8 Core with New $[Au_3(SR)_4]$ Staple Motif. *J. Am. Chem. Soc.* **2009**, *131*, 13619-13621.

48. Zhu, M.; Qian, H.; Jin, R., Thiolate-Protected Au_{20} Clusters with a Large Energy Gap of 2.1 eV. *J. Am. Chem. Soc.* **2009**, *131*, 7220-7221.

49. Zeng, C.; Liu, C.; Chen, Y.; Rosi, N. L.; Jin, R., Gold–Thiolate Ring as a Protecting Motif in the $Au_{20}(SR)_{16}$ Nanocluster and Implications. *J. Am. Chem. Soc.* **2014**, *136*, 11922-11925.

50. Weerawardene, K. L. D. M.; Aikens, C. M., Effect of Aliphatic versus Aromatic Ligands on the Structure and Optical Absorption of $Au_{20}(SR)_{16}$. *J. Phys. Chem. C* **2016**, *120*, 8354-8363.

51. Malola, S.; Lehtovaara, L.; Knoppe, S.; Hu, K.-J.; Palmer, R. E.; Bürgi, T.; Häkkinen, H., $Au_{40}(SR)_{24}$ Cluster as a Chiral Dimer of 8-Electron Superatoms: Structure and Optical Properties. *J. Am. Chem. Soc.* **2012**, *134*, 19560-19563.

52. Pei, Y.; Lin, S.; Su, J.; Liu, C., Structure Prediction of $Au_{44}(SR)_{28}$: A Chiral Superatom Cluster. *J. Am. Chem. Soc.* **2013**, *135*, 19060-19063.

53. Jiang, D.-e.; Walter, M.; Akola, J., On the Structure of a Thiolated Gold Cluster: $Au_{44}(SR)_{28}^{2-}$. *J. Phys. Chem. C* **2010**, *114*, 15883-15889.

54. Jiang, D.-e., The Expanding Universe of Thiolated Gold Nanoclusters and Beyond. *Nanoscale* **2013**, *5*, 7149-7160.

55. Tlahuice-Flores, A.; Jose-Yacaman, M.; Whetten, R. L., On the Structure of the Thiolated Au_{15} Cluster. *Phys. Chem. Chem. Phys.* **2013**, *15*, 19557-19560.

56. Jiang, D.-e.; Overbury, S. H.; Dai, S., Structure of $Au_{15}(SR)_{13}$ and Its Implication for the Origin of the Nucleus in Thiolated Gold Nanoclusters. *J. Am. Chem. Soc.* **2013**, *135*, 8786-8789.

57. Pei, Y.; Tang, J.; Tang, X.; Huang, Y.; Zeng, X. C., New Structure Model of $Au_{22}(SR)_{18}$: Bitetrahederon Golden Kernel Enclosed by $[Au_6(SR)_6]$ Au(I) Complex. *J. Phys. Chem. Lett.* **2015**, *6*, 1390-1395.

58. Yu, Y.; Luo, Z.; Chevrier, D. M.; Leong, D. T.; Zhang, P.; Jiang, D.-e.; Xie, J., Identification of a Highly Luminescent $Au_{22}(SG)_{18}$ Nanocluster. *J. Am. Chem. Soc.* **2014**, *136*, 1246-1249.

59. Das, A.; Li, T.; Li, G.; Nobusada, K.; Zeng, C.; Rosi, N. L.; Jin, R., Crystal Structure and Electronic Properties of a Thiolate-Protected Au_{24} Nanocluster. *Nanoscale* **2014**, *6*, 6458-6462.

60. Das, A.; Li, T.; Nobusada, K.; Zeng, C.; Rosi, N. L.; Jin, R., Nonsuperatomic $[Au_{23}(SC_6H_{11})_{16}]^-$ Nanocluster Featuring Bipyramidal Au15 Kernel and Trimeric $Au_3(SR)_4$ Motif. *J. Am. Chem. Soc.* **2013**, *135*, 18264-18267.

61. Crasto, D.; Malola, S.; Brosofsky, G.; Dass, A.; Häkkinen, H., Single Crystal XRD Structure and Theoretical Analysis of the Chiral $Au_{30}S(S$-t-Bu$)_{18}$ Cluster. *J. Am. Chem. Soc.* **2014**, *136*, 5000-5005.

62. Zhu, M.; Qian, H.; Jin, R., Thiolate-Protected $Au_{24}(SC_2H_4Ph)_{20}$ Nanoclusters: Superatoms or Not? *J. Phys. Chem. Lett.* **2010**, *1*, 1003-1007.

63.   Zeng, C.; Liu, C.; Pei, Y.; Jin, R., Thiol Ligand-Induced Transformation of Au$_{38}$(SC$_2$H$_4$Ph)$_{24}$ to Au$_{36}$(SPh-*t*-Bu)$_{24}$. *ACS Nano* **2013**, *7*, 6138-6145.

64.   Nimmala, P. R.; Knoppe, S.; Jupally, V. R.; Delcamp, J. H.; Aikens, C. M.; Dass, A., Au$_{36}$(SPh)$_{24}$ Nanomolecules: X-ray Crystal Structure, Optical Spectroscopy, Electrochemistry, and Theoretical Analysis. *J. Phys. Chem. B* **2014**, *118*, 14157-14167.

65.   Knoppe, S.; Malola, S.; Lehtovaara, L.; Bürgi, T.; Häkkinen, H., Electronic Structure and Optical Properties of the Thiolate-Protected Au$_{28}$(SMe)$_{20}$ Cluster. *J. Phys. Chem. A* **2013**, *117*, 10526-10533.

66.   Aikens, C. M., Origin of Discrete Optical Absorption Spectra of M$_{25}$(SH)$_{18}^-$ Nanoparticles (M = Au, Ag). *J. Phys. Chem. C* **2008**, *112*, 19797-19800.

67.   Joshi, C. P.; Bootharaju, M. S.; Alhilaly, M. J.; Bakr, O. M., [Ag$_{25}$(SR)$_{18}$]$^-$: The "Golden" Silver Nanoparticle. *J. Am. Chem. Soc.* **2015**, *137*, 11578-11581.

68.   Harkness, K. M.; Tang, Y.; Dass, A.; Pan, J.; Kothalawala, N.; Reddy, V. J.; Cliffel, D. E.; Demeler, B.; Stellacci, F.; Bakr, O. M.; McLean, J. A., Ag$_{44}$(SR)$_{30}^{4-}$: A Silver-Thiolate Superatom Complex. *Nanoscale* **2012**, *4*, 4269-4274.

69.   Desireddy, A.; Conn, B. E.; Guo, J.; Yoon, B.; Barnett, R. N.; Monahan, B. M.; Kirschbaum, K.; Griffith, W. P.; Whetten, R. L.; Landman, U.; Bigioni, T. P., Ultrastable silver nanoparticles. *Nature* **2013**, *501*, 399-402.

70.   Yang, H.; Wang, Y.; Huang, H.; Gell, L.; Lehtovaara, L.; Malola, S.; Häkkinen, H.; Zheng, N., All-thiol-stabilized Ag$_{44}$ and Au$_{12}$Ag$_{32}$ nanoparticles with single-crystal structures. *Nat. Commun.* **2013**, *4*, 2422.

71.   Bertorelle, F.; Hamouda, R.; Rayane, D.; Broyer, M.; Antoine, R.; Dugourd, P.; Gell, L.; Kulesza, A.; Mitric, R.; Bonacic-Koutecky, V., Synthesis, Characterization and Optical Properties of Low Nuclearity Liganded Silver Clusters: Ag$_{31}$(SG)$_{19}$ and Ag$_{15}$(SG)$_{11}$. *Nanoscale* **2013**, *5*, 5637-5643.

72.   Kelly, K. L.; Coronado, E.; Zhao, L. L.; Schatz, G. C., The Optical Properties of Metal Nanoparticles: The Influence of Size, Shape, and Dielectric Environment. *J. Phys. Chem. B* **2003**, *107*, 668-677.

73.   Szymańska-Chargot, M.; Gruszecka, A.; Smolira, A.; Bederski, K.; Głuch, K.; Cytawa, J.; Michalak, L., Formation of Nanoparticles and Nanorods via UV Irradiation of AgNO$_3$ Solutions. *J. Alloys Compd.* **2009**, *486*, 66-69.

74.   Wiley, B. J.; Chen, Y.; McLellan, J. M.; Xiong, Y.; Li, Z.-Y.; Ginger, D.; Xia, Y., Synthesis and Optical Properties of Silver Nanobars and Nanorice. *Nano Lett.* **2007**, *7*, 1032-1036.

75.   Sun, Y.; Gates, B.; Mayers, B.; Xia, Y., Crystalline Silver Nanowires by Soft Solution Processing. *Nano Lett.* **2002**, *2*, 165-168.

76.   Wei, H.; Hao, F.; Huang, Y.; Wang, W.; Nordlander, P.; Xu, H., Polarization Dependence of Surface-Enhanced Raman Scattering in Gold Nanoparticle−Nanowire Systems. *Nano Lett.* **2008**, *8*, 2497-2502.

77.   Seo, D.; Park, J. C.; Song, H., Polyhedral Gold Nanocrystals with O$_h$ Symmetry: From Octahedra to Cubes. *J. Am. Chem. Soc.* **2006**, *128*, 14863-14870.

78.   Im, S. H.; Lee, Y. T.; Wiley, B.; Xia, Y., Large-Scale Synthesis of Silver Nanocubes: The Role of HCl in Promoting Cube Perfection and Monodispersity. *Angew. Chem., Int. Ed.* **2005**, *44*, 2154-2157.

79.   Eguchi, M.; Mitsui, D.; Wu, H.-L.; Sato, R.; Teranishi, T., Simple Reductant Concentration-Dependent Shape Control of Polyhedral Gold Nanoparticles and Their Plasmonic Properties. *Langmuir* **2012**, *28*, 9021-9026.

80.   Kim, F.; Connor, S.; Song, H.; Kuykendall, T.; Yang, P., Platonic Gold Nanocrystals. *Angew. Chem.* **2004**, *116*, 3759-3763.

81.   Jin, R.; Cao, Y.; Mirkin, C. A.; Kelly, K. L.; Schatz, G. C.; Zheng, J. G., Photoinduced Conversion of Silver Nanospheres to Nanoprisms. *Science* **2001**, *294*, 1901-1903.

82.   Millstone, J. E.; Park, S.; Shuford, K. L.; Qin, L.; Schatz, G. C.; Mirkin, C. A., Observation of a Quadrupole Plasmon Mode for a Colloidal Solution of Gold Nanoprisms. *J. Am. Chem. Soc.* **2005**, *127*, 5312-5313.

83.   Fedrigo, S.; Harbich, W.; Buttet, J., Collective Dipole Oscillations in Small Silver Clusters Embedded in Rare-Gas Matrices. *Phys. Rev. B* **1993**, *47*, 10706-10715.

84.   Tiggesbäumker, J.; Köller, L.; Meiwes-Broer, K.-H.; Liebsch, A., Blue Shift of the Mie Plasma Frequency in Ag Clusters and Particles. *Phys. Rev. A* **1993**, *48*, R1749-R1752.

85.   Johnson, H. E.; Aikens, C. M., Electronic Structure and TDDFT Optical Absorption Spectra of Silver Nanorods. *J. Phys. Chem. A* **2009**, *113*, 4445-4450.

86.   Fernando, A.; Weerawardene, K. L. D. M.; Karimova, N. V.; Aikens, C. M., Quantum Mechanical Studies of Large Metal, Metal Oxide, and Metal Chalcogenide Nanoparticles and Clusters. *Chem. Rev.* **2015**, *115*, 6112-6216.

87.   Bae, G.-T.; Aikens, C. M., Time-Dependent Density Functional Theory Studies of Optical Properties of Au Nanoparticles: Octahedra, Truncated Octahedra, and Icosahedra. *J. Phys. Chem. C* **2015**, *119*, 23127-23137.

88.   Lopez-Lozano, X.; Barron, H.; Mottet, C.; Weissker, H.-C., Aspect-Ratio- and Size-Dependent Emergence of the Surface-Plasmon Resonance in Gold Nanorods - an *ab initio* TDDFT study. *Phys. Chem. Chem. Phys.* **2014**, *16*, 1820-1823.

89.   Weissker, H. C.; Escobar, H. B.; Thanthirige, V. D.; Kwak, K.; Lee, D.; Ramakrishna, G.; Whetten, R. L.; López-Lozano, X., Information on Quantum States Pervades the Visible Spectrum of the Ubiquitous $Au_{144}(SR)_{60}$ Gold Nanocluster. *Nat. Commun.* **2014**, *5*, 3785.

90.   Bae, G.-T.; Aikens, C. M., Time-Dependent Density Functional Theory Studies of Optical Properties of Ag Nanoparticles: Octahedra, Truncated Octahedra, and Icosahedra. *J. Phys. Chem. C* **2012**, *116*, 10356-10367.

91.   Aikens, C. M.; Li, S.; Schatz, G. C., From Discrete Electronic States to Plasmons: TDDFT Optical Absorption Properties of Ag_n (n = 10, 20, 35, 56, 84, 120) Tetrahedral Clusters. *J. Phys. Chem. C* **2008**, *112*, 11272-11279.

92.   Barcaro, G.; Broyer, M.; Durante, N.; Fortunelli, A.; Stener, M., Alloying Effects on the Optical Properties of Ag–Au Nanoclusters from TDDFT Calculations. *J. Phys. Chem. C* **2011**, *115*, 24085-24091.

93.   Stener, M.; Nardelli, A.; De Francesco, R.; Fronzoni, G., Optical Excitations of Gold Nanoparticles: A Quantum Chemical Scalar Relativistic Time Dependent Density Functional Study. *J. Phys. Chem. C* **2007**, *111*, 11862-11871.

94.   Weissker, H.-C.; Lopez-Lozano, X., Surface Plasmons in Quantum-Sized Noble-Metal Clusters: TDDFT Quantum Calculations and the Classical Picture of Charge Oscillations. *Phys. Chem. Chem. Phys.* **2015**, *17*, 28379-28386.

95.   Weissker, H. C.; Mottet, C., Optical Properties of Pure and Core-Shell Noble-Metal Nanoclusters from TDDFT: The Influence of the Atomic Structure. *Phys. Rev. B* **2011**, *84*, 165443.

96.   Iida, K.; Noda, M.; Ishimura, K.; Nobusada, K., First-Principles Computational Visualization of Localized Surface Plasmon Resonance in Gold Nanoclusters. *J. Phys. Chem. A* **2014**, *118*, 11317-11322.

97.   Liu, J.; Yu, M.; Zhou, C.; Yang, S.; Ning, X.; Zheng, J., Passive Tumor Targeting of Renal-Clearable Luminescent Gold Nanoparticles: Long Tumor Retention and Fast Normal Tissue Clearance. *J. Am. Chem. Soc.* **2013**, *135*, 4978-4981.

98.   Liu, J.; Yu, M.; Ning, X.; Zhou, C.; Yang, S.; Zheng, J., PEGylation and Zwitterionization: Pros and Cons in Renal Clearance and Tumor Targeting of Near-IR-Emitting Gold Nanoparticles. *Angew. Chem., Int. Ed.* **2013**, *52*, 12572-12576.

99.   Shiang, Y.-C.; Huang, C.-C.; Chen, W.-Y.; Chen, P.-C.; Chang, H.-T., Fluorescent Gold and Silver Nanoclusters for the Analysis of Biopolymers and Cell Imaging. *J. Mater. Chem.* **2012**, *22*, 12972-12982.

100.   Yuan, X.; Luo, Z.; Yu, Y.; Yao, Q.; Xie, J., Luminescent Noble Metal Nanoclusters as an Emerging Optical Probe for Sensor Development. *Chem.–Asian J.* **2013**, *8*, 858-871.

101.   Shang, L.; Dong, S.; Nienhaus, G. U., Ultra-Small Fluorescent Metal Nanoclusters: Synthesis and Biological Applications. *Nano Today* **2011**, *6*, 401-418.

102.   Luo, Z.; Zheng, K.; Xie, J., Engineering Ultrasmall Water-Soluble Gold and Silver Nanoclusters for Biomedical Applications. *Chem. Commun.* **2014**, *50*, 5143-5155.

103.   Chang, W. H.; Lin, C.-A. J.; Lee, C.-H.; Hsieh, J.-T.; Wang, H.-H.; Li, J. K.; Shen, J.-L.; Chan, W.-H.; Yeh, H.-I., Review: Synthesis of Fluorescent Metallic Nanoclusters toward Biomedical Application: Recent Progress and Present Challenges. *J. Med. Biol. Eng.* **2009**, *29*, 276-283.

104.   Bigioni, T. P.; Whetten, R. L.; Dag, Ö., Near-Infrared Luminescence from Small Gold Nanocrystals. *J. Phys. Chem. B* **2000**, *104*, 6983-6986.

105.   Huang, T.; Murray, R. W., Visible Luminescence of Water-Soluble Monolayer-Protected Gold Clusters. *J. Phys. Chem. B* **2001**, *105*, 12498-12502.

106.   Wang, G.; Huang, T.; Murray, R. W.; Menard, L.; Nuzzo, R. G., Near-IR Luminescence of Monolayer-Protected Metal Clusters. *J. Am. Chem. Soc.* **2005**, *127*, 812-813.

107.   Negishi, Y.; Takasugi, Y.; Sato, S.; Yao, H.; Kimura, K.; Tsukuda, T., Magic-Numbered Au_n Clusters Protected by Glutathione Monolayers (n = 18, 21, 25, 28, 32, 39): Isolation and Spectroscopic Characterization. *J. Am. Chem. Soc.* **2004**, *126*, 6518-6519.

108.   Link, S.; Beeby, A.; FitzGerald, S.; El-Sayed, M. A.; Schaaff, T. G.; Whetten, R. L., Visible to Infrared Luminescence from a 28-Atom Gold Cluster. *J. Phys. Chem. B* **2002**, *106*, 3410-3415.

109.   Lee, D.; Donkers, R. L.; Wang, G.; Harper, A. S.; Murray, R. W., Electrochemistry and Optical Absorbance and Luminescence of Molecule-like Au_{38} Nanoparticles. *J. Am. Chem. Soc.* **2004**, *126*, 6193-6199.

110.   Shibu, E. S.; Muhammed, M. A. H.; Tsukuda, T.; Pradeep, T., Ligand Exchange of $Au_{25}SG_{18}$ Leading to Functionalized Gold Clusters: Spectroscopy, Kinetics, and Luminescence. *J. Phys. Chem. C* **2008**, *112*, 12168-12176.

111.   Shibu, E. S.; Pradeep, T., Photoluminescence and Temperature-Dependent Emission Studies of Au_{25} Clusters in the Solid State. *Int. J. Nanosci.* **2009**, *08*, 223-226.

112.   Devadas, M. S.; Kim, J.; Sinn, E.; Lee, D.; Goodson, T.; Ramakrishna, G., Unique Ultrafast Visible Luminescence in Monolayer-Protected Au_{25} Clusters. *J. Phys. Chem. C* **2010**, *114*, 22417-22423.

113.   Wang, G.; Guo, R.; Kalyuzhny, G.; Choi, J.-P.; Murray, R. W., NIR Luminescence Intensities Increase Linearly with Proportion of Polar Thiolate Ligands in Protecting Monolayers of Au_{38} and Au_{140} Quantum Dots. *J. Phys. Chem. B* **2006**, *110*, 20282-20289.

114.   Wu, Z.; Jin, R., On the Ligand's Role in the Fluorescence of Gold Nanoclusters. *Nano Lett.* **2010**, *10*, 2568-2573.

115.   Green, T. D.; Yi, C.; Zeng, C.; Jin, R.; McGill, S.; Knappenberger, K. L., Temperature-Dependent Photoluminescence of Structurally-Precise Quantum-Confined $Au_{25}(SC_8H_9)_{18}$ and $Au_{38}(SC_{12}H_{25})_{24}$ Metal Nanoparticles. *J. Phys. Chem. A* **2014**, *118*, 10611-10621.

116.   Wijngaarden, J. T. v.; Toikkanen, O.; Liljeroth, P.; Quinn, B. M.; Meijerink, A., Temperature-Dependent Emission of Monolayer-Protected Au_{38} Clusters. *J. Phys. Chem. C* **2010**, *114*, 16025-16028.

117.   Pyo, K.; Thanthirige, V. D.; Kwak, K.; Pandurangan, P.; Ramakrishna, G.; Lee, D., Ultrabright Luminescence from Gold Nanoclusters: Rigidifying the Au(I)–Thiolate Shell. *J. Am. Chem. Soc.* **2015**, *137*, 8244-8250.

118.   Li, G.; Lei, Z.; Wang, Q.-M., Luminescent Molecular Ag−S Nanocluster $[Ag_{62}S_{13}(SBu^t)_{32}](BF_4)_4$. *J. Am. Chem. Soc.* **2010**, *132*, 17678-17679.

119.   AbdulHalim, L. G.; Bootharaju, M. S.; Tang, Q.; Del Gobbo, S.; AbdulHalim, R. G.; Eddaoudi, M.; Jiang, D.-e.; Bakr, O. M., $Ag_{29}(BDT)_{12}(TPP)_4$: A Tetravalent Nanocluster. *J. Am. Chem. Soc.* **2015**, *137*, 11970-11975.

120.   Liu, X.; Yuan, J.; Yao, C.; Chen, J.; Li, L.; Bao, X.; Yang, J.; Wu, Z., Crystal and Solution Photoluminescence of $MAg_{24}(SR)_{18}$ (M = Ag/Pd/Pt/Au) Nanoclusters and Some Implications for the Photoluminescence Mechanisms. *J. Phys. Chem. C* **2017**, *121*, 13848-13853.

Chapter 2 - Theory and computational methods

2.1 Quantum mechanics

2.1.1 The Schrödinger equation

Classical mechanics, which covers the laws of motion of macroscopic objects, does not correctly describe the behavior of very small particles such as the electrons and nuclei of atoms and molecules. Quantum mechanics should be applied to describe the behavior of such particles. A state function or wave function Ψ, which depends on both the coordinates of the particles of the system (r) and time (t), defines the state of a quantum-mechanical system. It contains all the information one can possibly know about the system. The state function changes with time according to the time-dependent Schrödinger equation (TDSE). For a one particle, one-dimensional system, the TDSE equation is,

$$i\hbar \frac{\partial \Psi(x,t)}{\partial t} = \hat{H}\Psi(x,t)$$
$$= -\frac{\hbar^2}{2m}\frac{\partial^2 \Psi(x,t)}{\partial x^2} + V(x,t)\Psi(x,t)$$

(2.1)

where the constant $\hbar$ is defined as $h/2\rho$, $i = \sqrt{-1}$, and m is the mass of the particle. The first term of the Hamiltonian ($\hat{H}$) represents the kinetic energy of the particles and $V(x,t)$ is the potential energy of the system. For a one particle, one-dimensional system, the probability of finding the particle at time t in the region of the x axis lying between x and $x + dx$ is,

$$\left| \Psi(x,t) \right|^2 dx$$

(2.2)

When the system experiences no time-dependent external forces, the potential energy V is not a function of time but depends only on x. For such systems, the simpler time-independent Schrödinger equation (TISE) can be applied.

$$E\psi(x) = \hat{H}\psi(x)$$
$$= -\frac{\hbar^2}{2m}\frac{d^2\psi(x)}{dx^2} + V(x)\psi(x)$$

(2.3)

The $\psi(x)$ represents stationary states, where the probability density does not change with time. E is the energy of the system.

2.1.2 Born-Oppenheimer approximation

The non-relativistic, time-independent Hamiltonian for a system of nuclei and electrons has the following form:

$$\hat{H} = -\frac{\hbar^2}{2}\sum_{\alpha}\frac{1}{m_\alpha}\nabla_\alpha^2 - \frac{\hbar^2}{2m_e}\sum_i\nabla_i^2 - \sum_\alpha\sum_i\frac{Z_\alpha e'^2}{r_{i\alpha}} + \sum_j\sum_{i>j}\frac{e'^2}{r_{ij}} + \sum_\alpha\sum_{\beta>\alpha}\frac{Z_\alpha Z_\beta e'^2}{r_{\alpha\beta}}$$

$$\upsilon(r_i) = -\sum_\alpha\frac{Z_\alpha}{r_{i\alpha}}$$

(2.4)

where α and β refer to nuclei and i and j refer to electrons. The first and second terms in (2.4) are the operators for the kinetic energy of the nuclei and electrons respectively. The third term is the potential energy of the attractions between the electrons and the nuclei with $r_{i\alpha}$ being the distance between electron i and nucleus α. The fourth and fifth terms denote the potential energies of the repulsions between i and j electrons and α and β nuclei respectively, where r_{ij} and $r_{\alpha\beta}$ are the inter-electron and inter-nuclei distances and Z_α and Z_β are the atomic numbers of the α and β nuclei.

Solving even the time-independent Schrödinger equation (2.3) with the full molecular Hamiltonian (2.4) is challenging. Therefore, approximations such as the Born-Oppenheimer approximation are usually applied to simplify the problem. Since nuclei are much heavier than electrons, the electrons move faster than the nuclei. Hence, to a good approximation, one can consider nuclei as fixed while the electrons are moving. Thus, the nuclear kinetic energy term can be omitted from (2.4) to obtain the electronic Hamiltonian,

$$\hat{H} = \hat{H}_{el} + V_{NN}$$

(2.5)

where the purely electronic Hamiltonian $\hat{H}_{el}$ is,

$$\hat{H}_{el} = -\frac{\hbar^2}{2m_e}\sum_i\nabla_i^2 - \sum_\alpha\sum_i\frac{Z_\alpha e'^2}{r_{i\alpha}} + \sum_j\sum_{i>j}\frac{e'^2}{r_{ij}}$$

(2.6)

and nuclear repulsion term is,

$$V_{NN} = \sum_\alpha\sum_{\beta>\alpha}\frac{Z_\alpha Z_\beta e'^2}{r_{\alpha\beta}}$$

(2.7)

The quantity V_{NN} is independent of electronic coordinates and is a constant for a given nuclear configuration. The omission of a constant term from the Hamiltonian does not affect the eigenfunctions and simply decreases each eigenvalue by that constant. Therefore, omitting V_{NN} results in,

$$\hat{H}_{el}\psi_{el} = E_{el}\psi_{el} \tag{2.8}$$

where the purely electronic energy E_{el} depends parametrically on the nuclear coordinates and is related to the electronic energy including internuclear repulsion by

$$U = E_{el} + V_{NN} \tag{2.9}$$

2.2 Computational methods

2.2.1 Density functional theory

Density functional theory (DFT) provides a computationally efficient method to calculate ground state energies (E_0) and other properties reasonably accurately based on the ground state density (ρ_0). Unlike the electronic wave function of an *n*-electron molecule that depends on $3n$ spatial and *n* spin coordinates, the ground state density is a function of only 3 coordinates (x, y, z). Since all ground state properties can be calculated as a function of electron density, the dependence on fewer variables results in higher computational efficiency.

2.2.1.1 The Hohenberg-Kohn theorem

The ground state electronic wave function ψ_0 of an *n*-electron molecule is an eigenfunction of the purely electronic Hamiltonian (2.6) and this equation in atomic units is,

$$\hat{H}_{el} = -\frac{1}{2}\sum_{i=1}^{n}\nabla_i^2 + \sum_{i=1}^{n}U(r_i) + \sum_{i=1}^{n}\sum_{j>i}^{n}\frac{1}{r_{ij}} \tag{2.10}$$

$$U(r_i) = -\sum_{a}\frac{Z_a}{r_{ia}} \tag{2.11}$$

The potential energy of interaction $\upsilon(r_i)$ between electron *i* and the nuclei depends on the electron coordinates x_i, y_i, z_i and the nuclear coordinates. However, since the nuclei are fixed, the nuclear coordinates are not variables for the electronic Schrödinger equation. Since $U(r_i)$ is

produced by charges external to the system of electrons it is called the external potential (acting on electron *i*).

Hohenberg and Kohn[1] proved that for systems with a nondegenerate ground state, the ground state electron probability density $\rho_0(r)$ determines the external potential and the number of electrons. Hence, the ground state wave function and energy are determined by the ground state electron density.

$$\int \rho_0(r)\ dr = n \tag{2.12}$$

The ground state electronic energy E_0 is thus a functional of $\rho_0(r)$,

$$E_0 = E_v[\rho_0] \tag{2.13}$$

where the *v* subscript emphasizes the dependence of E_0 on the external potential $v(r)$. The purely electronic Hamiltonian (2.10) is the sum of electronic kinetic energy *T*, electron-nuclear attractions V_{Ne}, and electron-electron repulsions V_{ee}. Taking the average of (2.10) (overbars denote averages) gives,

$$E_0 = E_v\left[\rho_0\right] = \overline{T}\left[\rho_0\right] + \overline{V}_{Ne}\left[\rho_0\right] + \overline{V}_{ee}\left[\rho_0\right] \tag{2.14}$$

Each of these averages is a function of ρ_0. The $\overline{V}_{Ne}$ is known and given by the following equation, but the functionals $\overline{T}\left[\rho_0\right]$ and $\overline{V}_{ee}\left[\rho_0\right]$ are unknown.

$$\overline{V}_{Ne} = \left\langle \psi_0 \left| \sum_{i=1}^{n} \upsilon(r_i) \right| \psi_0 \right\rangle = \int \rho_0(r)\,\upsilon(r)\,dr \tag{2.15}$$

2.2.1.2 The Kohn-Sham method

The Hohenberg-Kohn theorem does not show how to calculate E_0 from ρ_0 nor how to find ρ_0 without first finding the wavefunction. The Kohn-Sham method provides a solution to this. Kohn and Sham[2] considered a fictitious reference system of *n* noninteracting electrons experiencing an external potential-energy function $\upsilon_s(r_i)$, which is constructed such that the ground state electron probability density $\rho_s(r)$ of the reference system is equal to the exact ground state electron density $\rho_0(r)$ of the molecule we are interested in,

$$\rho_s(r) = \rho_0(r) \tag{2.16}$$

The Hamiltonian of the reference system of noninteracting electrons can be written as,

$$\hat{H}_s = \sum_{i=1}^{n} \left[-\frac{1}{2}\nabla_i^2 + v_s\left(\mathbf{r}_i\right) \right] \equiv \sum_i^n \hat{h}_i^{KS} \tag{2.17}$$

where $\hat{h}_i^{KS}$ is the one-electron Kohn-Sham Hamiltonian,

$$\hat{h}_i^{KS} = -\frac{1}{2}\nabla_i^2 + v_s\left(\mathbf{r}_i\right) \tag{2.18}$$

Since the reference system s consists of noninteracting particles, the ground-state wave function can be written as a Slater determinant,

$$\psi_{s,0} = \left| \chi_1^{KS} \chi_2^{KS} \cdots \chi_N^{KS} \right|, \qquad \chi_i^{KS} = \theta_i^{KS}(r_i)\sigma_i \tag{2.19}$$

where σ_i is a spin function. In closed-shell systems, the electrons are paired in the spatial orbitals, one with spin α and the other with spin β. The spatial part $q_i^{KS}(r_i)$ of each spin-orbital is an eigenfunction of the one-electron operator $\hat{h}_i^{KS}$,

$$\hat{h}_i^{KS}\theta_i^{KS} = \varepsilon_i^{KS}\theta_i^{KS} \tag{2.20}$$

where the ε_i^{KS}'s are Kohn-Sham orbital energies. The electron density can be derived from these orbitals by the relation:

$$\rho_0(r) = \rho_s(r) = \sum_{i=1}^{n} \left| \theta_i \right|^2 \tag{2.21}$$

Kohn and Sham rewrote the unknown components of the Hohenberg-Kohn equation (2.14) as follows,

$$\bar{T}[\rho_0] = -\frac{1}{2}\left\langle \psi_{s,0} \left| \sum_{i=1}^{n}\nabla_i^2 \right| \psi_{s,0} \right\rangle + \Delta\bar{T}[\rho_0] \tag{2.22}$$

where the first term of the sum represents the kinetic energy contribution to the ground state of the noninteracting system ($\bar{T}_s[\rho_0]$) and $\Delta\bar{T}$ is the difference in the average ground state electronic kinetic energy between the molecule and the reference system. Using the Slater-Condon rules, we can rewrite (2.22) as:

$$\bar{T}[\rho_0] = -\frac{1}{2}\sum_i \left\langle \theta_i^{KS}(1) \left| \nabla_1^2 \right| \theta_i^{KS}(1) \right\rangle + \Delta\bar{T}[\rho_0] \tag{2.23}$$

Next, let

$$\bar{V}_{ee}[\rho_0] = \frac{1}{2}\iint \frac{\rho(r_1)\rho(r_2)}{r_{12}}dr_1dr_2 + \Delta\bar{V}_{ee}[\rho_0] \tag{2.24}$$

where r_{12} is the distance between r_1 and r_2. The quantity $\frac{1}{2}\iint \rho(r_1)\rho(r_2) \; r_{12}^{-1}dr_1dr_2$ is the classical expression in atomic units for the electrostatic interelectronic repulsion energy if the electrons are smeared out into a continuous distribution of charge with electron density ρ. The term $\Delta\bar{V}_{ee}[\rho_0]$ accounts for all of the non-classical terms and for the difference in inter-electronic repulsion energy between the real system and the noninteracting system. With definitions (2.23) and (2.24), equation (2.14) becomes,

$$E_v[\rho_0] = \int \rho_0(r) \; v(r) \; dr + \bar{T}_s[\rho_0] + \frac{1}{2}\iint \frac{\rho(r_1)\rho(r_2)}{r_{12}} dr_1dr_2 + \Delta\bar{T}[\rho_0] + \Delta\bar{V}_{ee}[\rho_0] \qquad \textbf{(2.25)}$$

The two unknown terms $\Delta\bar{V}_{ee}[\rho_0]$ and $\Delta\bar{T}[\rho_0]$ define the exchange-correlation energy functional:

$$E_{xc}[\rho_0] = \Delta\bar{T}[\rho_0] + \Delta\bar{V}_{ee}[\rho_0] \qquad \textbf{(2.26)}$$

2.2.1.3 Exchange-Correlation energy functionals

The exchange-correlation energy functional must be approximated in DFT calculations. The accuracy of a given $E_{xc}[\rho]$ is generally validated by using it in DFT calculations and comparing the calculated molecular properties with experimental ones. The Jacob's ladder[3] in Table 2.1 summarizes the types of exchange-correlation functionals that are in current use. Climbing up the ladder, the accuracy is expected to increase and the required computational resources will also rise. The first rung of the ladder is the local-density approximation (LDA), which only depends on the local density (ρ). The second rung is the generalized gradient approximation (GGA), which depends on the local density and the gradient of the density ($\nabla\rho$). The third rung is called meta-GGA, which builds on the first two rungs and adds the kinetic energy density (τ) or the second derivative of the density ($\nabla^2\rho$) or both. The next rung is hybrid functionals; they are based on the lower rungs and incorporate exact HF exchange (E_x),

$$E_x = -\frac{1}{4}\sum_{i=1}^{n}\sum_{j=1}^{n}\left\langle \theta_i^{KS}(1)\theta_j^{KS}(2)\middle|1/r_{12}\middle|\theta_j^{KS}(1)\theta_i^{KS}(2)\right\rangle \qquad \textbf{(2.27)}$$

Table 2.1 Jacob's ladder

Functional category	Density dependence	Examples
Local Density Approximation (LDA)	ρ	VWN[4]
Generalized-Gradient Approximation (GGA)	$\rho, \nabla\rho$	BP86,[5, 6] PW91,[7] PBE[8]
Meta-GGA	$\rho, \nabla\rho, \nabla^2\rho/\tau$	TPSS[9]
Hybrid	$\rho, \nabla\rho, \nabla^2\rho/\tau, E_x$	B3LYP[6, 10]

2.2.2 Basis sets

In most quantum-mechanical methods, a set of basis functions χ_r is used to express the molecular orbitals (MOs) ϕ_i as $\phi_i = \sum_i c_{ri}\chi_r$. The basis functions are usually taken as atomic orbitals (AOs) and these can be expanded as linear combination of one or more Slater-type orbitals (STOs) or Gaussian-type orbitals (GTOs). The STOs have the form of:

$$\chi_{\zeta,n,l,m} = N\, Y_{l,m}(\theta,\varphi)\; r^{n-1}\, e^{-\zeta r} \tag{2.28}$$

and GTOs have the following form,

$$\chi_{\zeta,n,l,m} = N\, Y_{l,m}(\theta,\varphi)\; r^{2n-2-l}\, e^{-\zeta r^2} \tag{2.29}$$

A Gaussian function does not have the desired cusp at the nucleus as in STOs and hence gives a poor representation of the AOs. The GTO also falls off too quickly at distances far from the nucleus and the tail of the wave function is represented poorly. Moreover, to accurately represent an AO, a linear combination of several Gaussians need to be used. However, GTOs are often used in calculations, since four-index integrals that have to be calculated can be expressed analytically as opposed to numerically with STOs.

The Amsterdam Density Functional (ADF)[11] program used in this thesis uses Slater orbitals. A minimal basis set consists of one STO for each inner-shell and valence-shell AO of each atom. A double-zeta (DZ) basis set is obtained by replacing each STO of a minimal basis set by two STOs that differ in their orbital exponents ζ (zeta). A triple-zeta (TZ) basis set uses three Slater functions per AO, a quadruple zeta (QZ) basis set uses four Slater functions, and so forth. A larger basis set yields higher accuracy but also increases the computational cost. Upon bonding, AO are distorted in shape and have their centers of charge shifted. To allow for this polarization, basis function STOs are added with higher l quantum numbers than the maximum l

of the valence shell of the ground state atom. These are called polarized basis sets. For example, in a double zeta plus polarization set (DZP), a set of 5 3d functions are added to Li - Ne and a set of 2p functions are added to H and He in addition to the double-zeta basis set. When studying anions and other systems that have significant electron density away from the nuclei, diffuse functions that have very small orbital exponents are added to improve the accuracy. These basis sets are labeled with "-nD" where n is the number of diffuse functions (e.g. QZ3P- 2D).

2.2.3 Relativistic effects: The zeroth order regular approximation (ZORA)

When an electron is traveling with a velocity v that is an appreciable fraction of the speed of light c, its effective mass m behaves as follows:

$$m = \frac{m_0}{\sqrt{[1-(v/c)^2]}} \tag{2.30}$$

where m_0 is the rest mass of the electron. The speed of light c is approximately 137 au and the average orbital velocity $\langle v \rangle$ of a 1s electron in an atom is approximately Z au, where Z is the atomic number. Hence, a 1s electron in a heavy atom travels at a significant fraction of speed of light. Moving at this speed, the effective mass of the electron m increases and the 1s orbital contracts since the radius of a hydrogen-like 1s orbital is inversely proportional to electron mass. Bohr radius $a = 4\pi\varepsilon_0\hbar^2/me^2$ where ε_0 is the permittivity of vacuum with a value of 8.8541878×10^{-12} $C^2N^{-1}m^{-2}$, $\hbar = 1.0545718\times10^{-34}$ Js/rad, e is the elementary charge with a value of 1.6021765×10^{-19} C and m is the relativistic electron mass. In order to maintain orthogonality, the higher s orbitals (and to a lesser extent the p orbitals) must also shrink and therefore lie lower in energy. On the other hand, the d and f orbitals are expanded and destabilized due to the higher shielding of the inner s electrons. These relativistic effects can strongly impact the geometries, optical and electronic properties of heavy metal compounds. Since this thesis deals with gold and silver nanoparticles, relativistic effects are a major component to include in the calculations.

In ADF program, relativistic effects are included using zeroth order regular approximation (ZORA).[11] The ZORA equation is the zeroth order of the regular expansion of the Dirac equation.[11, 12] When only a time-independent electric field is present, the one-electron ZORA Kohn-Sham equations can be written as follows in atomic units:

$$(V + T[V])\Psi_i = \varepsilon_i \Psi_i \tag{2.31}$$

with $p = -i\nabla$,

$$T^{ZORA}[V] = S \times p \frac{c^2}{2c^2 - V} S \times p$$

$$T^{ZORA}[V] = p \cdot \frac{c^2}{2c^2 - V} p + \frac{c^2}{(2c^2 - V)^2} S \cdot (\nabla V \times p) \tag{2.32}$$

$$T_{SR}^{ZORA}[V] = p \cdot \frac{c^2}{2c^2 - V} p \tag{2.33}$$

Here, the following identity is used for the Pauli spin matrices σ.

$$(\sigma \cdot a)(\sigma \cdot b) = a \cdot b + i\sigma \cdot (a \times b) \tag{2.34}$$

The effective molecular Kohn-Sham potential V is the sum of the nuclear potential, the Coulomb potential due to the total electron density, and the exchange-correlation potential. The scalar relativistic (SR) ZORA kinetic energy operator, T_{SR}^{ZORA}, is the ZORA kinetic energy operator without spin-orbit coupling.

2.2.3 Time-Dependent Density Functional Theory (TDDFT)

Conventional DFT is a static ground state theory and is not appropriate for handling time-dependent phenomena or excited states. This excludes many interesting problems in the design of optical materials, in photochemistry and in spectroscopy. TDDFT provides an answer to these problems. However, the demands on the functionals for accurate results can be challenging.

2.2.3.1 Runge-Gross Theorem

Runge and Gross[13] proved the existence of a time-dependent analogue of the first Hohenberg-Kohn theorem by establishing one-to-one mapping between the time dependent electron density, $\rho(r,t)$ and the time dependent potential $V_{ext}(r,t)$ for a given initial state y_0. This means the external potential can be expressed as a functional of the electron density and all properties of the system can be obtained. Both the time-dependent potential and the many body wave function are functionals of the density.

$$V_{ext}(r,t) = V_{ext}[\rho,\psi_0](r,t) \tag{2.35}$$

$$\psi(t) = \psi[\rho,\psi_0](t) \tag{2.36}$$

2.2.3.2 Time-dependent Kohn-Sham equations

Van Leeuwen[14] showed that the time-dependent density $\rho(r,t)$ of an interacting system could be identical to that of a noninteracting system evolving in a different potential, such that the initial noninteracting wave function Φ_0 reproduces the initial density and its first time derivative. Similar to ground state DFT, the potential of the noninteracting system is unknown and should be approximated. Furthermore, the noninteracting system can be described by a single Slater determinant of Kohn-Sham one-electron orbitals that become time-dependent orbitals $\phi_j(r,t)$.

$$\Phi(r,t) = \left|\phi_1(r,t)\phi_2(r,t)...\phi_j(r,t)\right| \tag{2.37}$$

The time dependent density can be written as the sum over occupied orbitals.

$$\rho(r,t) = \sum_{j=1}^{n}\left|\phi_j(r,t)\right|^2 \tag{2.38}$$

The time-dependent effective single-particle Kohn-Sham equation can be written as,

$$i\frac{\partial \phi_j(r,t)}{\partial t} = \hat{H}(r,t)\phi_j(r,t)$$

$$= \left[-\frac{\nabla^2}{2} + \int dr' \frac{\rho(r',t)}{|r-r'|} + V_{xc}[\rho,\psi_0,\phi_0](r,t) + V_{ext}(r,t)\right]\phi_j(r,t) \tag{2.39}$$

The terms on the right hand side give the kinetic energy of an electron in a Kohn-Sham orbital, the Coulomb repulsion or the Hartree potential which depends only on the density at a given time t, the time-dependent exchange-correlation potential $V_{xc}[\rho,\psi_0,\phi_0](r,t)$ which includes dependence on the density at all previous points in time as well as the initial interacting and noninteracting states, and the time-dependent single particle external potential $V_{ext}(r,t)$ (which includes both the external time-dependent perturbation and the Coulombic attractive potential) respectively.

The Kohn-Sham molecular orbitals can be expanded as a linear combination of basis functions χ_μ as $\phi_j(t) = \sum_\mu c_{\mu,i}(t)\chi_\mu$; the elements of the Kohn-Sham density matrix P are created from these time-dependent coefficients as,

$$P_{\mu\nu}(t) = \sum_i c_{\mu,i}^*(t)c_{\nu,i}(t) \qquad \text{(2.40)}$$

In an orthonormal basis, the TDDFT equation for the density matrix can be written as,

$$i\frac{dP(t)}{dt} = [H(t), P(t)] \qquad \text{(2.41)}$$

Where H is the Hamiltonian in matrix form with matrix elements given by $H_{\mu\nu}(t) = \langle \chi_\mu | H(t) | \chi_\nu \rangle$. Equation (2.41) is known as the quantum Liouville equation of motion.[15] This is the starting point for either propagating the electron density in time via numerical integration for the RT-TDDFT method or applying a small perturbation and retaining only the linear response of the density to derive the LR matrix formulation of TDDFT.

2.2.3.3 Adiabatic approximation

As mentioned before, the exchange-correlation potential is a functional of the initial state of the system as well as the entire history of the density, $V_{xc}[\rho, \psi_0, \phi_0](r,t)$. This is referred to as the memory dependence and it stems from the reduced nature of the density compared to the full many-body wave function which contains the complete information about the system at any time. However, within the adiabatic approximation, it is assumed that the electron density varies slowly. Therefore, all history of the density, as well as initial state dependence, is ignored. Almost all TDDFT applications use the adiabatic approximation for V_{xc},

$$V_{xc}[\rho, \psi_0, \phi_0](t) = V_{xc}[\rho(t)] \qquad \text{(2.42)}$$

2.2.3.4 Linear-response time-dependent density functional theory (LR–TDDFT)

Generally, light-matter interactions can be categorized as either weak or strong. If the interaction with the field is much smaller than the magnitude of intermolecular interactions, the corresponding excitation is identified as weak. When the applied external field is weak, it induces only a small perturbation away from the ground state of the system. Perturbation theories such as linear-response time-dependent density functional theory (LR–TDDFT) are capable of accounting for weak excitations and predicting properties such as the absorption spectra of molecules.

In a LR-TDDFT calculation, the excitation energies are computed as solutions to the non-Hermitian eigenvalue equation derived from retaining only the first-order response of the density to a perturbation (Casida Equations).[16] Assuming that the electronic transitions occur with an infinitesimal perturbation, the excitation energies are calculated by,

$$
\begin{pmatrix} A & B \\ B^* & A^* \end{pmatrix} \begin{pmatrix} X \\ Y \end{pmatrix} = \omega \begin{pmatrix} 1 & 0 \\ 0 & -1 \end{pmatrix} \begin{pmatrix} X \\ Y \end{pmatrix}
\tag{2.43}
$$

where the matrices A and B are given by,

$$
A_{ai\sigma,bj\tau} = \delta_{ij}\delta_{ab}\delta_{\sigma\tau}(\varepsilon_{a\sigma} - \varepsilon_{i\tau}) + \Lambda_{ai\sigma,bj\tau}
\tag{2.44}
$$

$$
B_{ai\sigma,bj\tau} = \Lambda_{ai\sigma,bj\tau}
\tag{2.45}
$$

In the above equations i, j, … represent occupied orbitals; a, b, … represent virtuals; σ and τ represent the spin indices; and ε represents the eigenvalues. Λ is the interaction kernel given by,

$$
\Lambda_{ai\sigma,bj\tau} = (a_\sigma i_\sigma \mid j_\tau b_\tau) + (a_\sigma i_\sigma \mid w_{\sigma\tau} \mid j_\tau b_\tau)
\tag{2.46}
$$

where

$$
w_{\sigma\tau} \equiv \frac{\delta^2 E_{xc}}{\delta\rho_c(r)\delta\rho_\tau(r')}
\tag{2.47}
$$

$w_{\sigma\tau}$ is the second derivative response from the exchange-correlation functional. Within the Tamm-Dancoff approximation (TDA),[17] the above eigenvalue equation reduces to the Hermitian equation $AX = \omega X$. The excitation energies are the eigenvalues of the linear response matrix. This matrix is diagonally dominant due to the large contribution from the Kohn-Sham orbital energy gaps to the diagonal entries.

2.2.3.5 Real-time time-dependent density functional theory (RT-TDDFT)

When the external field is comparable to or greater than the static electric field due to the nuclei, it requires methodologies that go beyond perturbation theory. Real-time time-dependent density functional theory (RT-TDDFT) received significant attention during the past few years for its capability to capture radiation-molecule interaction in both the strong and weak applied field regimes. The real-time, real-space, and time-correlation approach accounts well for the strong field limit. Here, the electron density is monitored in time and space, which helps to understand fundamental mechanisms of excitation.

The TDDFT equation for the density matrix (2.41) can be numerically integrated using standard techniques for solving ordinary differential equations as long as the density matrix remains idempotent: $PP=P$.[15]

The solution to (2.40) is

$$P(t) = U(t,t_0)P(t_0)U^\dagger(t,t_0) \tag{2.48}$$

where $U(t,t_0)$ is a time evolution operator, which for a Hermitian Hamiltonian will be unitary $\hat{U}^\dagger\hat{U} = 1$. The propagator can be expressed as,

$$U(t,t_0) = T \exp\left[-i\int_{t_0}^{t} H(t) \, dt\right] \tag{2.49}$$

where T is a time-ordering operator and $H(t)$ is the time-dependent Hamiltonian, which for RT-TDDFT is the time-dependent Kohn-Sham matrix. The density is propagated with discrete time steps Δt through a product of time-evolution operators,

$$U(t,t_0) = \prod_{i=0}^{N-1} U(t_i + \Delta t, t_i) \tag{2.50}$$

This simplifies the problem with the approximation,

$$U(t_i + \Delta t, t_i) \approx \exp[-iH(t_i + \Delta t, t_i)] \tag{2.51}$$

Errors made in the evolution are due to the approximations to the propagator.

An optical absorption spectrum can be obtained from a real-time simulation via Fourier transform of the time-dependent dipole moment resulting from a small δ-function like electric field "kick". First, the on-diagonals of the complex polarizability tensor are computed from x,y,z kick-type excitation simulations:[18]

$$\alpha_{ii}(\omega) = \frac{\mu_i(\omega)}{E_i(\omega)} \tag{2.52}$$

where $\mu_i(\omega)$ and $E_i(\omega)$ are the Fourier transforms of the dipole moment and the applied electric fields in the i direction. The absorption cross section tensor is then given by,

$$\sigma(\omega) = \frac{4\pi\omega}{c} \ \text{Im}[\alpha(\omega)] \tag{2.53}$$

and the resulting dipole strength function is then,

$$S(\omega) = \frac{1}{3}Tr\left[\sigma(\omega)\right] \tag{2.54}$$

2.3 References

1.   Hohenberg, P.; Kohn, W., Inhomogeneous Electron Gas. *Phys. Rev.* **1964**, *136*, B864-B871.
2.   Kohn, W.; Sham, L. J., Self-Consistent Equations Including Exchange and Correlation Effects. *Phys. Rev.* **1965**, *140*, A1133-A1138.
3.   Perdew, J. P.; Schmidt, K., Jacob's Ladder of Density Functional Approximations for the Exchange-Correlation Energy. *AIP Conf. Proc.* **2001**, *577*, 1-20.
4.   Vosko, S. H.; Wilk, L.; Nusair, M., Accurate Spin-Dependent Electron Liquid Correlation Energies for Local Spin Density Calculations: A Critical Analysis. *Can. J. Phys.* **1980**, *58*, 1200-1211.
5.   Perdew, J. P., Density-Functional Approximation for the Correlation Energy of the Inhomogeneous Electron Gas. *Phys. Rev. B* **1986**, *33*, 8822-8824.
6.   Becke, A. D., Density-Functional Exchange-Energy Approximation with Correct Asymptotic Behavior. *Phys. Rev. A* **1988**, *38*, 3098-3100.
7.   Perdew, J. P.; Wang, Y., Accurate and Simple Analytic Representation of the Electron-Gas Correlation Energy. *Phys. Rev. B* **1992**, *45*, 13244-13249.
8.   Perdew, J. P.; Burke, K.; Ernzerhof, M., Generalized Gradient Approximation Made Simple. *Phys. Rev. Lett.* **1996**, *77*, 3865-3868.
9.   Tao, J.; Perdew, J. P.; Staroverov, V. N.; Scuseria, G. E., Climbing the Density Functional Ladder: Nonempirical Meta-Generalized Gradient Approximation Designed for Molecules and Solids. *Phys. Rev. Lett.* **2003**, *91*, 146401.
10.   Lee, C.; Yang, W.; Parr, R. G., Development of the Colle-Salvetti Correlation-Energy Formula into a Functional of the Electron Density. *Phys. Rev. B* **1988**, *37*, 785-789.
11.   te Velde, G.; Bickelhaupt, F. M.; Baerends, E. J.; Fonseca Guerra, C.; van Gisbergen, S. J. A.; Snijders, J. G.; Ziegler, T., Chemistry with ADF. *J. Comput. Chem.* **2001**, *22*, 931-967.
12.   Lenthe, E. v.; Ehlers, A.; Baerends, E.-J., Geometry Optimizations in the Zero Order Regular Approximation for Relativistic Effects. *J. Chem. Phys.* **1999**, *110*, 8943-8953.
13.   Runge, E.; Gross, E. K. U., Density-Functional Theory for Time-Dependent Systems. *Phys. Rev. Lett.* **1984**, *52*, 997-1000.
14.   van Leeuwen, R., Mapping from Densities to Potentials in Time-Dependent Density-Functional Theory. *Phys. Rev. Lett.* **1999**, *82*, 3863-3866.
15.   Provorse, M. R.; Isborn, C. M., Electron Dynamics with Real-Time Time-Dependent Density Functional Theory. *Int. J. Quantum Chem.* **2016**, *116*, 739-749.
16.   Casida, M. E., Time-dependent density-functional theory for molecules and molecular solids. *J. Mol. Struct.: THEOCHEM* **2009**, *914*, 3-18.
17.   Hirata, S.; Head-Gordon, M., Time-Dependent Density Functional Theory within the Tamm–Dancoff Approximation. *Chem. Phys. Lett.* **1999**, *314*, 291-299.
18.   Yabana, K.; Nakatsukasa, T.; Iwata, J. I.; Bertsch, G. F., Real-Time, Real-Space Implementation of the Linear Response Time-Dependent Density-Functional Theory. *phys. stat. sol. (b)* **2006**, *243*, 1121-1138.

Chapter 3 - Theoretical Insights into Origin of Photoluminescence of

Au$_{25}$(SR)$_{18}^{-}$ Nanoparticles

3.1 Abstract

Understanding fundamental behavior of luminescent nanomaterials upon photoexcitation is necessary to expand photocatalytic and biological imaging applications. Despite the significant amount of experimental work into the luminescence of Au$_{25}$(SR)$_{18}^{-}$ clusters, the origin of photoluminescence in these clusters still remains unclear. In this study, the geometric and electronic structural changes of the Au$_{25}$(SR)$_{18}^{-}$ (R = H, CH$_3$, CH$_2$CH$_3$, CH$_2$CH$_2$CH$_3$) nanoclusters upon photoexcitation are discussed using time-dependent density functional theory (TDDFT) methods. Geometric relaxations in the optimized excited states of up to 0.33 Å impart remarkable effects on the energy levels of the frontier orbitals of Au$_{25}$(SR)$_{18}^{-}$ nanoclusters. This gives rise to a Stokes shift of 0.49 eV for Au$_{25}$(SH)$_{18}^{-}$ in agreement with experiments. Even larger Stokes shifts are predicted for longer ligands. Vibrational frequencies in the 75−80 cm^{-1} range are calculated for the nuclear motion involved in the excited-state nuclear relaxation; this value is in excellent agreement with vibrational beating observed in time-resolved spectroscopy experiments. Several excited states around 0.8, 1.15, and 1.25 eV are calculated for the Au$_{25}$(SH)$_{18}^{-}$ nanocluster. Considering the typical underestimation of DFT excitation energies, these states are likely responsible for the emission observed experimentally in the 1.15 – 1.55 eV range. All excited states arise from core-based orbitals; charge-transfer states or other "semi-ring" or ligand-based states are not implicated.

3.2 Introduction

Gold nanoparticles (AuNPs) have received increasing research interest due to the tunability of their electronic and optical properties by changing size and shape, which enables a wide range of applications in chemical sensing,[1] biomedicine and imaging,[2] catalysis,[3-5] photocatalysis,[6-9] etc. In order to improve photocatalytic applications, a more complete

understanding of the fundamental mechanisms involving photoexcitation and excited state relaxation dynamics of these nanomaterials is required. During the past decade, luminescent AuNPs in the size range of 0.3 to 20 nm have been synthesized by tuning structural parameters like particle size, surface ligands, valence state and grain size,[10] and luminescence quantum yields of up to ~10% have been reported.[11, 12] Although the surface plasmon absorption of larger (5+ nm diameter) AuNPs as well as the discrete molecular-like absorption of gold nanoclusters with a core diameter of less than 2 nm are well studied and understood, the luminescence properties of AuNPs still remain unclear.

The observation of luminescence from bulk gold can be dated back to as early as 1969, when Mooradian observed photoluminescence of gold at 564 nm after excitation using a 488 nm laser.[13] However, bulk gold has a very low quantum yield. About 30 years later, Kelley and coworkers[14] identified blue emitting AuNPs with emission at 440 nm in systems with diameters smaller than 5 nm. In 2000, luminescent gold nanorods emitting at 560 nm were reported.[15] Shortly thereafter, Whetten and coworkers[16] observed a novel near-infrared (1.1 - 1.6 μm) photoluminescence for AuNPs with core sizes of 1.1 and 1.7 nm with an estimated quantum yield of $(4.4 \pm 1.5) \times 10^{-5}$, which is more than five orders of magnitude greater than that of bulk gold. This photoluminescence was attributed to sp to sp-like (intraband) transitions. However, Huang and Murray[17] reported visible wavelength fluorescence (700-800 nm) for four water soluble monolayer-protected AuNPs with a core size smaller than 2 nm and hypothesized the luminescence mechanism to be associated with interband (d-sp) transitions. Furthermore, Murray and coworkers observed that five AuNPs with a wide range of gold cores (11-201 atoms) and protecting ligands emit over a similar range of energies from 700 nm (1.8 eV) to 1.3 μm (0.9 eV) when excited at 451 nm, and suggested that the core size-independence of the emission may be due to surface states related to the ligands rather than to core-based transitions.[18] In comparison, Tsukuda and coworkers[19, 20] studied photoexcitation and emission of a group of glutathione protected gold nanoclusters having 18–39 gold atoms with photoluminescence quantum yields ranging from 1×10^{-3} to 7×10^{-4}. These clusters were found to emit around 1.6–1.8 eV with a maximum Stokes shift of 0.4 eV. They suggested that emission occurs from vibrationally relaxed states of the first electronically excited state.

Zheng et al.[10] have summarized studies on different sized luminescent gold nanoparticles and the factors that influence luminescence properties and emission mechanisms. Therefore, only

the luminescence of the thiolate protected 25-atom gold nanocluster will be discussed in the remainder of this paper. The crystallographic structure of the thiolate protected 25-atom gold nanocluster was solved in 2008.[21, 22] It consists of an approximately icosahedral Au_{13} core surrounded by six v-shaped –S–Au–S–Au–S– staple motifs (sometimes called "semi-rings") in an almost T_h symmetry (Figure 3.1).[21-23] In 2002, Link et al.[24, 25] reported luminescence extending over the visible to infrared region for the $Au_{25}(SG)_{18}$ cluster (SG = glutathione). This nanocluster was originally mis-assigned as Au_{28}.[26, 27] They observed two different bands with maxima around 1.5 and 1.15 eV that indicated radiative recombination between the ground state and two excited states.[24] They proposed two possible models for the origin of the two luminescence bands: a "solid state" model in which the high and low energy bands correspond to interband and intraband (HOMO-LUMO) transitions, respectively, and a "molecular" model in which the two bands could be due to fluorescence and phosphorescence, respectively. The overall quantum yield for the cluster at ambient temperature was found to be $(3.5 \pm 1.0) \times 10^{-3}$. They also found that the luminescence decay dynamics are complex, which could be due to the presence of several closely spaced energy levels. Subsequently, Murray and coworkers[28] also reported two emission peaks at 1.38 and 1.2 eV for the $Au_{25}(SR)_{18}$ (R = CH_2CH_2Ph) nanocluster, which was originally mis-assigned as Au_{38}. Since the HOMO-LUMO gap energy of 1.33 eV matched well with the 1.38 eV emission energy, they assigned this emission as relaxed luminescence across the HOMO-LUMO gap while the 1.2 eV emission was thought to be sub-bandgap energy luminescence. They found that both emission peaks were strong when the nanocluster was excited at 680 nm, but that the 1.38 eV component was favored with higher energy (600 nm) excitation.

Pradeep and coworkers[29, 30] studied the photoluminescence and temperature dependent solid-state emission of Au_{25} clusters. An emission peak at 700 nm was observed for $Au_{25}(SG)_{18}$, whereas ligand exchange with a fluorescein based dye red-shifted the peak by 25 nm.[29] This luminescence peak (~1.7-1.8 eV) is much higher in energy than the 1.38 or 1.5 eV emission bands observed previously. Furthermore, they observed that the ligand exchanged products of $Au_{25}(SG)_{18}$ with acetyl- and formyl-glutathione give rise to similar emission spectra whereas the 3-mercapto-2-butanol ligand blue-shifts the spectrum by 20 nm.[30] The observed emission was attributed to electronic transitions associated with the gold core, regardless of different ligands. In the temperature range of 80K to 300K, the emission of $Au_{25}(SG)_{18}$ occurred at the same

position which suggested that there are no major geometric changes in the system affecting its electronic structure.[29, 30] However, the intensity of the fluorescence was observed to decrease with decreasing temperature suggesting that the non-radiative vibrational relaxation channel becomes prominent. Conversely, later work by Knappenberger and coworkers[31] showed that the luminescence intensity of a neutral phenylethanethiolate-stabilized Au_{25} nanoparticle *decreased* as the temperature increased from 50 to 200 K.

Miller et al.[32] studied the excited-state relaxation dynamics of $Au_{25}(SCH_2CH_2Ph)_{18}^-$ with femtosecond laser spectroscopy. They excited the two lowest absorption peaks at 450 nm (assigned to an approximately six-fold degenerate HOMO→LUMO excitation) and 680 nm (approximately nine-fold degenerate HOMO→LUMO+1 excitation) and watched the relaxation of the system until it reached the lowest-energy fluorescing state ($\lambda_{em} \sim 1000$ nm). They observed time constants greater than 4 ps measured at 725-800 nm detection wavelengths that they attributed to emission from "semi-ring" states (thought to be present below the HOMO-LUMO state arising from orbitals in the nanoparticle core) to the ground state. Furthermore, they detected an 80 cm^{-1} vibration localized to the Au_{13} core, which implies strong vibronic coupling of a delocalized Au-Au bond stretching vibration. Similar lifetimes (a short-lived ~1 ps component and a long-lived component) and phonon modes for the anionic $Au_{25}(SR)_{18}$ cluster were later observed by Qian et al.,[33] but they suggested that the 80 cm^{-1} vibration is not an acoustic, spherically symmetric phonon mode as originally thought. In addition, they proposed that the electron dynamics they observed may be due to two slightly nondegenerate HOMO-LUMO transitions located in the core.

In 2006, Wang et al.[34] found that increasing the number of polar ligands on the nanocluster linearly increases the luminescence intensity of the near-infrared peak. Wu and Jin later studied the ligand and charge state dependence of fluorescence of $[Au_{25}(SR)_{18}]^q$ nanoclusters.[35] Weak fluorescence around 750 nm was observed for $Au_{25}(SR)_{18}^-$ and they found that the ligand's ability to donate electron density to the metal core via the S-Au bond can enhance the fluorescence quantum yield. The intensity of the fluorescence signal was also observed to increase with the increasing electropositivity of the metal core (increasing q from -1 to +2). The observed fluorescence was attributed to a ligand to metal nanoparticle core charge transfer (LMNCT) mechanism. Recently, Wang et al.[36] reported similar results with Au_{25} nanoclusters protected by 2-(naphthalene-2-yl)ethanethiolate.

Ramakrishna, Goodson, and coworkers[37-39] reported a low quantum yield visible photoluminescence (~500 nm) for monolayer protected Au_{25} nanoclusters in addition to near-infrared luminescence (around 710 nm for glutathione-protected nanoparticles[38] and around 830 nm[37] for hexanethiolate-protected nanoparticles) using ultrafast spectroscopy. They suggested that luminescence arises out of the Au_{25} core states since the growth time constants are independent of the passivating ligand.[37] However, the ligand-dependent decay of luminescence was attributed to the relaxation of Au_{25} core states to semi-ring states.[37]

More recently, Knappenberger and coworkers[31] studied temperature dependent photoluminescence of neutral phenylethanethiolate-stabilized Au_{25} nanoparticles. Broad near-infrared photoluminescence was reported that consisted of several peaks at 1.72, 1.57, and 1.51 eV, implying multiple relaxation pathways. Increasing emission intensities were observed as the temperature was raised from 4.5 to 50 K. However, photoluminescence intensity decreased and red shifted in energy at temperatures above 65 K. Two low-frequency vibrations associated with the ligand shell were identified: Au(I)-S stretching (180 cm^{-1}) and Au(0)-Au(I) stretching (105 cm^{-1}) that are responsible for nonradiative relaxation dynamics above 45 K. The amount of electronic-vibration coupling involved in each photoluminescence component was found to be state-specific and larger for the high-energy portions. (Table A1 summarizes the experimental photoluminescence results.)

Even though extensive experimental studies have been performed on synthesizing and characterizing luminescent monolayer protected Au_{25} nanoclusters, their luminescence mechanism is still unclear. The luminescence has alternately been assigned to intraband and interband transitions, fluorescence and phosphorescence, surface or "semi-ring" states, or ligand-metal charge transfer states. Herein, we perform a theoretical investigation to determine the origin of the emission of $Au_{25}(SR)_{18}^{-}$ (R = H, $-CH_3$, $-CH_2CH_3$, $-CH_2CH_2CH_3$) nanoclusters using density functional theory (DFT) and time-dependent density functional theory (TDDFT) calculations.

3.3 Computational Methods

All geometry optimizations are performed using density functional theory (DFT) as implemented in the Amsterdam Density Functional (ADF) 2012.01 package.[40] The BP86 exchange-correlation functional[41, 42] and the double-ζ (DZ) basis set are used for all the

calculations. Generalized gradient approximation (GGA) functionals have been employed successfully in geometry relaxations and time-dependent DFT (TDDFT) calculations of gold and silver nanoclusters previously.[21, 43-49] All structures are optimized in the gas phase. The energy and gradient convergence criteria are tightened to 1×10^{-4} and 1×10^{-3} to obtain well-converged geometries. Further tightening these values to 1×10^{-5} and 1×10^{-4} correspondingly gives energies lowered only by about a hundredth of an electronvolt with respect to the looser convergence criteria. Scalar relativistic effects are included by utilizing the zeroth-order regular approximation (ZORA). On the basis of the optimized ground state geometries, the vertical excitations are calculated with the TDDFT method using the same level of theory. The excited state gradients are then calculated to optimize the excited state geometry. Only singlet excited states (S_n) are considered here. Similar studies have been carried out to investigate luminescence properties of Au(I) complexes with thiolate and phosphine ligands.[44, 50] The experimental and theoretical results have shown a good agreement, even though calculated emission peak energies are around 0.3 eV lower than the experimental results. Herein, we calculate the optimized structure for excited states of $Au_{25}(SR)_{18}^-$ (R = H, $-CH_3$, $-CH_2CH_3$, $-CH_2CH_2CH_3$) nanoclusters in order to determine the origin of the emission in these systems. Stokes shifts are calculated by taking the energy differences between excitation and emission. For this, electronic ground and excited states are considered without accounting for vibrational contributions. All structures are visualized using the MacMolPlt[51] visualization tool.

3.4 Results and Discussion

3.4.1 $Au_{25}(SH)_{18}^-$

The average bond lengths calculated at the BP86/DZ level of theory of the ground state structure of $Au_{25}(SH)_{18}^-$ in the gas phase are summarized in Table 3.1. Within the Au_{13} core, the average Au_{center}–Au_{shell} bond length is 2.825 ± 0.003 Å whereas the Au_{shell}–Au_{shell} bond length is 2.972 ± 0.073 Å. These two bonds are 1.9% shorter and 3.2% longer respectively compared to the Au – Au distance of 2.88 Å in bulk gold. The average Au_{shell}–$S_{terminal}$ bond length is about 0.12 Å longer than the Au – S distances within the staple motifs.
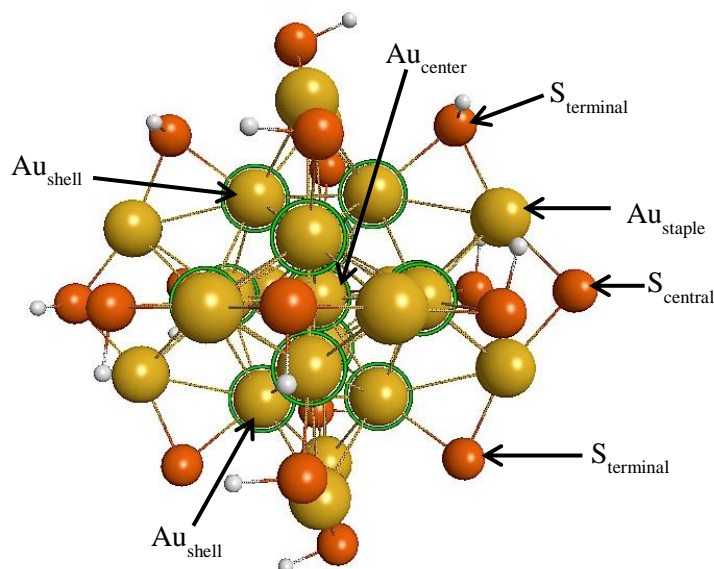
Figure 3.1 Structure of $Au_{25}(SH)_{18}^-$. A shell of 12 gold atoms in an approximate icosahedron surrounds the central gold atom. The orange, yellow, black, and white color spheres represent sulfur, gold, carbon, and hydrogen atoms, respectively. This color code is consistent in all the figures presented in this article. The Au_{13} core gold atoms are marked with green circles.

Table 3.1 Geometrical parameters of the ground state and S_1 excited state structures of $Au_{25}(SH)_{18}^-$ at the BP86/DZ level of theory.

	Average Bond Length (Å)	
Bond	Ground State (S_0)	Excited State (S_1)
Au_{center}–Au_{shell}	2.825 ± 0.003	2.846 ± 0.019
Au_{shell}–Au_{shell}	2.972 ± 0.073	2.995 ± 0.139
Au_{shell}–$S_{terminal}$	2.560 ± 0.005	2.566 ± 0.032
Au_{staple}–$S_{terminal}$	2.447 ± 0.006	2.452 ± 0.041
Au_{staple}–$S_{central}$	2.444 ± 0.002	2.457 ± 0.027

The HOMO, HOMO-1, and HOMO-2 orbitals of $Au_{25}(SR)_{18}^-$ (R=H, CH$_3$) are approximately triply degenerate and represent superatomic P orbitals delocalized over the Au_{13} core.[21, 23, 52, 53] (In many papers, these three orbitals are sometimes collectively referred to as the "HOMO".) The ligand-field splitting from the six $Au_2(SR)_3$ units divides the unoccupied superatomic D orbitals into two sets: essentially doubly degenerate LUMO and LUMO+1 and

41

essentially triply degenerate LUMO+2, LUMO+3, and LUMO+4.[23, 52, 53] The "superatom electronic theory"[23, 54] has been successfully used to explain structure property relationships of various monolayer-protected AuNPs previously. Figure A1 demonstrates the Kohn-Sham orbitals of $Au_{25}(SH)_{18}^-$ in the ground state, calculated at the BP86/DZ level of theory.

A time-dependent density functional theory (TDDFT) calculation was performed on the relaxed ground state geometry of $Au_{25}(SH)_{18}^-$ and the first six singlet excited state energies and the oscillator strengths are tabulated in Table 3.2. All the states $S_1 - S_6$ vary within ~0.1 eV and correspond to HOMO, HOMO-1, or HOMO-2 to LUMO or LUMO+1 excitations. The oscillator strengths of the $S_4 - S_6$ states are two orders of magnitude higher compared to the S_1 state that has an oscillator strength of 4.536×10^{-4} au. Moreover, the $S_4 - S_6$ states lie around 1.4 eV and represent the experimental absorption peak at 1.8 eV[21] with an underestimation of approximately 0.4 eV. (It has been established[43, 55] that GGA functionals generally underestimate excitation energies.)

Table 3.2 Excited state energies and oscillator strengths for $Au_{25}(SH)_{18}^-$ at the S_0 geometry.

State	Energy (eV)	Oscillator Strength (au)
S_1	1.317	4.536×10^{-4}
S_2	1.320	1.277×10^{-3}
S_3	1.334	4.660×10^{-4}
S_4	1.403	2.374×10^{-2}
S_5	1.418	2.301×10^{-2}
S_6	1.433	2.337×10^{-2}
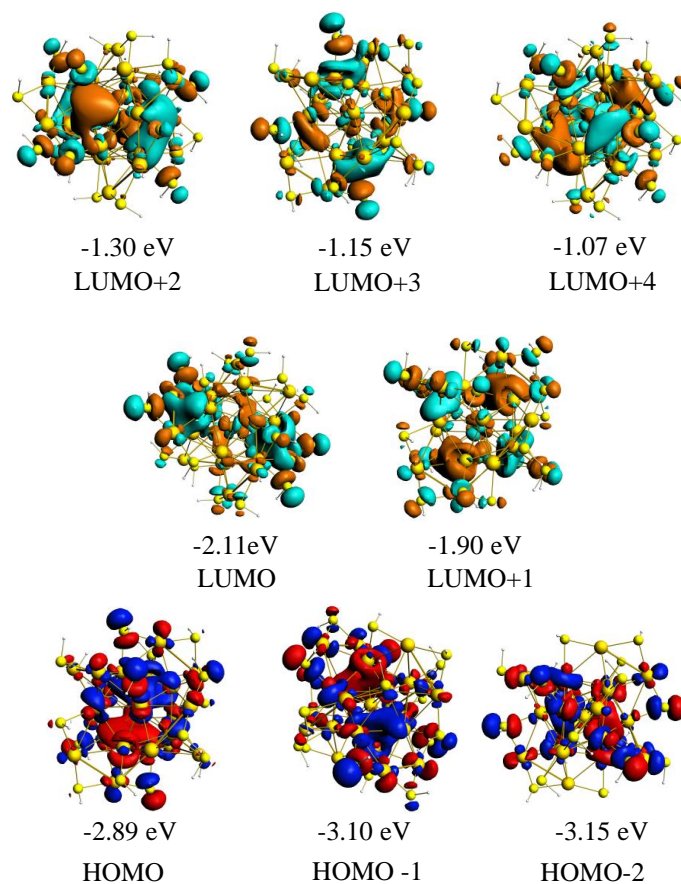
Figure 3.2 BP86/DZ Kohn-Sham orbitals and orbital energies for the S$_1$ state of Au$_{25}$(SH)$_{18}$$^-$ |Isovalue| = 0.02.

Herein, we calculate the optimized S$_1$ excited state structure in order to determine the origin of the lowest energy emission of the Au$_{25}$(SH)$_{18}$$^-$ nanocluster. Kasha's rule establishes that photon emission occurs in appreciable yield from the lowest excited state of a given multiplicity. Therefore, we initially consider the first excited state, S$_1$. The fluorescence wavelength is the energy gap between the S$_0$ and S$_1$ states at the optimized S$_1$ state geometry. This energy gap calculated for the Au$_{25}$(SH)$_{18}$$^-$ nanocluster is 0.83 eV, which corresponds to a fluorescence wavelength of 1495 nm. If one expects a similar 0.4 eV underestimation for the calculations relative to experiment, this would imply that the experimental emission from the S$_1$ state would occur around 1.2 eV, in good agreement with reported values of 1.15-1.2 eV.[24, 28] The oscillator strength for the emission is 2.462×10^{-3} au, which is one order of magnitude higher than that of the first excitation at the ground state geometry. The emission energy is significantly smaller than the excitation energy of 1.32 eV, and thus the difference between the excitation energy and

the emission energy is large. At the BP86/DZ level of theory, the Stokes shift calculated for the $Au_{25}(SH)_{18}^-$ nanocluster is 0.49 eV. This is in good agreement with the Stokes shifts of around 0.4 eV found by Tsukuda et al.[19, 20]

Table 3.1 shows the geometrical parameters of the S_1 excited state structure of $Au_{25}(SH)_{18}^-$ in the gas phase. The average bond lengths of the ground state structure increase by less than 0.03 Å upon formation of the optimized S_1 state geometry. However, several bonds lengthened considerably in the excited state. Table A2 shows the individual Au_{shell}–Au_{shell} bond lengths that significantly differ between the ground and excited state geometries. The most prominent difference between S_0 and S_1 geometries is the elongation of 5–6 and 11–12 bonds by 0.25 Å in the S_1 optimized geometry. Sets of bonds 4–5, 10–11 and 5–7, 11–13 are also elongated by 0.10 Å compared to the S_0 optimized geometry. While most of the Au_{shell}–$S_{terminal}$ bond lengths vary by less than 0.03 Å, Au_7–S and Au_{13}–S bond lengths increase by about 0.06 Å. Consequently, the related Au_{staple}–$S_{terminal}$ and Au_{staple}–$S_{central}$ bond distances also increase by about 0.09 and 0.07 Å, respectively, in the optimized S_1 geometry. Calculated ground state vibrational frequencies of the cluster demonstrated that the mode at 75.2 cm^{-1} corresponds to vibrations in Au_{13} core and specifically vibrations of the 5–6 and 11–12 bonds that have significant elongation in the S_1 state. This data suggests that the 75-80 cm^{-1} vibrations observed in various experimental studies[32, 33, 37-39] of the excited state dynamics of $Au_{25}(SR)_{18}^-$ are likely due to the elongation of Au-Au bonds within the shell of the core during excited state relaxation.

This geometry relaxation upon photoexcitation is related to a remarkable effect on the energy levels of the frontier orbitals of $Au_{25}(SH)_{18}^-$ nanocluster. In fact, it is expected due to the Jahn-Teller effect that nuclear changes must occur when there is incomplete occupation of a set of degenerate (or in the case of $Au_{25}(SR)_{18}^-$, nearly degenerate) orbitals, such as when there are five electrons in the P orbitals and one electron in the lowest set of D orbitals, as in the S_1 state of $Au_{25}(SR)_{18}^-$. In fact, recently Ackerson and coworkers described the structural evolution of neutral and cationic counterparts of the $Au_{25}(SCH_2CH_2Ph)_{18}^-$ nanocluster using the Jahn-Teller effect.[56] Figure 3.2 demonstrates the Kohn Sham orbitals for the S_1 state. Similar to Figure A1, these orbitals still retain their superatomic P and D character in the S_1 state geometry. The near triple-degeneracy of the highest occupied orbitals and the near double-degeneracy of the lowest unoccupied orbitals at the S_0 state geometry are disrupted for the optimized S_1 state. The HOMO is destabilized by 0.22 eV whereas the LUMO is stabilized by 0.27 eV at the S_1 state compared

to that at the S_0 state geometry (Figure 3.3). As a result, the energy gap between the HOMO and LUMO decreases by 0.49 eV with the geometry relaxation at S_1. Figure 3.3 demonstrates the splitting of frontier orbitals in the excited state with respect to the ground state. The splitting of superatomic P orbitals increases by 0.23 eV compared to the S_0 state geometry and the doubly-degenerate D orbitals have a splitting of 0.20 eV in the S_1 state geometry. This type of splitting shows that the nanoparticle becomes less isotropic in the excited state.
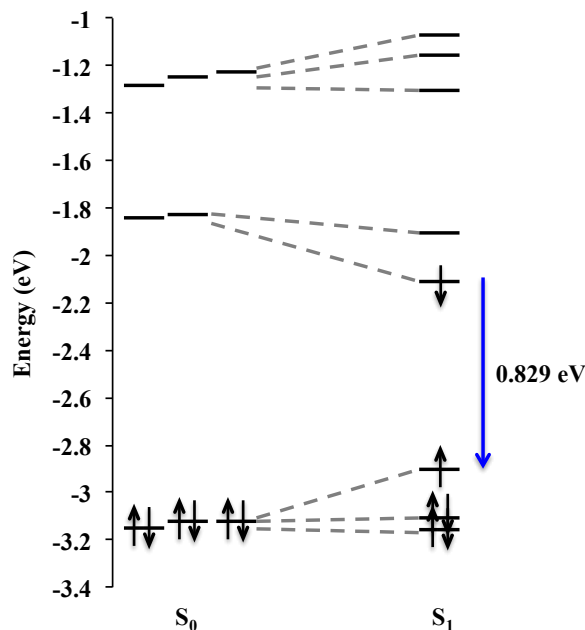
Figure 3.3 Comparison of energy levels of the frontier orbitals in S_0 and S_1 states. The S_1 state is shown in a cartoon representation with a single electron in one of the D orbitals. Dashed lines are drawn to show the splitting of triply-degenerate HOMO/HOMO-1/HOMO-2, doubly-degenerate LUMO/LUMO+1, and triply degenerate LUMO+2/LUMO+3/LUMO+4 orbitals of the ground state upon photoexcitation.

Because the S_1 state is not the only state contributing to the luminescence of the $Au_{25}(SR)_{18}^{-}$ nanocluster, we have also considered geometrical relaxation of other higher-lying states after photoexcitation. Although the calculation did not fully converge to our desired convergence criteria, excitation into the S_2 state results in similar geometrical changes as the S_1 state, with a similar Stokes shift. On the other hand, excitation into the S_3 state leads to much less dramatic changes in the bond lengths, with average Au_{shell}-Au_{shell} bond lengths of 2.987 Å (Table 3.3) and a maximum increase of 0.069 Å in any of these bonds. As a result, the orbitals

maintain the near degeneracies observed in the ground state. In contrast to the S_1 optimized structure, the S_1-S_3 states are degenerate at 1.15 eV for the S_3 optimized structure. Optimization of the S_4 state appears to lead to similar results as S_3. Like S_3, excitation into the S_5 state also yields bond distances that are only slightly elongated compared to the ground state; the average Au_{shell}-Au_{shell} bond length is 2.986 Å with a maximum change of 0.064 Å in any of these bonds. At the optimized S_5 geometry, the S_4 and S_5 states are essentially degenerate at 1.247 eV. Excitation into the S_6 state also appears to lead to a very isotropic system. Although not fully converged to our desired convergence criteria, the S_1-S_3 states at the final S_6 geometry are essentially degenerate at 1.12-1.16 eV, and the S_4-S_6 states are essentially degenerate at about 1.25 eV.

Table 3.3 Geometrical parameters of the S_3, S_5, and S_7 excited state structures of $Au_{25}(SH)_{18}{}^-$ at the BP86/DZ level of theory.

Bond	Average Bond Length (Å)		
	S_3 Structure	S_5 Structure	S_7 Structure
Au_{center}–Au_{shell}	2.838 ± 0.010	2.836 ± 0.009	2.833 ± 0.021
Au_{shell}–Au_{shell}	2.987 ± 0.107	2.986 ± 0.105	2.981 ± 0.092
Au_{shell}–$S_{terminal}$	2.564 ± 0.017	2.560 ± 0.012	2.582 ± 0.026
Au_{staple}–$S_{terminal}$	2.447 ± 0.016	2.446 ± 0.014	2.454 ± 0.014
Au_{staple}–$S_{central}$	2.453 ± 0.010	2.454 ± 0.008	2.457 ± 0.008

Overall, these excited state calculations suggest that several states could be responsible for the observed emission: a state calculated to lie around 0.8 eV (populated from photoexcitation into S_1 or S_2, or transitions from higher states into these states), a state around 1.15 eV (populated from photoexcitation into S_3 or S_4, or transitions from higher states into these states), or a state around 1.25 eV (populated from photoexcitation into S_5 or S_6, or transitions from higher states into these states). Given the typical underestimation of GGA calculations, these states could yield the emission in the 1.15-1.55 eV (or similar) range observed experimentally.

Furthermore, we have also optimized the S_7 excited state geometry. At the ground state, the S_7 state lies over 0.4 eV above the S_1-S_6 excited states. However, geometrical relaxation in the S_7 state leads to a dramatic decrease in the state energy to 1.46 eV. Given the typical underestimation of GGA calculations, the S_7 state likely lies too high in energy for the observed emission to arise from this state. However, optimization of the S_7 state leads to near-degeneracies with the S_6 and S_5 states (Table 3.4). This would facilitate nonadiabatic excitation transfer to lower excited states, and could provide a mechanism by which higher excited states relax to the S_1-S_6 states.

Table 3.4 Energies (eV) for the S_1-S_7 state energies at selected optimized excited state structures.

State	Energy (eV)			
	S_1 Structure	S_3 Structure	S_5 Structure	S_7 Structure
S_1	0.829	1.152	1.152	1.161
S_2	1.059	1.153	1.159	1.223
S_3	1.124	1.153	1.189	1.285
S_4	1.148	1.247	1.247	1.367
S_5	1.234	1.282	1.247	1.405
S_6	1.354	1.286	1.324	1.456
S_7	N/A	N/A	1.799	1.461

3.4.2 $Au_{25}(SR)_{18}^-$ (R = CH_3, CH_2CH_3, $CH_2CH_2CH_3$)

In order to understand how the ligand affects the emission, we now discuss the geometric, electronic, and luminescence properties of the $Au_{25}(SR)_{18}^-$ nanoclusters, where the alkyl ligand, R increases in length from methyl to propyl. Table 3.5 summarizes the average bond lengths of the ground state structures of these clusters in the gas phase. The average Au_{shell}–$S_{terminal}$ bond lengths are shortened by about 1% in the ground state structures with alkyl ligands compared to $Au_{25}(SH)_{18}^-$. However, Au–Au bond lengths do not vary noticeably with the changing ligand.

Table 3.5 Geometrical parameters of the ground state and excited state structures of $Au_{25}(SR)_{18}^-$ at the BP86/DZ level of theory.

Bond	Average Bond Length (Å)					
	$Au_{25}(SCH_3)_{18}^-$		$Au_{25}(SCH_2CH_3)_{18}^-$		$Au_{25}(SCH_2CH_2CH_3)_{18}^-$	
	S_0	S_1	S_0	S_1	S_0	S_1
$Au_{center}-Au_{shell}$	2.831 ± 0.004	2.858 ± 0.031	2.828 ± 0.006	2.852 ± 0.027	2.830 ± 0.009	2.859 ± 0.033
$Au_{shell}-Au_{shell}$	2.978 ± 0.089	3.009 ± 0.177	2.976 ± 0.088	3.001 ± 0.157	2.977 ± 0.095	3.012 ± 0.188
$Au_{shell}-S_{terminal}$	2.539 ± 0.003	2.546 ± 0.028	2.534 ± 0.005	2.543 ± 0.030	2.539 ± 0.005	2.559 ± 0.041
$Au_{staple}-S_{terminal}$	2.431 ± 0.010	2.434 ± 0.033	2.431 ± 0.011	2.438 ± 0.036	2.431 ± 0.011	2.442 ± 0.037
$Au_{staple}-S_{central}$	2.430 ± 0.003	2.443 ± 0.021	2.430 ± 0.003	2.444 ± 0.022	2.430 ± 0.002	2.448 ± 0.023
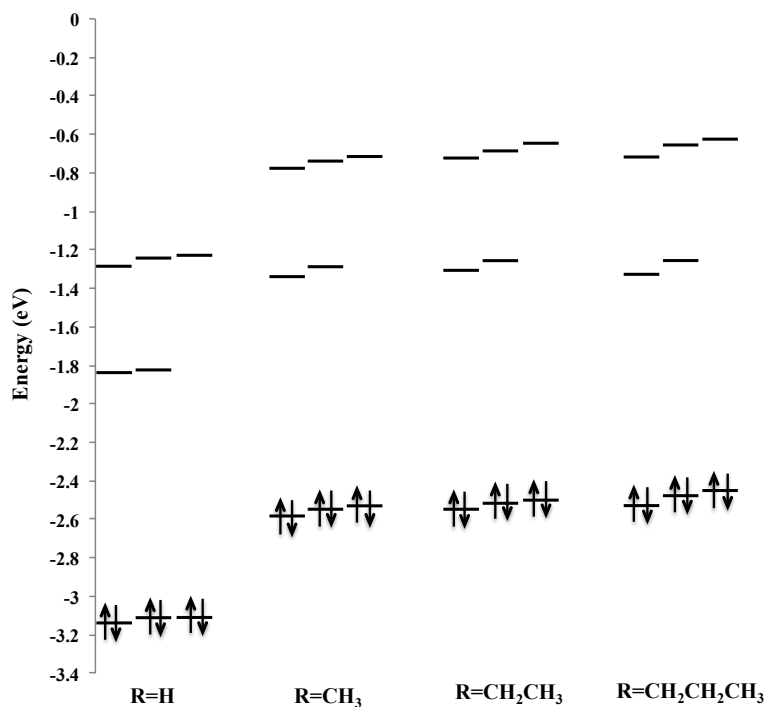
Figure 3.4 Comparison of ground state orbital energy levels of $Au_{25}(SR)_{18}^-$ nanoclusters.

The ground state electronic structure of $Au_{25}(SCH_3)_{18}^-$ is significantly affected by changing the ligand from H to methyl. However, further increasing the carbon chain length from methyl to propyl has only slight effects on the ground state electronic structure of these nanoclusters. Figure 3.4 and Table A3 compare ground state energy levels of the frontier orbitals and HOMO−LUMO gaps of $Au_{25}(SR)_{18}^-$ (R = H, CH_3, CH_2CH_3, $CH_2CH_2CH_3$) nanoclusters. The essentially triply-degenerate HOMO/HOMO-1/HOMO-2 orbitals are destabilized by 0.6 eV whereas the doubly-degenerate LUMO/LUMO+1 and triply−degenerate LUMO+2/LUMO+3/LUMO+4 orbitals are destabilized by 0.5 eV upon changing the ligand from H to methyl. Nevertheless, the splitting of the P and D orbital sets are increased only by 0.03, 0.05, and 0.01 eV due to the ligand variation from H to methyl. When the ligand is changed from methyl to propyl, the frontier orbitals are generally destabilized by a few hundredths of an electron-volt.

We performed TDDFT calculations based on the relaxed ground state geometries of methyl-, ethyl-, and propyl-thiolate protected Au_{25} nanoclusters. The first six singlet excited state energies and the oscillator strengths of $Au_{25}(SR)_{18}^-$ nanoclusters are tabulated in Table A4. The S_1 state energy of $Au_{25}(SR)_{18}^-$ (R = CH_3, CH_2CH_3, $CH_2CH_2CH_3$) is increased correspondingly by 0.08, 0.06, and 0.13 eV from that of $Au_{25}(SH)_{18}^-$. The oscillator strength of the first excited state is increased by one order of magnitude whereas that of the S_4, S_5, and S_6 states are not changed significantly for these three clusters as compared to $Au_{25}(SH)_{18}^-$. The prominent peak that arises due to S_4−S_6 states in the optical absorption spectra of $Au_{25}(SR)_{18}^-$ is red-shifted by ~0.1 eV upon substituting the H-ligand by alkyl ligands. However, the S_1 state energy is increased by 0.02 eV from methyl to ethyl thiolate ligated cluster, whereas it is reduced by 0.07 eV from ethyl to propyl.

Next, the optimized excited state structures of $Au_{25}(SR)_{18}^-$ (R = CH_3, CH_2CH_3, $CH_2CH_2CH_3$) nanoclusters are calculated in order to determine the origin of their emission. In this section, we consider the first excited state, S_1, only. The fluorescence wavelengths and the calculated Stokes shifts for these three clusters are compared with $Au_{25}(SH)_{18}^-$ in Table 3.6. It should be noted that because of the inverse relationship between energy and wavelength, small changes in energy in the near-IR region result in large changes in the wavelength. The emission energy decreases by 0.17 eV upon changing the SH ligand to SCH_3. However, when the alkyl ligand is changed from methyl to ethyl, the emission energy is increased by 0.037 eV and it is

reduced by 0.18 eV when the ligand is changed from ethyl to propyl similar to the trend observed for the S_1 state energy. Furthermore, Stokes shifts have the same trend with the increasing length of the alkyl ligand as shown in Table 3.6. The large Stokes shifts can be attributed to the notable modifications in the geometric and electronic structures of the optimized S_1 states of these clusters as compared to their S_0 states. This Stokes shift trend suggests that the largest geometrical changes occur in the excited state of the propylthiolate-protected Au_{25} cluster, followed by methylthiolate- and then ethylthiolate-protected clusters.

Table 3.6 Comparison of emission energies (fluorescence wavelengths) and Stokes shifts.

Nanocluster	Emission		Stokes Shift	
	Energy (eV)	Wavelength (nm)	Energy (eV)	Wavelength (nm)
$Au_{25}(SH)_{18}^{-}$	0.829	1495	0.488	553
$Au_{25}(SCH_3)_{18}^{-}$	0.655	1892	0.579	887
$Au_{25}(SCH_2CH_3)_{18}^{-}$	0.692	1791	0.563	803
$Au_{25}(SCH_2CH_2CH_3)_{18}^{-}$	0.512	2424	0.676	1379

Table 3.5 summarizes the excited state geometrical parameters of $Au_{25}(SR)_{18}^{-}$ (R = H, CH_3, CH_2CH_3, $CH_2CH_2CH_3$) nanoclusters in the gas phase. Analogous to $Au_{25}(SH)_{18}^{-}$, the average bond lengths of the ground state structures of $Au_{25}(SR)_{18}^{-}$ change by less than 0.04 Å upon formation of the optimized S_1 state geometries. However, the increased standard deviations of Au_{shell}–Au_{shell} bond lengths show that several bonds vary considerably in the excited state. Table 3.7 lists the individual Au_{shell}–Au_{shell} bond lengths that significantly differ between the ground and excited state geometries.

Table 3.7 Comparison of Au_shell–Au_shell bond lengths in relaxed geometries of the ground state (S_0) and the first excited state (S_1) of the $Au_{25}(SR)_{18}^-$ nanoclusters.

Au₁₃ – core Structure	Bond	Bond Length (Å)					
		$Au_{25}(SCH_3)_{18}^-$		$Au_{25}(SCH_2CH_3)_{18}^-$		$Au_{25}(SCH_2CH_2CH_3)_{18}^-$	
		S_0	S_1	S_0	S_1	S_0	S_1
	4 – 3	3.002	2.906	3.018	2.932	3.017	2.898
	9 – 10	3.002	2.904	3.017	2.932	3.017	2.897
	4 – 13	3.077	3.190	3.065	3.152	3.089	3.299
	7 – 10	3.076	3.195	3.062	3.151	3.088	3.299
	5 – 6	3.075	2.954	3.084	2.966	3.100	3.041
	11 –	3.079	2.956	3.080	2.965	3.100	3.041
	6 – 8	3.028	3.257	3.014	3.232	3.042	3.206
	2 – 12	3.021	3.248	3.014	3.235	3.042	3.206
	8 – 13	3.012	2.895	3.021	2.905	2.991	2.899
	2 – 7	3.013	2.897	3.022	2.904	2.991	2.899
	2 – 3	3.088	3.360	3.064	3.290	3.110	3.444
	8 – 9	3.089	3.370	3.066	3.289	3.111	3.444
	3 – 12	3.016	3.242	3.007	3.200	2.996	3.180
	6 – 9	3.017	3.242	3.004	3.198	2.995	3.181

As listed in Table 3.7, the largest bond increases (bonds 2 – 3 and 8 – 9) in $Au_{25}(SCH_3)_{18}^-$, $Au_{25}(SCH_2CH_3)_{18}^-$, and $Au_{25}(SCH_2CH_2CH_3)_{18}^-$ are 0.28, 0.23, and 0.33 Å, respectively. This correlates with the smallest Stokes shift found for ethyl and the greatest Stokes shift calculated for propyl. Bonds 4 – 3, 9 – 10, 5 – 6, 11 – 12, 8 – 13, and 2 – 7 are shortened in the excited states of $Au_{25}(SR)_{18}^-$ compared to the related ground state geometries. The essentially icosahedral Au₁₃ core of the $Au_{25}(SR)_{18}^-$ clusters diverges even more from a true icosahedron due to these bond length changes in the excited state. As shown for the $Au_{25}(SH)_{18}^-$ cluster in the previous section, these geometrical changes can affect the energy levels of the frontier orbitals of

Au$_{25}$(SR)$_{18}^-$ clusters significantly. Figure 3.5 and Table A5 demonstrate the splitting of frontier orbitals in the excited states of Au$_{25}$(SR)$_{18}^-$ clusters with respect to their ground states.
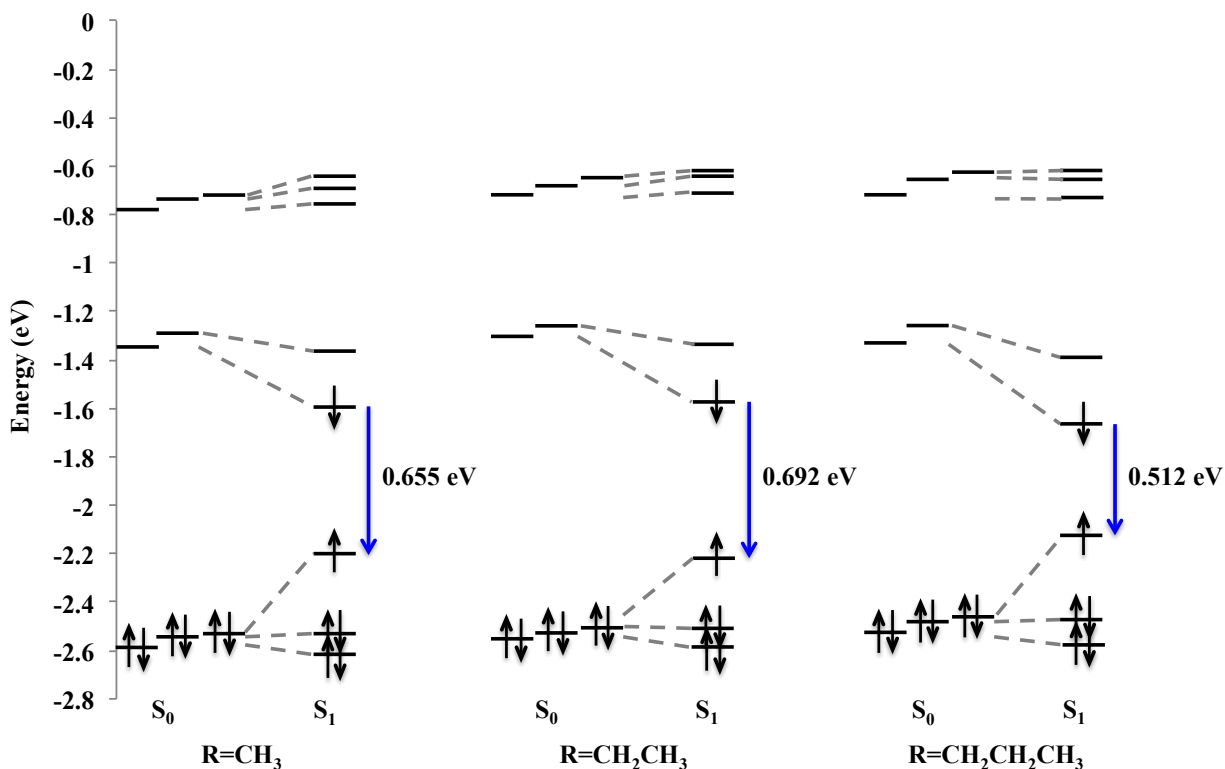
Figure 3.5 Comparison of energy levels of the frontier orbitals in S$_0$ and S$_1$ states of Au$_{25}$(SR)$_{18}^-$ clusters. The S$_1$ state is shown in a cartoon representation with a single electron in one of the D orbitals. Dashed lines are drawn to show the splitting of triply-degenerate HOMO/HOMO-1/HOMO-2, doubly-degenerate LUMO/LUMO+1, and triply degenerate LUMO+2/LUMO+3/LUMO+4 orbitals of the ground state upon photoexcitation.

Upon excitation, the HOMO orbitals of Au$_{25}$(SR)$_{18}^-$ (R = H, CH$_3$, CH$_2$CH$_3$, CH$_2$CH$_2$CH$_3$) clusters are destabilized by 0.33, 0.28, and 0.34 eV whereas the LUMO orbitals are stabilized by 0.25, 0.27, and 0.34 eV respectively. This gives rise to a large HOMO-LUMO gap reduction of 0.67 eV for the Au$_{25}$(SCH$_2$CH$_2$CH$_3$)$_{18}^-$ cluster. Moreover, HOMO-LUMO energy gaps are reduced by 0.58 and 0.55 eV in the relaxed excited state geometries of methyl- and ethyl-thiolate protected Au$_{25}$ clusters. However, LUMO+2, LUMO+3 and LUMO+4 orbitals of all three clusters do not vary significantly as shown in Table A5. The approximate degeneracy of the highest occupied orbitals in the S$_0$ state is again lost in the S$_1$ state. The highest splitting of

these orbitals is 0.5 eV in the S_1 state of $Au_{25}(SCH_2CH_2CH_3)_{18}^-$ cluster, whereas a splitting of 0.4 eV can be observed for methyl and ethyl-thiolate protected clusters. Similarly, the approximate double-degeneracy of the lowest unoccupied orbitals with a maximum splitting of 0.07 eV for these three clusters in the S_0 state is increased by ~0.2 eV in their S_1 states.

As suggested by the low emission energy and the large Stokes shift, the $Au_{25}(SCH_2CH_2CH_3)_{18}^-$ cluster has undergone the most geometric and electronic structure changes upon excitation. On the contrary, the highest emission energy and the lowest Stokes shift is observed for the $Au_{25}(SCH_2CH_3)_{18}^-$ cluster. This can be attributed to the relatively smaller bond length changes and frontier orbital energy level changes of this cluster. Thus, longer ligands appear to control luminescence via their effects on the geometry and electronic structure of the gold core.

Relatively small changes in emission energy are observed between the alkyl ligands examined in this work. A larger change is noted for the alkyl ligands relative to the small SH model ligand. Studies including larger ligands are of interest in order to elucidate the differences previously observed between nanoparticles with phenylethylthiol ligands and those with the glutathione ligand. At present, open questions exist about the role of ligands on the emission energies and intensities, as well as the potential impact of solvent (aqueous or organic) on these items. Nonetheless, this study demonstrates the intriguing geometrical and electronic changes that occur in the $Au_{25}(SR)_{18}^-$ nanoparticle upon photoexcitation.

3.5 Conclusions

DFT and TDDFT calculations were performed to investigate the origin of photoluminescence of $Au_{25}(SR)_{18}^-$ (R = H, CH_3, CH_2CH_3, $CH_2CH_2CH_3$) nanoclusters in the gas phase. The Au-Au bonds in the Au_{13} icosahedral shell expand slightly on average in the first excited state as compared to the ground state geometry. However, the bonds do not expand uniformly, with some bond lengths increasing by up to 0.33 Å. As a result, the shell becomes less symmetrical causing an increased splitting among HOMO/HOMO-1/HOMO-2 orbitals and the LUMO/LUMO+1 orbitals, which were approximately triply and doubly degenerate, respectively, in the ground state. In consequence, the geometrical changes in the structure lead to significant changes in the electronic structure. Stokes shifts of 0.49, 0.58, 0.56, and 0.68 eV are observed for $Au_{25}(SR)_{18}^-$ (R = H, CH_3, CH_2CH_3, $CH_2CH_2CH_3$) nanoclusters, respectively. The

nuclear relaxation after photoexcitation gives rise to vibrational beating observed in the 75-80 cm^{-1} range.

Higher excited state calculations suggest that several states could be responsible for the observed emission of Au$_{25}$(SH)$_{18}^-$. The lowest calculated state that lies around 0.8 eV is populated from photoexcitation into S$_1$ or S$_2$, or transitions from higher states into these states. Two other states around 1.15 eV and 1.25 eV are populated from photoexcitation into S$_3$ or S$_4$ and S$_5$ or S$_6$ or transitions from higher energy states into these states. The calculated states agree well with the experimentally observed emission in the 1.15-1.55 eV range, when the typical underestimation of GGA calculations is considered.

Overall, several excited states are involved in the photoemission from Au$_{25}$(SR)$_{18}^-$ nanoclusters. All of these excited states arise from excitations out of superatom P orbitals into the lowest two superatom D orbitals, which are core-based transitions. No charge-transfer or semi-ring states are observed in this work, which suggests that ligands primarily affect luminescence via their interactions with the gold nanoparticle core.

3.6 Acknowledgements

3.7 References

1.   Zhang, Y.; Chu, W.; Foroushani, A.; Wang, H.; Li, D.; Liu, J.; Barrow, C.; Wang, X.; Yang, W., New Gold Nanostructures for Sensor Applications: A Review. *Materials* **2014**, *7*, 5169.
2.   Yang, X.; Yang, M.; Pang, B.; Vara, M.; Xia, Y., Gold Nanomaterials at Work in Biomedicine. *Chem. Rev.* **2015**, *115*, 10410-10488.
3.   Herzing, A. A.; Kiely, C. J.; Carley, A. F.; Landon, P.; Hutchings, G. J., Identification of Active Gold Nanoclusters on Iron Oxide Supports for CO Oxidation. *Science* **2008**, *321*, 1331-1335.

4.   Liu, Y.; Tsunoyama, H.; Akita, T.; Xie, S.; Tsukuda, T., Aerobic Oxidation of Cyclohexane Catalyzed by Size-Controlled Au Clusters on Hydroxyapatite: Size Effect in the Sub-2 nm Regime. *ACS Catal.* **2011**, *1*, 2-6.

5.   Yamazoe, S.; Koyasu, K.; Tsukuda, T., Nonscalable Oxidation Catalysis of Gold Clusters. *Acc. Chem. Res.* **2014**, *47*, 816-824.

6.   Ide, Y.; Matsuoka, M.; Ogawa, M., Efficient Visible-Light-Induced Photocatalytic Activity on Gold-Nanoparticle-Supported Layered Titanate. *J. Am. Chem. Soc.* **2010**, *132*, 16762-16764.

7.   Sarina, S.; Waclawik, E. R.; Zhu, H., Photocatalysis on Supported Gold and Silver Nanoparticles under Ultraviolet and Visible Light Irradiation. *Green Chem.* **2013**, *15*, 1814-1833.

8.   Primo, A.; Corma, A.; Garcia, H., Titania Supported Gold Nanoparticles as Photocatalyst. *Phys. Chem. Chem. Phys.* **2011**, *13*, 886-910.

9.   Alvaro, M.; Cojocaru, B.; Ismail, A. A.; Petrea, N.; Ferrer, B.; Harraz, F. A.; Parvulescu, V. I.; Garcia, H., Visible-Lght Photocatalytic Activity of Gold Nanoparticles Supported on Template-Synthesized Mesoporous Titania for the Decontamination of the Chemical Warfare Agent Soman. *Appl. Catal. B* **2010**, *99*, 191-197.

10.   Zheng, J.; Zhou, C.; Yu, M.; Liu, J., Different Sized Luminescent Gold Nanoparticles. *Nanoscale* **2012**, *4*, 4073-4083.

11.   Iida, K.; Noda, M.; Ishimura, K.; Nobusada, K., First-Principles Computational Visualization of Localized Surface Plasmon Resonance in Gold Nanoclusters. *J. Phys. Chem. A* **2014**, *118*, 11317-11322.

12.   Xie, J.; Zheng, Y.; Ying, J. Y., Protein-Directed Synthesis of Highly Fluorescent Gold Nanoclusters. *J. Am. Chem. Soc.* **2009**, *131*, 888-889.

13.   Mooradian, A., Photoluminescence of Metals. *Phys. Rev. Lett.* **1969**, *22*, 185-187.

14.   Wilcoxon, J. P.; Martin, J. E.; Parsapour, F.; Wiedenman, B.; Kelley, D. F., Photoluminescence from Nanosize Gold Clusters. *J. Chem. Phys.* **1998**, *108*, 9137-9143.

15.   Mohamed, M. B.; Volkov, V.; Link, S.; El-Sayed, M. A., The `Lightning' Gold Nanorods: Fluorescence Enhancement of over a Million Compared to the Gold Metal. *Chem. Phys. Lett.* **2000**, *317*, 517-523.

16.   Bigioni, T. P.; Whetten, R. L.; Dag, Ö., Near-Infrared Luminescence from Small Gold Nanocrystals. *J. Phys. Chem. B* **2000**, *104*, 6983-6986.

17.   Huang, T.; Murray, R. W., Visible Luminescence of Water-Soluble Monolayer-Protected Gold Clusters. *J. Phys. Chem. B* **2001**, *105*, 12498-12502.

18.   Wang, G.; Huang, T.; Murray, R. W.; Menard, L.; Nuzzo, R. G., Near-IR Luminescence of Monolayer-Protected Metal Clusters. *J. Am. Chem. Soc.* **2005**, *127*, 812-813.

19.   Negishi, Y.; Nobusada, K.; Tsukuda, T., Glutathione-Protected Gold Clusters Revisited: Bridging the Gap between Gold(I)−Thiolate Complexes and Thiolate-Protected Gold Nanocrystals. *J. Am. Chem. Soc.* **2005**, *127*, 5261-5270.

20.   Negishi, Y.; Takasugi, Y.; Sato, S.; Yao, H.; Kimura, K.; Tsukuda, T., Magic-Numbered Au_n Clusters Protected by Glutathione Monolayers (n = 18, 21, 25, 28, 32, 39): Isolation and Spectroscopic Characterization. *J. Am. Chem. Soc.* **2004**, *126*, 6518-6519.

21.   Zhu, M.; Aikens, C. M.; Hollander, F. J.; Schatz, G. C.; Jin, R., Correlating the Crystal Structure of A Thiol-Protected Au_{25} Cluster and Optical Properties. *J. Am. Chem. Soc.* **2008**, *130*, 5883-5885.

22.   Heaven, M. W.; Dass, A.; White, P. S.; Holt, K. M.; Murray, R. W., Crystal Structure of the Gold Nanoparticle [N(C$_8$H$_{17}$)$_4$][Au$_{25}$(SCH$_2$CH$_2$Ph)$_{18}$]. *J. Am. Chem. Soc.* **2008**, *130*, 3754-3755.

23.   Akola, J.; Walter, M.; Whetten, R. L.; Häkkinen, H.; Grönbeck, H., On the Structure of Thiolate-Protected Au$_{25}$. *J. Am. Chem. Soc.* **2008**, *130*, 3756-3757.

24.   Link, S.; Beeby, A.; FitzGerald, S.; El-Sayed, M. A.; Schaaff, T. G.; Whetten, R. L., Visible to Infrared Luminescence from a 28-Atom Gold Cluster. *J. Phys. Chem. B* **2002**, *106*, 3410-3415.

25.   Link, S.; El-Sayed, M. A.; Gregory Schaaff, T.; Whetten, R. L., Transition from Nanoparticle to Molecular Behavior: A Femtosecond Transient Absorption Study of a Size-Selected 28 atom Gold Cluster. *Chem. Phys. Lett.* **2002**, *356*, 240-246.

26.   Schaaff, T. G.; Whetten, R. L., Giant Gold−Glutathione Cluster Compounds: Intense Optical Activity in Metal-Based Transitions. *J. phys. Chem. B* **2000**, *104*, 2630-2641.

27.   Schaaff, T. G.; Knight, G.; Shafigullin, M. N.; Borkman, R. F.; Whetten, R. L., Isolation and Selected Properties of a 10.4 kDa Gold:Glutathione Cluster Compound. *J. Phys. Chem. B* **1998**, *102*, 10643-10646.

28.   Lee, D.; Donkers, R. L.; Wang, G.; Harper, A. S.; Murray, R. W., Electrochemistry and Optical Absorbance and Luminescence of Molecule-like Au$_{38}$ Nanoparticles. *J. Am. Chem. Soc.* **2004**, *126*, 6193-6199.

29.   Shibu, E. S.; Pradeep, T., Photoluminescence and Temperature-Dependent Emission Studies of Au$_{25}$ Clusters in the Solid State. *Int. J. Nanosci.* **2009**, *08*, 223-226.

30.   Shibu, E. S.; Muhammed, M. A. H.; Tsukuda, T.; Pradeep, T., Ligand Exchange of Au$_{25}$SG$_{18}$ Leading to Functionalized Gold Clusters: Spectroscopy, Kinetics, and Luminescence. *J. Phys. Chem. C* **2008**, *112*, 12168-12176.

31.   Green, T. D.; Yi, C.; Zeng, C.; Jin, R.; McGill, S.; Knappenberger, K. L., Temperature-Dependent Photoluminescence of Structurally-Precise Quantum-Confined Au$_{25}$(SC$_8$H$_9$)$_{18}$ and Au$_{38}$(SC$_{12}$H$_{25}$)$_{24}$ Metal Nanoparticles. *J. Phys. Chem. A* **2014**, *118*, 10611-10621.

32.   Miller, S. A.; Womick, J. M.; Parker, J. F.; Murray, R. W.; Moran, A. M., Femtosecond Relaxation Dynamics of Au$_{25}$L$_{18}$$^-$ Monolayer-Protected Clusters. *J. Phys. Chem. C* **2009**, *113*, 9440-9444.

33.   Qian, H.; Y. Sfeir, M.; Jin, R., Ultrafast Relaxation Dynamics of [Au$_{25}$(SR)$_{18}$]^q Nanoclusters: Effects of Charge State. *J. Phys. Chem. C* **2010**, *114*, 19935-19940.

34.   Wang, G.; Guo, R.; Kalyuzhny, G.; Choi, J.-P.; Murray, R. W., NIR Luminescence Intensities Increase Linearly with Proportion of Polar Thiolate Ligands in Protecting Monolayers of Au$_{38}$ and Au$_{140}$ Quantum Dots. *J. Phys. Chem. B* **2006**, *110*, 20282-20289.

35.   Wu, Z.; Jin, R., On the Ligand's Role in the Fluorescence of Gold Nanoclusters. *Nano Lett.* **2010**, *10*, 2568-2573.

36.   Wang, S.; Zhu, X.; Cao, T.; Zhu, M., A Simple Model for Understanding the Fluorescence Behavior of Au$_{25}$ Nanoclusters. *Nanoscale* **2014**, *6*, 5777-5781.

37.   Devadas, M. S.; Kim, J.; Sinn, E.; Lee, D.; Goodson, T.; Ramakrishna, G., Unique Ultrafast Visible Luminescence in Monolayer-Protected Au$_{25}$ Clusters. *J. Phys. Chem. C* **2010**, *114*, 22417-22423.

38.   Ramakrishna, G.; Varnavski, O.; Kim, J.; Lee, D.; Goodson, T., Quantum-Sized Gold Clusters as Efficient Two-Photon Absorbers. *J. Am. Chem. Soc.* **2008**, *130*, 5032-5033.

39.   Yau, S. H.; Varnavski, O.; Gilbertson, J. D.; Chandler, B.; Ramakrishna, G.; Goodson, T., Ultrafast Optical Study of Small Gold Monolayer Protected Clusters: A Closer Look at Emission. *J. Phys. Chem. C* **2010**, *114*, 15979-15985.

40.   te Velde, G.; Bickelhaupt, F. M.; Baerends, E. J.; Fonseca Guerra, C.; van Gisbergen, S. J. A.; Snijders, J. G.; Ziegler, T., Chemistry with ADF. *J. Comput. Chem.* **2001**, *22*, 931-967.

41.   Becke, A. D., Density-Functional Exchange-Energy Approximation with Correct Asymptotic Behavior. *Phys. Rev. A* **1988**, *38*, 3098-3100.

42.   Perdew, J. P., Density-Functional Approximation for the Correlation Energy of the Inhomogeneous Electron Gas. *Phys. Rev. B* **1986**, *33*, 8822-8824.

43.   Aikens, C. M., Effects of Core Distances, Solvent, Ligand, and Level of Theory on the TDDFT Optical Absorption Spectrum of the Thiolate-Protected Au_{25} Nanoparticle. *J. Phys. Chem. A* **2009**, *113*, 10811-10817.

44.   Guidez, E. B.; Aikens, C. M., Time-Dependent Density Functional Theory Study of the Luminescence Properties of Gold Phosphine Thiolate Complexes. *J. Phys. Chem. A* **2015**, *119*, 3337-3347.

45.   Chen, S.; Wang, S.; Zhong, J.; Song, Y.; Zhang, J.; Sheng, H.; Pei, Y.; Zhu, M., The Structure and Optical Properties of the $[Au_{18}(SR)_{14}]$ Nanocluster. *Angew. Chem. Int. Ed.* **2015**, *54*, 3145-3149.

46.   Bae, G.-T.; Aikens, C. M., Time-Dependent Density Functional Theory Studies of Optical Properties of Au Nanoparticles: Octahedra, Truncated Octahedra, and Icosahedra. *J. Phys. Chem. C* **2015**, *119*, 23127-23137.

47.   Hulkko, E.; Lopez-Acevedo, O.; Koivisto, J.; Levi-Kalisman, Y.; Kornberg, R. D.; Pettersson, M.; Häkkinen, H., Electronic and Vibrational Signatures of the $Au_{102}(p\text{-}MBA)_{44}$ Cluster. *J. Am. Chem. Soc.* **2011**, *133*, 3752-3755.

48.   Liao, M.-S.; Bonifassi, P.; Leszczynski, J.; Ray, P. C.; Huang, M.-J.; Watts, J. D., Structure, Bonding, and Linear Optical Properties of a Series of Silver and Gold Nanorod Clusters: DFT/TDDFT Studies. *J. Phys. Chem. A* **2010**, *114*, 12701-12708.

49.   Aikens, C. M.; Li, S.; Schatz, G. C., From Discrete Electronic States to Plasmons: TDDFT Optical Absorption Properties of Ag_n (n = 10, 20, 35, 56, 84, 120) Tetrahedral Clusters. *J. Phys. Chem. C* **2008**, *112*, 11272-11279.

50.   Costa, P. J.; Calhorda, M. J., A DFT and MP2 Study of Luminescence of Gold(I) Complexes. *Inorg. Chim. Acta.* **2006**, *359*, 3617-3624.

51.   Bode, B. M.; Gordon, M. S., Macmolplt: A Graphical User Interface for GAMESS. *J. Mol. Graphics and Modelling* **1998**, *16*, 133-138.

52.   Aikens, C. M., Origin of Discrete Optical Absorption Spectra of $M_{25}(SH)_{18}^{-}$ Nanoparticles (M = Au, Ag). *J. Phys. Chem. C* **2008**, *112*, 19797-19800.

53.   Aikens, C. M., Electronic Structure of Ligand-Passivated Gold and Silver Nanoclusters. *J. Phys. Chem. Lett.* **2011**, *2*, 99-104.

54.   Walter, M.; Akola, J.; Lopez-Acevedo, O.; Jadzinsky, P. D.; Calero, G.; Ackerson, C. J.; Whetten, R. L.; Grönbeck, H.; Häkkinen, H., A unified view of ligand-protected gold clusters as superatom complexes. *Proc. Natl. Acad. Sci.* **2008**, *105*, 9157-9162.

55.   Marques, M. A. L.; Castro, A.; Rubio, A., Assessment of Exchange-Correlation Functionals for the Calculation of Dynamical Properties of Small Clusters in Time-Dependent Density Functional Theory. *J. Chem. Phys.* **2001**, *115*, 3006-3014.

56.   Tofanelli, M. A.; Salorinne, K.; Ni, T. W.; Malola, S.; Newell, B.; Phillips, B.; Hakkinen, H.; Ackerson, C. J., Jahn-Teller effects in $Au_{25}(SR)_{18}$. *Chem. Sci.* **2016**, *7*, 1882-1890.

Chapter 4 - Photoluminescence Origin of $Au_{38}(SR)_{24}$ and $Au_{22}(SR)_{18}$ Nanoparticles: A Theoretical Perspective

4.1 Abstract

Photoluminescence of metal nanoparticles has drawn considerable research interest due to their potential fundamental and industrial applications in optoelectronics and biomedicine. However, the origin and underlying mechanism of photoluminescence in these clusters still need to be explored. Herein, the geometrical and electronic structural changes upon photoexcitation in the $Au_{38}(SH)_{24}$ and $Au_{22}(SH)_{18}$ nanoclusters are discussed using time-dependent density functional theory (TDDFT) methods. Geometric relaxations in the Au_{23} core of $Au_{38}(SH)_{24}$ up to a maximum of 0.05 Å lead to slight electronic structure changes in the optimized singlet excited states with different state symmetries. The observed geometric and electronic structure variations upon photoexcitation are minor compared to the previously studied $Au_{25}(SH)_{18}^-$ nanoparticle. These small distortions can be correlated with small Stokes shifts calculated in the range of 0.06-0.09 eV, in comparison to 0.49 eV for the $Au_{25}(SH)_{18}^-$ nanoparticle. Compared to $Au_{38}(SH)_{24}$, the optimized first singlet and triplet excited states of $Au_{22}(SH)_{18}$ nanoparticle show larger structural flexibility in the Au_7 core, which leads to significant electronic structure modifications and large Stokes shifts. These states are predicted to have microsecond-scale lifetimes, in agreement with available experimental data.

4.2 Introduction

Luminescence properties of gold nanoclusters (NCs) have drawn increasing research interest during the past decade. Their ultrafine size, good biocompatibility, and excellent stability can replace semiconductor quantum dots and organic dye molecules in a variety of biomedical applications including bio-imaging, sensing, and cancer therapy.[1-7] Initially, atomically precise thiolate-protected gold NCs ($Au_n(SR)_m$) showed very weak visible to near-infrared (NIR)

luminescence with a typical quantum yield (QY) of <0.1%.[8-12] However, more recently, luminescent thiolate-stabilized Au NCs have been synthesized with a QY of ~10-60%.[13-16]

A recent review from Zheng et al.[17] summarizes the emission properties and mechanisms of different-sized luminescent gold nanoparticles. The luminescence properties of $Au_{25}(SR)_{18}^-$ nanoclusters have been studied extensively. Broad emission spanning the range of 1.8 to 1.1 eV is reported for $Au_{25}(SR)_{18}^-$ NCs where SR includes alkanethiols and glutathione.[12, 18-22] Several investigations proposed that the observed emission arises due to core based orbitals (interband or intraband transitions),[12, 19] and some studies suggested that it is due to emission from 'semi-ring' states (states below the HOMO-LUMO state arising from orbitals based on the gold-thiolate units),[23, 24] or charge-transfer states.[22] Recently, we performed a theoretical investigation to determine the origin of emission of $Au_{25}(SR)_{18}^-$ nanoclusters using time-dependent density functional theory (TDDFT) methods.[25] An excellent agreement was observed between the calculated states and experimental emission energies, once the typical underestimation of GGA calculations was considered. Moreover, we concluded that several excited states are involved in the photoemission from $Au_{25}(SR)_{18}^-$ nanoclusters and that core-based excitations arising from electrons excited from superatom P orbitals into the lowest two superatom D orbitals are responsible for all of these states.

Herein, a similar study is performed to understand the luminescence mechanisms of monolayer protected Au_{38} and Au_{22} nanoclusters. The total structure of $Au_{38}(SH)_{24}$ is chiral and the particle is prolate in shape as shown in Figure 4.1. It consists of a face fused biicosahedral Au_{23} core and the fusion of icosahedra occurs along a common C_3 axis.[26, 27] This Au_{23} core is protected by three monomeric –SR–Au–SR– staple motifs. The two icosahedra are further capped by three –SR–Au–SR–Au–SR– dimeric staples each, which are arranged in a rotary fashion.

In 2010, the temperature-dependent emission of monolayer protected Au_{38} NC[28] was studied in the temperature regime between 4 and 300 K using a 468 nm excitation wavelength.[29, 30] A broad emission band around 1.35 eV was observed at room temperature whereas cooling gave rise to a fine structure. At low temperatures, four emission bands were observed in the energy range of 0.97 – 1.47 eV. The energies and intensities of these peaks did not change significantly as a function of temperature. The lowest energy peak at 0.98 eV was attributed to the HOMO–LUMO transition and higher energy peaks at 1.15, 1.26, 1.46 eV were attributed to

transitions from higher excited states within the core. Recently, Knappenberger and coworkers[31] also studied temperature-dependent photoluminescence of $Au_{38}(SC_{12}H_{25})_{24}$ using time-resolved spectroscopy in the temperature range of 4.5 – 200 K. However, this study is limited to the 1.4 - 1.8 eV energy portion of the photoluminescence spectrum of Au_{38} due to the low quantum efficiencies of their sensor for NIR detection. No significant change in emission intensities was observed in the 4.5 – 50 K temperature range, similar to the previous study. However, the intensity decreased and peaks red-shifted in the 50 – 200 K temperature range. Two emission bands at 1.58 and 1.74 eV were observed in the broad spectrum spanning the energy range 1.4 - 1.8 eV. The energy shift and peak width analyses results showed that the nonradiative decay of $Au_{38}(SC_{12}H_{25})_{24}$ is mediated by two vibrational modes: Au(I)-S stretching (200 cm^{-1}) and Au(0)-Au(I) stretching (90 cm^{-1}) above 45 K.

Zheng and coworkers synthesized strongly luminescent ~2 nm gold nanoparticles by dissociation of glutathione-gold(I) polymers.[32] Their time-resolved spectroscopic studies showed that luminescence lifetimes measured at the same emission wavelength changed from microseconds to nanoseconds when the excitation wavelength was changed, and they suggested that singlet and triplet excited states are degenerate in these NPs. They proposed that the valence state of the gold atoms influences the emission of luminescent gold NPs because orange and yellow emitting NPs had different ratios of Au(0)/Au(I).[32] However, the origin of emission of gold NPs in this size regime including how the oxidation state of gold plays a role is still unclear. Recently, a novel nanocluster with the molecular formula of $Au_{22}(SG)_{18}$ was synthesized that showed unexpectedly strong red emission under UV illumination.[13, 15] Unique absorption peaks were observed at 450 and 515 nm and luminescence at 665 nm with a high quantum yield of ~8%.[13] Previously reported related systems $Au_{22}(SR)_{16}$ and $Au_{22}(SR)_{17}$[11] with the same number of Au atoms but different numbers of thiolate ligands as well as the well-characterized $Au_{25}(SR)_{18}$[33-35] that has the same number of thiolates but a different number of Au atoms luminesce very weakly. For the $Au_{22}(SG)_{18}$ cluster, a Stokes shift of 145 nm was identified and the microsecond-scale lifetime was attributed to possible long motifs on the NC surface.[13] However, the geometric structure of $Au_{22}(SR)_{18}$ NC is not yet solved crystallographically, which restricts our understanding of the structure-property relationships involved in highly luminescent thiolate-protected gold NCs. DFT calculations predicted a prolate Au_8 core protected by two

$Au_3(SR)_4$ (trimeric staples) and two $Au_4(SR)_5$ (tetrameric staples) motifs arranged in a way such that on each end a trimeric and a tetrameric staple are interlocked.[13]

Subsequently, Pyo et al. reported a novel strategy to enhance the luminescence efficiency of gold clusters based on the $Au_{22}(SG)_{18}$ NC.[15] Their time resolved photoluminescence measurements assigned fast, visible luminescence to relaxation within gold core states or to relaxation of gold core to gold shell. Furthermore, decreasing temperature from 303 to 77 K increased the NIR luminescence intensity and shifted the luminescence maximum from 670 to 580 nm. They suggested that the emission of the $Au_{22}(SG)_{18}$ cluster is primarily phosphorescence and its efficiency increases in the frozen media. They attributed the high quantum yield luminescence to ligand-to-metal–metal charge transfer (LMMCT) relaxation occurring at a triplet metal-centered state in the long, interlocked gold shell, based on the previously predicted structural model[13] of the $Au_{22}(SG)_{18}$ cluster. They enhanced the quantum yield of the cluster up to 60% by rigidifying its Au(I)–thiolate shell with tetraoctylammonium (TOA) cations.[15]

Recently, Zeng and coworkers[36] suggested a novel structure for the $Au_{22}(SR)_{18}$ cluster using DFT calculations. The optimized structure contains an Au_7 kernel similar to $Au_{20}(SR)_{16}$[37, 38] and the kernel is surrounded by a unique $[Au_6(SR)_6]$ ring type motif and three $Au_3(SR)_4$ staples.[36] The simulated optical absorption spectrum using the PBE/TZP level of theory qualitatively agreed well with the experimental spectrum. Two measured absorption peaks at ~450 and ~515 nm were well reproduced by TDDFT calculations at about 475 and 565 nm. They suggested that the intriguing luminescence properties of $Au_{22}(SR)_{18}$ cluster may originate from the $Au_6(SR)_6$ ring. In the current study, we use the well-characterized $Au_{38}(SR)_{24}$ cluster and the theoretically predicted $Au_{22}(SR)_{18}$ cluster by Zeng and coworkers to investigate the origin of their luminescence properties.

4.3 Computational Methods

The Amsterdam Density Functional (ADF) 2012.01 package was used for density functional theory (DFT) and time-dependent density functional theory (TDDFT) calculations.[39] The BP86 exchange-correlation functional[40, 41] and a full core double-ζ (DZ) basis set are used for all calculations. Generalized gradient approximation (GGA) functionals have been employed successfully in geometry relaxations, TDDFT, and excited state gradient calculations of gold and silver nanoclusters previously.[25, 35, 42-48] All structures are optimized in the gas phase. The energy

and gradient convergence criteria are tightened to 1×10^{-4} and 1×10^{-3} to obtain well-converged geometries. Scalar relativistic effects are included by utilizing the zeroth-order regular approximation (ZORA).[49] The vertical excitations are calculated using the same level of theory as the optimized ground state geometries. Then, excited state gradients are calculated to optimize the excited state geometry. Luminescence properties of Au(I) complexes with thiolate and phosphine ligands have been studied previously[43, 50] and the experimental and theoretical results have agreed well, with an underestimation of calculated emission peak energies by about 0.3 eV compared to the experimental results. Herein, we calculate the optimized structure for excited states of $Au_{38}(SH)_{24}$ and $Au_{22}(SH)_{18}$ nanoclusters in order to determine the origin of the emission in these systems. All structures are visualized using the MacMolPlt[51] visualization tool.

4.4 Results and Discussion

4.4.1 $Au_{38}(SH)_{24}$
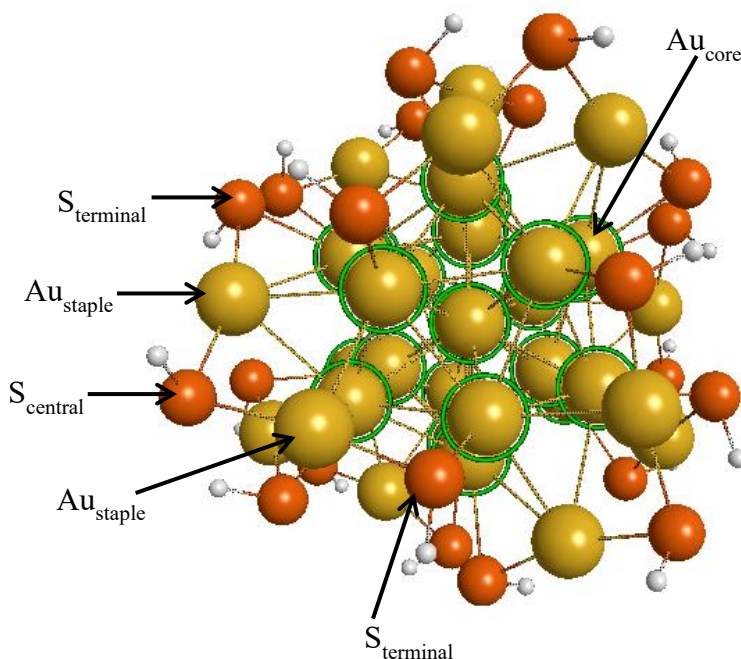
Figure 4.1 Structure of $Au_{38}(SH)_{24}$. Face-fused biicosahedral Au_{23} core gold atoms are marked with green circles. The orange, yellow, and white color spheres represent sulfur, gold, and hydrogen atoms, respectively. This color code is consistent in all figures presented in this article.

The average bond lengths calculated at the BP86/DZ level of theory of the ground state structure of $Au_{38}(SH)_{24}$ in the gas phase are summarized in Table 4.1. The average Au–Au bond distance within the Au_{23} core is 2.919 ± 0.105 Å, which is 1.4% longer than the Au–Au distance of 2.88 Å in bulk gold. The average Au_{core}–$S_{terminal}$ bond length is about 0.1 Å longer than the other Au_{staple}–S_{staple} distances within monomeric and dimeric staple motifs.

The electronic structure of the prolate D_3 isomer of $Au_{38}(SH)_{24}$ cluster has been analyzed considering a nanorod-like particle-in-a-cylinder (PIC) model.[26] As shown in Figure 4.2, the occupied and unoccupied orbitals near the HOMO-LUMO gap have Σ, Π, and Δ symmetries analogous to those identified previously for pentagonal silver nanorods.[52] The orbitals are labeled M_l, where the azimuthal quantum number M = 0, 1, 2, … corresponds to Σ, Π, Δ orbitals and l = 1, 2, 3, corresponds to the axial quantum number. The HOMO and LUMO orbitals of this nanocluster are doubly degenerate and the two orbitals in each set are labeled as "a" and "b". A TDDFT calculation was performed on the relaxed ground state geometry of the $Au_{38}(SH)_{24}$ cluster and the first five singlet excited state energies, oscillator strengths, state symmetries, and major MO $\rightarrow$ MO transitions responsible for each excitation are tabulated in Table 4.2. The two calculated state symmetries agree well with the interpretation of this cluster as a nanorod, and these states correspond to transverse (E) and longitudinal (A_2) excitations. The optical absorption spectrum calculated using the BP86/DZ level of theory well-reproduces experimental absorption features[53] with ~0.1 eV underestimation of peak positions. This discrepancy is expected, since GGA functionals are known to produce underestimated excitation and emission energies.[25, 42, 54] The calculated HOMO-LUMO gap of 0.9 eV is in excellent agreement with the reported experimental optical gap of ~0.9 eV.[53]

We optimized the geometries of first singlet excited states with both E and A_2 symmetries (S_1 and S_2), in order to determine the origin of the lowest energy emission of $Au_{38}(SH)_{24}$. Kasha's rule states that substantial yield of photon emission occurs from the lowest excited state of a given multiplicity. Hence, only the lowest singlet excited states of the different state symmetries are considered here. The calculated fluorescence energies of $Au_{38}(SH)_{24}$ are 0.88 and 0.99 eV for E and A_2 symmetries respectively, which are obtained by taking the energy gaps between the S_0 and S_1 (S_0 and S_2) states at the optimized excited state geometries. These energies correspond to 1412 and 1252 nm fluorescence wavelengths, respectively. The calculated emission energies are in good agreement (again, given typical underestimation) with the

experimental emission energies of 0.98 and 1.15 eV reported by Wijngaarden et al.[29] In agreement with their suggestion, we observe that the two lowest energy emission peaks arise due to HOMO-LUMO transitions and it appears that higher energy peaks arise from other transitions that involve core-based orbitals. It should be noted that there have been some questions related to the stoichiometry and purity of the sample in Ref. 29,[30] but the experimentally reported peaks are in good agreement with the theoretical results reported here.

Table 4.1 Geometrical parameters of the ground state and first singlet excited state structures of $Au_{38}(SH)_{24}$ at the BP86/DZ level of theory.

Bond	Average Bond Length (Å)		
	Ground State (S_0)	Excited State	
		E Symmetry	A_2 Symmetry
Au_{core}–Au_{core}	2.919 ± 0.105	2.923 ± 0.108	2.922 ± 0.107
Au_{core}–$S_{terminal}$	2.534 ± 0.008	2.536 ± 0.004	2.537 ± 0.005
Au_{staple}–$S_{terminal}$	2.430 ± 0.013	2.430 ± 0.013	2.430 ± 0.013
Au_{staple}–$S_{central}$	2.437 ± 0.004	2.441 ± 0.005	2.441 ± 0.005

Table 4.2 Excited-state energies, oscillator strengths, state symmetries, and major MO → MO transitions responsible for the first five excitations of $Au_{38}(SH)_{24}$ at the optimized S_0 geometry.

State	Energy (eV)	Oscillator Strength (au)	Symmetry	Major MO→MO Transitions
S_1	0.967	4.238×10^{-4}	E	HOMO → LUMO
S_2	1.055	4.032×10^{-2}	A_2	HOMO → LUMO
S_3	1.175	4.625×10^{-3}	E	HOMO-1 → LUMO
S_4	1.264	1.503×10^{-5}	E	HOMO → LUMO+1
S_5	1.284	9.161×10^{-4}	A_2	HOMO-2 → LUMO

Δ_1

-4.02 eV
LUMO+2$_a$

-4.02 eV
LUMO+2$_b$

Σ_4

-4.13 eV
LUMO+1

Π_3

-4.44 eV
LUMO$_a$

-4.44 eV
LUMO$_b$

Π_2

-5.35 eV
HOMO$_a$

-5.35 eV
HOMO$_b$

Σ_3

-5.55 eV
HOMO-1

Π_1

-5.70 eV
HOMO-2$_a$

-5.70 eV
HOMO-2$_b$
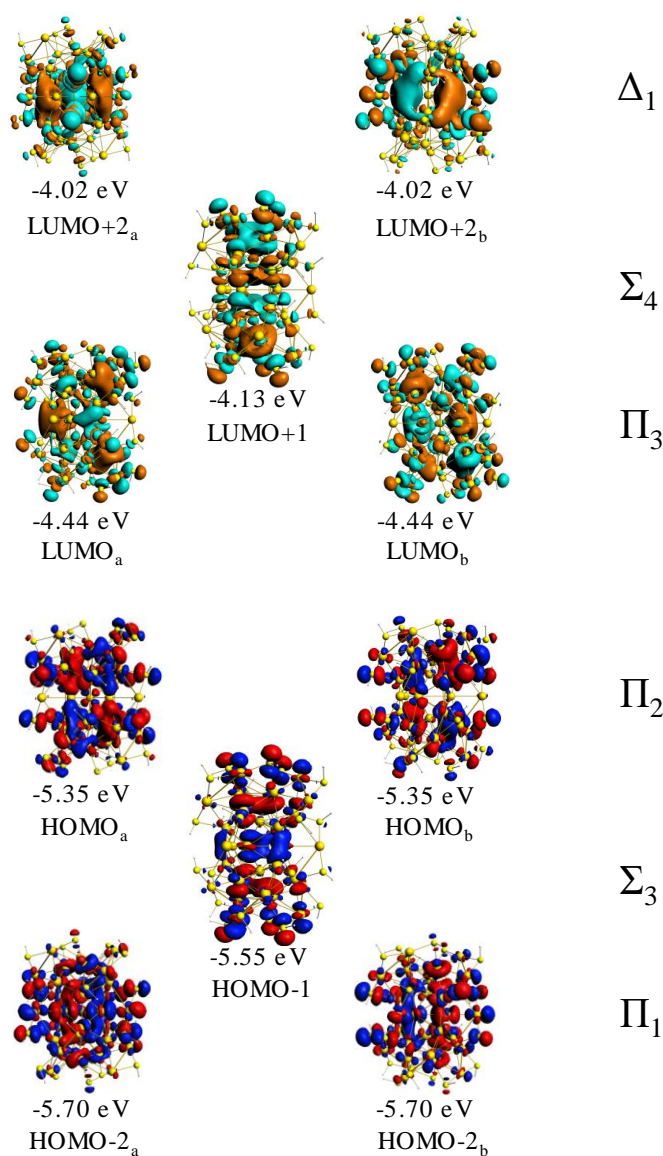
Figure 4.2 BP86/DZ Kohn-Sham orbitals and orbital energies for ground state (S$_0$) of Au$_{38}$(SR)$_{24}$. |Isovalue| = 0.015.

The geometrical parameters of the S$_1$ excited state structures of Au$_{38}$(SH)$_{24}$ in the gas phase are summarized in Table 4.1. The average bond lengths of the ground state structure increase by less than 0.005 Å in the excited state geometries of Au$_{38}$(SH)$_{24}$ cluster for both state symmetries. In contrast to ~0.25 Å Au$_{core}$–Au$_{core}$ bond length changes observed in the S$_1$ state geometry of Au$_{25}$(SH)$_{18}{}^-$,[25] a maximum 0.05 Å elongation of the entire Au$_{23}$ core of the

$Au_{38}(SH)_{24}$ cluster was found upon photoexcitation. These slight geometrical changes have minor effects on the energy levels of the frontier orbitals of Au_{38} cluster. Moreover, the Kohn-Sham orbitals of the lowest energy singlet excited states for E and A_2 symmetries preserve their Σ, Π, and Δ character similar to the ground state orbitals shown in Figure 4.2. The doubly degenerate HOMO orbitals are destabilized by 0.04 and 0.03 eV whereas doubly degenerate LUMO orbitals are stabilized by 0.05 and 0.04 eV in the optimized geometries of the excited E and A_2 states, respectively. (Note: Although the orbital occupation changes in the excited states, we will retain the "HOMO" and "LUMO" labels for consistency.) Therefore, the corresponding HOMO-LUMO gaps are reduced to 0.82 and 0.84 eV upon photoexcitation. Furthermore, we optimized the lowest energy triplet state (T_1) of the $Au_{38}(SH)_{24}$ nanoparticle as well. The calculated emission energy is 0.60 eV, which is significantly lower in energy than the experimental emission energies reported by Wijngaarden et al.[29] Some Au-Au bonds in the Au_{23} core are found to be shortened by a maximum of 0.18 Å in the optimized T_1 state compared to the ground state geometry. However, the length of the entire Au_{23} core does not change noticeably while its width increases by ~0.1 Å in the T_1 state.

It is evident that the structural distortion in the $Au_{38}(SH)_{24}$ nanoparticle is less than that previously reported for the $Au_{25}(SH)_{18}^-$ nanoparticle. Upon excitation of $Au_{25}(SH)_{18}^-$, one electron is excited from an essentially triply degenerate P orbital into an essentially doubly degenerate D orbital.[25] Because of the unequal filling of orbitals, a Jahn-Teller distortion must occur, which causes large geometric changes.[25] No triply degenerate P orbitals are present in the $Au_{38}(SH)_{24}$ nanoparticle, and the excitation between Π orbitals does not appear to cause large structural distortions.

4.4.2 $Au_{22}(SH)_{18}$

Figure 4.3 demonstrates the model cluster for $Au_{22}(SR)_{18}$ proposed by Zeng and coworkers,[36] which consists of a vertex-sharing Au_7 bitetrahedral unit, an $[Au_6(SR)_6]$ ring motif, and three $Au_3(SR)_4$ staple motifs. The average bond lengths calculated at the BP86/DZ level of theory for this structure in the gas phase are summarized in Table 4.3. The average Au–Au bond distance within the Au_7 core is calculated to be 2.779 ± 0.047 Å, which is 3.5% shorter than the Au–Au distance of 2.88 Å in bulk gold. Unlike other staple motifs, the $[Au_6(SR)_6]$ ring motif

interacts with the gold core through gold-gold bonds. However, these Au_{core}–Au_{ring} bonds are 7.6% longer than the Au_{core}–Au_{core} bonds within the Au_7 core.
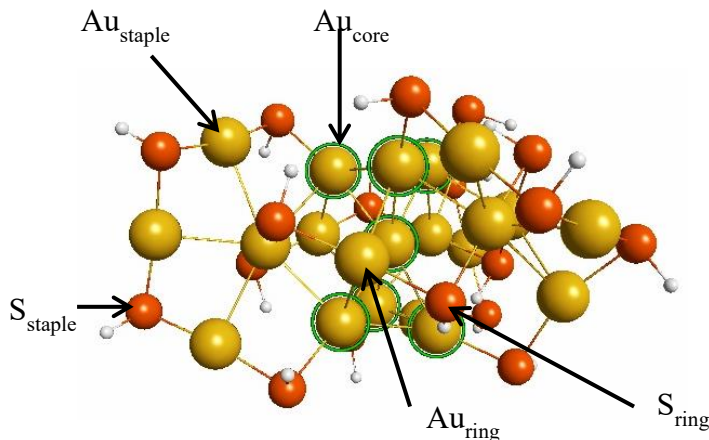
Figure 4.3 Structure of Au₂₂(SH)₁₈. Vertex-sharing bitetrahedral Au₇ core gold atoms are marked with green circles.

Table 4.3 Optimized geometrical parameters of the ground state and the singlet and triplet excited state structures of Au₂₂(SH)₁₈ at the BP86/DZ level of theory.

Bond	Average Bond Length (Å)		
	Ground State (S_0)	Excited States	
		Singlet (S_1)	Triplet (T_1)
Au_{core}–Au_{core}	2.779 ± 0.047	2.790 ± 0.102	2.794 ± 0.113
Au_{core}–Au_{ring}	2.989 ± 0.051	2.953 ± 0.061	2.957 ± 0.053
Au_{ring}–S_{ring}	2.443 ± 0.030	2.460 ± 0.035	2.461 ± 0.032
Au_{core}–$S_{terminal}$	2.506 ± 0.011	2.524 ± 0.018	2.521 ± 0.012
Au_{staple}–S_{staple}	2.428 ± 0.012	2.429 ± 0.014	2.430 ± 0.014
Angle	Average Bond Angle (°)		
Au_{core}–Au_{core}–Au_{core}	60.00 ± 1.46	60.22 ± 3.36	60.00 ± 3.63

Table 4.4 Excited state energies, oscillator strengths, and major MO → MO transitions responsible for the first eight excitations of $Au_{22}(SH)_{18}$ at the optimized S_0 geometry.

State	Energy (eV)	Oscillator Strength (au)	Major MO→MO Transitions
T_1	1.765	0.000	HOMO → LUMO
S_1	1.791	2.206×10^{-4}	HOMO → LUMO
T_2	1.813	0.000	HOMO-1 → LUMO
T_3	1.824	0.000	HOMO → LUMO+1
T_4	1.889	0.000	HOMO-2 → LUMO
S_2	1.899	4.103×10^{-3}	HOMO → LUMO+1
T_5	1.906	0.000	HOMO-1 → LUMO+1
S_3	1.924	1.179×10^{-3}	HOMO-1 → LUMO+1

A population analysis of the Kohn-Sham molecular orbitals of the $Au_{22}(SR)_{18}$ cluster has been performed and the occupied molecular orbitals mainly arise from Au(5d) atomic orbitals whereas the unoccupied orbitals have significant contributions from the Au(6sp) atomic orbitals.[36] Therefore, the absorption peaks have been assigned to d→sp interband transitions. Analysis of the calculations performed in our work agrees with this assignment. The ground state frontier orbitals shown in Figure 4.4 indicate that the HOMO→LUMO transition involves some electron excitation from motif layers to the Au_7 core. The HOMO is a combination of Au atomic orbitals from the Au_7 core and staple motifs with some contribution from S atomic orbitals. The nearly doubly degenerate LUMO and LUMO+1 orbitals are concentrated in the Au_7 core, and display superatomic 1P orbital character (Figure 4.4). We performed a TDDFT calculation on the relaxed ground state geometry of the $Au_{22}(SH)_{18}$ cluster. The first eight singlet and triplet excited state energies, oscillator strengths, and major MO → MO transitions responsible for each excitation are tabulated in Table 4.4. Triplet states have zero oscillator strengths since excitations to these states are spin-forbidden. The optical absorption spectrum calculated using the BP86/DZ level of theory well-reproduces the experimental absorption

features with the typical underestimation (<0.4 eV) of peak positions and also reproduces the previous[36] TDDFT/PBE results.
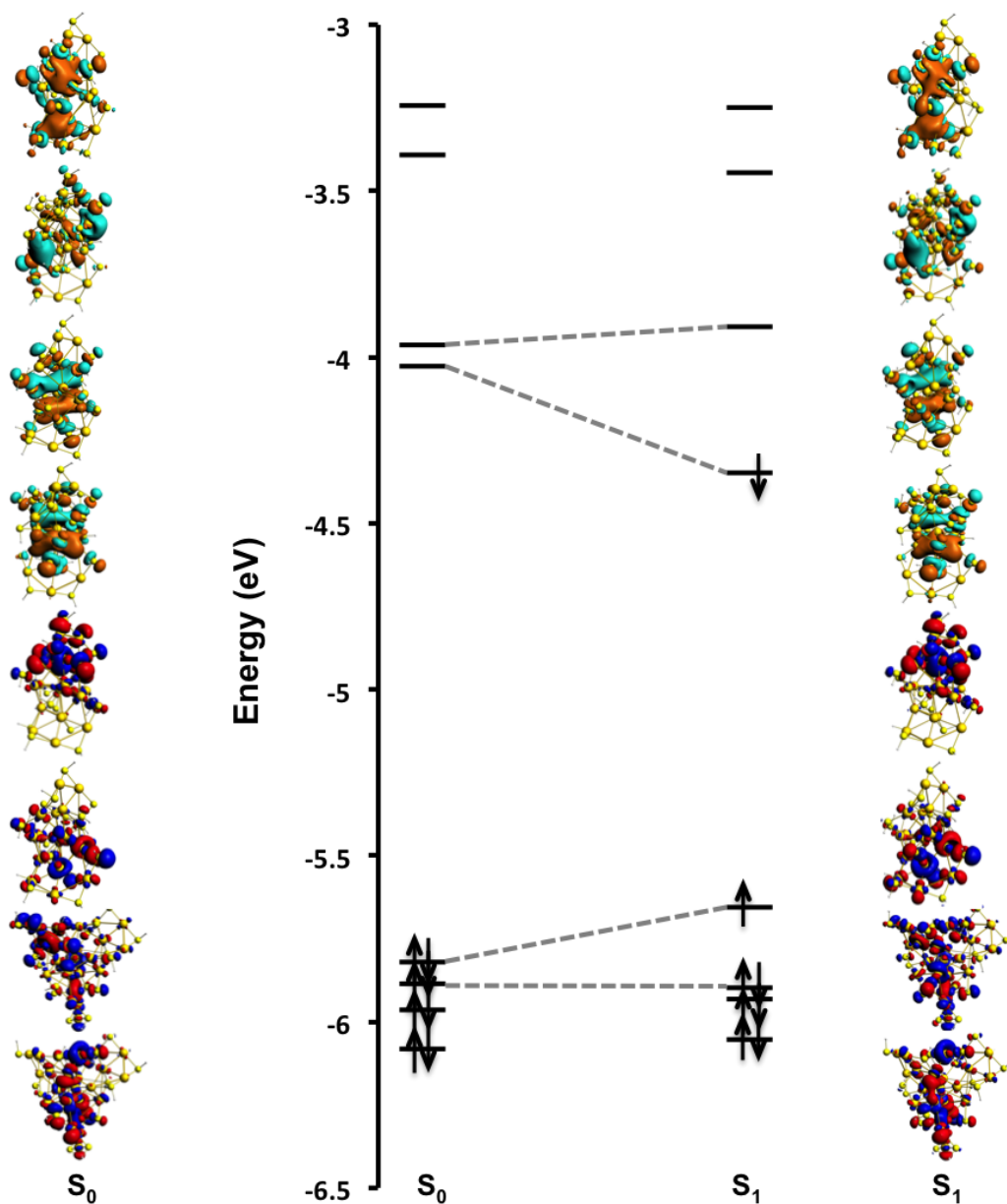
Figure 4.4 Comparison of energy levels and Kohn-Sham orbitals (|Isovalue|=0.025) in the optimized S_0 and S_1 states of the $Au_{22}(SH)_{18}$ nanocluster. The S_1 state is shown in a cartoon representation with a single electron excited to one of the superatomic P orbitals. Dashed lines are drawn to show the splitting of the ground state HOMO/HOMO-1 and LUMO/LUMO+1 orbitals upon photoexcitation.

Table 4.5 Spin-orbit coupled excited state energies oscillator strengths and radiative lifetimes at the S_0 and S_1 geometries of the $Au_{22}(SH)_{18}$ nanocluster.

State	S_0 geometry			S_1 geometry		
	Energy (eV)	Oscillator strength (au)	Electric dipole radiative lifetimes (s)	Energy (eV)	Oscillator strength (au)	Electric dipole radiative lifetimes (s)
1	1.576	2.756×10^{-5}	3.365×10^{-4}	1.193	1.283×10^{-4}	1.263×10^{-4}
2	1.577	3.540×10^{-5}	2.618×10^{-4}	1.193	1.505×10^{-5}	1.075×10^{-3}
3	1.594	4.366×10^{-4}	2.079×10^{-5}	1.194	4.351×10^{-5}	3.712×10^{-4}
4	1.600	4.920×10^{-4}	1.830×10^{-5}	1.218	6.035×10^{-4}	2.572×10^{-5}
5	1.640	2.720×10^{-4}	3.150×10^{-5}	1.372	2.270×10^{-5}	5.394×10^{-4}
6	1.641	7.273×10^{-5}	1.176×10^{-4}	1.373	4.965×10^{-5}	2.461×10^{-4}
7	1.653	7.972×10^{-4}	1.058×10^{-5}	1.390	1.166×10^{-3}	1.023×10^{-5}

Spin-orbit coupling (SOC) can be important for gold and may affect excited state energies and oscillator strengths. A single-point TDDFT excitation calculation was performed with spin-orbit coupling at the optimized S_0 geometry. The spin-orbit coupled excitations at the S_0 geometry (Table 4.5) show that the first four excited states have very similar energies. These four states can be correlated with the components of the T_1 and S_1 states from non-SOC calculations shown in Table 4.4. (Because of spin-orbit coupling, states 1-4 cannot technically be assigned as singlet or triplet states. However, we will continue to use these common terms in this section.) Their non-zero oscillator strengths and energy degeneracy show that SOC is significant at the ground state geometry of $Au_{22}(SH)_{18}$ and hence intersystem crossing to triplet states is possible. Therefore, we optimize the geometries of both the first excited singlet (S_1) and triplet (T_1) states in order to determine the origin of the lowest energy emission of $Au_{22}(SH)_{18}$. Since TDDFT gradients with spin-orbit coupling are not supported in ADF, only scalar relativistic effects are taken into account during the optimization. The fluorescence energy is calculated by taking the energy gap between the S_0 and S_1 states at the optimized S_1 geometry,

which is 1.32 eV (939 nm). Similarly, the energy gap between the S_0 and T_1 states at the optimized T_1 geometry gives the phosphorescence energy of 1.23 eV (1008 nm). The low oscillator strength (8.76×10^{-4} au) of the S_1 state correlates with a long lifetime for radiative emission. Previously, the experimentally observed microsecond-scale lifetime[13, 15] has been attributed to a phosphorescence-type emission.[15] Our calculations show that the singlet and triplet states (represented by the four lowest energy states in Table 4.5) all have long lifetimes. This is likely due to the low spatial overlap of the HOMO and LUMO orbitals.

A single-point TDDFT excitation calculation was also performed with spin-orbit coupling at the optimized S_1 geometry. As shown in Table 4.5, the fourth excited state is slightly separated from first three in comparison to the ground state geometry, which suggests that the S_1 and T_1 states are less spin-orbit coupled at the optimized S_1 geometry. The fourth state, which closely corresponds to the singlet S_1 state, has a radiative lifetime of 26 μs, whereas the excited state lifetimes range between 0.1-1.1 ms for T_1 states. These results suggest that the S_1 state might be responsible for experimentally observed microsecond-scale lifetimes. (Similar results were observed when a single-point TDDFT excitation calculation was performed with SOC at the optimized T_1 geometry)

The fluorescence emission energy is significantly lower than the first singlet excitation energy of 1.79 eV at the ground state geometry, which gives rise to a large Stokes shift of 0.47 eV. This is in good agreement with the large experimental Stokes shift of ~0.5 eV observed by Yu et al.[13] Moreover, we observed similar Stokes shifts for $Au_{25}(SR)_{18}^{-}$ nanoclusters that are associated with significant geometrical alterations upon photoexcitation.[25] Thus, we examine the geometric structures of the first excited singlet and triplet states of the $Au_{22}(SR)_{18}$ nanocluster in order to identify their geometrical changes from the ground state structure. These results are tabulated in Table 4.3. On average, bonds are elongated by less than 0.04 Å in S_1 and T_1 optimized structures. However, we observed that the standard deviations of the $Au_{core}–Au_{core}$ bonds as well as bond angles within the core are increased as compared to that of the ground state structure. Table 4.6 summarizes specific $Au_{core}–Au_{core}$ bonds and $Au_{core}–Au_{core}–Au_{core}$ bond angles that vary upon photoexcitation. It is interesting to notice that both the S_1 and T_1 optimized structures have similar geometrical modifications, which are slightly more pronounced for the T_1 state. Two $Au_{core}–Au_{core}$ bonds elongate with a maximum of 0.18 Å in the S_1 state, unlike in excited state geometries of $Au_{38}(SH)_{24}$ nanocluster. These bond length modifications introduce

changes in Au-Au-Au angles within the core with a maximum of 5-6°, reducing the bending angle between the two tetrahedra of vertex sharing bi-tetrahedral Au_7 core in the singlet and triplet excited states. Although the existing hypothesis in literature suggests that the luminescence of the $Au_{22}(SR)_{18}$ nanocluster is related to the $Au_6(SR)_6$ ring, overall we observe minor geometrical changes associated with this ring motif between the ground and excited states. However, we observe that four $Au_{core}(0)$–$Au_{ring}(I)$ bonds are shortened by a maximum of 0.095 and 0.073 Å in the S_1 and T_1 optimized structures, respectively. Thus, it is possible that the increased luminescence quantum yield of this system could be due to strengthened $Au_{core}(0)$–$Au_{ring}(I)$ bonds in the excited state, but more work will need to be done with other systems to support or refute this hypothesis. It should be noted that in the $Au_{25}(SH)_{18}^-$ cluster, two of the $Au_{core}(0)$–$Au_{staple}(I)$ bonds elongate with a maximum of 0.31 Å while some of these bonds shrink with a maximum of 0.18 Å upon photoexcitation.

Table 4.6 Comparison of Au_{core}–Au_{core} bond lengths and Au_{core}–Au_{core}–Au_{core} bond angles in relaxed geometries of the ground state (S_0), the first singlet (S_1), and triplet (T_1) excited states of the $Au_{22}(SH)_{18}$ nanocluster.

	Bond/Angle	Bond Length (Å) / Bond Angle (°)		
		Ground State (S₀)	Excited States	
			Singlet (S₁)	Triplet (T₁)
	3–4	2.813	2.988	3.016
	5–6	2.826	2.965	3.017
	4–2–3	61.30	66.24	67.07
	5–2–6	62.33	66.70	68.08
	4–1–3	60.13	64.33	65.35
	5–7–6	59.85	63.85	65.05
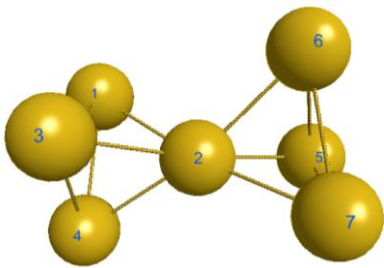
Geometric relaxations in the excited states affect the electronic structure of the $Au_{22}(SH)_{18}$ nanocluster significantly. The ground state HOMO and LUMO orbitals are

respectively destabilized by 0.16 eV and stabilized by 0.32 eV in the S_1 state. Moreover, the almost doubly degenerate LUMO and LUMO+1 orbitals in the ground state have a splitting of ~0.4 eV in the first excited state. Consequently, the HOMO-LUMO gap decreases from 1.77 to 1.30 eV (Figure 4.4) upon photoexcitation. However, as shown in Figure 4.4, these orbitals retain their character in both S_0 and S_1 states.

We propose that the larger degree of structural flexibility and the electronic structure modifications in the excited state of $Au_{22}(SH)_{18}$ nanocluster may contribute to its high photoluminescence quantum yield observed experimentally.[13, 15] However, the crystal structure of this nanocluster is not known yet, so this flexibility could alternatively indicate that the theoretically predicted structure[36] is not optimal. Additional work is needed to determine the importance of core flexibility on photoluminescence energies and quantum yields, because this may be a significant factor for these systems.

4.5 Conclusions

DFT and TDDFT calculations were performed to investigate the origin of photoluminescence of $Au_{38}(SH)_{24}$ and $Au_{22}(SH)_{18}$ nanoparticles in the gas phase. The calculated emission energies of 0.88 and 0.99 eV for the lowest energy E and A_2 states of $Au_{38}(SH)_{24}$ are in good agreement with the lowest two of four experimental emission bands. The geometric relaxations in the Au_{23} core up to a maximum of 0.05 Å are minor compared to relaxations of up to 0.25 Å for the previously studied $Au_{25}(SH)_{18}^-$ nanocluster.[25] These small geometrical changes lead to slight electronic structure changes in the optimized singlet excited states and relatively small Stokes shifts calculated to be in the range of 0.06-0.09 eV, in comparison to a Stokes shift of 0.49 eV for the $Au_{25}(SH)_{18}^-$ nanoparticle.[25] The two lowest energy fluorescence bands of the $Au_{38}(SH)_{24}$ nanoparticle arise predominantly due to HOMO→LUMO transition that involve core based orbitals.

The fluorescence and phosphorescence energies are calculated to be 1.32 and 1.23 eV for $Au_{22}(SH)_{18}$ nanoparticle, which correspond to a HOMO→LUMO transition. The large calculated Stokes shift of 0.47 eV agrees well with the experimental results. Lifetimes calculated for this system are in the microsecond range (or longer), in agreement with available experimental results. The optimized first singlet and triplet excited states of $Au_{22}(SH)_{18}$ nanoparticle show a

larger degree of structural flexibility in the Au_7 core that leads to significant electronic structure modifications upon photoexcitation. However, the current lack of knowledge on the crystallographic structure of $Au_{22}(SH)_{18}$ nanocluster demands further investigations to determine this structure-property relationship.

Overall, we observe a very small Stokes shift for $Au_{38}(SH)_{24}$ that correlates with a relatively rigid structure with small bond length changes, and a large Stokes shift for $Au_{22}(SH)_{18}$ with a large degree of structural flexibility in its core. This suggests that structural flexibility may be a factor that can be tuned to change the Stokes shift of gold-thiolate nanoparticles.

4.6 Acknowledgements

4.7 References

1.   Liu, J.; Yu, M.; Zhou, C.; Yang, S.; Ning, X.; Zheng, J., Passive Tumor Targeting of Renal-Clearable Luminescent Gold Nanoparticles: Long Tumor Retention and Fast Normal Tissue Clearance. *J. Am. Chem. Soc.* **2013**, *135*, 4978-4981.
2.   Liu, J.; Yu, M.; Ning, X.; Zhou, C.; Yang, S.; Zheng, J., PEGylation and Zwitterionization: Pros and Cons in Renal Clearance and Tumor Targeting of Near-IR-Emitting Gold Nanoparticles. *Angew. Chem., Int. Ed.* **2013**, *52*, 12572-12576.
3.   Shiang, Y.-C.; Huang, C.-C.; Chen, W.-Y.; Chen, P.-C.; Chang, H.-T., Fluorescent Gold and Silver Nanoclusters for the Analysis of Biopolymers and Cell Imaging. *J. Mater. Chem.* **2012**, *22*, 12972-12982.
4.   Yuan, X.; Luo, Z.; Yu, Y.; Yao, Q.; Xie, J., Luminescent Noble Metal Nanoclusters as an Emerging Optical Probe for Sensor Development. *Chem.–Asian J.* **2013**, *8*, 858-871.
5.   Shang, L.; Dong, S.; Nienhaus, G. U., Ultra-Small Fluorescent Metal Nanoclusters: Synthesis and Biological Applications. *Nano Today* **2011**, *6*, 401-418.
6.   Luo, Z.; Zheng, K.; Xie, J., Engineering Ultrasmall Water-Soluble Gold and Silver Nanoclusters for Biomedical Applications. *Chem. Commun.* **2014**, *50*, 5143-5155.
7.   Chang, W. H.; Lin, C.-A. J.; Lee, C.-H.; Hsieh, J.-T.; Wang, H.-H.; Li, J. K.; Shen, J.-L.; Chan, W.-H.; Yeh, H.-I., Review: Synthesis of Fluorescent Metallic Nanoclusters toward Biomedical Application: Recent Progress and Present Challenges. *J. Med. Biol. Eng.* **2009**, *29*, 276-283.

8.   Bigioni, T. P.; Whetten, R. L.; Dag, Ö., Near-Infrared Luminescence from Small Gold Nanocrystals. *J. Phys. Chem. B* **2000**, *104*, 6983-6986.

9.   Huang, T.; Murray, R. W., Visible Luminescence of Water-Soluble Monolayer-Protected Gold Clusters. *J. Phys. Chem. B* **2001**, *105*, 12498-12502.

10.   Wang, G.; Huang, T.; Murray, R. W.; Menard, L.; Nuzzo, R. G., Near-IR Luminescence of Monolayer-Protected Metal Clusters. *J. Am. Chem. Soc.* **2005**, *127*, 812-813.

11.   Negishi, Y.; Nobusada, K.; Tsukuda, T., Glutathione-Protected Gold Clusters Revisited: Bridging the Gap between Gold(I)−Thiolate Complexes and Thiolate-Protected Gold Nanocrystals. *J. Am. Chem. Soc.* **2005**, *127*, 5261-5270.

12.   Link, S.; Beeby, A.; FitzGerald, S.; El-Sayed, M. A.; Schaaff, T. G.; Whetten, R. L., Visible to Infrared Luminescence from a 28-Atom Gold Cluster. *J. Phys. Chem. B* **2002**, *106*, 3410-3415.

13.   Iida, K.; Noda, M.; Ishimura, K.; Nobusada, K., First-Principles Computational Visualization of Localized Surface Plasmon Resonance in Gold Nanoclusters. *J. Phys. Chem. A* **2014**, *118*, 11317-11322.

14.   Xie, J.; Zheng, Y.; Ying, J. Y., Protein-Directed Synthesis of Highly Fluorescent Gold Nanoclusters. *J. Am. Chem. Soc.* **2009**, *131*, 888-889.

15.   Pyo, K.; Thanthirige, V. D.; Kwak, K.; Pandurangan, P.; Ramakrishna, G.; Lee, D., Ultrabright Luminescence from Gold Nanoclusters: Rigidifying the Au(I)–Thiolate Shell. *J. Am. Chem. Soc.* **2015**, *137*, 8244-8250.

16.   Luo, Z.; Yuan, X.; Yu, Y.; Zhang, Q.; Leong, D. T.; Lee, J. Y.; Xie, J., From Aggregation-Induced Emission of Au(I)–Thiolate Complexes to Ultrabright Au(0)@Au(I)–Thiolate Core–Shell Nanoclusters. *J. Am. Chem. Soc.* **2012**, *134*, 16662-16670.

17.   Zheng, J.; Zhou, C.; Yu, M.; Liu, J., Different Sized Luminescent Gold Nanoparticles. *Nanoscale* **2012**, *4*, 4073-4083.

18.   Link, S.; El-Sayed, M. A.; Gregory Schaaff, T.; Whetten, R. L., Transition from Nanoparticle to Molecular Behavior: A Femtosecond Transient Absorption Study of a Size-Selected 28 atom Gold Cluster. *Chem. Phys. Lett.* **2002**, *356*, 240-246.

19.   Lee, D.; Donkers, R. L.; Wang, G.; Harper, A. S.; Murray, R. W., Electrochemistry and Optical Absorbance and Luminescence of Molecule-like Au_{38} Nanoparticles. *J. Am. Chem. Soc.* **2004**, *126*, 6193-6199.

20.   Shibu, E. S.; Muhammed, M. A. H.; Tsukuda, T.; Pradeep, T., Ligand Exchange of $Au_{25}SG_{18}$ Leading to Functionalized Gold Clusters: Spectroscopy, Kinetics, and Luminescence. *J. Phys. Chem. C* **2008**, *112*, 12168-12176.

21.   Shibu, E. S.; Pradeep, T., Photoluminescence and Temperature-Dependent Emission Studies of Au_{25} Clusters in the Solid State. *Int. J. Nanosci.* **2009**, *08*, 223-226.

22.   Wu, Z.; Jin, R., On the Ligand's Role in the Fluorescence of Gold Nanoclusters. *Nano Lett.* **2010**, *10*, 2568-2573.

23.   Miller, S. A.; Womick, J. M.; Parker, J. F.; Murray, R. W.; Moran, A. M., Femtosecond Relaxation Dynamics of $Au_{25}L_{18}^-$ Monolayer-Protected Clusters. *J. Phys. Chem. C* **2009**, *113*, 9440-9444.

24.   Devadas, M. S.; Bairu, S.; Qian, H.; Sinn, E.; Jin, R.; Ramakrishna, G., Temperature-Dependent Optical Absorption Properties of Monolayer-Protected Au_{25} and Au_{38} Clusters. *J. Phys. Chem. Lett.* **2011**, *2*, 2752-2758.

25.   Weerawardene, K. L. D. M.; Aikens, C. M., Theoretical Insights into the Origin of Photoluminescence of $Au_{25}(SR)_{18}^-$ Nanoparticles. *J. Am. Chem. Soc.* **2016**, *138*, 11202-11210.

26.   Lopez-Acevedo, O.; Tsunoyama, H.; Tsukuda, T.; Häkkinen, H.; Aikens, C. M., Chirality and Electronic Structure of the Thiolate-Protected Au_{38} Nanocluster. *J. Am. Chem. Soc.* **2010**, *132*, 8210-8218.

27.   Qian, H.; Eckenhoff, W. T.; Zhu, Y.; Pintauer, T.; Jin, R., Total Structure Determination of Thiolate-Protected Au_{38} Nanoparticles. *J. Am. Chem. Soc.* **2010**, *132*, 8280-8281.

28.   Toikkanen, O.; Ruiz, V.; Rönnholm, G.; Kalkkinen, N.; Liljeroth, P.; Quinn, B. M., Synthesis and Stability of Monolayer-Protected Au_{38} Clusters. *J. Am. Chem. Soc.* **2008**, *130*, 11049-11055.

29.   Wijngaarden, J. T. v.; Toikkanen, O.; Liljeroth, P.; Quinn, B. M.; Meijerink, A., Temperature-Dependent Emission of Monolayer-Protected Au_{38} Clusters. *J. Phys. Chem. C* **2010**, *114*, 16025-16028.

30.   The stoichiometry of Au38 nanocluster is reported as Au38(SR)22 in Ref 28. However, the absorption peaks identified by taking the derivative of spectra agree well with absorption spectrum of Au38(SR)24 nanocluster in Ref 24 and 27. The Ref 28 has originally misassigned the stoichiometry of Au38(SR)24 nanoclusters as Au38(SR)22.

31.   Green, T. D.; Yi, C.; Zeng, C.; Jin, R.; McGill, S.; Knappenberger, K. L., Temperature-Dependent Photoluminescence of Structurally-Precise Quantum-Confined $Au_{25}(SC_8H_9)_{18}$ and $Au_{38}(SC_{12}H_{25})_{24}$ Metal Nanoparticles. *J. Phys. Chem. A* **2014**, *118*, 10611-10621.

32.   Zhou, C.; Sun, C.; Yu, M.; Qin, Y.; Wang, J.; Kim, M.; Zheng, J., Luminescent Gold Nanoparticles with Mixed Valence States Generated from Dissociation of Polymeric Au(I) Thiolates. *J. Phys. Chem. C* **2010**, *114*, 7727-7732.

33.   Heaven, M. W.; Dass, A.; White, P. S.; Holt, K. M.; Murray, R. W., Crystal Structure of the Gold Nanoparticle $[N(C_8H_{17})_4][Au_{25}(SCH_2CH_2Ph)_{18}]$. *J. Am. Chem. Soc.* **2008**, *130*, 3754-3755.

34.   Parker, J. F.; Fields-Zinna, C. A.; Murray, R. W., The Story of a Monodisperse Gold Nanoparticle: $Au_{25}L_{18}$. *Acc. Chem. Res.* **2010**, *43*, 1289-1296.

35.   Zhu, M.; Aikens, C. M.; Hollander, F. J.; Schatz, G. C.; Jin, R., Correlating the Crystal Structure of A Thiol-Protected Au_{25} Cluster and Optical Properties. *J. Am. Chem. Soc.* **2008**, *130*, 5883-5885.

36.   Pei, Y.; Tang, J.; Tang, X.; Huang, Y.; Zeng, X. C., New Structure Model of $Au_{22}(SR)_{18}$: Bitetrahederon Golden Kernel Enclosed by $[Au_6(SR)_6]$ Au(I) Complex. *J. Phys. Chem. Lett.* **2015**, *6*, 1390-1395.

37.   Zeng, C.; Liu, C.; Chen, Y.; Rosi, N. L.; Jin, R., Gold–Thiolate Ring as a Protecting Motif in the $Au_{20}(SR)_{16}$ Nanocluster and Implications. *J. Am. Chem. Soc.* **2014**, *136*, 11922-11925.

38.   Weerawardene, K. L. D. M.; Aikens, C. M., Effect of Aliphatic versus Aromatic Ligands on the Structure and Optical Absorption of $Au_{20}(SR)_{16}$. *J. Phys. Chem. C* **2016**, *120*, 8354-8363.

39.   te Velde, G.; Bickelhaupt, F. M.; Baerends, E. J.; Fonseca Guerra, C.; van Gisbergen, S. J. A.; Snijders, J. G.; Ziegler, T., Chemistry with ADF. *J. Comput. Chem.* **2001**, *22*, 931-967.

40.   Becke, A. D., Density-Functional Exchange-Energy Approximation with Correct Asymptotic Behavior. *Phys. Rev. A* **1988**, *38*, 3098-3100.

41.   Perdew, J. P., Density-Functional Approximation for the Correlation Energy of the Inhomogeneous Electron Gas. *Phys. Rev. B* **1986**, *33*, 8822-8824.

42.   Aikens, C. M., Effects of Core Distances, Solvent, Ligand, and Level of Theory on the TDDFT Optical Absorption Spectrum of the Thiolate-Protected Au_{25} Nanoparticle. *J. Phys. Chem. A* **2009**, *113*, 10811-10817.

43.   Guidez, E. B.; Aikens, C. M., Time-Dependent Density Functional Theory Study of the Luminescence Properties of Gold Phosphine Thiolate Complexes. *J. Phys. Chem. A* **2015**, *119*, 3337-3347.

44.   Chen, S.; Wang, S.; Zhong, J.; Song, Y.; Zhang, J.; Sheng, H.; Pei, Y.; Zhu, M., The Structure and Optical Properties of the [$Au_{18}(SR)_{14}$] Nanocluster. *Angew. Chem. Int. Ed.* **2015**, *54*, 3145-3149.

45.   Bae, G.-T.; Aikens, C. M., Time-Dependent Density Functional Theory Studies of Optical Properties of Au Nanoparticles: Octahedra, Truncated Octahedra, and Icosahedra. *J. Phys. Chem. C* **2015**, *119*, 23127-23137.

46.   Hulkko, E.; Lopez-Acevedo, O.; Koivisto, J.; Levi-Kalisman, Y.; Kornberg, R. D.; Pettersson, M.; Häkkinen, H., Electronic and Vibrational Signatures of the Au_{102}(p-MBA)$_{44}$ Cluster. *J. Am. Chem. Soc.* **2011**, *133*, 3752-3755.

47.   Liao, M.-S.; Bonifassi, P.; Leszczynski, J.; Ray, P. C.; Huang, M.-J.; Watts, J. D., Structure, Bonding, and Linear Optical Properties of a Series of Silver and Gold Nanorod Clusters: DFT/TDDFT Studies. *J. Phys. Chem. A* **2010**, *114*, 12701-12708.

48.   Aikens, C. M.; Li, S.; Schatz, G. C., From Discrete Electronic States to Plasmons: TDDFT Optical Absorption Properties of Ag_n (n = 10, 20, 35, 56, 84, 120) Tetrahedral Clusters. *J. Phys. Chem. C* **2008**, *112*, 11272-11279.

49.   Lenthe, E. v.; Baerends, E. J.; Snijders, J. G., Relativistic Regular Two- Component Hamiltonians. *J. Chem. Phys.* **1993**, *99*, 4597-4610.

50.   Costa, P. J.; Calhorda, M. J., A DFT and MP2 Study of Luminescence of Gold(I) Complexes. *Inorg. Chim. Acta.* **2006**, *359*, 3617-3624.

51.   Bode, B. M.; Gordon, M. S., Macmolplt: A Graphical User Interface for GAMESS. *J. Mol. Graphics and Modelling* **1998**, *16*, 133-138.

52.   Johnson, H. E.; Aikens, C. M., Electronic Structure and TDDFT Optical Absorption Spectra of Silver Nanorods. *J. Phys. Chem. A* **2009**, *113*, 4445-4450.

53.   Qian, H.; Zhu, M.; Andersen, U. N.; Jin, R., Facile, Large-Scale Synthesis of Dodecanethiol-Stabilized Au_{38} Clusters. *J. Phys. Chem. A* **2009**, *113*, 4281-4284.

54.   Marques, M. A. L.; Castro, A.; Rubio, A., Assessment of Exchange-Correlation Functionals for the Calculation of Dynamical Properties of Small Clusters in Time-Dependent Density Functional Theory. *J. Chem. Phys.* **2001**, *115*, 3006-3014.

Chapter 5 - Origin of Photoluminescence of $Ag_{25}(SR)_{18}^-$ Nanoparticles: Ligand and Doping Effect

5.1 Abstract

Recent theoretical insights into the origin of photoluminescence of thiolate-protected gold nanoclusters raise the question whether the observed luminescence mechanism is valid for their silver counterparts. To this end, we perform density functional theory (DFT) and time-dependent density functional theory (TDDFT) calculations on the $Ag_{25}(SR)_{18}^-$ (R=H, PhMe$_2$) nanocluster, which is currently the only thiolate-protected silver cluster that has a matching analogue in gold. The geometric and electronic structural modifications of $Ag_{25}(SH)_{18}^-$ upon photoexcitation are found to be similar but less pronounced than that of $Au_{25}(SH)_{18}^-$ at the same level of theory. The Stokes shift is calculated to be 0.37 eV and the replacement of R=H model ligands by R=PhMe$_2$ decreases the Stokes shift in contrast to an increase in Stokes shift for aliphatic ligands in the Au_{25} system. The calculated emission energy agrees well with the experimental crystal photoluminescence energy, when the typical underestimation of DFT calculations are considered. Similar to Au_{25}, luminescence of Ag_{25} arises from a HOMO-LUMO transition where core-based superatomic P and D orbitals are involved. Heteroatom doping of Au_{25} and Ag_{25} clusters with Ag/Au does not affect the origin of the photoemission of these systems. However, the radiative lifetimes of the lowest singlet excited states (S$_1$) and emission energies are slightly affected.

5.2 Introduction

Photoluminescent metal clusters are of great interest due to their potential applications in a range of fields including biomedicine.[1-8] Extensive research has been carried out to understand the origin of photoluminescence of metal nanoclusters and to elucidate their electronic-level details upon photoexcitation. Despite the similarities in atomic size and bulk lattices, gold and silver have shown discrete physical and chemical properties down to the nanoscale. During the past decade, a remarkable number of atomically precise, monolayer protected gold nanoclusters have been synthesized, isolated, and characterized using x-ray crystallography,[9-18] while only a

handful of silver clusters have been crystallized.[19-23] The only thiolate-protected silver cluster that has a matching analogue in gold is the recently characterized $Ag_{25}(SR)_{18}^{-}$,[21] which enables a direct comparison between gold and silver. This "golden" silver nanoparticle is comprised of an icosahedral Ag_{13} core with approximate I_h symmetry protected by six V-shaped –RS–Ag–SR–Ag–SR– motifs (Figure 5.1) similar to the Au_{25} nanocluster.

A majority of experimental luminescence studies have been carried out on the $Au_{25}(SR)_{18}^{-}$ nanocluster to explore temperature,[24-26] ligand,[27-30] and charge state[27] dependence of its emission that has been found to span an energy range of 1.1 to 1.8 eV. The observed emission has been attributed to intraband or interband transitions,[31, 32] charge-transfer states,[27] and semiring or ligand-based states.[25, 33] Our density functional theory (DFT) and time-dependent density functional theory (TDDFT) calculations on $Au_{25}(SR)_{18}^{-}$ (R=H, CH_3, C_2H_5, C_3H_7) nanoclusters[34] showed that the Au_{13} core-based orbitals are primarily involved in the transitions corresponding to emissions in 0.8-1.25 eV energy region, which agree well with the experimental emission energies in the 1.15-1.55 eV region when the typical underestimation of GGA calculations are considered. We concluded that semiring or ligand-based states are not involved and that the ligands primarily affect luminescence via their interactions with the gold nanoparticle core, leading to an increasing Stokes shifts with larger ligands (up to propyl ligands). However, it is unclear whether this mechanism is applicable to silver nanoclusters or not.

Bakr and coworkers reported that $Ag_{25}(SPhMe_2)_{18}^{-}$ exhibits luminescence in the near-infrared region ~1.5 eV (~850 nm) in dichloromethane.[21] More recently, Liu et al.[35] measured the crystal and solution photoluminescence of a series of center-doped $MAg_{24}(SR)_{18}$ (M = Ag/Pd/Pt/Au) nanoclusters. The solid-state emission energies were centered around 1.17-1.21 eV (1014-1042 nm), which may correlate to the HOMO-LUMO transition. While the emission energy of $Ag_{25}(SR)_{18}^{-}$ blue-shifted only by 28/32/23 nm upon doping with Pd/Pt/Au, the photoluminescence intensities followed a sequence of $PdAg_{24}(SR)_{18}$ < $Ag_{25}(SR)_{18}$ < $PtAg_{24}(SR)_{18}$ < $AuAg_{24}(SR)_{18}$ in good agreement with the order of dopant electron affinity. The calculated natural population analysis (NPA) charges of Ag_{12} inner shell were also found to follow the same sequence suggesting a core-atom-directing charge transfer from the ligands to the metal kernels. It was further revealed that the solvent plays an important role in the photoluminescence intensity rather than the emission wavelength of these systems. The

luminescence quantum yield (QY) of $Ag_{25}(SR)_{18}^-$ was found to increase almost 10-fold in acetone and toluene when the cluster was center-doped with Au. Soldan et al.[36] also achieved a 26-fold quantum yield enhancement of the $Ag_{29}(BDT)_{12}(TPP)_4$ (BDT: 1,3-benzenedithiol; TPP: triphenylphosphine) cluster by doping with 1-5 gold atoms. Moreover, it has been shown that a 200-fold QY raise can be achieved when rod-shaped $[Au_{25}(TPP)_{10}(SR)_5Cl_2]^{2+}$ clusters are doped with up to 13 silver atoms.[37]

Herein, we perform a theoretical investigation to understand the luminescence properties of the 25-atom thiolate protected anionic silver nanocluster and to compare and contrast the results with its gold counterpart that we have reported before. Furthermore, we study how the single-heteroatom doping of Au_{25} and Ag_{25} with Ag and Au respectively affects the origin of photoluminescence of these species. There are three basic possible dopant positions in the Au_{25}/Ag_{25} cluster: (1) in the staples, (2) in the icosahedral shell, and (3) at the center of the icosahedron. The available crystal structure details reveal that the $Ag_{24}Au(SR)_{18}^-$ is a center-doped cluster, which means the heteratom occupies the center of the icosahedral metal core.[35] However, when Au_{25} is doped with silver, the heteroatom has been found to occupy the icosahedral shell.[38-40] Hence, we use center-doped $Ag_{24}Au(SH)_{18}^-$ and shell-doped $Au_{24}Ag(SR)_{18}^-$ structures to determine how the doping affects the origin of photoluminescence of these clusters.

5.3 Computational Methods

All density functional theory (DFT) and time-dependent density functional theory (TDDFT) calculations are performed with the Amsterdam Density Functional (ADF) 2012.01 package.[41] The BP86 exchange-correlation functional[42, 43] and a full core double-ζ (DZ) basis set are used for all calculations. Generalized gradient approximation (GGA) functionals have been employed successfully in geometry relaxations, TDDFT, and excited state gradient calculations of gold and silver nanoclusters previously.[9, 34, 44-51] All structures are optimized in the gas phase. The energy and gradient convergence criteria are tightened to 1×10^{-4} and 1×10^{-3} to obtain well-converged geometries except for the excited state geometry of $Ag_{25}(SR)_{18}^-$ (R=PhMe$_2$). Scalar relativistic effects are included by utilizing the zeroth-order regular approximation (ZORA).[52] The excited state gradients are calculated to optimize the excited state geometry. Only the lowest singlet excited state (S_1) is considered here. Similar studies have been carried out to explore

luminescence properties of thiolate protected gold nanoclusters as well as Au(I) complexes with thiolate and phosphine ligands previously[45, 51, 53] and the experimental and theoretical results have agreed well, with an underestimation of calculated emission peak energies compared to the experimental results. Herein, we calculate the optimized structure for excited states of $Ag_{25}(SR)_{18}^-$ (R=H, PhMe$_2$), $Ag_{24}Au(SH)_{18}^-$, and $Au_{24}Ag(SH)_{18}^-$ nanoclusters in order to determine the origin of the emission in these systems. TDDFT gradient calculations with spin-orbit coupling are not supported in ADF. Therefore, we perform single-point TDDFT calculations with spin-orbit coupling on optimized excited (S_1) state geometries in order to obtain excited state radiative lifetimes. All structures are visualized using the MacMolPlt[54] visualization tool.

5.4 Results

5.4.1 $Ag_{25}(SR)_{18}^-$

The average bond lengths calculated at the BP86/DZ level of theory of the ground state structure of $Ag_{25}(SH)_{18}^-$ in the gas phase are summarized in Table 5.1. Within the Ag_{13} core, the average $Ag_{center}-Ag_{shell}$ bond length is 2.793 ± 0.014, whereas the average $Ag_{shell}-Ag_{shell}$ bond length is 2.937 ± 0.045. Both bonds are 1% shorter than the respective Au-Au bonds in the $Au_{25}(SH)_{18}^-$ nanocluster calculated at the same level of theory.[34]

Aikens predicted that the electronic structure of the $Ag_{25}(SR)_{18}^-$ compound is analogous to its gold counterpart.[55] The HOMO, HOMO-1, and HOMO-2 orbitals are approximately triply degenerate and correspond to a set of orbitals that possess P-character in agreement with the known 8-electron S^2P^6 shell closing in the superatom picture for metals with a single valence s electron.[56] (These orbitals are sometimes collectively referred to as the "HOMO"). The lowest unoccupied orbitals possess D-character and the ligand field splitting from the six $Ag_2(SR)_3$ units divides these into two sets: the essentially doubly degenerate LUMO and LUMO+1 and the triply degenerate LUMO+2, LUMO+3, LUMO+4. The Kohn-Sham orbitals of the ground state of $Ag_{25}(SR)_{18}^-$ are shown in Figure B1.
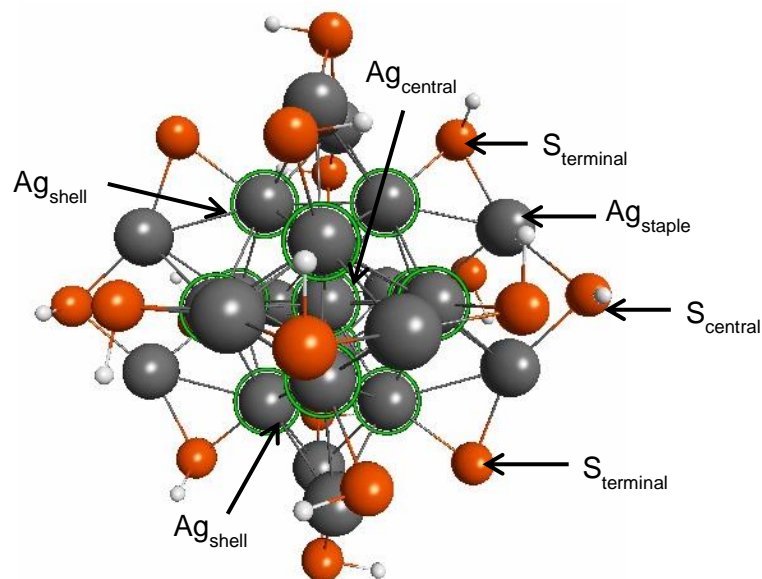
Figure 5.1 The geometric structure of $Ag_{25}(SH)_{18}^{-}$. The orange, gray, and white color spheres represent sulfur, silver, and hydrogen atoms respectively. This color code is consistent in all the figures presented here. The Ag_{13} core atoms are marked with green circles.

Table 5.1 Geometrical parameters of the ground state (S_0) and first singlet excited state (S_1) structures of $Ag_{25}(SH)_{18}^{-}$ at the BP86/DZ level of theory.

	Average Bond Length (Å)	
Bond	Ground State (S_0)	Excited State (S_1)
Ag_{center}–Ag_{shell}	2.793 ± 0.014	2.807 ± 0.020
Ag_{shell}–Ag_{shell}	2.937 ± 0.045	2.951 ± 0.082
Ag_{shell}–$S_{terminal}$	2.568 ± 0.009	2.569 ± 0.016
Ag_{staple}–$S_{terminal}$	2.511 ± 0.005	2.521 ± 0.030
Ag_{staple}–$S_{central}$	2.497 ± 0.006	2.511 ± 0.025

A time-dependent density functional theory (TDDFT) calculation was performed on the relaxed ground state geometry of $Ag_{25}(SR)_{18}^{-}$, and the first six singlet excited state energies and

oscillator strengths are tabulated in Table 5.2. The S_1-S_6 states vary within ~0.2 eV and arise due to transitions from the nearly triply degenerate HOMO, HOMO-1, and HOMO-2 to the nearly doubly degenerate LUMO and LUMO+1 orbitals. The calculated optical absorption spectrum reproduces the experimental[21] and previous theoretical[55] spectra well with an underestimation of peak positions. The GGA functionals generally underestimate excitation energies[44, 57] and this underestimation is ~0.4 eV for the first absorption peak of $Ag_{25}(SH)_{18}^-$ cluster. We observed similar results previously for the $Au_{25}(SH)_{18}^-$ cluster at the same level of theory.[34]

Table 5.2 Excited state energies and oscillator strengths for $Ag_{25}(SH)_{18}^-$ at the S_0 geometry.

State	Energy (eV)	Oscillator Strength (au)
S_1	1.255	7.838×10^{-4}
S_2	1.271	1.347×10^{-3}
S_3	1.287	5.435×10^{-4}
S_4	1.408	4.429×10^{-2}
S_5	1.424	4.304×10^{-2}
S_6	1.440	4.332×10^{-2}

To determine the origin of photoluminescence of the $Ag_{25}(SH)_{18}^-$ nanocluster, we optimized its first singlet excited state (S_1) geometry. The fluorescence energy is calculated by taking the energy difference between the S_0 and S_1 states at the optimized S_1 state geometry. For the $Ag_{25}(SH)_{18}^-$ nanocluster, the fluorescence energy is 0.89 eV, which corresponds to a 1393 nm fluorescence wavelength. The radiative lifetime of the S_1 state is found to be 26 μs. In comparison to the gold analog, the emission energy and the radiative lifetime are increased by 0.06 eV and 3 μs respectively. If an underestimation of 0.4 eV is considered for the calculated emission relative to experiment, experimental emission from S_1 state would occur around 1.3 eV. Our calculations show that the emission energy is significantly smaller than the first excitation energy at the S_0 geometry, 1.26 eV. Thus, the Stokes shift calculated for $Ag_{25}(SH)_{18}^-$ is 0.37 eV, which is 0.12 eV less than that for the $Au_{25}(SH)_{18}^-$ nanocluster.

Our previous investigations on the photoluminescence origin of $Au_{25}(SH)_{18}^-$ and $Au_{22}(SR)_{18}$ nanoclusters showed that larger Stokes shifts arise from significant geometrical modifications upon photoexcitation, specifically in the gold core.[34, 51] Therefore, we analyzed the geometrical parameters of the optimized S_1 geometry of $Ag_{25}(SH)_{18}^-$, which are summarized in Table 5.1. The average bond lengths of the ground state geometry increase by less than 0.02 Å upon formation of the optimized S_1 state geometry. However, similar to the gold analog, a couple of Ag_{shell}–Ag_{shell} bond lengths noticeably differ between the ground- and excited-state geometries, but to a lesser degree. The most prominent difference between the S_0 and S_1 geometries is the elongation of the 9-12 and 13-10 bond pairs by 0.10 and 0.17 Å, respectively. Unlike in $Au_{25}(SH)_{18}^-$, corresponding bond pairs in $Ag_{25}(SH)_{18}^-$ elongate by different amounts as shown in Table B1. None of the Ag-S bonds in the semi-rings differ significantly upon photoexcitation. However, some changes can be observed in $Ag_{shell}(0)$-$Ag_{staple}(I)$ bonds, where two bonds are lengthened and two bonds are shortened by ~0.1 Å in the S_1 geometry in comparison to the S_0.

-1.65 eV
LUMO+2

-1.57 eV
LUMO+3

-1.52 eV
LUMO+4

-2.50 eV
LUMO

-2.28 eV
LUMO+1

-3.35 eV
HOMO

-3.53 eV
HOMO -1

-3.57 eV
HOMO-2
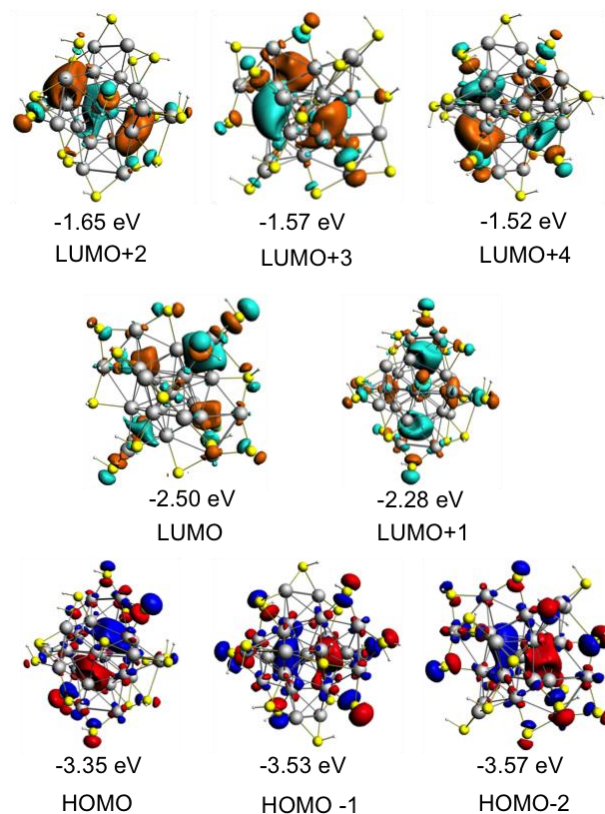
Figure 5.2 BP86/DZ Kohn-Sham orbitals and orbital energies at the S_1 state of $Ag_{25}(SH)_{18}^-$. |Isovalue| = 0.025.

These geometric relaxations in the first excited state affect the orbital energy levels around the HOMO-LUMO gap of $Ag_{25}(SH)_{18}^-$ considerably. We observed similar results previously for thiolate protected gold nanoparticles.[34] As we have discussed for $Au_{25}(SH)_{18}^-$, Jahn-Teller distortions must occur in the S_1 state geometry of $Ag_{25}(SH)_{18}^-$ as well since superatomic P orbitals are incompletely occupied at the excited state. Comparison of Figure 5.2 and Figure B1 shows that highest occupied and lowest unoccupied orbitals retain their superatomic P and D characters, regardless of photoexcitation. However, Figure 5.3 demonstrates that their degeneracies observed in the ground state are interrupted at the S_1 state geometry. The HOMO is destabilized by 0.11 eV whereas the LUMO is stabilized by 0.25 eV in comparison to the S_0 state. These modifications reduce the ground state HOMO-LUMO gap by 0.36 eV for the S_1 state. The nearly degenerate HOMO, HOMO-1, and HOMO-2 orbitals in the ground state have a splitting of 0.21 eV in the S_1 state, whereas the doubly degenerate LUMO and LUMO+1 orbitals become split by 0.22 eV upon photoexcitation. Furthermore, spitting among the LUMO+2, LUMO+3, and LUMO+4 orbitals increases by ~0.07 eV (Figure 5.3). These splittings imply that the $Ag_{25}(SH)_{18}^-$ nanoparticle is less isotropic in the excited state.

To understand the ligand effects on the emission of Ag_{25} nanoparticle, we considered the 2,4-dimethylbenzenethiol ($SPhMe_2$) protected system: $[Ag_{25}(SPhMe_2)_{18}]^-$. We optimized the recently determined crystal structure[21] coordinates using BP86/DZ level of theory. Table B2 summarizes geometric parameters of the ground state structure of this cluster in the gas phase. The average bond lengths do not vary noticeably with changing the ligand of $Ag_{25}(SR)_{18}^-$ from R=H to R=$PhMe_2$. However, the ground state frontier orbital energy levels are affected to some extent. The triply degenerate set of HOMO/HOMO-1/HOMO-2 orbitals is destabilized by ~0.2 eV, whereas the destabilization of the unoccupied orbitals is negligible compared to that of $Ag_{25}(SH)_{18}^-$. Thus, the HOMO-LUMO gap is calculated to be 1.00 eV for the $[Ag_{25}(SPhMe_2)_{18})]^-$ system.
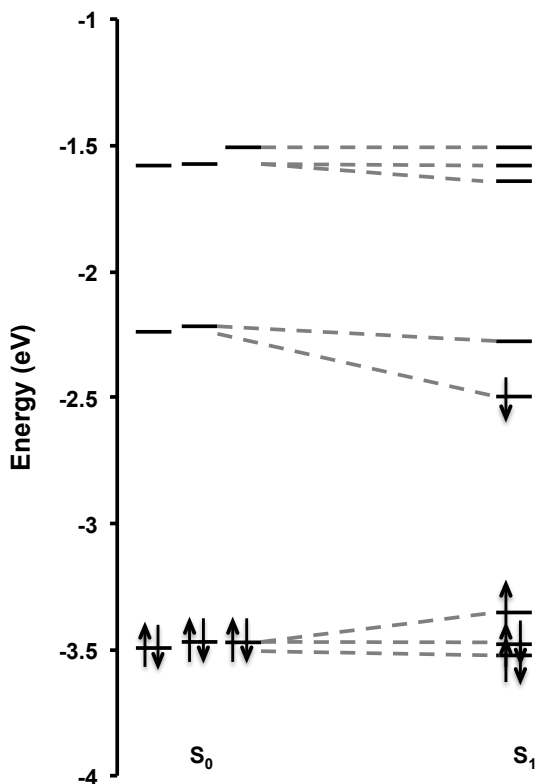
Figure 5.3 Comparison of energy levels of the frontier orbitals in S_0 and S_1 states of Ag$_{25}$(SH)$_{18}^-$. The S_1 state is shown in a cartoon representation with a single electron in one of the D orbitals. Dashed lines are drawn to show the splitting of triply-degenerate HOMO/HOMO-1/HOMO-2, doubly-degenerate LUMO/LUMO+1, and triply degenerate LUMO+2/LUMO+3/LUMO+4 orbitals of the ground state upon photoexcitation.

A TDDFT calculation is performed on the relaxed ground-state geometry of the [Ag$_{25}$(SPhMe$_2$)$_{18}$)]$^-$ nanocluster. The optical absorption spectrum reproduces the main absorption features observed for the Ag$_{25}$(SH)$_{18}^-$ cluster with slight deviations of peak positions to lower energy. The first strong absorption peak that arises mainly from S_4-S_6 states (due to HOMO/HOMO-1/HOMO-2 → LUMO/LUMO+1 transitions) appears at ~1.2 eV, which is underestimated by ~0.6 eV compared to the experimental spectrum.[21] The S_1 state energy is calculated to be 1.031 eV and it is 0.224 eV lower in energy than the S_1 energy of Ag$_{25}$(SH)$_{18}^-$.

Next, the lowest excited–state geometry of [Ag$_{25}$(SPhMe$_2$)$_{18}$)]$^-$ is optimized to determine origin of its emission. We calculated the lowest emission energy to be 0.793 eV, which corresponds to a 1563 nm fluorescence wavelength. The emission energy is lowered by 0.1 eV upon changing the ligand from -SH to -SPhMe$_2$ and it is less affected than the first excitation

energy. This gives rise to a smaller Stokes shift of 0.24 eV, which is in contrast to the ligand effect observed for the $Au_{25}(SR)_{18}^-$ nanocluster.[34] In our previous study, we observed that replacing –SH with alkyl ligands with increasing carbon chain lengths decreases the lowest emission energy while not affecting the lowest excited state energy considerably.[34] Hence, the Stokes shifts calculated for these clusters increased and the maximum value was reported for the propylthiolate-stabilized Au_{25} cluster. The current results imply that aromatic ligands may stabilize the Ag_{25} nanoparticle more in the excited state than alkyl ligands do for $Au_{25}(SR)_{18}^-$. The role of ligand as well as the role of metal in determining the Stokes shift needs to be further explored.

The smaller Stokes shift of the $[Ag_{25}(SPhMe_2)_{18})]^-$ cluster suggests minor geometrical and electronic structure modifications upon photoexcitation compared to $Ag_{25}(SH)_{18}^-$. Tables B2 and B3 summarize the geometrical parameters of the optimized S_1 geometry of $[Ag_{25}(SPhMe_2)_{18})]^-$. Two symmetric Ag_{shell}–Ag_{shell} bond pairs show noticeable changes in the S_0 and S_1 geometries. The 6-12, 3-13 bond pair is shortened by ~0.1 Å, while the 9-12, 10-13 pair is elongated by slightly less than 0.1 Å. Similar to $Ag_{25}(SH)_{18}^-$, none of the bonds associated with the semi-rings change significantly from the S_0 to S_1 geometry of $[Ag_{25}(SPhMe_2)_{18})]^-$ except for some $Ag_{shell}(0)$-$Ag_{staple}(I)$ bonds that vary by about 0.1 Å. The electronic structure changes at the S_1 state are found to be analogous but less pronounced than those observed for $Ag_{25}(SH)_{18}^-$. The splitting among ground state HOMO/HOMO-1/HOMO-2 orbitals is 0.16 eV and that between LUMO/LUMO+1 orbitals is 0.17 eV in the excited state. Overall, we can conclude that aromatic ligands on the Ag_{25} nanocluster impart geometrical and electronic structure modifications to a lesser degree upon photoexcitation than SH ligands that can be correlated with its smaller Stokes shift.

5.4.2 $Ag_{24}Au(SH)_{18}^-$

Table 5.3 summarizes the average bond lengths calculated at the BP86/DZ level of theory of the ground state structure of $Ag_{24}Au(SH)_{18}^-$ in the gas phase. Single heteratom-doping of the Ag_{25} cluster with Au at the center does not change the geometrical parameters or the electronic structure of the homometal cluster significantly. However, the HOMO-LUMO gap of the $Ag_{24}Au(SH)_{18}^-$ cluster is increased by 0.135 eV, suggesting that doping enhances the stability of the pure 25–metal atom cluster. The optical absorption spectrum of the $Ag_{24}Au(SH)_{18}^-$ cluster is

found to be essentially similar to that of the Ag_{25} nanocluster (Figure 5.4), with the first absorption peak blue-shifted by ~0.1 eV.

Table 5.3 Geometrical parameters of the ground state (S_0) and first singlet excited state (S_1) structures of $[Ag_{24}Au(SH)_{18})]^-$ at the BP86/DZ level of theory.

Bond	Average Bond Length (Å)	
	Ground State (S_0)	Excited State (S_1)
$Au_{center}-Ag_{shell}$	2.800 ± 0.013	2.815 ± 0.017
$Ag_{shell}-Ag_{shell}$	2.945 ± 0.034	2.960 ± 0.074
$Ag_{shell}-S_{terminal}$	2.557 ± 0.006	2.557 ± 0.012
$Ag_{staple}-S_{terminal}$	2.512 ± 0.005	2.521 ± 0.028
$Ag_{staple}-S_{central}$	2.495 ± 0.004	2.513 ± 0.025
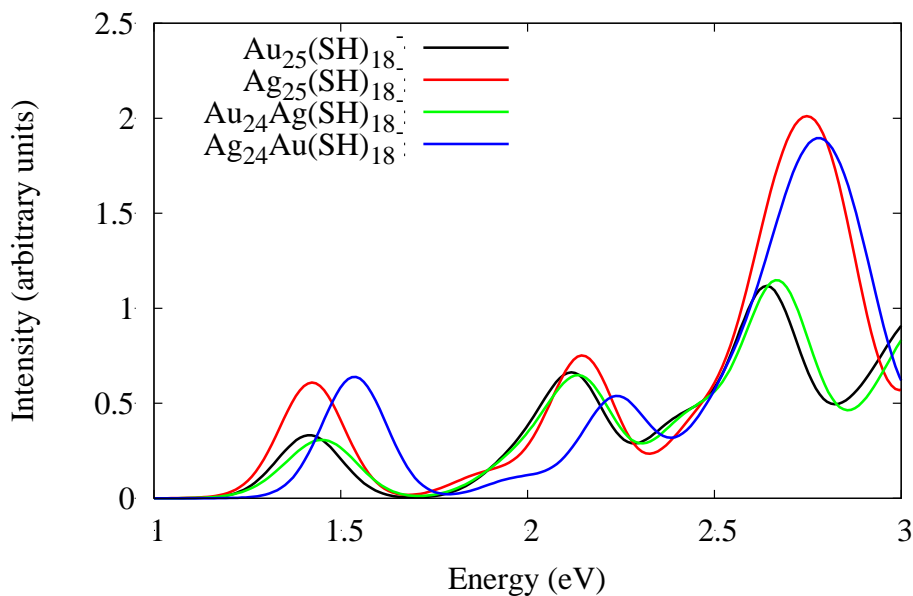
Figure 5.4 Comparison of optical absorption spectra for $M_{25}(SH)_{18}^-$ nanoclusters.

The S_1 state geometry of $Ag_{24}Au(SH)_{18}^-$ cluster is optimized and the calculated lowest emission energy is 1.01 eV, which corresponds to a fluorescence wavelength of 1228 nm. Both

the lowest excitation and emission that arise due to HOMO-LUMO transition of the doped cluster are ~0.1 eV higher in energy than that of the pure silver nanocluster. Moreover, the S_1 state is found to be relatively long-lived (34 μs) compared to both pure Ag_{25} and Au_{25} nanoclusters. The Stokes shift of the doped system is calculated to be 0.38 eV, which is slightly higher than Ag_{25} but still 0.11 eV lower than that of Au_{25}. Therefore, we expect geometrical changes in the $AuAg_{12}$ core of a similar degree as in the pure silver cluster, but not as significant as in Au_{25}. Table 5.3 summarizes the average geometric parameters of the optimized S_1 geometry of the $Ag_{24}Au(SH)_{18}^-$ system. As expected, the most prominent bond elongations between S_0 and S_1 geometries are the 9-12 and 13-10 bond pair which elongate by 0.10 and 0.17 Å, respectively, similar to $Ag_{25}(SH)_{18}^-$. Table B4 tabulates all the significant bond length changes of the doped system upon photoexcitation and these changes are essentially the same as for the Ag_{25} system. We did not observe any alterations in the bonds associated with the semi-rings except for some $Ag_{shell}(0)$-$Ag_{staple}(I)$ bonds that vary by about 0.1 Å. The electronic structure modifications of the doped system in the excited state are very similar to that of Ag_{25}, where the almost triply degenerate HOMO/HOMO-1/HOMO-2 ground state orbitals have a splitting of 0.21 eV and the almost doubly degenerate LUMO/LUMO+1 orbitals have a splitting of 0.22 eV in the S_1 state.

Overall, we observed that the emission energy is marginally blue shifted upon center-doping of Ag_{25} cluster with Au, in agreement with the solid state emission results reported by Liu et al.[35] Moreover, the calculated radiative lifetime of the S_1 state is increased by few microseconds. However, the doping does not affect the origin of photoluminescence of thiolate-protected 25-atom metal nanoclusters. Photoluminescence arises due to HOMO-LUMO transition that involves $AuAg_{12}$ core-based superatomic P and D orbitals, which is in contrast to the ligand-to-metal charge transfer mechanism proposed by Liu et al.[35]

5.4.3 $Au_{24}Ag(SH)_{18}^-$

Next, we considered the $Au_{24}Ag(SH)_{18}^-$ nanocluster to study the effect of Ag doping on the photoluminescence properties of the thiolate-protected Au_{25} cluster. Experimental and theoretical investigations have shown that the Ag dopant does not occupy the center of icosahedral core, and it instead prefers to occupy the icosahedral vertex positions.[38-40] The average bond lengths calculated at the BP86/DZ level of theory of the ground state structure of $Au_{24}Ag(SH)_{18}^-$ in the gas phase are summarized in Table 5.4. Single heteratom-doping of the

Au_{25} cluster with Ag does not change the geometrical parameters of the homometal cluster noticeably. However, the electronic structure of Au_{25} is affected to some extent by mono silver doping. In the pure 25-atom gold nanocluster, the HOMO/HOMO-1/HOMO-2 orbitals that represent the superatomic P orbitals are almost triply degenerate with a splitting of ~0.03 eV at the ground state, whereas this splitting is calculated to be 0.13 eV in the ground state of the doped system. The HOMO-LUMO energy gap is decreased by 0.04 eV upon doping. However, doping does not change the doubly degenerate LUMO/LUMO+1 and triply degenerate LUMO+2/LUMO+3/LUMO+4 superatomic D orbitals of the homometal cluster significantly.

The optical absorption spectra of the pure and doped clusters exhibit similar spectral features as shown in Figure 5.4, but the first absorption peak of the doped system is blue shifted by ~0.05 eV compared to the Au_{25} cluster. Next, we optimize the lowest singlet excited state geometry of the $Au_{24}Ag(SH)_{18}^-$ cluster, in order to explore how the origin of photoluminescence of Au_{25} is affected by mono silver doping. The calculated fluorescence energy is 0.81 eV, which is only 0.02 eV lower in energy than that of the $Au_{25}(SH)_{18}^-$. The calculated radiative lifetime of the S_1 state is 25 μs, which lies in between that of the Au_{25} (23 μs) and Ag_{25} (26 μs) clusters. The Stokes shift of the doped system is calculated to be 0.47 eV, which is only 0.02 eV lower than that of Au_{25}. The relatively large Stokes shift implies substantial geometrical and electronic structure alterations for the S_1 state of the $Au_{24}Ag(SH)_{18}^-$ cluster compared to its ground state. Table 5.4 summarizes the average geometric parameters of the optimized S_1 geometry of the $Au_{24}Ag(SH)_{18}^-$ system.

We observe significant bond elongations associated with the Ag dopant atom in the $Au_{12}Ag$ core. As shown in Table 5.5, a maximum bond elongation of 0.28 Å is observed for Au(8)-Au(9) bond which is opposite to Au(3)-Ag(2) bond in the approximately icosahedral $Au_{12}Ag$ core. Unlike in the homometal nanocluster, bond pairs elongate by different amounts upon photoexcitation (Table 5.5). Similar to previous systems, no alterations in the bonds associated with the semi-rings are noticed except for some $Ag_{shell}(0)/Au_{shell}(0)$-$Au_{staple}(I)$ bonds that vary by about 0.1 Å in the optimized S_1 geometry. Moreover, the electronic structure modifications of the $Au_{24}Ag(SH)_{18}^-$ system are analogous to that of Au_{25}. The ground state HOMO and LUMO orbitals are destabilized and stabilized by 0.23 and 0.24 eV respectively in the S_1 state. The splitting among HOMO/HOMO-1/HOMO-2 orbitals is calculated to be 0.37 eV and splitting between LUMO/LUMO+1 is 0.23 eV. However, the superatomic P and D character

of these orbitals are found to be preserved in the excited state. These major geometrical and electronic structure changes upon photoexcitation can be correlated with the large Stokes shift calculated for this doped 25-atom metal nanocluster. Mono-silver doping of the Au_{25} system does not affect the origin of photoluminescence, but the emission energy and the radiative lifetimes are slightly affected.

Table 5.4 Geometrical parameters of the ground state (S_0) and first singlet excited state (S_1) structures of $[Au_{24}Ag(SH)_{18})]^-$ at the BP86/DZ level of theory.

	Average Bond Length (Å)	
Bond	Ground State (S_0)	Excited State (S_1)
$Au_{center}-Au_{shell}/Ag_{shell}$	2.824 ± 0.016	2.842 ± 0.013
$Au_{shell}/Ag_{shell}-Au_{shell}/Ag_{shell}$	2.971 ± 0.076	2.991 ± 0.127
$Au_{shell}/Ag_{shell}-S_{terminal}$	2.568 ± 0.010	2.571 ± 0.029
$Au_{staple}-S_{terminal}$	2.443 ± 0.008	2.449 ± 0.035
$Au_{staple}-S_{central}$	2.441 ± 0.003	2.456 ± 0.024

5.5 Conclusions

The origin of photoluminescence of $Ag_{25}(SR)_{18}^-$ (R=H, PhMe$_2$) nanoclusters is investigated using DFT and TDDFT methods. The optimization of the S_1 state geometry showed bond elongations up to 0.17 Å in the Ag_{13} icosahedral core compared to the ground state geometry, analogous to the Au_{25} system. Asymmetric bond elongations make the shell asymmetric, which causes increased splitting among HOMO/HOMO-1/HOMO-2 and LUMO/LUMO+1 orbitals that were almost triply and doubly degenerate in the ground state. The calculated Stokes shift for the $Ag_{25}(SH)_{18}^-$ system is 0.37 eV, which reduces to 0.24 eV when the aromatic ligands are introduced. The ligand replacement imparts similar, but less significant, geometrical and electronic structure changes associated with the Ag_{13} core in the S_1 state. Heteroatom doping does not affect the origin of photoluminescence of the thiolate-protected, anionic 25-metal atom nanoclusters. However, the emission energies and radiative lifetimes of the S_1 states are slightly affected. In contrast to the ligand-to-metal charge transfer mechanism

proposed by Liu et al,[35] we propose that photoluminescence arises due to a HOMO-LUMO transition that involves excitations from core-based superatomic orbitals (P to D).

Table 5.5 Comparison of Au_{shell}/Ag_{shell}−Au_{shell} bond lengths in relaxed geometries of the ground state (S_0) and the first excited state (S_1) of the $Ag_{24}Au(SH)_{18}^-$ nanocluster. Atoms in the $Au_{12}Ag$ icosahedral core with elongated bonds in S_1 with respect to S_0 are highlighted in green.
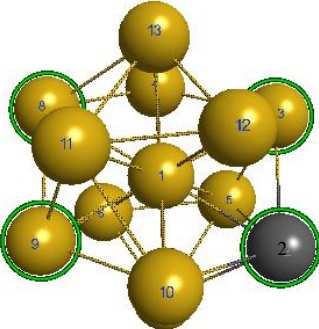
Bond	Bond Length (Å)	
	S_0	S_1
8 – 9	3.050	3.327
3 – 2	3.040	3.157
6 – 8	3.004	3.122
2 – 12	3.006	3.101
4 – 13	3.033	3.129
7 – 10	3.021	3.117
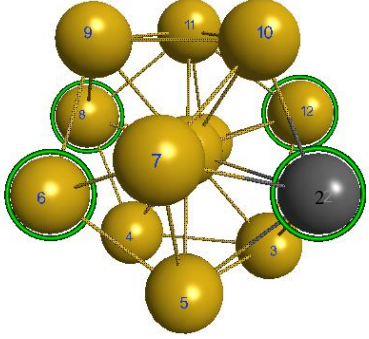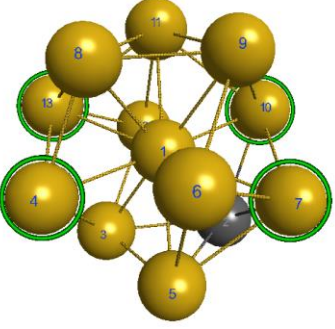
5.6 Acknowledgements

5.7 References

1.   Yu, M.; Zheng, J., Clearance Pathways and Tumor Targeting of Imaging Nanoparticles. *ACS Nano* **2015**, *9*, 6655-6674.

2.   Jin, R.; Zeng, C.; Zhou, M.; Chen, Y., Atomically Precise Colloidal Metal Nanoclusters and Nanoparticles: Fundamentals and Opportunities. *Chem. Rev.* **2016**, *116*, 10346-10413.

3.   Yang, X.; Yang, M.; Pang, B.; Vara, M.; Xia, Y., Gold Nanomaterials at Work in Biomedicine. *Chem. Rev.* **2015**, *115*, 10410-10488.

4.   Goswami, N.; Zheng, K.; Xie, J., Bio-NCs - the Marriage of Ultrasmall Metal Nanoclusters with Biomolecules. *Nanoscale* **2014**, *6*, 13328-13347.

5.   Wang, M.; Wu, Z.; Yang, J.; Wang, G.; Wang, H.; Cai, W., $Au_{25}(SG)_{18}$ as a Fluorescent Iodide Sensor. *Nanoscale* **2012**, *4*, 4087-4090.

6.   Wu, Z.; Wang, M.; Yang, J.; Zheng, X.; Cai, W.; Meng, G.; Qian, H.; Wang, H.; Jin, R., Well-Defined Nanoclusters as Fluorescent Nanosensors: A Case Study on $Au_{25}(SG)_{18}$. *Small* **2012**, *8*, 2028-2035.

7.   Wang, Y.; Wang, Y.; Zhou, F.; Kim, P.; Xia, Y., Protein-Protected Au Clusters as a New Class of Nanoscale Biosensor for Label-Free Fluorescence Detection of Proteases. *Small* **2012**, *8*, 3769-3773.

8.   Yang, J.; Xia, N.; Wang, X.; Liu, X.; Xu, A.; Wu, Z.; Luo, Z., One-Pot One-Cluster Synthesis of Fluorescent and Bio-Compatible Ag_{14} nanoclusters for cancer cell imaging. *Nanoscale* **2015**, *7*, 18464-18470.

9.   Zhu, M.; Aikens, C. M.; Hollander, F. J.; Schatz, G. C.; Jin, R., Correlating the Crystal Structure of A Thiol-Protected Au_{25} Cluster and Optical Properties. *J. Am. Chem. Soc.* **2008**, *130*, 5883-5885.

10.   Heaven, M. W.; Dass, A.; White, P. S.; Holt, K. M.; Murray, R. W., Crystal Structure of the Gold Nanoparticle $[N(C_8H_{17})_4][Au_{25}(SCH_2CH_2Ph)_{18}]$. *J. Am. Chem. Soc.* **2008**, *130*, 3754-3755.

11.   Qian, H.; Eckenhoff, W. T.; Zhu, Y.; Pintauer, T.; Jin, R., Total Structure Determination of Thiolate-Protected Au_{38} Nanoparticles. *J. Am. Chem. Soc.* **2010**, *132*, 8280-8281.

12.   Jadzinsky, P. D.; Calero, G.; Ackerson, C. J.; Bushnell, D. A.; Kornberg, R. D., Structure of a Thiol Monolayer-Protected Gold Nanoparticle at 1.1 Å Resolution. *Science* **2007**, *318*, 430-433.

13.   Nimmala, P. R.; Knoppe, S.; Jupally, V. R.; Delcamp, J. H.; Aikens, C. M.; Dass, A., $Au_{36}(SPh)_{24}$ Nanomolecules: X-ray Crystal Structure, Optical Spectroscopy, Electrochemistry, and Theoretical Analysis. *J. Phys. Chem. B* **2014**, *118*, 14157-14167.

14.   Crasto, D.; Malola, S.; Brosofsky, G.; Dass, A.; Häkkinen, H., Single Crystal XRD Structure and Theoretical Analysis of the Chiral $Au_{30}S(S\text{-}t\text{-}Bu)_{18}$ Cluster. *J. Am. Chem. Soc.* **2014**, *136*, 5000-5005.

15.   Das, A.; Liu, C.; Zeng, C.; Li, G.; Li, T.; Rosi, N. L.; Jin, R., Cyclopentanethiolato-Protected $Au_{36}(SC_5H_9)_{24}$ Nanocluster: Crystal Structure and Implications for the Steric and Electronic Effects of Ligand. *J. Phys. Chem. A* **2014**, *118*, 8264-8269.

16.   Dass, A.; Theivendran, S.; Nimmala, P. R.; Kumara, C.; Jupally, V. R.; Fortunelli, A.; Sementa, L.; Barcaro, G.; Zuo, X.; Noll, B. C., $Au_{133}(SPh\text{-}tBu)_{52}$ Nanomolecules: X-ray Crystallography, Optical, Electrochemical, and Theoretical Analysis. *J. Am. Chem. Soc.* **2015**, *137*, 4610-4613.

17.   Das, A.; Liu, C.; Byun, H. Y.; Nobusada, K.; Zhao, S.; Rosi, N.; Jin, R., Structure Determination of $[Au_{18}(SR)_{14}]$. *Angew. Chem. Int. Ed.* **2015**, *54*, 3140-3144.

18.   Zeng, C.; Liu, C.; Chen, Y.; Rosi, N. L.; Jin, R., Gold–Thiolate Ring as a Protecting Motif in the $Au_{20}(SR)_{16}$ Nanocluster and Implications. *J. Am. Chem. Soc.* **2014**, *136*, 11922-11925.

19.   Desireddy, A.; Conn, B. E.; Guo, J.; Yoon, B.; Barnett, R. N.; Monahan, B. M.; Kirschbaum, K.; Griffith, W. P.; Whetten, R. L.; Landman, U.; Bigioni, T. P., Ultrastable silver nanoparticles. *Nature* **2013**, *501*, 399-402.

20.   Yang, H.; Wang, Y.; Huang, H.; Gell, L.; Lehtovaara, L.; Malola, S.; Häkkinen, H.; Zheng, N., All-thiol-stabilized Ag_{44} and $Au_{12}Ag_{32}$ nanoparticles with single-crystal structures. *Nat. Commun.* **2013**, *4*, 2422.

21.   Joshi, C. P.; Bootharaju, M. S.; Alhilaly, M. J.; Bakr, O. M., $[Ag_{25}(SR)_{18}]^-$: The "Golden" Silver Nanoparticle. *J. Am. Chem. Soc.* **2015**, *137*, 11578-11581.

22.   Dhayal, R. S.; Liao, J.-H.; Liu, Y.-C.; Chiang, M.-H.; Kahlal, S.; Saillard, J.-Y.; Liu, C. W., $[Ag_{21}\{S_2P(OiPr)_2\}_{12}]^+$: An Eight-Electron Superatom. *Angew. Chem. Int. Ed.* **2015**, *54*, 3702-3706.

23.   Yang, H.; Wang, Y.; Zheng, N., Stabilizing Subnanometer Ag(0) Nanoclusters by Thiolate and Diphosphine Ligands and Their Crystal Structures. *Nanoscale* **2013**, *5*, 2674-2677.

24.   Shibu, E. S.; Pradeep, T., Photoluminescence and Temperature-Dependent Emission Studies of Au_{25} Clusters in the Solid State. *Int. J. Nanosci.* **2009**, *08*, 223-226.

25.   Devadas, M. S.; Bairu, S.; Qian, H.; Sinn, E.; Jin, R.; Ramakrishna, G., Temperature-Dependent Optical Absorption Properties of Monolayer-Protected Au_{25} and Au_{38} Clusters. *J. Phys. Chem. Lett.* **2011**, *2*, 2752-2758.

26.   Green, T. D.; Yi, C.; Zeng, C.; Jin, R.; McGill, S.; Knappenberger, K. L., Temperature-Dependent Photoluminescence of Structurally-Precise Quantum-Confined $Au_{25}(SC_8H_9)_{18}$ and $Au_{38}(SC_{12}H_{25})_{24}$ Metal Nanoparticles. *J. Phys. Chem. A* **2014**, *118*, 10611-10621.

27.   Wu, Z.; Jin, R., On the Ligand's Role in the Fluorescence of Gold Nanoclusters. *Nano Lett.* **2010**, *10*, 2568-2573.

28.   Shibu, E. S.; Muhammed, M. A. H.; Tsukuda, T.; Pradeep, T., Ligand Exchange of $Au_{25}SG_{18}$ Leading to Functionalized Gold Clusters: Spectroscopy, Kinetics, and Luminescence. *J. Phys. Chem. C* **2008**, *112*, 12168-12176.

29.   Devadas, M. S.; Kim, J.; Sinn, E.; Lee, D.; Goodson, T.; Ramakrishna, G., Unique Ultrafast Visible Luminescence in Monolayer-Protected Au_{25} Clusters. *J. Phys. Chem. C* **2010**, *114*, 22417-22423.

30.   Wang, G.; Guo, R.; Kalyuzhny, G.; Choi, J.-P.; Murray, R. W., NIR Luminescence Intensities Increase Linearly with Proportion of Polar Thiolate Ligands in Protecting Monolayers of Au_{38} and Au_{140} Quantum Dots. *J. Phys. Chem. B* **2006**, *110*, 20282-20289.

31.   Link, S.; Beeby, A.; FitzGerald, S.; El-Sayed, M. A.; Schaaff, T. G.; Whetten, R. L., Visible to Infrared Luminescence from a 28-Atom Gold Cluster. *J. Phys. Chem. B* **2002**, *106*, 3410-3415.

32.   Lee, D.; Donkers, R. L.; Wang, G.; Harper, A. S.; Murray, R. W., Electrochemistry and Optical Absorbance and Luminescence of Molecule-like Au_{38} Nanoparticles. *J. Am. Chem. Soc.* **2004**, *126*, 6193-6199.

33.   Miller, S. A.; Womick, J. M.; Parker, J. F.; Murray, R. W.; Moran, A. M., Femtosecond Relaxation Dynamics of $Au_{25}L_{18}^{-}$ Monolayer-Protected Clusters. *J. Phys. Chem. C* **2009**, *113*, 9440-9444.

34.   Weerawardene, K. L. D. M.; Aikens, C. M., Theoretical Insights into the Origin of Photoluminescence of $Au_{25}(SR)_{18}^{-}$ Nanoparticles. *J. Am. Chem. Soc.* **2016**, *138*, 11202-11210.

35.   Liu, X.; Yuan, J.; Yao, C.; Chen, J.; Li, L.; Bao, X.; Yang, J.; Wu, Z., Crystal and Solution Photoluminescence of $MAg_{24}(SR)_{18}$ (M = Ag/Pd/Pt/Au) Nanoclusters and Some Implications for the Photoluminescence Mechanisms. *J. Phys. Chem. C* **2017**, *121*, 13848-13853.

36.   Soldan, G.; Aljuhani, M. A.; Bootharaju, M. S.; AbdulHalim, L. G.; Parida, M. R.; Emwas, A.-H.; Mohammed, O. F.; Bakr, O. M., Gold Doping of Silver Nanoclusters: A 26-Fold Enhancement in the Luminescence Quantum Yield. *Angew. Chem. Int. Ed.* **2016**, *55*, 5749-5753.

37.   Wang, S.; Meng, X.; Das, A.; Li, T.; Song, Y.; Cao, T.; Zhu, X.; Zhu, M.; Jin, R., A 200-fold Quantum Yield Boost in the Photoluminescence of Silver-Doped Ag_xAu_{25-x} Nanoclusters: The 13 th Silver Atom Matters. *Angew. Chem. Int. Ed.* **2014**, *53*, 2376-2380.

38.   Guidez, E. B.; Mäkinen, V.; Häkkinen, H.; Aikens, C. M., Effects of silver doping on the geometric and electronic structure and optical absorption spectra of the $Au_{25-n}Ag_n(SH)_{18}^{-}$ (n = 1, 2, 4, 6, 8, 10, 12) bimetallic nanoclusters. *J. Phys. Chem. C* **2012**, *116*, 20617-20624.

39.   Kumara, C.; Aikens, C. M.; Dass, A., X-ray Crystal Structure and Theoretical Analysis of $Au_{25-x}Ag_x(SCH_2CH_2Ph)_{18}^{-}$ Alloy. *J. Phys. Chem. Lett.* **2014**, *5*, 461-466.

40.   Yamazoe, S.; Kurashige, W.; Nobusada, K.; Negishi, Y.; Tsukuda, T., Preferential location of coinage metal dopants (M = Ag or Cu) in $[Au_{25-x}M_x(SC_2H_4Ph)_{18}]^{-}$ (x ~ 1) as determined by extended X-ray absorption fine structure and density functional theory calculations. *J. phys. Chem. C* **2014**, *118*, 25284-25290.

41.   te Velde, G.; Bickelhaupt, F. M.; Baerends, E. J.; Fonseca Guerra, C.; van Gisbergen, S. J. A.; Snijders, J. G.; Ziegler, T., Chemistry with ADF. *J. Comput. Chem.* **2001**, *22*, 931-967.

42.   Becke, A. D., Density-Functional Exchange-Energy Approximation with Correct Asymptotic Behavior. *Phys. Rev. A* **1988**, *38*, 3098-3100.

43.   Perdew, J. P., Density-Functional Approximation for the Correlation Energy of the Inhomogeneous Electron Gas. *Phys. Rev. B* **1986**, *33*, 8822-8824.

44.   Aikens, C. M., Effects of Core Distances, Solvent, Ligand, and Level of Theory on the TDDFT Optical Absorption Spectrum of the Thiolate-Protected Au_{25} Nanoparticle. *J. Phys. Chem. A* **2009**, *113*, 10811-10817.

45.   Guidez, E. B.; Aikens, C. M., Time-Dependent Density Functional Theory Study of the Luminescence Properties of Gold Phosphine Thiolate Complexes. *J. Phys. Chem. A* **2015**, *119*, 3337-3347.

46.   Chen, S.; Wang, S.; Zhong, J.; Song, Y.; Zhang, J.; Sheng, H.; Pei, Y.; Zhu, M., The Structure and Optical Properties of the [$Au_{18}(SR)_{14}$] Nanocluster. *Angew. Chem. Int. Ed.* **2015**, *54*, 3145-3149.

47.   Bae, G.-T.; Aikens, C. M., Time-Dependent Density Functional Theory Studies of Optical Properties of Au Nanoparticles: Octahedra, Truncated Octahedra, and Icosahedra. *J. Phys. Chem. C* **2015**, *119*, 23127-23137.

48.   Hulkko, E.; Lopez-Acevedo, O.; Koivisto, J.; Levi-Kalisman, Y.; Kornberg, R. D.; Pettersson, M.; Häkkinen, H., Electronic and Vibrational Signatures of the $Au_{102}(p\text{-MBA})_{44}$ Cluster. *J. Am. Chem. Soc.* **2011**, *133*, 3752-3755.

49.   Liao, M.-S.; Bonifassi, P.; Leszczynski, J.; Ray, P. C.; Huang, M.-J.; Watts, J. D., Structure, Bonding, and Linear Optical Properties of a Series of Silver and Gold Nanorod Clusters: DFT/TDDFT Studies. *J. Phys. Chem. A* **2010**, *114*, 12701-12708.

50.   Aikens, C. M.; Li, S.; Schatz, G. C., From Discrete Electronic States to Plasmons: TDDFT Optical Absorption Properties of Ag_n (n = 10, 20, 35, 56, 84, 120) Tetrahedral Clusters. *J. Phys. Chem. C* **2008**, *112*, 11272-11279.

51.   Weerawardene, K. L. D. M.; Guidez, E. B.; Aikens, C. M., Photoluminescence Origin of $Au_{38}(SR)_{24}$ and $Au_{22}(SR)_{18}$ Nanoparticles: A Theoretical Perspective. *J. Phys. Chem. C* **2017**, *121*, 15416-15423.

52.   Lenthe, E. v.; Baerends, E. J.; Snijders, J. G., Relativistic Regular Two- Component Hamiltonians. *J. Chem. Phys.* **1993**, *99*, 4597-4610.

53.   Costa, P. J.; Calhorda, M. J., A DFT and MP2 Study of Luminescence of Gold(I) Complexes. *Inorg. Chim. Acta.* **2006**, *359*, 3617-3624.

54.   Bode, B. M.; Gordon, M. S., Macmolplt: A Graphical User Interface for GAMESS. *J. Mol. Graphics and Modelling* **1998**, *16*, 133-138.

55.   Aikens, C. M., Electronic Structure of Ligand-Passivated Gold and Silver Nanoclusters. *J. Phys. Chem. Lett.* **2011**, *2*, 99-104.

56.   Walter, M.; Akola, J.; Lopez-Acevedo, O.; Jadzinsky, P. D.; Calero, G.; Ackerson, C. J.; Whetten, R. L.; Grönbeck, H.; Häkkinen, H., A Unified View of Ligand-Protected Gold Clusters as Superatom Complexes. *Proc. Natl. Acad. Sci.* **2008**, *105*, 9157-9162.

57.   Marques, M. A. L.; Castro, A.; Rubio, A., Assessment of Exchange-Correlation Functionals for the Calculation of Dynamical Properties of Small Clusters in Time-Dependent Density Functional Theory. *J. Chem. Phys.* **2001**, *115*, 3006-3014.

Chapter 6 - Effect of Aliphatic vs. Aromatic Ligands on the Structure and Optical Absorption of Au$_{20}$(SR)$_{16}$

6.1 Abstract

Despite the recent determination of the crystal structure of the Au$_{20}$(TBBT)$_{16}$ (TBBT = SPh-*t*-Bu) nanocluster, it is not certain if Au$_{20}$(SR)$_{16}$ adopts the same structure when R is an aliphatic ligand. To this end, we perform a theoretical investigation using density functional theory (DFT) and time-dependent DFT (TDDFT). We optimize a methylthiolate version of the new crystal structure geometry of Au$_{20}$(TBBT)$_{16}$ and compare the stability and optical properties with the three lowest energy isomers of Au$_{20}$(SCH$_3$)$_{16}$ predicted previously. Furthermore, TDDFT calculations are performed for the Au$_{20}$(TBBT)$_{16}$ structure determined via x-ray crystallography and the related Au$_{20}$(SPh)$_{16}$ nanocluster. All the calculated optical absorption spectra are compared against the available experimental spectrum of Au$_{20}$(PET)$_{16}$ (PET = SCH$_2$CH$_2$Ph) and Au$_{20}$(TBBT)$_{16}$. We observe that the new geometry of the Au$_{20}$(SCH$_3$)$_{16}$ nanocluster with an Au$_7$ core is more stable than the previous isomers.

6.2 Introduction

Ligand protected gold nanoparticles with a core diameter less than 2 nm are of special interest due to their distinct electronic, optical, magnetic, and photoluminescent properties.[1-12] Their atomic packing structure places them in between small molecules such as metal ligand complexes and relatively large nanocrystals (3-100 nm) that exhibit localized surface plasmons depending on their size and shape.[4] Ultrasmall gold nanoparticles have enabled numerous technological applications such as catalysis,[13-17] biomedicine,[18] energy conversion,[19] and chemical sensing.[20] In particular, thiolate-stabilized gold nanoparticles (Au$_n$(SR)$_m$) have been extensively studied both experimentally and theoretically during the past decade jointly for fundamental science and useful applications.

Jin and coworkers have synthesized numerous atomically precise, thiolate protected gold nanoclusters since 2007.[4-6, 21, 22] They devised a methodology to control the nanocluster size with good precision without using electrophoretic or chromatographic isolation to separate size-mixed products, based upon previous studies by Whetten,[23-25] Tsukuda,[26] and other groups.[27] Single crystal x-ray crystallography is primarily used to determine the total structure of these nanoparticles, which is crucial to understand their stability and properties. However, growing single crystals is challenging. The $Au_{25}(SR)_{18}{}^q$ (q = -1, 0),[1, 28, 29] $Au_{38}(SR)_{24}$,[30] and $Au_{102}(SR)_{44}$[31] are some of the earliest nanoclusters whose crystallographic information was reported. A common structural picture of these thiolate-protected nanoclusters consists of a polyhedron based gold core and $Au_x(SR)_{x+1}$ staple motifs that protect the core. In the $Au_{25}(SR)_{18}$ cluster, the twelve surface atoms of the 13-atom icosahedral gold core are passivated by six v-shaped RS-Au-SR-Au-SR (level-2 or dimeric) staple motifs.[1] This is known as the "divide-and-protect" model.[32] Similarly, the chiral $Au_{38}(SR)_{24}$ cluster comprises a face-fused biicosahedral Au_{23} core, six level-2 staple motifs, and three RS-Au-SR (level-1 or monomeric) staple motifs.[30] However, the larger $Au_{102}(SR)_{44}$ cluster consists of 19 monomeric and only two dimeric staple motifs.[31] It is evident that the increasing gold to thiolate ratio has increased the number of monomeric and decreased the number of dimeric staple motifs. Pei *et al*. identified a generic rule on the basis of well-established cluster structures from both experiment and theory that higher-level staple motifs become dominant with the decreasing Au/SR ratio in a cluster.[33] During the past couple of years, the x-ray crystal structures of $Au_{18}(SR)_{14}$,[34, 35] $Au_{20}(SR)_{16}$,[36] $Au_{23}(SR)_{16}{}^-$,[37] $Au_{24}(SR)_{20}$,[38] $Au_{28}(SR)_{20}$,[22, 39] $Au_{30}S(SR)_{18}$,[40] $Au_{36}(SR)_{24}$,[21, 41, 42] and $Au_{133}(SR)_{52}$[43] were also reported. As expected, level-3 (trimeric) staple motifs were identified in the crystal structure of $Au_{30}S(SR)_{18}$[40] and four tetrameric staple motifs were observed in $Au_{24}(SR)_{20}$.[38] However, there are still a number of thiolate protected gold nanoclusters with known compositions but with structures that have not yet been determined experimentally such as $Au_{15}(SR)_{13}$,[44, 45] $Au_{40}(SR)_{24}$,[46] $Au_{44}(SR)_{28}$,[47, 48] etc.

In 2009, Zhu *et al*.[49] first reported the size-controlled synthesis of a phenylethylthiolate (PET)-protected gold nanocluster with the structural formula of $Au_{20}(SCH_2CH_2Ph)_{16}$. The optical absorption spectrum of this charge neutral cluster showed a distinct band around 485 nm (2.56 eV), a weak band around 420 nm (2.95 eV), and a large optical energy gap of about 2.2 eV. Subsequently Pei *et al*.[33] and Jiang *et al*.[50] performed DFT calculations to predict the atomic

structure of this 20-atom gold-thiolate cluster with simplified methylthiolate ligands. Both papers predicted the existence of level-3 extended staple motifs in view of the low Au/SR ratio of $Au_{20}(SR)_{16}$. With several constraints based on the $[Au]_{a+a'}[Au(SR)_2]_b[Au_2(SR)_3]_c[Au_3(SR)_4]_d$ structural formula, they found a unique set of data that gives rise to $Au_8[Au_3(SR)_4]_4$. Jiang *et al.*[50] found several promising candidates with the most stable structure featuring a prolate fcc core but a low HOMO-LUMO gap compared to the experimental value at the TPSS/def2-TZVP level of theory. Therefore, they suggested that more stable isomers should exist. The three lowest energy isomers (**Iso1**-**Iso3**) found by Pei *et al.* at the PBE/TZP level of theory have a prolate core that can be viewed as two edge-fused tetrahedral Au_4 units. The four level-3 staple motifs protect each Au atom in the Au_8 core as shown in Figure 6.1 and each motif connects two gold atoms in different Au_4 units, further enhancing the stability of the prolate gold core. **Iso1**-**Iso3** have only slightly different orientations of staple motifs and Au-Au bond lengths in the Au-core. Pei *et al.* showed using different levels of theory that these three isomers are nearly degenerate in energy and may coexist at room temperature. The optical absorption spectra computed by the time-dependent DFT method at the PBE/TZP level of theory well-reproduced the experimental absorption curve qualitatively, particularly for **Iso3**. The extrapolated optical band edges were found to be 2.14, 2.34, and 2.28 eV respectively for **Iso1**-**Iso3**, which are in good agreement with the 2.15 eV experimental optical band edge.

More recently in 2014, Jin and coworkers[36] re-synthesized a $Au_{20}(SR)_{16}$ nanocluster using 4-*tert*-butylbenzenethiol (TBBT) as the ligand. Furthermore, they reported the crystal structure of the two enantiomers of this chiral nanocluster. In contrast to the theoretical prediction, a vertex sharing bitetrahedral Au_7 kernel, an unusual $Au_8(SR)_8$ ring motif, one trimeric, and two monomeric staple motifs were identified. The giant octameric $Au_8(SR)_8$ ring motif adopts a chair conformation and circles the Au_7 kernel as shown in Figure 6.2. Remarkably, none of the thiolate ligands in the ring is bonded to the kernel gold atoms. However, the ring motif protects the kernel through strong aurophilic Au-Au bonds in contrast to the common staple motifs that bind to the kernel via terminal thiol groups. As shown in Figure 6.1, a trimeric staple motif binds to two of the gold atoms of the Au_7 bitetrahedron, which also connects to a gold atom of the ring through a short Au-Au bond. Two monomeric staple motifs bind to the rest of the four Au atoms of the edge sharing bitetrahedron. Since each gold atom contributes one 6s free electron and each thiolate ligand localizes one, the $Au_{20}(SR)_{16}$ cluster has

a total of 4 free electrons. The novel crystal structure of $Au_{20}(TBBT)_{16}$ compromises between its geometric and electronic necessities. The edge sharing bitetrahedron needs three staple motifs to protect the six gold atoms of the Au_7 kernel and the three staple motifs localize 3 electrons forming the Au_7^{3+} kernel, which holds four free electrons.

It is unknown whether the $Au_{20}(PET)_{16}$ adopts the same core structure as $Au_{20}(TBBT)_{16}$. In some nanoclusters such as $Au_{36}(SR)_{24}$,[21, 41, 42] ligands with sp^2 or sp^3 carbons adjacent to the sulfur atom lead to the same core structure. However, in $Au_{28}(SR)_{20}$, aromatic and aliphatic ligands generate different structures.[39] In addition, the effect of the ligands on the optical properties of this cluster is not yet established. However, several experimental and theoretical investigations have been carried out previously to study the ligand effect on the thiolate protected Au_{25} nanocluster. Wu *et al.*[51] demonstrated on the basis of NMR, mass spectroscopy, and optical spectroscopy analyses that $Au_{25}(SR)_{18}$ clusters capped by different types of thiol ligands adopt the same two-shell structure. Moreover, Knoppe and Bürgi[52] reported that the UV-Visible spectrum of $Au_{25}(PET)_{18}$ after ligand exchange with *S*-BINAS (BINAS = 1,1´-binaphthyl-2,2´-dithiol) becomes less defined over increasing reaction time, but maintains its basic features. Dass and coworkers[53] performed a combined mass spectrometric and computational investigation to study ligand exchange of the $Au_{25}(PET)_{18}$ cluster. They observed that the fine spectral features of the $Au_{25}(PET)_{18}$ cluster are not affected significantly even after three exchanges with 1,4-butanedithiol. DFT computations also confirmed that the electronic structure of the Au_{25} nanocluster retains its main features with ligand exchange. Additionally, DFT calculations performed by Jung *et al.*[54] suggested that Au_m cluster structures are insensitive to R for all the thiolate-stabilized Au_{25}, Au_{38}, and Au_{102} clusters. Aikens[55] also demonstrated that the size of the aliphatic ligand plays a minor role on the optical absorption spectrum of $Au_{25}(SR)_{18}$ cluster using DFT calculations.

Because the $Au_{20}(TBBT)_{16}$ nanocluster possesses aromatic ligands, it is not certain if the structure of the $Au_{20}(PET)_{16}$ nanocluster has the same structure as the novel crystal structure or whether it adopts a different structure such as the one proposed by Pei *et al.*[33] due to the presence of the aliphatic ligands. Herein, we investigate the ligand effects on the geometric and optical properties of the $Au_{20}(SR)_{16}$ nanocluster using DFT and TDDFT calculations.

6.3 Computational Details

All DFT and TDDFT calculations were performed using the Amsterdam Density Functional (ADF)[56] package. Pei *et al.*[33] used the PBE/TZP level of theory for geometry optimization and to calculate optical absorption spectra of the three lowest energy isomers (**Iso1-Iso3**) of $Au_{20}(SCH_3)_{16}$. Therefore, we used the same level of theory to optimize the methyl thiolate version of the new crystal structure geometry (**Iso**), to calculate its optical absorption spectrum, and reproduce the spectra of **Iso1-Iso3**. It is well established[55, 57, 58] that pure generalized gradient approximation (GGA) DFT methods tend to yield elongated bonds whereas local density approximation (LDA) functionals typically yield close or slightly underestimated bond lengths compared to experimental structures. Hence, we optimized the geometry of **Iso** using the Xα[59, 60] functional as well. Scalar relativistic effects were included in all calculations by utilizing the zeroth order regular approximation (ZORA).[61]

The asymptotically corrected LB94[62] functional has been found to be in good agreement with experiment for thiolate-protected gold nanoparticles, whereas GGA functionals generally underestimate excitation energies.[55] Therefore, the optical absorption spectrum of **Iso** was obtained using the LB94 functional for both PBE and Xα optimized geometries. However, it is also known that the LB94 functional often overestimates the excited-state energies of silver clusters compared to GGA and SAOP functionals.[63, 64] In addition, a TDDFT calculation was performed on the crystal structure coordinates of $Au_{20}(TBBT)_{16}$ using the LB94 functional and a double zeta (DZ) basis set. Furthermore, we reduced the tertiary butyl groups of TBBT by replacing them with hydrogen atoms and set the C—H bond lengths to 0.95 Å to get coordinates of $Au_{20}(SPh)_{16}$ for TDDFT calculations using the same level of theory. A double zeta basis set was employed in these calculations with the frozen core approximation for Au, S, and C up to the 4f, 2p, and 1s electrons, respectively, to save computational resources, since $Au_{20}(TBBT)_{16}$ and $Au_{20}(SPh)_{16}$ have a large number of atoms. Moreover, we performed a constrained geometry optimization of $Au_{20}(SCH_3)_{16}$ cluster by fixing the crystal structure coordinates for Au and S atoms and allowing only methyl groups to optimize, using the Xα/TZP level of theory. Then a TDDFT calculation was performed on the constrained optimized structure with LB94/DZ level of theory to compare and contrast the optical absorption spectrum with that of the fully optimized $Au_{20}(SCH_3)_{16}$ as well as the $Au_{20}(TBBT)_{16}$ cluster. All the optical absorption spectra were convoluted with a Gaussian with a full width at half maximum of 0.2 eV.

6.4 Results

6.4.1 Geometric properties of $Au_{20}(SCH_3)_{16}$

Although SCH_3 has not been used for the synthesis of thiolate-stabilized gold nanoclusters due to practical reasons, to represent aliphatic ligands at a reasonable computational cost we fully optimized the novel crystal structure geometry of the $Au_{20}(TBBT)_{16}$ nanocluster by replacing the aromatic TBBT ligands with small, aliphatic SCH_3 ligands. Table 6.1 compares the calculated geometric parameters of $Au_{20}(SCH_3)_{16}$ within the local density approximation and generalized gradient approximation against the crystal structure of the $Au_{20}(TBBT)_{16}$ nanocluster. As expected, the PBE functional produces longer bond lengths compared to $X\alpha$. Experimentally, the vertex sharing Au_7 bitetrahedral kernel has very short bond lengths with an average of 2.72 ± 0.03 Å. The replacement of large TBBT ligands with small methyl thiolate ligands does not affect the strong bonding in tetrahedra significantly. The calculated $Au_{kernel} - Au_{kernel}$ bond length of $Au_{20}(SCH_3)_{16}$ is 2.75 ± 0.06 Å using the $X\alpha$/TZP level of theory, which is about 4.5% shorter than the Au – Au distance of 2.88 Å in bulk gold. As discussed in the Introduction, except for the giant $Au_8(SR)_8$ octameric ring wrapped around the Au_7 kernel there are two monomeric and one trimeric staple motifs protecting the kernel. The average $Au_{kernel} - S_{staple}$ and $Au_{staple} - S_{staple}$ bond lengths calculated with the $X\alpha$ functional are within the experimental uncertainty whereas those bond lengths calculated with the PBE functional are 0.08 and 0.03 Å longer respectively.

Typically, gold-thiolate staple motifs interact with the gold kernel via Au – S bonds. Nonetheless, the $Au_8(SR)_8$ octameric ring interacts with the kernel exclusively through $Au_{ring} - Au_{kernel}$ bonding, which are only about 5% longer than the bulk Au – Au bonds. The presence of strong Au – Au bonding and the absence of Au – S bonding indicates that this novel ring structural motif is clearly different from the well-known gold-thiolate staple motifs reported previously for thiolate protected nanoclusters. Table 6.1 shows that the replacement of large aromatic TBBT ligands by small aliphatic SCH_3 ligands does not appear to change the structural parameters of the $Au_{20}(SR)_{16}$ cluster significantly. The $Au_{ring} - S_{ring}$ bond is elongated by ~3-4% in calculated structures as compared to the $Au_{20}(TBBT)_{16}$ crystal structure. The ring motif adopts a chair conformation as shown in Figure 6.2 and both the Au_{ring}–SR–Au_{ring} and SR–Au_{ring}–SR

angles are slightly decreased, but within the uncertainty range relative to the experimental structure.
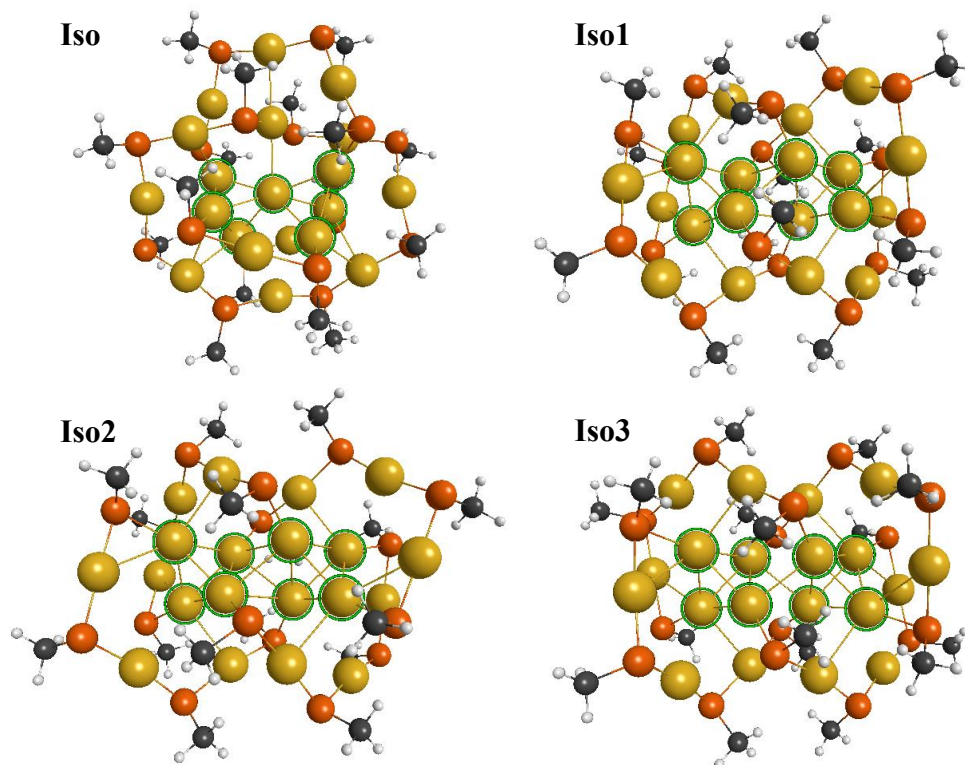
Figure 6.1 The four isomers of Au$_{20}$(SCH$_3$)$_{16}$. Iso is the methylthiolate version of the new crystal structure geometry. Iso1-Iso3 are the lowest energy isomers found by Pei *et al*.[33] (Kernel gold atoms are highlighted in green.)

The relative stability and the optical absorption spectra calculated for the novel crystal structure geometry (**Iso**) and the three lowest energy isomers (**Iso1**-**Iso3**) of Au$_{20}$(SCH$_3$)$_{16}$ found by Pei *et al*. were compared. We found that the PBE/TZP optimized **Iso1** – **Iso3** are about 0.25 – 0.30 eV higher in energy than **Iso**, which suggests that even small aliphatic ligands prefer the new experimental crystal structure geometry obtained for the Au$_{20}$(TBBT)$_{16}$ cluster. Figure 6.1 shows the four isomers of Au$_{20}$(SCH$_3$)$_{16}$ considered in the current study.

Table 6.1 The geometric parameters of calculated Au$_{20}$(SCH$_3$)$_{16}$ and the experimental crystal structure of Au$_{20}$(TBBT)$_{16}$ nanocluster.

	Au$_{20}$(SCH$_3$)$_{16}$		Au$_{20}$(TBBT)$_{16}$
	PBE/TZP	Xα/TZP	crystal structure
Au$_{kernel}$ − Au$_{kernel}$	2.80 ± 0.04 Å	2.75 ± 0.06 Å	2.72 ± 0.03 Å
Au$_{kernel}$ − S$_{staple}$	2.42 ± 0.02 Å	2.38 ± 0.01 Å	2.34 ± 0.05 Å
Au$_{staple}$ − S$_{staple}$	2.35 ± 0.01 Å	2.32 ± 0.01 Å	2.33 ± 0.05 Å
Au$_{ring}$ − Au$_{kernel}$	3.20 ± 0.32 Å	3.05 ± 0.33 Å	3.02 ± 0.10 Å
Au$_{ring}$ − S$_{ring}$	2.36 ± 0.01 Å	2.33 ± 0.01 Å	2.27 ± 0.03 Å
Au$_{ring}$–SR–Au$_{ring}$	100.99 ± 3.89°	97.28 ± 4.43°	102.11 ± 4.64°
SR–Au$_{ring}$–SR	171.16 ± 3.88°	169.58 ± 3.70°	172.25 ± 3.89°
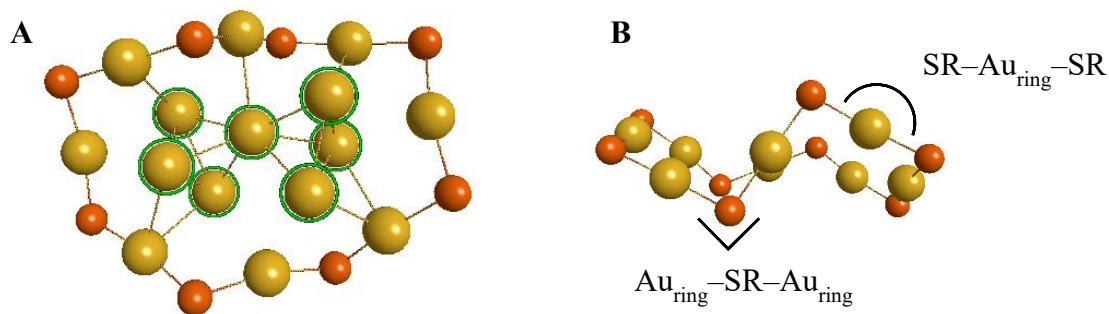
Figure 6.2 (A) Au$_7$ kernel and the octameric ring motif of the novel crystal structure geometry of Au$_{20}$(TBBT)$_{16}$. (B) Chair conformation of the octameric ring. Color code: orange, S; yellow, Au (kernel gold atoms are highlighted in green and methyl groups are not shown for clarity)

6.4.2 Optical properties of $Au_{20}(SCH_3)_{16}$

TDDFT calculations are performed at the PBE/TZP level of theory for all four isomers of $Au_{20}(SCH_3)_{16}$ and the optical absorption spectra are compared with the experimental spectrum obtained for $Au_{20}(PET)_{16}$[33, 49] in Figure 6.3.
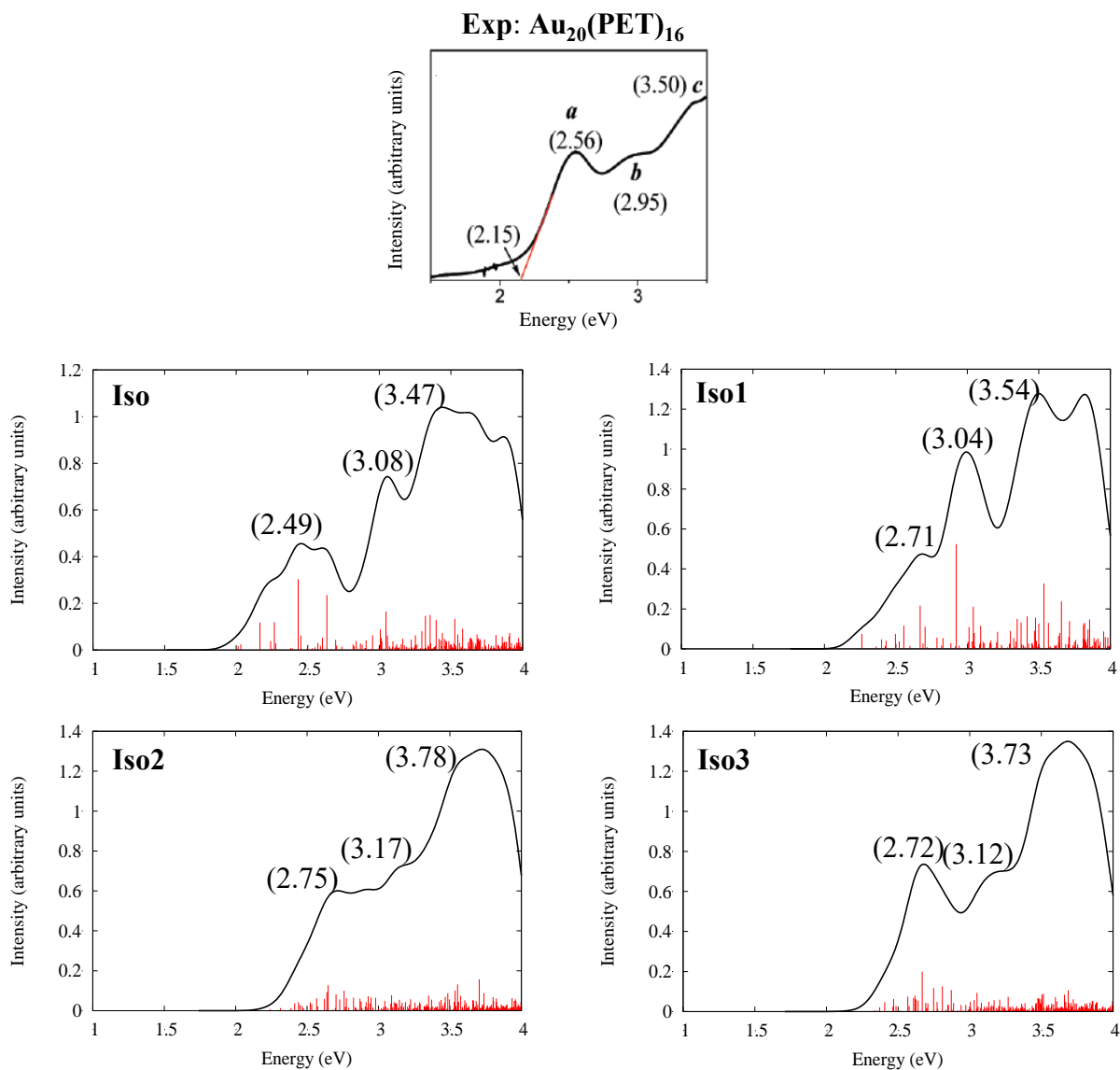
Figure 6.3 Comparison of experimental[33, 49] and theoretical optical absorption spectra of Iso and Iso –Iso3 of $Au_{20}(SCH_3)_{16}$. Iso1–Iso3 have the same prolate Au_8 core whereas Iso has the edge sharing bitetrahedral core. $Au_{20}(PET)_{16}$ spectrum reprinted with permission from Pei, Y.; Gao, Y.; Shao, N.; Zeng, X. C., *J. Am. Chem. Soc.* 2009, *131*, 13619-13621. Copyright 2009 American Chemical Society.

The optical absorption spectrum of a thiolate protected gold cluster can be very sensitive to the gold core structure. Jin and coworkers identified three prominent absorption features in the experimental spectrum at 2.56, 2.95, and 3.50 eV.[33, 49] We found that the absorption spectrum of **Iso** of $Au_{20}(SCH_3)_{16}$ with the Au_7 core has its most noticeable peaks at 2.49, 3.08, and 3.47 eV, which are comparable to the experiment. Pei *et al*. also reported that their three calculated isomers reproduce experimental peak positions well and the overall shape of the optical absorption spectrum of **Iso3** particularly agrees well with the experiment. However, their peaks were predicted at energies slightly higher than experiment using the PBE/TZP level of theory. We also predict optical absorption spectra for **Iso1** – **Iso3** with peak energies higher than the experimental bands, although the overall spectra appear to have a similar shape to the experimental spectrum. Table 6.2 summarizes the energies of most prominent peaks of the four calculated isomers with two different kernel geometries.

Table 6.2 Prominent peak energies for the calculated isomers of $Au_{20}(SCH_3)_{16}$ at the PBE/TZP level of theory and experimental $Au_{20}(PET)_{16}$ with extrapolated optical band gaps.

	Calculated $Au_{20}(SCH_3)_{16}$ (eV)				Experimental $Au_{20}(PET)_{16}$ (eV)
	Iso	**Iso1**	**Iso2**	**Iso3**	
Peak 1	2.49	2.71	2.75	2.72	2.56
Peak 2	3.08	3.04	3.17	3.12	2.95
Peak 3	3.47	3.54	3.78	3.73	3.50
Band gap*	2.01	2.26	2.24	2.21	2.15

* First excited state energies are provided as the extrapolated optical band gaps

It has been established[55, 65] that GGA functionals generally underestimate excitation energies. Therefore, if the calculated geometries represent the original cluster geometry of $Au_{20}(PET)_{16}$ accurately, slightly underestimated peak positions should appear in the optical absorption spectra as compared to the experimental ones. However, from Table 6.2 it is evident

that the first peak of **Iso1** – **Iso3** lies around 2.7 eV and the other two peaks also lie higher in energy than expected. This suggest that even though the overall shape of the spectra agrees with the experiment, **Iso1** – **Iso3** with a Au_8 kernel might not represent the geometry of $Au_{20}(PET)_{16}$ correctly. In contrast, the **Iso** geometry reproduces all peak positions in good agreement with experiment. These results imply that the $Au_{20}(SR)_{16}$ nanoparticle may have the same structure whether aliphatic ligands or aromatic ligands are employed.

6.4.3 Theory and geometry dependence of the optical absorption spectrum of Iso

In order to evaluate the theory dependence of the optical properties, we calculated the optical absorption spectrum of **Iso** at the LB94/TZP level of theory using the PBE/TZP optimized geometry. Figure 6.4A shows that the LB94 functional reproduces the experimental peak positions in better agreement than the PBE functional (Figure 6.3). The first prominent peak in Figure 6.4A lies at 2.59 eV and the second peak at 2.94 eV. However, the third peak lies about 0.2 eV higher in energy than the experimental spectrum. In agreement with literature,[55, 63, 64] the LB94 functional produces slightly overestimated excitation energies as compared to the PBE functional, but closer to experimental values.
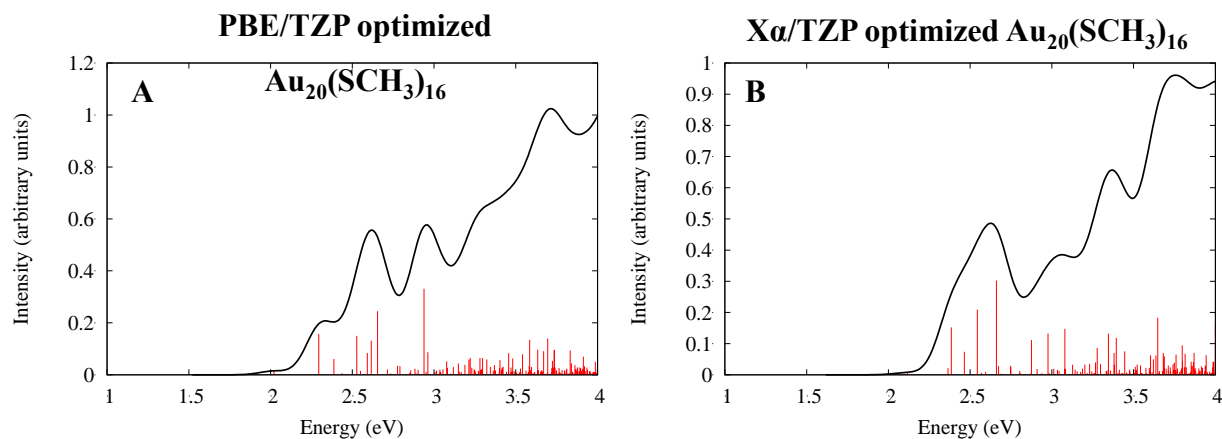

Figure 6.4 Optical absorption spectra of new crystal structure geometry of $Au_{20}(SCH_3)_{16}$ (Iso) calculated at the LB94/TZP level of theory. The geometry is optimized at A) the PBE/TZP and B) the Xα/TZP levels of theory.

Moreover, we analyzed the geometry effects on the optical absorption spectrum of **Iso** by performing another TDDFT calculation using the same level of theory but on the Xα/TZP optimized structure. The overall shape of the spectrum shown in Figure 6.4B has a remarkable resemblance to the experimental optical absorption spectrum of $Au_{20}(PET)_{16}$ in Figure 6.3. Its three main absorption features at 2.58, 2.97, and 3.34 eV are also in good agreement with the experimental peak positions. Furthermore, it is evident that the peak energies of the two LB94/TZP calculated spectra are very close in energy and agree well with the experimental values. The differences of the details of the two spectra can be attributed to the bond length variances of the two geometries as shown in Table 6.1.

6.4.4 Ligand effects on the optical properties of $Au_{20}(SR)_{16}$

To further analyze the ligand effects on the optical properties of the $Au_{20}(SR)_{16}$ nanocluster, we performed a TDDFT calculation using the crystal structure coordinates of the $Au_{20}(TBBT)_{16}$ cluster. Furthermore, we reduced the tertiary butyl groups of TBBT by replacing them with hydrogen atoms and performed another TDDFT calculation. The optical absorption spectra obtained at the LB94/DZ level of theory using the crystal structure coordinates of $Au_{20}(TBBT)_{16}$ and $Au_{20}(SPh)_{16}$ are compared with those of the Xα/TZP optimized geometry of $Au_{20}(SCH_3)_{16}$ and the experimental spectrum of $Au_{20}(PET)_{16}$ in Figure 6.5. The reduction in basis set for $Au_{20}(SCH_3)_{16}$ from TZP to DZ shifts the peak energies slightly to the blue, but overall the spectrum still agrees well with the experimental spectrum of $Au_{20}(PET)_{16}$.

The spectra of $Au_{20}(TBBT)_{16}$ and $Au_{20}(SPh)_{16}$ nanoclusters are very similar despite the reduction of the ligands from TBBT to SPh, suggesting that the aromatic rings and Au-core structure are the dominant factors for the absorption. Similar to the methylthiolate version of the novel crystal structure geometry, multiple absorption features can be observed in the energy region of 2.5 – 3.5 eV for both of these clusters; however, the absorption spectra for the aromatic ligands also have a peak around 2.4 eV. Two main peaks can be observed around 2.7-3.0 eV. Another prominent peak is visible around 3.5 eV in the calculated spectra. The observed difference in the calculated spectra for the aromatic vs. aliphatic ligands may be due in part to the use of an optimized geometry for $Au_{20}(SCH_3)_{16}$ rather than a crystal structure geometry, or it may represent a ligand effect. The experimental optical absorption spectrum of $Au_{20}(TBBT)_{16}$ is also shown in Figure 6.5. This spectrum is very broad and the absorption features are not clear.

However, it appears to have multiple bands within the energy range of 2.0-3.5 eV, in agreement with the calculated spectra for aromatic ligands.
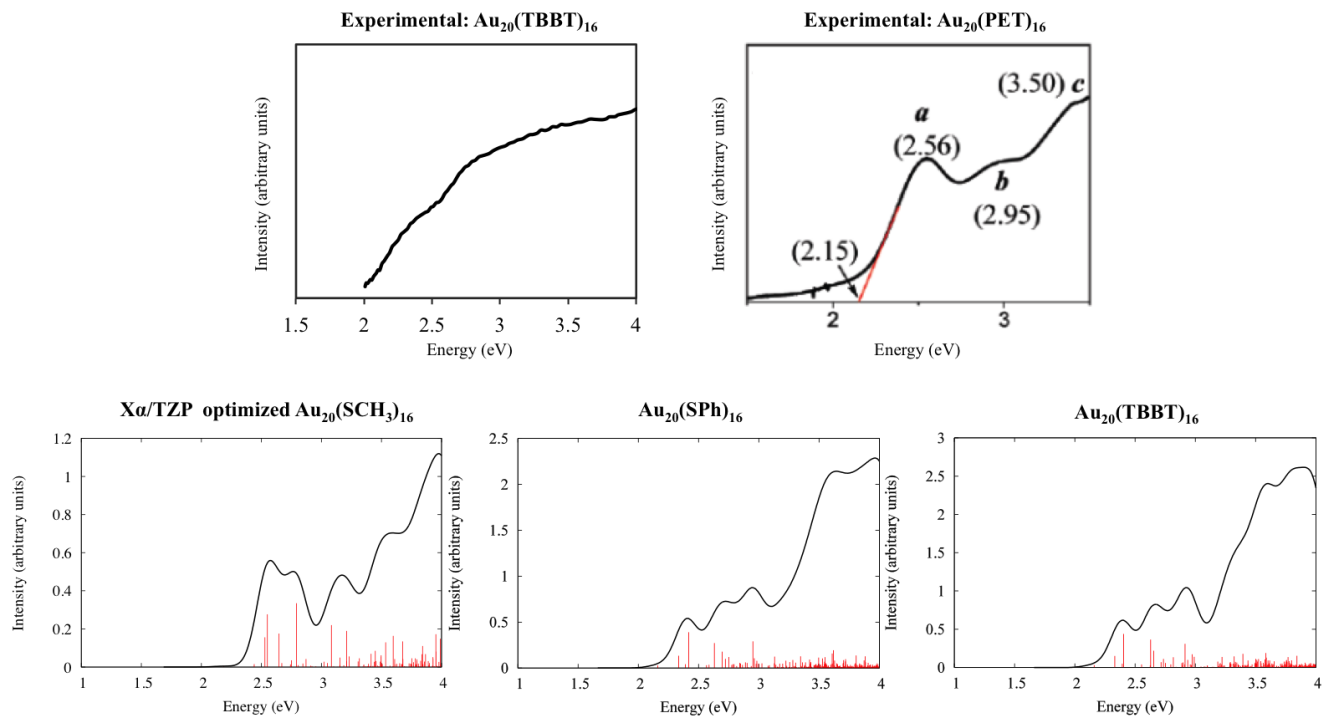
Figure 6.5 Comparison of optical absorption spectra of Au$_{20}$(SR)$_{16}$ nanoclusters calculated at the LB94/DZ level of theory with the experimental spectra of Au$_{20}$(TBBT)$_{16}$[36] and Au$_{20}$(PET)$_{16}$.[33, 49] Au$_{20}$(PET)$_{16}$ spectrum reprinted with permission from Pei, Y.; Gao, Y.; Shao, N.; Zeng, X. C., *J. Am. Chem. Soc.* 2009, *131*, 13619-13621. Copyright 2009 American Chemical Society.

6.4.5 Electronic structure of Au$_{20}$(SR)$_{16}$

In this section, we examine the origin of the prominent peaks of the optical absorption spectra of Au$_{20}$(SR)$_{16}$ nanoclusters. Figure 6.6 demonstrates the numbering of the analyzed peaks in the optical absorption spectra of the fully optimized and constrained optimized Au$_{20}$(SCH$_3$)$_{16}$ clusters as well as the Au$_{20}$(TBBT)$_{16}$ cluster. Table 6.3 shows the energy, oscillator strength, the transitions involved, weight contribution from each transition, and the transition dipole moments in *x*, *y*, *z* directions for each numbered peak in Figure 6.6.

Figure 6.6 and Table 6.3 indicate that the optical absorption spectra and the origin of peaks in the energy range of 2.5-3.2 eV are in good agreement between Au$_{20}$(SR)$_{16}$, for R= CH$_3$ (constrained geometry) and TBBT. Two transitions, HOMO-3→LUMO and HOMO-1→

LUMO, are responsible for the first prominent absorption peak, whereas the second peak is mainly due to HOMO-5→LUMO, HOMO→LUMO+1, and HOMO→LUMO+2 transitions in both constrained $Au_{20}(SCH_3)_{16}$ and $Au_{20}(TBBT)_{16}$ clusters. However, Table 6.3 shows that the origin of the third main peak (state 18 for constrained $Au_{20}(SCH_3)_{16}$ and state 21 for $Au_{20}(TBBT)_{16}$) is different for the two structures. This suggests that the ligand effects play a minor role at low energy, although these effects become more noticeable at higher energy. Furthermore, some differences can be observed in the origin of the main peaks in fully and constrained optimized $Au_{20}(SCH_3)_{16}$ clusters, which can be attributed to the changes in core geometries shown in Table 6.1. Again, this suggests that the optical properties of $Au_{20}(SR)_{16}$ nanoclusters are highly dependent on the gold core structure and bond lengths.
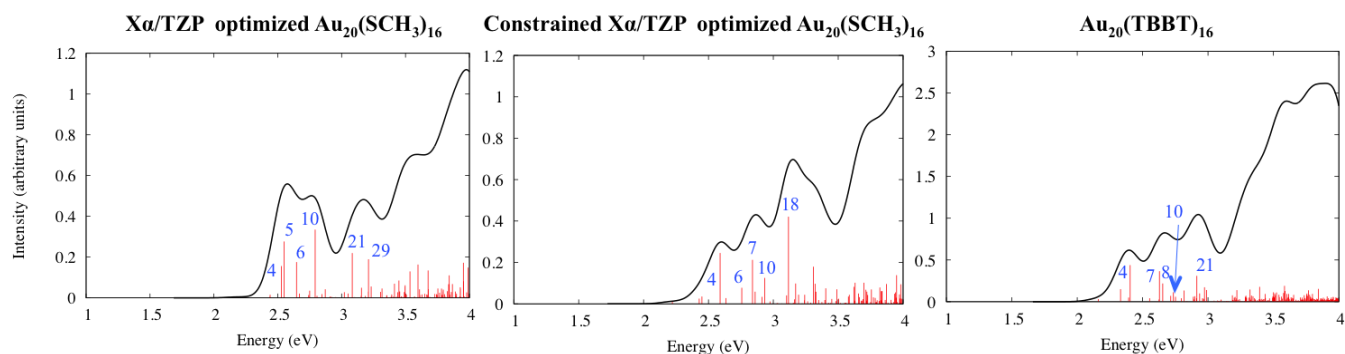

Figure 6.6 The optical absorption spectra of $Au_{20}(SR)_{16}$ nanoclusters calculated at the LB94/DZ level of theory. The numbering of the most prominent and analyzed peaks of each spectrum are shown.

For further analysis, we plotted the electronic structure of the TBBT and methylthiolate (core geometry constrained) versions of the $Au_{20}(SR)_{16}$ clusters and the orbitals involved in transitions corresponding to strong peaks in their absorption spectra (Figure 6.7). Although the choice of ligand affects the absolute orbital energies, there are minimal perturbations in the relative energies, orbital appearance, and orbital ordering due to the difference between the large aromatic TBBT ligands and the small aliphatic methyl ligands. One change in orbital ordering between the HOMO-2 and HOMO-3 is noted. The total number of free valence electrons associated with this cluster is four, because it has 20 Au atoms and 16 one-electron withdrawing thiolate ligands. Consequently, superatomic P-like character can be observed for both HOMO and LUMO orbitals in Figure 6.7. Lower lying occupied orbitals show a major contribution from atomic Au d_{z^2} orbitals and some minor contribution from atomic S p orbitals.

Table 6.3 The energy, oscillator strength, transitions involved, weight, and the transition dipole moments in x, y, z directions of each numbered peak in Figure 6.6.

|	Energy (eV)	Oscillator Strength (au)	Transitions	Weight	Transition Dipole Moment (au)		
Au$_{20}$(SCH$_3$)$_{16}$							
4:	2.529	0.03327	HOMO-3→LUMO	0.7425	-0.0007	2.1638	-0.0005
			HOMO-1→LUMO	0.0937	0.0012	-0.5495	0.0005
5:	2.550	0.05892	HOMO→LUMO+1	0.8667	-0.1016	0.0004	3.4894
6:	2.647	0.03741	HOMO→LUMO+2	0.7897	0.0001	1.3740	-0.0007
			HOMO-3→LUMO	0.0754	-0.0002	0.6738	-0.0001
10:	2.793	0.07128	HOMO-2→LUMO+1	0.8402	0.6899	0.0006	-2.1927
21:	3.083	0.04681	HOMO-9→LUMO	0.665	-0.5610	0.0006	1.0083
			HOMO-4→LUMO+1	0.2355	0.2262	0.0000	0.5875
29:	3.210	0.04037	HOMO-6→LUMO+1	0.4464	-0.0005	-0.7484	-0.0001
			HOMO→LUMO+3	0.3225	-0.0003	-1.1819	0.0000
Au$_{20}$(SCH$_3$)$_{16}$-constrained optimization							
4:	2.590	0.05233	HOMO-3→LUMO	0.7983	0.0024	2.1066	-0.0067
			HOMO-1→LUMO	0.1347	-0.0059	0.694	-0.0100
6:	2.757	0.01653	HOMO-5→LUMO	0.9293	0.0045	-1.5456	0.0014
7:	2.839	0.04522	HOMO→LUMO+1	0.9037	-0.202	-0.0044	-3.0456
10:	2.933	0.02666	HOMO→LUMO+2	0.6001	-0.0049	1.3726	-0.0006
18:	3.117	0.08965	HOMO-13→LUMO	0.9337	0.3733	-0.0055	-0.1293
Au$_{20}$(TBBT)$_{16}$							
4:	2.405	0.09326	HOMO-3→LUMO	0.7457	0.0009	1.5318	0.0027
			HOMO-1→LUMO	0.2221	0.0002	1.2854	-0.0007
7:	2.628	0.07792	HOMO-5→LUMO	0.9477	0.004	-2.0678	0.0045
8:	2.654	0.04658	HOMO→LUMO+1	0.7896	-0.7295	0.0040	-2.4733
			HOMO→LUMO+3	0.1210	0.1189	0.0004	0.2279
10:	2.735	0.02417	HOMO→LUMO+2	0.5657	0.0002	1.4400	0.0027
21:			HOMO-2→LUMO+1	0.6158	-1.0171	0.0003	1.9942
21:	2.914	0.06599	HOMO-2→LUMO+3	0.1351	0.1396	0.0003	-0.1718
21:			HOMO-1→LUMO+2	0.1027	-0.4560	-0.0006	-0.0241
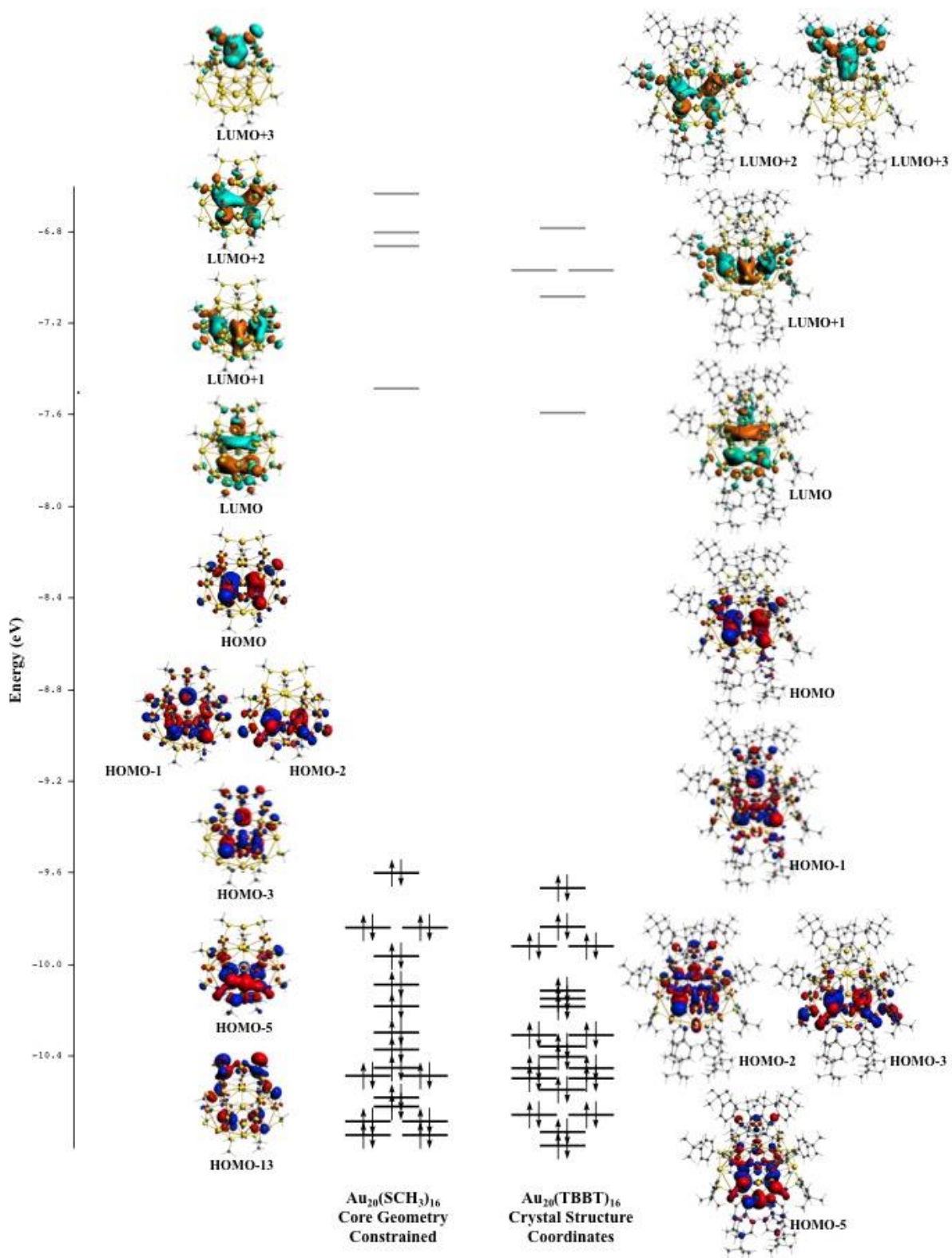
Figure 6.7 Comparison of orbitals and energy level diagrams of core geometry constrained Au$_{20}$(SR)$_{16}$, R=CH$_3$ and R=TBBT nanoclusters. |Isovalue| = 0.02

6.5 Conclusion

In conclusion, we employed density functional theory to determine the effect of ligands on the geometric structure and optical properties of the thiolate-protected 20-atom gold nanocluster. The methylthiolate version of the novel crystal structure geometry with a Au_7 edge sharing bitetrahedral kernel (**Iso**) was found to be more stable than the three previous lowest energy isomers with the structural formula of $Au_8[Au_3(SR)_4]$. In addition, we showed that the geometric parameters of this thiolate-protected nanoparticle are also affected marginally by the variation in ligand. The optical absorption spectrum of **Iso** calculated at the LB94/TZP level of theory on the Xα/TZP optimized geometry agrees with the experimental spectrum remarkably well. These results suggest that the $Au_{20}(SR)_{16}$ nanoparticle may have the same structure whether aliphatic ligands or aromatic ligands are employed. The comparison of calculated optical absorption spectra of $Au_{20}(SR)_{16}$ where R=CH_3, Ph, Ph-t-Bu against the experimental spectra of $Au_{20}(PET)_{16}$ and $Au_{20}(TBBT)_{16}$ demonstrated that the ligand effect on optical properties of $Au_{20}(SR)_{16}$ is relatively small, although a slight ligand effect is apparent. A good agreement in electronic structure and optical properties was observed between $Au_{20}(TBBT)_{16}$ and the core geometry constrained $Au_{20}(SCH_3)_{16}$ nanocluster.

6.6 Acknowledgement

6.7 References

1.   Zhu, M.; Aikens, C. M.; Hollander, F. J.; Schatz, G. C.; Jin, R., Correlating the Crystal Structure of A Thiol-Protected Au_{25} Cluster and Optical Properties. *J. Am. Chem. Soc.* **2008**, *130*, 5883-5885.

2.   Zhu, M.; Aikens, C. M.; Hendrich, M. P.; Gupta, R.; Qian, H.; Schatz, G. C.; Jin, R., Reversible Switching of Magnetism in Thiolate-Protected Au$_{25}$ Superatoms. *J. Am. Chem. Soc.* **2009**, *131*, 2490-2492.

3.   Wang, G.; Huang, T.; Murray, R. W.; Menard, L.; Nuzzo, R. G., Near-IR Luminescence of Monolayer-Protected Metal Clusters. *J. Am. Chem. Soc.* **2005**, *127*, 812-813.

4.   Jin, R., Atomically Precise Metal Nanoclusters: Stable Sizes and Optical Properties. *Nanoscale* **2015**, *7*, 1549-1565.

5.   Jin, R., Quantum Sized, Thiolate-Protected Gold Nanoclusters. *Nanoscale* **2010**, *2*, 343-362.

6.   Qian, H.; Zhu, M.; Wu, Z.; Jin, R., Quantum Sized Gold Nanoclusters with Atomic Precision. *Acc. Chem. Res.* **2012**, *45*, 1470-1479.

7.   Aikens, C. M., Origin of Discrete Optical Absorption Spectra of M$_{25}$(SH)$_{18}^{-}$ Nanoparticles (M = Au, Ag). *J. Phys. Chem. C* **2008**, *112*, 19797-19800.

8.   Negishi, Y.; Tsunoyama, H.; Suzuki, M.; Kawamura, N.; Matsushita, M. M.; Maruyama, K.; Sugawara, T.; Yokoyama, T.; Tsukuda, T., X-ray Magnetic Circular Dichroism of Size-Selected, Thiolated Gold Clusters. *J. Am. Chem. Soc.* **2006**, *128*, 12034-12035.

9.   Xie, J.; Zheng, Y.; Ying, J. Y., Protein-Directed Synthesis of Highly Fluorescent Gold Nanoclusters. *J. Am. Chem. Soc.* **2009**, *131*, 888-889.

10.   Lin, C.-A. J.; Yang, T.-Y.; Lee, C.-H.; Huang, S. H.; Sperling, R. A.; Zanella, M.; Li, J. K.; Shen, J.-L.; Wang, H.-H.; Yeh, H.-I.; Parak, W. J.; Chang, W. H., Synthesis, Characterization, and Bioconjugation of Fluorescent Gold Nanoclusters toward Biological Labeling Applications. *ACS Nano* **2009**, *3*, 395-401.

11.   Parker, J. F.; Fields-Zinna, C. A.; Murray, R. W., The Story of a Monodisperse Gold Nanoparticle: Au$_{25}$L$_{18}$. *Acc. Chem. Res.* **2010**, *43*, 1289-1296.

12.   Varnavski, O.; Ramakrishna, G.; Kim, J.; Lee, D.; Goodson, T., Critical Size for the Observation of Quantum Confinement in Optically Excited Gold Clusters. *J. Am. Chem. Soc.* **2010**, *132*, 16-17.

13.   Herzing, A. A.; Kiely, C. J.; Carley, A. F.; Landon, P.; Hutchings, G. J., Identification of Active Gold Nanoclusters on Iron Oxide Supports for CO Oxidation. *Science* **2008**, *321*, 1331-1335.

14.   Liu, Y.; Tsunoyama, H.; Akita, T.; Xie, S.; Tsukuda, T., Aerobic Oxidation of Cyclohexane Catalyzed by Size-Controlled Au Clusters on Hydroxyapatite: Size Effect in the Sub-2 nm Regime. *ACS Catal.* **2011**, *1*, 2-6.

15.   Turner, M.; Golovko, V. B.; Vaughan, O. P. H.; Abdulkin, P.; Berenguer-Murcia, A.; Tikhov, M. S.; Johnson, B. F. G.; Lambert, R. M., Selective Oxidation with Dioxygen by Gold Nanoparticle Catalysts Derived from 55-Atom Clusters. *Nature* **2008**, *454*, 981-983.

16.   Yamazoe, S.; Koyasu, K.; Tsukuda, T., Nonscalable Oxidation Catalysis of Gold Clusters. *Acc. Chem. Res.* **2014**, *47*, 816-824.

17.   Li, G.; Jin, R., Atomically Precise Gold Nanoclusters as New Model Catalysts. *Acc. Chem. Res.* **2013**, *46*, 1749-1758.

18.   Yang, X.; Yang, M.; Pang, B.; Vara, M.; Xia, Y., Gold Nanomaterials at Work in Biomedicine. *Chem. Rev.* **2015**, *115*, 10410-10488.

19.   Chen, Y.-S.; Choi, H.; Kamat, P. V., Metal-Cluster-Sensitized Solar Cells. A New Class of Thiolated Gold Sensitizers Delivering Efficiency Greater Than 2%. *J. Am. Chem. Soc.* **2013**, *135*, 8822-8825.

20.   Wu, Z.; Wang, M.; Yang, J.; Zheng, X.; Cai, W.; Meng, G.; Qian, H.; Wang, H.; Jin, R., Well-Defined Nanoclusters as Fluorescent Nanosensors: A Case Study on $Au_{25}(SG)_{18}$. *Small* **2012**, *8*, 2028-2035.

21.   Zeng, C.; Qian, H.; Li, T.; Li, G.; Rosi, N. L.; Yoon, B.; Barnett, R. N.; Whetten, R. L.; Landman, U.; Jin, R., Total Structure and Electronic Properties of the Gold Nanocrystal $Au_{36}(SR)_{24}$. *Angew. Chem. Int. Ed.* **2012**, *51*, 13114-13118.

22.   Zeng, C.; Li, T.; Das, A.; Rosi, N. L.; Jin, R., Chiral Structure of Thiolate-Protected 28-Gold-Atom Nanocluster Determined by X-ray Crystallography. *J. Am. Chem. Soc.* **2013**, *135*, 10011-10013.

23.   Whetten, R. L.; Khoury, J. T.; Alvarez, M. M.; Murthy, S.; Vezmar, I.; Wang, Z. L.; Stephens, P. W.; Cleveland, C. L.; Luedtke, W. D.; Landman, U., Nanocrystal Gold Molecules. *Adv. Mater.* **1996**, *8*, 428-433.

24.   Price, R. C.; Whetten, R. L., All-Aromatic, Nanometer-Scale, Gold-Cluster Thiolate Complexes. *J. Am. Chem. Soc.* **2005**, *127*, 13750-13751.

25.   Schaaff, T. G.; Knight, G.; Shafigullin, M. N.; Borkman, R. F.; Whetten, R. L., Isolation and Selected Properties of a 10.4 kDa Gold:Glutathione Cluster Compound. *J. Phys. Chem. B* **1998**, *102*, 10643-10646.

26.   Negishi, Y.; Nobusada, K.; Tsukuda, T., Glutathione-Protected Gold Clusters Revisited: Bridging the Gap between Gold(I)−Thiolate Complexes and Thiolate-Protected Gold Nanocrystals. *J. Am. Chem. Soc.* **2005**, *127*, 5261-5270.

27.   Tracy, J. B.; Kalyuzhny, G.; Crowe, M. C.; Balasubramanian, R.; Choi, J.-P.; Murray, R. W., Poly(ethylene glycol) Ligands for High-Resolution Nanoparticle Mass Spectrometry. *J. Am. Chem. Soc.* **2007**, *129*, 6706-6707.

28.   Heaven, M. W.; Dass, A.; White, P. S.; Holt, K. M.; Murray, R. W., Crystal Structure of the Gold Nanoparticle $[N(C_8H_{17})_4][Au_{25}(SCH_2CH_2Ph)_{18}]$. *J. Am. Chem. Soc.* **2008**, *130*, 3754-3755.

29.   Zhu, M.; Eckenhoff, W. T.; Pintauer, T.; Jin, R., Conversion of Anionic $[Au_{25}(SCH_2CH_2Ph)_{18}]^-$ Cluster to Charge Neutral Cluster via Air Oxidation. *J. Phys. Chem. C* **2008**, *112*, 14221-14224.

30.   Qian, H.; Eckenhoff, W. T.; Zhu, Y.; Pintauer, T.; Jin, R., Total Structure Determination of Thiolate-Protected Au_{38} Nanoparticles. *J. Am. Chem. Soc.* **2010**, *132*, 8280-8281.

31.   Jadzinsky, P. D.; Calero, G.; Ackerson, C. J.; Bushnell, D. A.; Kornberg, R. D., Structure of a Thiol Monolayer-Protected Gold Nanoparticle at 1.1 Å Resolution. *Science* **2007**, *318*, 430-433.

32.   Häkkinen, H.; Walter, M.; Grönbeck, H., Divide and Protect: Capping Gold Nanoclusters with Molecular Gold−Thiolate Rings. *J. Phys. Chem. B* **2006**, *110*, 9927-9931.

33.   Pei, Y.; Gao, Y.; Shao, N.; Zeng, X. C., Thiolate-Protected $Au_{20}(SR)_{16}$ Cluster: Prolate Au_8 Core with New $[Au_3(SR)_4]$ Staple Motif. *J. Am. Chem. Soc.* **2009**, *131*, 13619-13621.

34.   Chen, S.; Wang, S.; Zhong, J.; Song, Y.; Zhang, J.; Sheng, H.; Pei, Y.; Zhu, M., The Structure and Optical Properties of the $[Au_{18}(SR)_{14}]$ Nanocluster. *Angew. Chem. Int. Ed.* **2015**, *54*, 3145-3149.

35.   Das, A.; Liu, C.; Byun, H. Y.; Nobusada, K.; Zhao, S.; Rosi, N.; Jin, R., Structure Determination of $[Au_{18}(SR)_{14}]$. *Angew. Chem. Int. Ed.* **2015**, *54*, 3140-3144.

36.   Zeng, C.; Liu, C.; Chen, Y.; Rosi, N. L.; Jin, R., Gold–Thiolate Ring as a Protecting Motif in the $Au_{20}(SR)_{16}$ Nanocluster and Implications. *J. Am. Chem. Soc.* **2014**, *136*, 11922-11925.

37.   Das, A.; Li, T.; Nobusada, K.; Zeng, C.; Rosi, N. L.; Jin, R., Nonsuperatomic [Au$_{23}$(SC$_6$H$_{11}$)$_{16}$]⁻ Nanocluster Featuring Bipyramidal Au$_{15}$ Kernel and Trimeric Au$_3$(SR)$_4$ Motif. *J. Am. Chem. Soc.* **2013**, *135*, 18264-18267.

38.   Das, A.; Li, T.; Li, G.; Nobusada, K.; Zeng, C.; Rosi, N. L.; Jin, R., Crystal Structure and Electronic Properties of a Thiolate-Protected Au$_{24}$ Nanocluster. *Nanoscale* **2014**, *6*, 6458-6462.

39.   Chen, Y.; Liu, C.; Tang, Q.; Zeng, C.; Higaki, T.; Das, A.; Jiang, D.-e.; Rosi, N. L.; Jin, R., Isomerism in Au$_{28}$(SR)$_{20}$ Nanocluster and Stable Structures. *J. Am. Chem. Soc.* **2016**.

40.   Crasto, D.; Malola, S.; Brosofsky, G.; Dass, A.; Häkkinen, H., Single Crystal XRD Structure and Theoretical Analysis of the Chiral Au$_{30}$S(S-*t*-Bu)$_{18}$ Cluster. *J. Am. Chem. Soc.* **2014**, *136*, 5000-5005.

41.   Das, A.; Liu, C.; Zeng, C.; Li, G.; Li, T.; Rosi, N. L.; Jin, R., Cyclopentanethiolato-Protected Au$_{36}$(SC$_5$H$_9$)$_{24}$ Nanocluster: Crystal Structure and Implications for the Steric and Electronic Effects of Ligand. *J. Phys. Chem. A* **2014**, *118*, 8264-8269.

42.   Nimmala, P. R.; Knoppe, S.; Jupally, V. R.; Delcamp, J. H.; Aikens, C. M.; Dass, A., Au$_{36}$(SPh)$_{24}$ Nanomolecules: X-ray Crystal Structure, Optical Spectroscopy, Electrochemistry, and Theoretical Analysis. *J. Phys. Chem. B* **2014**, *118*, 14157-14167.

43.   Dass, A.; Theivendran, S.; Nimmala, P. R.; Kumara, C.; Jupally, V. R.; Fortunelli, A.; Sementa, L.; Barcaro, G.; Zuo, X.; Noll, B. C., Au$_{133}$(SPh-*t*Bu)$_{52}$ Nanomolecules: X-ray Crystallography, Optical, Electrochemical, and Theoretical Analysis. *J. Am. Chem. Soc.* **2015**, *137*, 4610-4613.

44.   Jiang, D.-e.; Overbury, S. H.; Dai, S., Structure of Au$_{15}$(SR)$_{13}$ and Its Implication for the Origin of the Nucleus in Thiolated Gold Nanoclusters. *J. Am. Chem. Soc.* **2013**, *135*, 8786-8789.

45.   Tlahuice-Flores, A.; Jose-Yacaman, M.; Whetten, R. L., On the Structure of the Thiolated Au$_{15}$ Cluster. *Phys. Chem. Chem. Phys.* **2013**, *15*, 19557-19560.

46.   Malola, S.; Lehtovaara, L.; Knoppe, S.; Hu, K.-J.; Palmer, R. E.; Bürgi, T.; Häkkinen, H., Au$_{40}$(SR)$_{24}$ Cluster as a Chiral Dimer of 8-Electron Superatoms: Structure and Optical Properties. *J. Am. Chem. Soc.* **2012**, *134*, 19560-19563.

47.   Zeng, C.; Chen, Y.; Li, G.; Jin, R., Synthesis of a Au$_{44}$(SR)$_{28}$ Nanocluster: Structure Prediction and Evolution from Au$_{28}$(SR)$_{20}$, Au$_{36}$(SR)$_{24}$ to Au$_{44}$(SR)$_{28}$. *Chem. Commun.* **2014**, *50*, 55-57.

48.   Pei, Y.; Lin, S.; Su, J.; Liu, C., Structure Prediction of Au$_{44}$(SR)$_{28}$: A Chiral Superatom Cluster. *J. Am. Chem. Soc.* **2013**, *135*, 19060-19063.

49.   Zhu, M.; Qian, H.; Jin, R., Thiolate-Protected Au$_{20}$ Clusters with a Large Energy Gap of 2.1 eV. *J. Am. Chem. Soc.* **2009**, *131*, 7220-7221.

50.   Jiang, D.-e.; Chen, W.; Whetten, R. L.; Chen, Z., What Protects the Core When the Thiolated Au Cluster is Extremely Small? *J. Phys. Chem. C* **2009**, *113*, 16983-16987.

51.   Wu, Z.; Gayathri, C.; Gil, R. R.; Jin, R., Probing the Structure and Charge State of Glutathione-Capped Au$_{25}$(SG)$_{18}$ Clusters by NMR and Mass Spectrometry. *J. Am. Chem. Soc.* **2009**, *131*, 6535-6542.

52.   Knoppe, S.; Burgi, T., The Fate of Au$_{25}$(SR)$_{18}$ Clusters upon Ligand Exchange with Binaphthyl-Dithiol: Interstaple Binding vs. Decomposition. *Phys. Chem. Chem. Phys.* **2013**, *15*, 15816-15820.

53.   Jupally, V. R.; Kota, R.; Dornshuld, E. V.; Mattern, D. L.; Tschumper, G. S.; Jiang, D.-e.; Dass, A., Interstaple Dithiol Cross-Linking in Au$_{25}$(SR)$_{18}$ Nanomolecules: A Combined Mass Spectrometric and Computational Study. *J. Am. Chem. Soc.* **2011**, *133*, 20258-20266.

54.   Jung, J.; Kang, S.; Han, Y.-K., Ligand Effects on the Stability of Thiol-Stabilized Gold Nanoclusters: $Au_{25}(SR)_{18}^-$, $Au_{38}(SR)_{24}$, and $Au_{102}(SR)_{44}$. *Nanoscale* **2012**, *4*, 4206-4210.

55.   Aikens, C. M., Effects of Core Distances, Solvent, Ligand, and Level of Theory on the TDDFT Optical Absorption Spectrum of the Thiolate-Protected Au_{25} Nanoparticle. *J. Phys. Chem. A* **2009**, *113*, 10811-10817.

56.   te Velde, G.; Bickelhaupt, F. M.; Baerends, E. J.; Fonseca Guerra, C.; van Gisbergen, S. J. A.; Snijders, J. G.; Ziegler, T., Chemistry with ADF. *J. Comput. Chem.* **2001**, *22*, 931-967.

57.   Ivanov, S. A.; Arachchige, I.; Aikens, C. M., Density Functional Analysis of Geometries and Electronic Structures of Gold-Phosphine Clusters. The Case of $Au_4(PR_3)_4^{2+}$ and $Au_4(\mu_2\text{-}I)_2(PR_3)_4$. *J. Phys. Chem. A* **2011**, *115*, 8017-8031.

58.   Häberlen, O. D.; Chung, S.-C.; Stener, M.; Rösch, N., From Clusters to Bulk: A Relativistic Density Functional Investigation on a Series of Gold Clusters Au_n,n=6,…,147. *J. Chem. Phys.* **1997**, *106*, 5189-5201.

59.   Hohenberg, P.; Kohn, W., Inhomogeneous Electron Gas. *Phys. Rev.* **1964**, *136*, B864-B871.

60.   Kohn, W.; Sham, L. J., Self-Consistent Equations Including Exchange and Correlation Effects. *Phys. Rev.* **1965**, *140*, A1133-A1138.

61.   Lenthe, E. v.; Baerends, E. J.; Snijders, J. G., Relativistic Regular Two‐Component Hamiltonians. *J. Chem. Phys.* **1993**, *99*, 4597-4610.

62.   van Leeuwen, R.; Baerends, E. J., Exchange-Correlation Potential with Correct Asymptotic Behavior. *Phys. Rev. A* **1994**, *49*, 2421-2431.

63.   Aikens, C. M.; Li, S.; Schatz, G. C., From Discrete Electronic States to Plasmons: TDDFT Optical Absorption Properties of Ag_n (n = 10, 20, 35, 56, 84, 120) Tetrahedral Clusters. *J. Phys. Chem. C* **2008**, *112*, 11272-11279.

64.   Bae, G.-T.; Aikens, C. M., Time-Dependent Density Functional Theory Studies of Optical Properties of Ag Nanoparticles: Octahedra, Truncated Octahedra, and Icosahedra. *J. Phys. Chem. C* **2012**, *116*, 10356-10367.

65.   Marques, M. A. L.; Castro, A.; Rubio, A., Assessment of Exchange-Correlation Functionals for the Calculation of Dynamical Properties of Small Clusters in Time-Dependent Density Functional Theory. *J. Chem. Phys.* **2001**, *115*, 3006-3014.

Chapter 7 - Comparison of Linear-Response and Real-Time Time-Dependent Density Functional Theories for Noble Metal Nanoparticles

7.1 Abstract

The real-time time-dependent density functional theory (RT-TDDFT) is rapidly gaining prominence as an alternative approach to capture optical properties of molecular systems, which warrants the necessity to benchmark the traditional linear response (LR) method and the RT approach. We calculate the absorption spectra of noble metal nanoparticles with a variety of sizes and shapes to demonstrate the consistency of the two methods over a broad range of energy. The RT spectrum obtained using a grid-based basis set with pseudopotentials achieves results in good agreement with the LR spectrum obtained with large QZ4P atom-centered basis sets. In addition, the real-time variation of the electron density is visualized to show the collective oscillation of electron density for the plasmon modes of noble metal nanoparticles. The RT approach is most useful when calculating wide absorption spectra of larger gold or silver nanoparticles.

7.2 Introduction

Noble metal nanoparticles have received significant research interest due to their wide variety of applications in catalysis,[1, 2] energy conversion and storage,[3, 4] sensing,[5-7] and biomedicine.[5, 8, 9] Noble metal nanoparticles in the size regime of 10-100 nm show a strong absorption peak in the visible-IR region due to surface plasmon resonances (SPR), which is the collective oscillation of the conduction electrons in the presence of an electric field. The wavelength and intensity of this absorption can be tuned by modifying the particle size, shape, composition and dielectric environment.[10-15] During the past few years, different synthetic approaches have been used to successfully synthesize various gold and silver nanoparticles including nanorods,[16] nanobars,[17] nanowires,[18, 19] cubes,[20-23] triangular prisms,[24, 25] octahedra,[20, 22] truncated octahedra,[20, 22] cuboctahedra,[20, 22] and icosahedra.[23]

The optical properties of gold and silver nanoparticles have been studied using classical electromagnetic theory. In particular, Mie theory[26] has been successfully employed to investigate plasmonic extinction spectra of spherical particles. However, applying Mie theory for complex shapes and larger sizes of nanoparticles is not straightforward. Numerical methods such as the finite-difference time domain (FDTD)[27] and discrete dipole approximation (DDA)[28] can be used instead. These methods have modeled the plasmon of such systems successfully.[29-32] Nevertheless, classical electromagnetic theory does not account for quantum effects of smaller nanoparticles. Moreover, gold and silver nanoclusters (< 2nm) display molecular properties and discrete absorption spectra. Therefore, quantum mechanical calculations need to be used in modeling optical properties of nanoclusters in this size regime. Time-dependent density functional theory (TDDFT) has been used extensively to unravel the origin of the discrete absorption spectra of noble metal clusters, mostly using the linear response (LR) approach,[33-40] which is also known as the Casida equation.[41] The LR-TDDFT method provides reliable linear-response properties of molecules and materials when the light-matter interaction is much smaller than the magnitude of intermolecular interactions, which results in a small perturbation away from the ground state. In this approach, excitation energies are calculated by solving an eigenvalue problem derived by considering only the first order response of the density to a perturbation.

Currently, the real-time time-dependent density functional theory (RT-TDDFT) method is rapidly gaining ground as one of the computationally affordable techniques to model electron dynamics in molecular systems under the influence of external fields. Many implementations of RT-TDDFT can be found in literature[42-50] with a wide variety of applications such as plasmons in noble metal nanoparticles,[49-57] magnetic circular dichroism spectroscopy,[58] molecular conductance,[59-61] nonlinear spectra of single molecules[46] and charge transfer between states or spatial regions.[62, 63] However, previously most applications for calculating optical absorption spectra of molecular systems employed the LR form of TDDFT. Therefore, it is important to benchmark the LR and RT TDDFT approaches for different molecular systems. Recently, Tussupbayev et al. compared the RT and LR TDDFT methods for 12 organic dye molecules relevant to photovoltaics and dye-sensitized solar cells.[47] They emphasized the ability of the RT approach to capture excitations across broad spectral regions in large systems and for systems with high densities of states (DOSs). Furthermore, the consistency of the two approaches was

demonstrated for a broad range of systems and exchange correlation functionals. The calculation of absorption spectra for small systems can require longer simulation times with the RT-TDDFT method as compared to LR-TDDFT.[47] However, the RT approach is efficient when calculating wide absorption spectra of large complexes and systems with high DOSs.

Herein, we present a systematic benchmark study by calculating optical absorption spectra using the real-time, real-space OCTOPUS code. These spectra are compared with traditional LR-TDDFT for the optical properties of a variety of gold and silver nanoclusters with numerous sizes and shapes previously studied by Aikens and co-workers.[34-38] We study the basis set effect on the LR-TDDFT spectrum using the smallest system we consider: the Ag_6 nanowire. Furthermore, we investigate how the spacing of the real-space grid, the total simulation time, and the delta kick strength variables affect the RT-TDDFT optical absorption spectrum of the Ag_6 nanowire. We also present the isosurfaces of the time-dependent density along the long axis of Ag_6 nanowire, which shows the collective charge oscillation that corresponds to its longitudinal plasmon mode. LR and RT calculations are compared for gold and silver nanoclusters of various shapes and sizes. The main goal of this paper is to demonstrate the consistency of the LR and RT methods in calculating the optical properties of distinct noble metal nanoclusters and to examine the factors required for achieving accuracy in the calculations.

7.3 Methodology

7.3.1 RT-TDDFT

All RT-TDDFT calculations were performed using the real-space code OCTOPUS 5.0.1.[42, 64] The gradient-corrected PBE exchange-correlation potential[65-68] and norm-conserving Troullier-Martins pseudopotentials[69] (11 valence electrons for each atom) were employed. It has been shown that lack of long-range correction in PBE functional does not qualitatively change the optical absorption spectra of noble metal nanoparticles even though the excitation energies are underestimated.[70-74] Relativistic effects are included as a scalar relativistic correction in the radial part of the pseudopotential.[69] Unless otherwise noted, the spacing of the real-space grid was set to 0.18 Å. The radius of the spheres centered on each atom that makes up the calculation domain was set to 6 Å.

First, a ground state calculation was performed to obtain well-converged Kohn-Sham orbitals. Then, the scheme proposed by Yabana and Bertsch was followed to calculate the linear optical absorption spectra.[45] Herein, all frequencies of the system are excited by giving a small perturbation to the electrons at t=0. To achieve this, the ground state orbitals are multiplied by a phase factor $e^{i\kappa z}$ that imposes a coherent velocity field and causes a dipole moment to develop as the system evolves freely (without further perturbation) for a certain time t=T.[45] The spectrum can then be obtained from the expression for the dipole strength function,[75] $S(w)$:

$$S(w) = \frac{2w}{p} \operatorname{Im} a(w),$$

where the dynamical polarizability $a(w)$, is essentially the Fourier transformed dipole moment $d(t)$ of the system:

$$a(w) = \frac{1}{k} \int dt \; e^{iwt} \left[d(t) - d(0) \right]$$

However, if three time-dependent runs are performed, the average absorption coefficient ($Tr \; s \, / \, 3$) is plotted, where the optical absorption cross section $s(w)$ is related to the dynamical polarizability $a(w)$ via,[42]

$$s(w) = \frac{4pw}{c} \operatorname{Im} a(w)$$

In our calculations, the propagation time step and total propagation time were set to 0.0024 and 50.0 ℏ/eV, which correspond to 0.00158 and 33 fs respectively. The Approximated Enforced Time-Reversal Symmetry (AETRS) propagator[76] was used as implemented in the OCTOPUS code. Three time-dependent simulations in the direction of each Cartesian axis, which define the direction of the initial applied perturbation, were performed for each system.

7.3.2 LR-TDDFT

All LR-TDDFT calculations were performed using the ADF 2016.101 program.[77] The PBE exchange correlation functional[68] was employed in order to compare the optical absorption spectra obtained from the two methods. The Slater-type all-electron quadruple-ζ polarized (QZ4P) basis set was used unless otherwise mentioned. Scalar relativistic effects were included

in all calculations by utilizing the zeroth-order regular approximation (ZORA).[78] All spectra were convoluted with a Gaussian with a full width at half-maximum of 0.15 eV.

Coordinates for optimized geometries of gold and silver nanoparticles with different sizes and shapes were obtained from the literature. Gold and silver nanowires (Au_n, Ag_n; $n = 6, 8, 10, 20$),[35] tetrahedra (Au_n^{m+}, Ag_n^{m+}; when $n = 8, 20$, $m=0$; when $n=10$, $m=2$),[34, 79] and octahedral and icosahedral[36, 37] Au_{13}^{5+} and Ag_{13}^{5+} were considered in this study. The charge states are introduced such that the clusters correspond to electronic shell closings.

7.4 Results

7.4.1 Ag nanowires

Guidez and Aikens discussed three distinct features in the optical absorption spectra of silver nanowires: a sharp low-energy longitudinal peak that arises due to a HOMO→LUMO transition, a low-intensity d-band, and a transverse peak.[35] The longitudinal peak was found to linearly red shift as the length of the nanowire increases in accordance with the particle-in-a-cylinder model, whereas the energy of the transverse peak remains relatively constant. As one benchmark measure, we compared the longitudinal and transverse peak energies of Ag_n ($n = 6, 8, 10, 20$) nanowires calculated with LR- and RT-TDDFT methods (Figure 7.1). The excitation energies calculated with the two methods are in excellent agreement with each other, with the largest deviation being 0.17 eV for the transverse peak of the Ag_6 nanowire.

7.4.1.1 Effect of the Basis Set

In order to explore the basis set effect on the optical absorption spectra, we performed LR-TDDFT calculations employing all-electron DZ, TZP, and QZ4P basis sets on the Ag_6 nanowire. The QZ4P basis set can be roughly described as a core triple zeta, valence quadruple zeta with 4 polarization functions, which can offer the highest accuracy. The TZP basis set has a smaller valence space with triple zeta quality, and contains one set of polarization functions. The smallest basis set in this work is the double zeta (DZ) basis set, which has the smallest number of functions in the valence. A comparison of the calculated spectra with different basis sets is shown in Figure 7.2. The longitudinal peak at ~1.6 eV is calculated with high precision and a standard deviation of 0.02 eV using diverse basis sets. Nevertheless, discrepancies in the

transverse peak energies can be observed between QZ4P and the smaller basis sets. The TZP and DZ transverse peaks deviate slightly from each other (0.09 eV) whereas the QZ4P transverse peak is ~1 eV lower in energy. The RT spectrum agrees well with the QZ4P spectrum with marginal deviations of peak positions within a broad range of energies. The effects of basis set size observed here agree well with previous work; Aikens previously observed that the excitation peaks lie lower in energy when a larger basis set is used to obtain the absorption spectrum of $Au_{25}(SR)_{18}{}^-$ nanoparticles.[70] Overall, it appears that the RT spectrum using a grid-based basis set with pseudopotentials achieves results in good agreement with large QZ4P atom-centered basis sets.
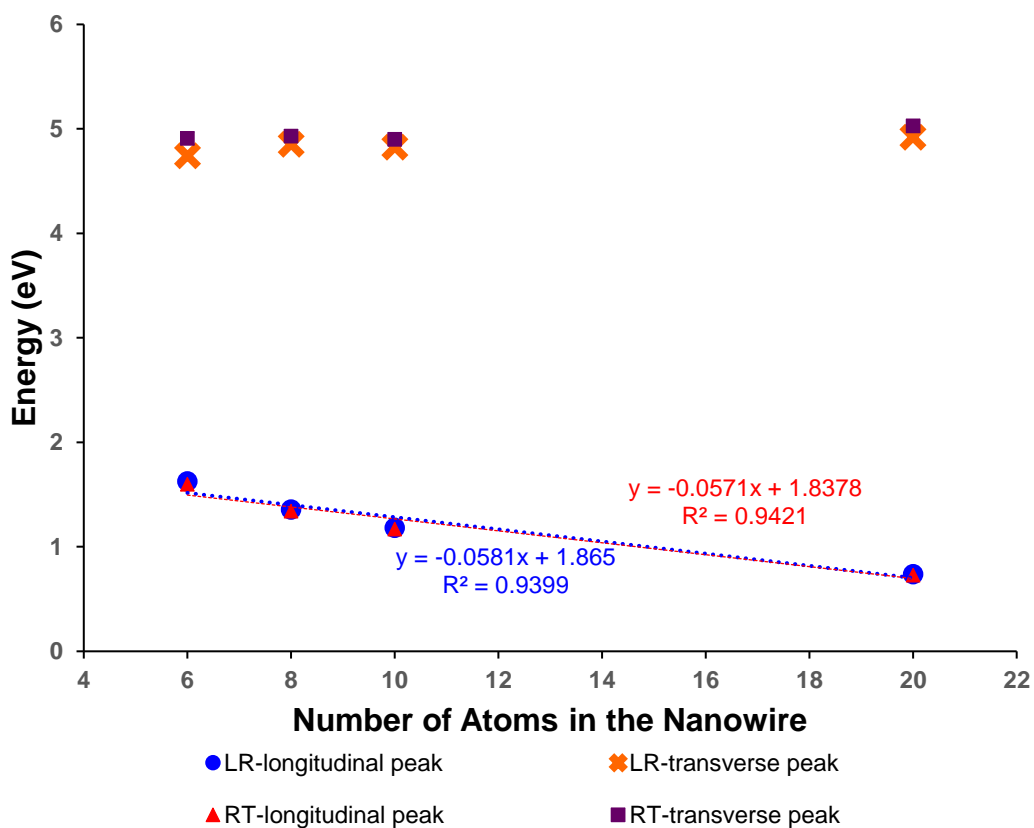

Figure 7.1 Longitudinal and transverse peak energies of Ag$_n$ (n = 6, 8, 10, 20) nanowires calculated with LR- and RT-TDDFT methods.
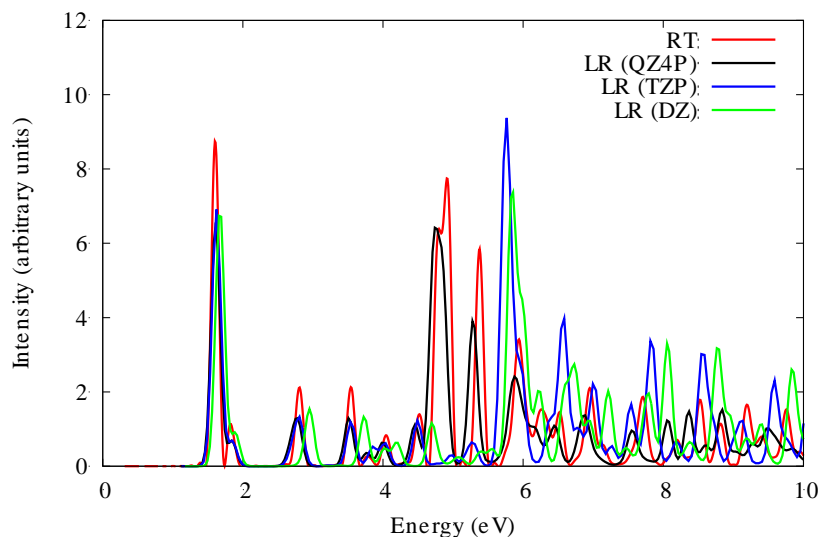
Figure 7.2 Basis set effect of LR-TDDFT calculations on the optical absorption spectrum of the Ag$_6$ nanowire.

7.4.1.2 Effect of Grid Spacing

Next, we consider the effects of changing parameters in the RT-TDDFT calculations to explore how each variable affects the optical absorption spectrum of the Ag$_6$ nanowire. First, we changed the spacing of the real-space grid. In real-space grid based techniques, a function f is represented by a set of point values $f_k \circ f(x_k)$, where x_k are the sampling points of the simulation domain. The separation between points or spacing is vital in this setting. If the given spacing value is too large the functions will not be represented well, whereas a very small value will increase the number of points and consequently increase memory use and computation time. Figure 7.3 demonstrates how the variation of the real-space grid spacing value affects the optical absorption spectrum of the Ag$_6$ nanowire. Overall, most of the LR spectral features are well reproduced in the RT spectra with different spacing values. However, the spectra calculated with 0.18 and 0.20 Å spacing agree with the LR spectrum better than the spectrum calculated with 0.23 Å spacing. The spectrum calculated with the 0.23 Å spacing does not contain the shoulder peak at ~4.5 eV, and the peak at ~5.3 eV appears as a doublet. Moreover, the intensity of the longitudinal and transverse peaks grows with the increasing spacing value, whereas the time required for each time-dependent simulation decreases. The results for 0.20 Å and 0.18 Å appear to be well-converged with respect to grid spacing.
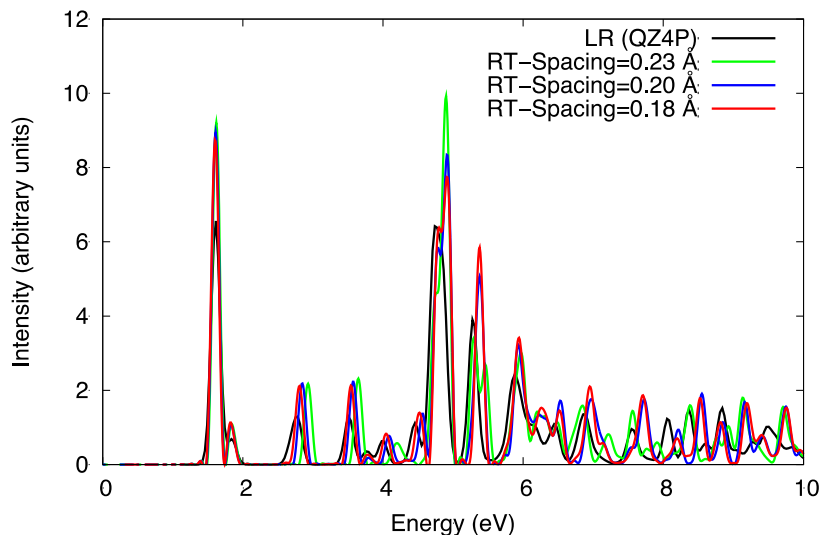
Figure 7.3 The effect of real-space grid spacing value on the RT-TDDFT optical absorption spectra of the Ag$_6$ nanowire.

7.4.1.3 Effect of Simulation Time

Next, we changed the propagation time of the time-dependent runs in order to demonstrate how the optical absorption spectra are affected. Figure 7.4 displays that increasing the total propagation time reduces the width of the peaks. In this method, the peak width is inversely proportional to the total propagation time and it is entirely artificial. However, the area under the peak specifies the oscillator strength of the transition. As shown in Figure 7.4, when the total propagation time is 13 fs the absorption peaks are broadened and the fine structure details disappear. The absorption spectrum obtained with a propagation time of 33 fs has a comparable peak width to the LR spectrum, which is artificially broadened by a Gaussian with a full width at half-maximum of 0.15 eV. A longer propagation time of 53 fs can resolve features such as the doublet near 4.6 eV. Understandably, a longer propagation time demands more computational resources. Therefore, it is important to select a reasonable value for this parameter so that the simulated peak widths provide sufficient detail to reproduce the experimental spectra.
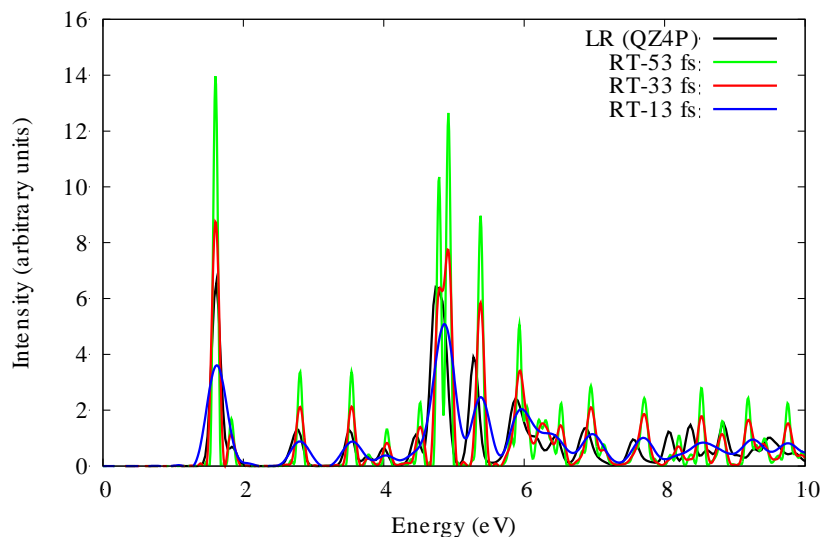
Figure 7.4 The effect of simulation time on the RT-TDDFT optical absorption spectra of the Ag$_6$ nanowire.

7.4.1.4 Effect of δ-kick Strength

In the most common approach to the RT-TDDFT method, the system is excited with an infinitesimal electric-field pulse and then the time-dependent Kohn-Sham equations are propagated for a certain time. The applied perturbation should be small to keep the response linear, yet sufficiently large to avoid numerical problems. We plotted the optical absorption spectra obtained with increasing electric field strengths by one order of magnitude (Figure 7.5). Figure 7.5 demonstrates that the spectra calculated with 0.001 and 0.01 Å^{-1} kick strengths have identical shapes and show the best agreement with the LR spectrum in terms of peak positions (up to ~7 eV). The strongest kick strength exhibits some differences in peak positions, which may be due to nonlinearities or to known problems with accuracy of RT-TDDFT methods.[80, 81] However, the longitudinal and transverse peaks of the Ag$_6$ nanowire are predicted well with all three field strengths examined here. The required computation time was minimized with smaller kick strengths, whereas the calculation with the 0.1 Å^{-1} kick strength took ~10% more computation time. The energy convergence at each time step took slightly longer with the highest kick strength.
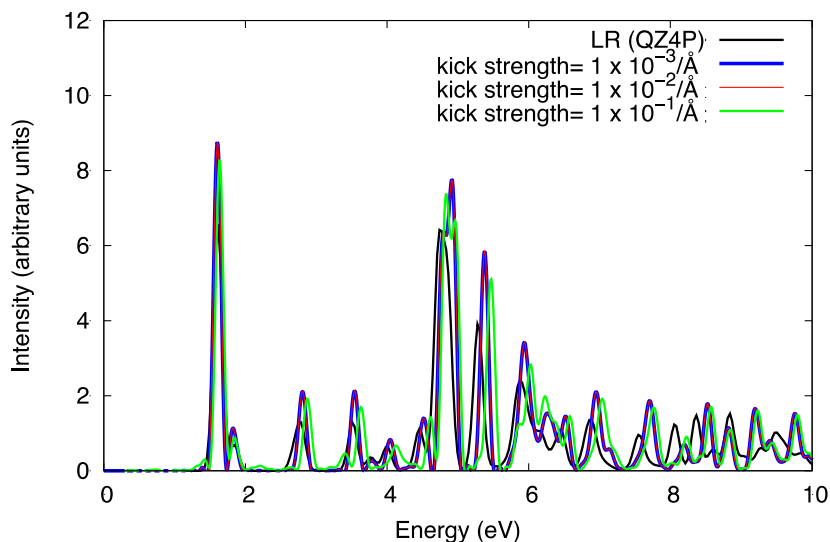
Figure 7.5 The effect of applied δ-kick strength on the optical absorption spectra of the Ag$_6$ nanowire.

7.4.1.5 Analysis using Time-Dependent Electron Densities

A surface plasmon resonance is a collective oscillation of confined free electrons of a nanoparticle upon excitation by an electromagnetic wave. A strong peak in the optical absorption spectrum is characteristic of plasmonic excitation. Transition densities calculated using the ADF package have previously been plotted for the longitudinal and transverse plasmon modes of the Ag$_6$ nanowire using the LR method.[38] Unlike the LR method, the RT method does not directly provide insight into the orbitals involved in each excitation. However, in the RT approach, the isosurfaces of time-dependent density can show the collective charge oscillation that corresponds to plasmon modes.[51] At the beginning of a time evolution calculation, a $\delta(t)$ perturbation excites all possible frequencies. Energy is absorbed at particular excitation energies and stored in corresponding modes. If the absorption spectrum consists of a strong absorption peak, which corresponds to a surface plasmon resonance, that mode dominates the charge oscillations. When a perturbation is applied along the long axis (z-direction) of the Ag$_6$ nanowire, the time-dependent dipole moment shows an approximate periodicity due to the dominating longitudinal SPR mode. Figure 7.6 shows isosurfaces of the time-dependent density pictured at two maximal polarization moments and at two moments of zero polarization. Since the oscillations are small compared to the density itself, the difference between the time-dependent density and the ground state density is shown. Snapshots (a) and (c) in Figure 7.6 show a strong coherent oscillation of

valence electrons over the full length of the Ag_6 nanowire indicating a longitudinal dipolar plasmon. These areas of increased/decreased electron density are important because they lead to enhanced local electric fields at the ends of the nanowires, which are critical for practical applications.
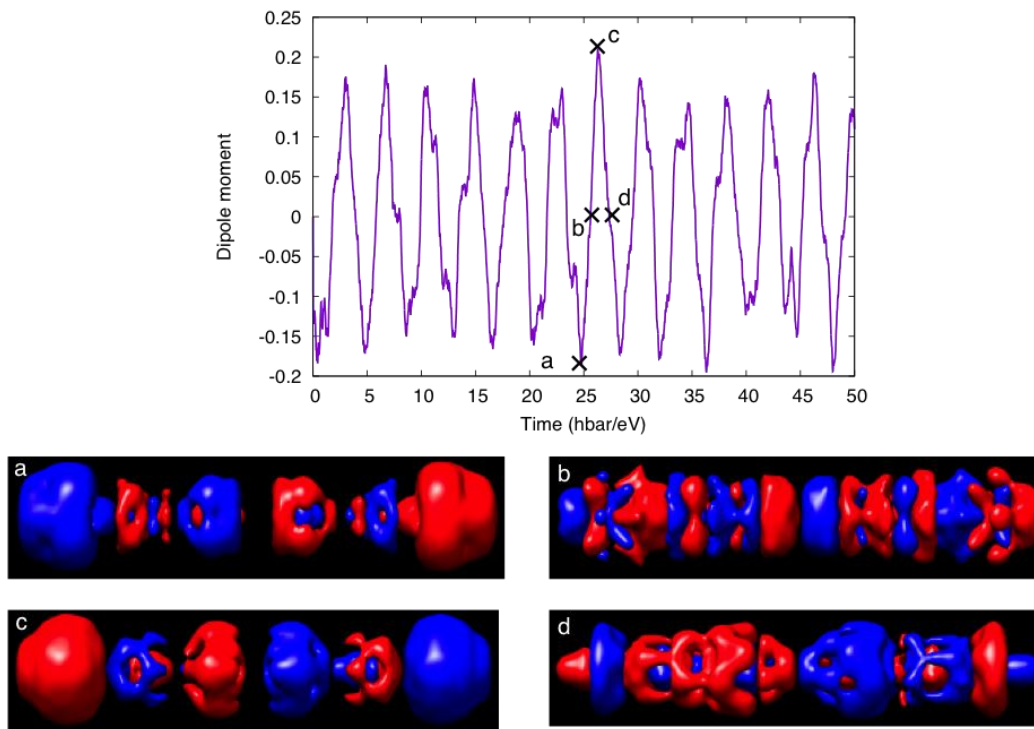

Figure 7.6 Oscillation of charge density along the long axis of the Ag_6 nanowire. The four snapshots (a, b, c, d) are taken at times of opposite maximal polarization (a, c) and at two consecutive times of zero polarization (b, d) as indicated on the time-dependent dipole moment plots. Red and blue indicate negative and positive differences, respectively.

7.4.2 Au nanowires

In gold nanowires, transitions originating from the d-band are important.[35] These transitions significantly affect the longitudinal and transverse peak energies and intensities unlike in silver nanowires. Since the HOMO-LUMO transition and the d-based transitions have the same symmetry, they couple and this causes a splitting of the longitudinal peak. However, as the nanowire grows, the energy difference between d-based transitions and the sp-based HOMO-LUMO longitudinal peak increases, reaching about 1 eV for the Au_{20} nanowire.[35] In contrast to silver nanowires, a transverse peak cannot be distinguished in gold nanowires; instead, a broad band that begins about 4 eV can be observed. As shown in Figure 7.7, the absorption spectra

calculated for Au$_n$ (*n*= 6, 8, 10, 20) nanowires using LR and RT methods agree reasonably well. The LR transitions are calculated only up to 8 eV for the Au$_{20}$ nanowire due to computational limitations; RT methods have the advantage of providing spectra over a much wider range. The RT and LR spectra agree well in the 0-8 eV energy region for these systems.
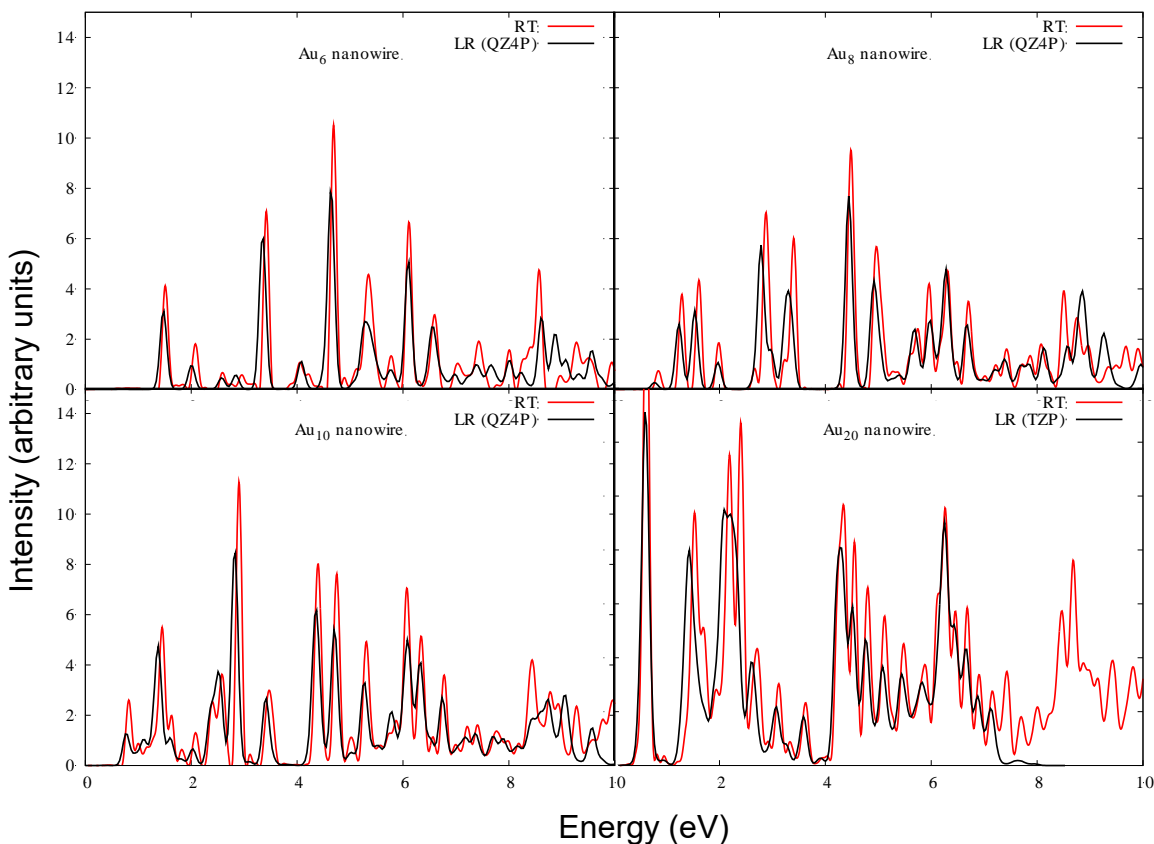

Figure 7.7 Comparison of absorption spectra calculated for Au$_n$ (*n*= 6, 8, 10, 20) nanowires using LR and RT methods.

To verify that both methods accurately predict the transitions along the long axis of gold nanowires, in Figure 7.8a we plot the transitions with Σ_u^+ symmetry (longitudinal direction) for the Au$_6$ nanowire from the LR calculation and the dipole strength function when a delta-kick is applied in the z-direction from the RT calculation. Similarly, Figure 7.8b shows the transitions with Π_u symmetry from the LR calculation and the dipole strength function from the RT calculation when a delta-kick is applied in the x-direction, which represents the transverse peak. In Figure 8a, the spectra calculated using the two methods converge well up to 6 eV, whereas the higher energy peaks agree to a lesser extent. The LR and RT transverse absorption spectra

(Figure 7.8b) are consistent in the 5-10 eV energy region. A good agreement between the RT and LR approaches can be observed in the full spectra of Au_n (n= 6, 8, 10, 20) nanowires as well as in longitudinal and transverse spectra of the Au_6 nanowire.
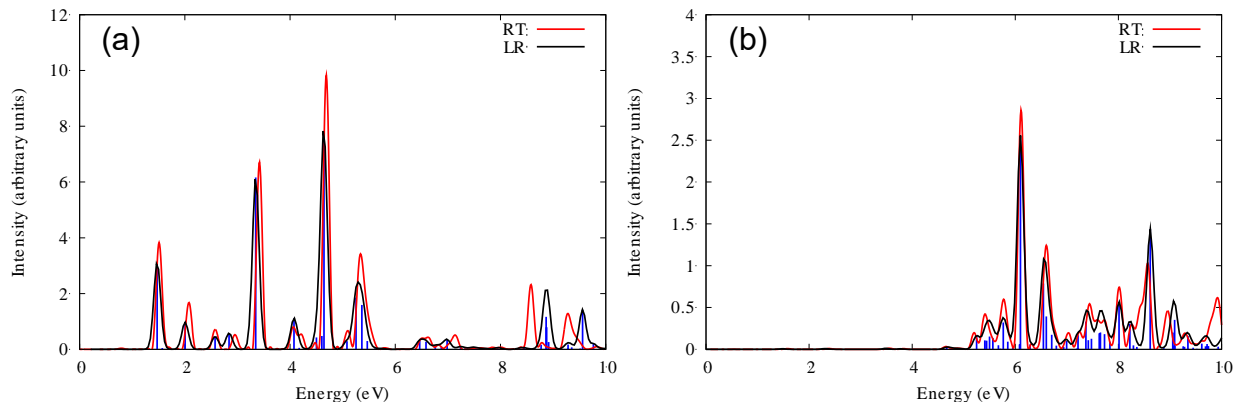

Figure 7.8 Comparison of RT and LR-TDDFT calculated absorption spectra of the Au₆ nanowire for (a) longitudinal and (b) transverse peaks. The strength function [$S(W)$] values calculated in RT simulations are divided by a factor of three to compare with the LR spectra.

7.4.3 Tetrahedra

The optical properties of silver tetrahedra have been theoretically studied using LR-TDDFT.[34, 82] Previous LR-TDDFT calculations on a tetrahedral Ag_{20} cluster predicted a single sharp peak in the 3-4 eV energy region that depends on the level of theory used.[34, 82] This prominent peak was found to originate from a collective sp ← sp intraband transition in analogy to a localized surface plasmon resonance.[34] Figure 7.9 demonstrates that the optical absorption spectra calculated using LR and RT methods for Ag_{20}, Ag_{10}^{2+}, and Ag_8 tetrahedral clusters are dominated by a sharp peak, which slightly blue shifts with the reduced size of the cluster. The LR and RT spectra have identical shapes up to ~8 eV with marginal deviations in peak positions.

Contrary to the Ag_{20} tetrahedron, the Au_{20} tetrahedral cluster shows a collection of weak peaks. However, the Au_8 and Au_{10}^{2+} clusters show prominent peaks around 6.5 and 7.5 eV, respectively. For the Ag_{20} and Au_{20} systems, LR spectra are calculated only up to 8 eV and for Au_{20}, the density was converged to 8×10^{-7} instead of the usual 1×10^{-8}. Both LR and RT methods produce similar optical absorption spectra with slight deviations of peak positions towards the higher end of the spectra.
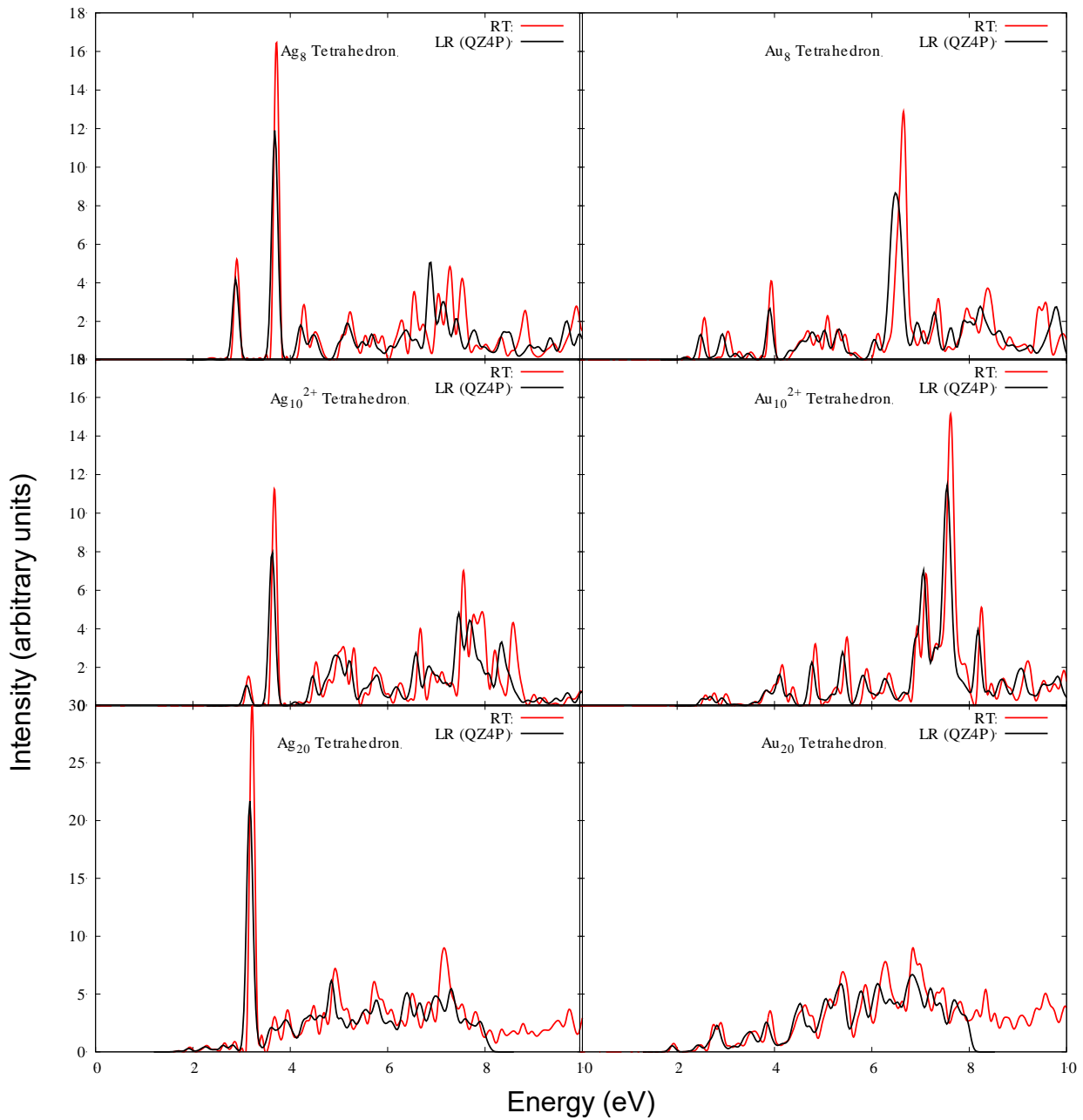
Figure 7.9 Comparison of absorption spectra calculated for M₈, M₁₀²⁺, and M₂₀ (M=Ag, Au) tetrahedra using LR and RT methods.

7.4.4 Octahedra

The truncated octahedral Ag_{13}/Au_{13} cluster has been modeled by removing the six vertex atoms from the octahedral Ag_{19}/Au_{19} cluster.[37] $Ag_{13}{}^{5+}$ and $Au_{13}{}^{5+}$ are magic numbered clusters that have 8 valence electrons. Bae and Aikens studied the optical properties of the octahedral $Au_{13}{}^{5+}$ cluster and assigned the first peak to a HOMO→LUMO (P → D) intraband transition and higher energy peaks to d → sp interband transitions.[37] Examining orbital contributions for $Ag_{13}{}^{5+}$ revealed that similar transitions are responsible for its optical absorption spectrum.[79] The LR and RT calculated absorption spectra for octahedral $Ag_{13}{}^{5+}$ and $Au_{13}{}^{5+}$ clusters are shown in Figure 7.10 and both spectra contain prominent peaks above 7 eV. Analogously to the other silver and gold systems discussed in previous sections, the LR and RT spectra are in good agreement even up to 10 eV with a slight deviation of the RT spectrum to higher energy. Factors such as the differences in grid-based vs. atom-centered basis set, method for inclusion of relativistic effects, etc. between the two types of calculations could be responsible for these slight differences; however, overall the two approaches agree very well.
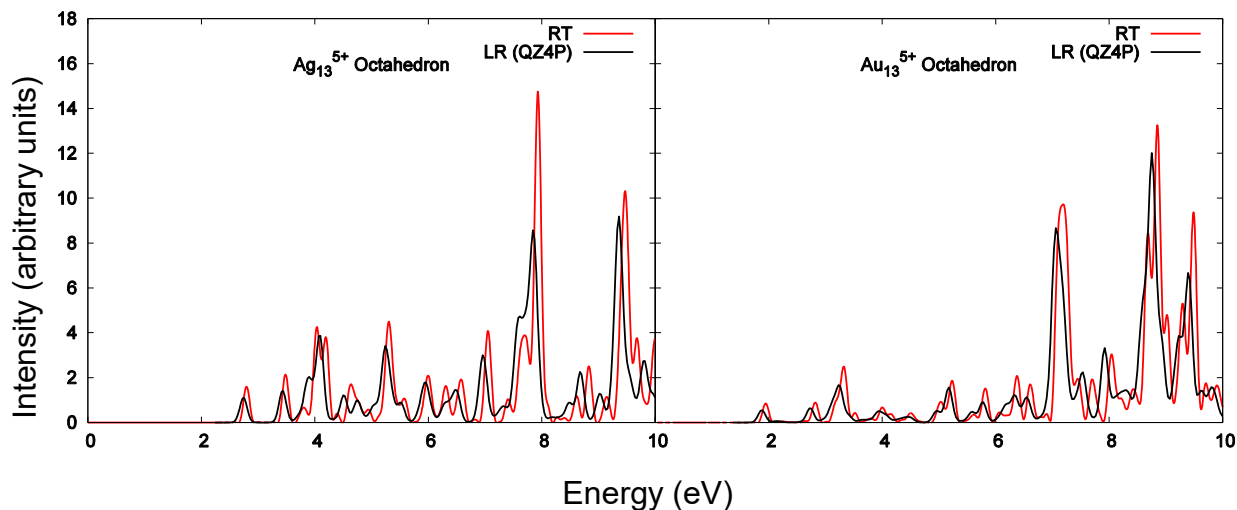

Figure 7.10 Comparison of RT and LR-TDDFT calculated absorption spectra of octahedral clusters (a) $Ag_{13}{}^{5+}$ and (b) $Au_{13}{}^{5+}$.

7.4.5 Icosahedra

Icosahedral clusters are more spherical than the octahedral shapes. The smallest icosahedral clusters are Ag_{13}^{5+} and Au_{13}^{5+}, which have been optimized using D_{5d} symmetry.[36, 37] Dipole allowed irreducible representations of this symmetry are A_{2u} and E_{1u}. Since the symmetry was lowered from I_h to D_{5d}, each peak appears as two degenerate peaks due to splitting. Bae and Aikens reported that the prominent peaks of the Ag_{13}^{5+} and Au_{13}^{5+} clusters arise from intraband and interband transitions in the 0-6 eV energy region.[36, 37] Figure 7.11 shows that the LR and RT spectra are consistent for both silver and gold 13-atom icosahedral structures for a broad range of energy (2-10 eV). Similar to the results for the octahedral systems, strong absorption features can be observed at the higher energy end of the spectra of icosahedral clusters.
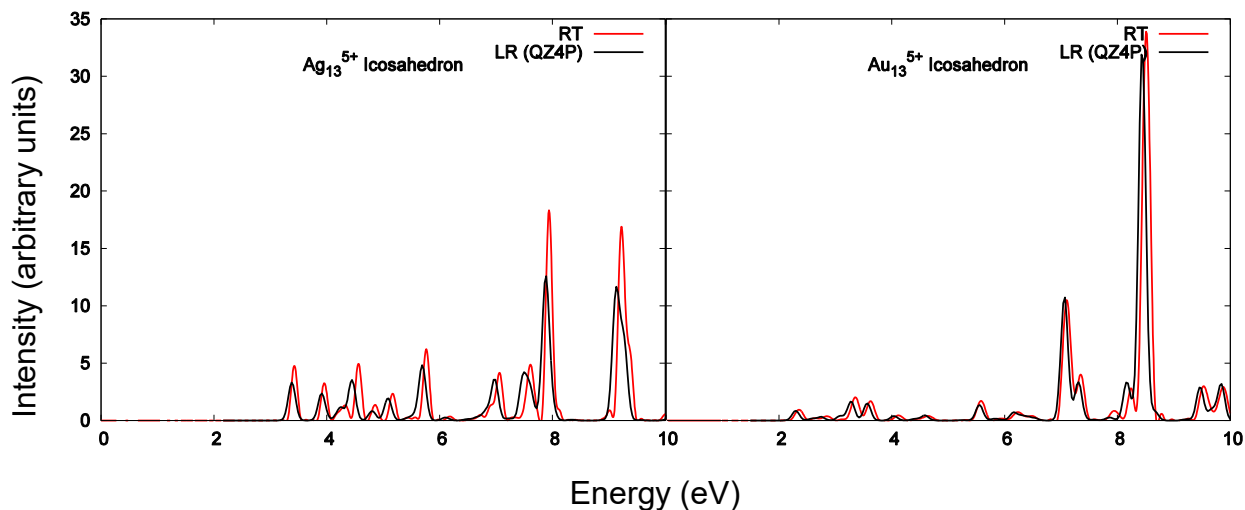

Figure 7.11 Comparison of RT and LR-TDDFT calculated absorption spectra of icosahedral clusters of (a) Ag_{13}^{5+} and (b) Au_{13}^{5+}.

7.5 Conclusions

In this systematic benchmark study, we demonstrate the consistency of LR and RT methods for calculating the optical absorption spectra of distinct noble metal nanoclusters. The RT approach is very useful in calculating wide absorption spectra even up to 20 eV, which is unfeasible with the LR approach. Our calculations reveal that the RT spectrum obtained using a grid-based basis set with pseudopotentials achieves results in good agreement with the LR

spectrum obtained with large QZ4P atom-centered basis sets. RT-TDDFT calculations require more computation time compared to LR-TDDFT for smaller systems like the Ag_6 nanowire; however, a crossover will occur as the system size increases. The RT method can be more effective when calculating wide absorption spectra of larger systems like the Au_{20} nanowire. The RT approach does not directly provide insight into the orbitals involved in excitations unlike the traditional LR-TDDFT method. However, real-time variation of the electron density can be visualized to show the collective oscillation of electron density at the plasmon modes of noble metal nanoparticles.

7.6 Acknowledgements

7.7 References

1.   Sun, Y., Conversion of Ag Nanowires to AgCl Nanowires Decorated with Au Nanoparticles and Their Photocatalytic Activity. *J. Phys. Chem. C* **2010**, *114*, 2127-2133.
2.   Rashid, M. H.; Bhattacharjee, R. R.; Kotal, A.; Mandal, T. K., Synthesis of Spongy Gold Nanocrystals with Pronounced Catalytic Activities. *Langmuir* **2006**, *22*, 7141-7143.
3.   Chen, Y.-S.; Choi, H.; Kamat, P. V., Metal-Cluster-Sensitized Solar Cells. A New Class of Thiolated Gold Sensitizers Delivering Efficiency Greater Than 2%. *J. Am. Chem. Soc.* **2013**, *135*, 8822-8825.
4.   Hirakawa, T.; Kamat, P. V., Photoinduced Electron Storage and Surface Plasmon Modulation in $Ag@TiO_2$ Clusters. *Langmuir* **2004**, *20*, 5645-5647.
5.   Jiang, S.; Win, K. Y.; Liu, S.; Teng, C. P.; Zheng, Y.; Han, M.-Y., Surface-Functionalized Nanoparticles for Biosensing and Imaging-Guided Therapeutics. *Nanoscale* **2013**, *5*, 3127-3148.
6.   Mahmoud, M. A.; El-Sayed, M. A., Different Plasmon Sensing Behavior of Silver and Gold Nanorods. *J. Phys. Chem. Lett.* **2013**, *4*, 1541-1545.
7.   Saha, K.; Agasti, S. S.; Kim, C.; Li, X.; Rotello, V. M., Gold Nanoparticles in Chemical and Biological Sensing. *Chem. Rev.* **2012**, *112*, 2739-2779.

8.   Arvizo, R. R.; Bhattacharyya, S.; Kudgus, R. A.; Giri, K.; Bhattacharya, R.; Mukherjee, P., Intrinsic Therapeutic Applications of Noble Metal Nanoparticles: Past, Present and Future. *Chem. Soc. Rev.* **2012**, *41*, 2943-2970.

9.   Zhou, W.; Gao, X.; Liu, D.; Chen, X., Gold Nanoparticles for In Vitro Diagnostics. *Chem. Rev.* **2015**, *115*, 10575-10636.

10.   Kelly, K. L.; Coronado, E.; Zhao, L. L.; Schatz, G. C., The Optical Properties of Metal Nanoparticles: The Influence of Size, Shape, and Dielectric Environment. *J. Phys. Chem. B* **2003**, *107*, 668-677.

11.   Burda, C.; Chen, X.; Narayanan, R.; El-Sayed, M. A., Chemistry and Properties of Nanocrystals of Different Shapes. *Chem. Rev.* **2005**, *105*, 1025-1102.

12.   Liz-Marzán, L. M., Tailoring Surface Plasmons through the Morphology and Assembly of Metal Nanoparticles. *Langmuir* **2006**, *22*, 32-41.

13.   Fernanda Cardinal, M.; Rodríguez-González, B.; Alvarez-Puebla, R. A.; Pérez-Juste, J.; Liz-Marzán, L. M., Modulation of Localized Surface Plasmons and SERS Response in Gold Dumbbells through Silver Coating. *J. Phys. Chem. C* **2010**, *114*, 10417-10423.

14.   Link, S.; Wang, Z. L.; El-Sayed, M. A., Alloy Formation of Gold−Silver Nanoparticles and the Dependence of the Plasmon Absorption on Their Composition. *J. Phys. Chem. B* **1999**, *103*, 3529-3533.

15.   Link, S.; Mohamed, M. B.; El-Sayed, M. A., Simulation of the Optical Absorption Spectra of Gold Nanorods as a Function of Their Aspect Ratio and the Effect of the Medium Dielectric Constant. *J. Phys. Chem. B* **1999**, *103*, 3073-3077.

16.   Szymańska-Chargot, M.; Gruszecka, A.; Smolira, A.; Bederski, K.; Głuch, K.; Cytawa, J.; Michalak, L., Formation of Nanoparticles and Nanorods via UV Irradiation of $AgNO_3$ Solutions. *J. Alloys Compd.* **2009**, *486*, 66-69.

17.   Wiley, B. J.; Chen, Y.; McLellan, J. M.; Xiong, Y.; Li, Z.-Y.; Ginger, D.; Xia, Y., Synthesis and Optical Properties of Silver Nanobars and Nanorice. *Nano Lett.* **2007**, *7*, 1032-1036.

18.   Sun, Y.; Gates, B.; Mayers, B.; Xia, Y., Crystalline Silver Nanowires by Soft Solution Processing. *Nano Lett.* **2002**, *2*, 165-168.

19.   Wei, H.; Hao, F.; Huang, Y.; Wang, W.; Nordlander, P.; Xu, H., Polarization Dependence of Surface-Enhanced Raman Scattering in Gold Nanoparticle−Nanowire Systems. *Nano Lett.* **2008**, *8*, 2497-2502.

20.   Seo, D.; Park, J. C.; Song, H., Polyhedral Gold Nanocrystals with O_h Symmetry: From Octahedra to Cubes. *J. Am. Chem. Soc.* **2006**, *128*, 14863-14870.

21.   Im, S. H.; Lee, Y. T.; Wiley, B.; Xia, Y., Large-Scale Synthesis of Silver Nanocubes: The Role of HCl in Promoting Cube Perfection and Monodispersity. *Angew. Chem., Int. Ed.* **2005**, *44*, 2154-2157.

22.   Eguchi, M.; Mitsui, D.; Wu, H.-L.; Sato, R.; Teranishi, T., Simple Reductant Concentration-Dependent Shape Control of Polyhedral Gold Nanoparticles and Their Plasmonic Properties. *Langmuir* **2012**, *28*, 9021-9026.

23.   Kim, F.; Connor, S.; Song, H.; Kuykendall, T.; Yang, P., Platonic Gold Nanocrystals. *Angew. Chem.* **2004**, *116*, 3759-3763.

24.   Jin, R.; Cao, Y.; Mirkin, C. A.; Kelly, K. L.; Schatz, G. C.; Zheng, J. G., Photoinduced Conversion of Silver Nanospheres to Nanoprisms. *Science* **2001**, *294*, 1901-1903.

25.   Millstone, J. E.; Park, S.; Shuford, K. L.; Qin, L.; Schatz, G. C.; Mirkin, C. A., Observation of a Quadrupole Plasmon Mode for a Colloidal Solution of Gold Nanoprisms. *J. Am. Chem. Soc.* **2005**, *127*, 5312-5313.

26.   Mie, G., Beiträge zur Optik trüber Medien, speziell kolloidaler Metallösungen. *Ann. Phys.* **1908**, *330*, 377-445.

27.   Gedney, S. D., Introduction to the Finite-Difference Time-Domain (FDTD) Method for Electromagnetics. *Synthesis Lectures on Computational Electromagnetics* **2011**, *6*, 1-250.

28.   Draine, B. T.; Flatau, P. J., Discrete-Dipole Approximation For Scattering Calculations. *J. Opt. Soc. Am. A* **1994**, *11*, 1491-1499.

29.   Oubre, C.; Nordlander, P., Optical Properties of Metallodielectric Nanostructures Calculated Using the Finite Difference Time Domain Method. *J. Phys. Chem. B* **2004**, *108*, 17740-17747.

30.   González, A. L.; Reyes-Esqueda, J. A.; Noguez, C., Optical Properties of Elongated Noble Metal Nanoparticles. *J. Phys. Chem. C* **2008**, *112*, 7356-7362.

31.   Brioude, A.; Pileni, M. P., Silver Nanodisks: Optical Properties Study Using the Discrete Dipole Approximation Method. *J. Phys. Chem. B* **2005**, *109*, 23371-23377.

32.   Wu, Y.; Nordlander, P., Finite-Difference Time-Domain Modeling of the Optical Properties of Nanoparticles near Dielectric Substrates. *J. Phys. Chem. C* **2010**, *114*, 7302-7307.

33.   Fernando, A.; Weerawardene, K. L. D. M.; Karimova, N. V.; Aikens, C. M., Quantum Mechanical Studies of Large Metal, Metal Oxide, and Metal Chalcogenide Nanoparticles and Clusters. *Chem. Rev.* **2015**, *115*, 6112-6216.

34.   Aikens, C. M.; Li, S.; Schatz, G. C., From Discrete Electronic States to Plasmons: TDDFT Optical Absorption Properties of Ag_n (n = 10, 20, 35, 56, 84, 120) Tetrahedral Clusters. *J. Phys. Chem. C* **2008**, *112*, 11272-11279.

35.   Guidez, E. B.; Aikens, C. M., Theoretical Analysis of the Optical Excitation Spectra of Silver and Gold Nanowires. *Nanoscale* **2012**, *4*, 4190-4198.

36.   Bae, G.-T.; Aikens, C. M., Time-Dependent Density Functional Theory Studies of Optical Properties of Ag Nanoparticles: Octahedra, Truncated Octahedra, and Icosahedra. *J. Phys. Chem. C* **2012**, *116*, 10356-10367.

37.   Bae, G.-T.; Aikens, C. M., Time-Dependent Density Functional Theory Studies of Optical Properties of Au Nanoparticles: Octahedra, Truncated Octahedra, and Icosahedra. *J. Phys. Chem. C* **2015**, *119*, 23127-23137.

38.   Guidez, E. B.; Aikens, C. M., Quantum Mechanical Origin of the Plasmon: Fom Molecular Systems to Nanoparticles. *Nanoscale* **2014**, *6*, 11512-11527.

39.   Johnson, H. E.; Aikens, C. M., Electronic Structure and TDDFT Optical Absorption Spectra of Silver Nanorods. *J. Phys. Chem. A* **2009**, *113*, 4445-4450.

40.   Liao, M.-S.; Bonifassi, P.; Leszczynski, J.; Ray, P. C.; Huang, M.-J.; Watts, J. D., Structure, Bonding, and Linear Optical Properties of a Series of Silver and Gold Nanorod Clusters: DFT/TDDFT Studies. *J. Phys. Chem. A* **2010**, *114*, 12701-12708.

41.   Casida, M. E.; Jamorski, C.; Casida, K. C.; Salahub, D. R., Molecular Excitation Energies to High-Lying Bound States from Time-Dependent Density-Functional Response Theory: Characterization and   Correction of the Time-Dependent Local Density Approximation Ionization Threshold. *J. Chem. Phys.* **1998**, *108*, 4439-4449.

42.	Castro, A.; Appel, H.; Oliveira, M.; Rozzi, C. A.; Andrade, X.; Lorenzen, F.; Marques, M. A. L.; Gross, E. K. U.; Rubio, A., Octopus: A Tool for the Application of Time-Dependent Density Functional Theory. *phys. stat. sol. (b)* **2006**, *243*, 2465-2488.

43.	Meng, S.; Kaxiras, E., Real-Time, Local Basis-Set Implementation of Time-Dependent Density Functional Theory for Excited State Dynamics Simulations. *J. Chem. Phys.* **2008**, *129*, 054110.

44.	Baer, R.; Neuhauser, D., Real-Time Linear Response for Time-Dependent Density-Functional Theory. *J. Chem. Phys.* **2004**, *121*, 9803-9807.

45.	Yabana, K.; Bertsch, G. F., Time-Dependent Local-Density Approximation in Real Time. *Phys. Rev. B* **1996**, *54*, 4484-4487.

46.	Lopata, K.; Govind, N., Modeling Fast Electron Dynamics with Real-Time Time-Dependent Density Functional Theory: Application to Small Molecules and Chromophores. *J. Chem. Theory Comput.* **2011**, *7*, 1344-1355.

47.	Tussupbayev, S.; Govind, N.; Lopata, K.; Cramer, C. J., Comparison of Real-Time and Linear-Response Time-Dependent Density Functional Theories for Molecular Chromophores Ranging from Sparse to High Densities of States. *J. Chem. Theory Comput.* **2015**, *11*, 1102-1109.

48.	Sun, J.; Song, J.; Zhao, Y.; Liang, W.-Z., Real-Time Propagation of the Reduced One-Electron Density Matrix in Atom-Centered Gaussian Orbitals: Application to Absorption Spectra of Silicon Clusters. *J. Chem. Phys.* **2007**, *127*, 234107.

49.	Gao, B.; Ruud, K.; Luo, Y., Plasmon Resonances in Linear Noble-Metal Chains. *J. Chem. Phys.* **2012**, *137*, 194307.

50.	Ding, F.; Guidez, E. B.; Aikens, C. M.; Li, X., Quantum Coherent Plasmon in Silver Nanowires: A Real-Time TDDFT Study. *J. Chem. Phys.* **2014**, *140*, 244705.

51.	Weissker, H.-C.; Lopez-Lozano, X., Surface Plasmons in Quantum-Sized Noble-Metal Clusters: TDDFT Quantum Calculations and the Classical Picture of Charge Oscillations. *Phys. Chem. Chem. Phys.* **2015**, *17*, 28379-28386.

52.	Lopez-Lozano, X.; Barron, H.; Mottet, C.; Weissker, H.-C., Aspect-Ratio- and Size-Dependent Emergence of the Surface-Plasmon Resonance in Gold Nanorods - an *ab initio* TDDFT study. *Phys. Chem. Chem. Phys.* **2014**, *16*, 1820-1823.

53.	Townsend, E.; Bryant, G. W., Plasmonic Properties of Metallic Nanoparticles: The Effects of Size Quantization. *Nano Lett.* **2012**, *12*, 429-434.

54.	Iida, K.; Noda, M.; Ishimura, K.; Nobusada, K., First-Principles Computational Visualization of Localized Surface Plasmon Resonance in Gold Nanoclusters. *J. Phys. Chem. A* **2014**, *118*, 11317-11322.

55.	Peng, B.; Lingerfelt, D. B.; Ding, F.; Aikens, C. M.; Li, X., Real-Time TDDFT Studies of Exciton Decay and Transfer in Silver Nanowire Arrays. *J. Phys. Chem. C* **2015**, *119*, 6421-6427.

56.	Ma, J.; Wang, Z.; Wang, L.-W., Interplay between plasmon and single-particle excitations in a metal nanocluster. *Nat. Commun.* **2015**, *6*, 10107.

57.	Yan, L.; Wang, F.; Meng, S., Quantum Mode Selectivity of Plasmon-Induced Water Splitting on Gold Nanoparticles. *ACS Nano* **2016**, *10*, 5452-5458.

58.	Lee, K.-M.; Yabana, K.; Bertsch, G. F., Magnetic Circular Dichroism in Real-Time Time-Dependent Density Functional Theory. *J. Chem. Phys.* **2011**, *134*, 144106.

59.	Cheng, C.-L.; Evans, J. S.; Van Voorhis, T., Simulating Molecular Conductance Using Real-Time Density Functional Theory. *Phys. Rev. B* **2006**, *74*, 155112.

60.   Evans, J. S.; Voorhis, T. V., Dynamic Current Suppression and Gate Voltage Response in Metal−Molecule−Metal Junctions. *Nano Lett.* **2009**, *9*, 2671-2675.

61.   Nobusada, K.; Yabana, K., Photoinduced Electric Currents in Ring-Shaped Molecules by Circularly Polarized Laser Pulses. *Phys. Rev. A* **2007**, *75*, 032518.

62.   Chapman, C. T.; Liang, W.; Li, X., Ultrafast Coherent Electron–Hole Separation Dynamics in a Fullerene Derivative. *J. Phys. Chem. Lett.* **2011**, *2*, 1189-1192.

63.   Ding, F.; Chapman, C. T.; Liang, W.; Li, X., Mechanisms of Bridge-Mediated Electron Transfer: A TDDFT Electronic Dynamics Study. *J. Chem. Phys.* **2012**, *137*, 22A512.

64.   Andrade, X.; Strubbe, D.; De Giovannini, U.; Larsen, A. H.; Oliveira, M. J. T.; Alberdi-Rodriguez, J.; Varas, A.; Theophilou, I.; Helbig, N.; Verstraete, M. J.; Stella, L.; Nogueira, F.; Aspuru-Guzik, A.; Castro, A.; Marques, M. A. L.; Rubio, A., Real-Space Grids and the Octopus Code as Tools for the Development of New Simulation Approaches for Electronic Systems. *Phys. Chem. Chem. Phys.* **2015**, *17*, 31371-31396.

65.   Perdew, J. P., Accurate Density Functional for the Energy: Real-Space Cutoff of the Gradient Expansion for the Exchange Hole. *Phys. Rev. Lett.* **1985**, *55*, 1665-1668.

66.   Perdew, J. P.; Yue, W., Accurate and Simple Density Functional for the Electronic Exchange Energy: Generalized Gradient Approximation. *Phy. Rev. B* **1986**, *33*, 8800-8802.

67.   Becke, A. D., Density‐Functional Thermochemistry. I. The Effect of the Exchange‐only Gradient Correction. *J. Chem. Phys.* **1992**, *96*, 2155-2160.

68.   Perdew, J. P.; Burke, K.; Ernzerhof, M., Generalized Gradient Approximation Made Simple. *Phys. Rev. Lett.* **1996**, *77*, 3865-3868.

69.   Troullier, N.; Martins, J. L., Efficient Pseudopotentials for Plane-Wave Calculations. *Phys. Rev. B* **1991**, *43*, 1993-2006.

70.   Aikens, C. M., Effects of Core Distances, Solvent, Ligand, and Level of Theory on the TDDFT Optical Absorption Spectrum of the Thiolate-Protected Au_{25} Nanoparticle. *J. Phys. Chem. A* **2009**, *113*, 10811-10817.

71.   Weissker, H. C.; Escobar, H. B.; Thanthirige, V. D.; Kwak, K.; Lee, D.; Ramakrishna, G.; Whetten, R. L.; López-Lozano, X., Information on Quantum States Pervades the Visible Spectrum of the Ubiquitous $Au_{144}(SR)_{60}$ Gold Nanocluster. *Nat. Commun.* **2014**, *5*, 3785.

72.   Weerawardene, K. L. D. M.; Aikens, C. M., Effect of Aliphatic versus Aromatic Ligands on the Structure and Optical Absorption of $Au_{20}(SR)_{16}$. *J. Phys. Chem. C* **2016**, *120*, 8354-8363.

73.   Negishi, Y.; Nakazaki, T.; Malola, S.; Takano, S.; Niihori, Y.; Kurashige, W.; Yamazoe, S.; Tsukuda, T.; Häkkinen, H., A Critical Size for Emergence of Nonbulk Electronic and Geometric Structures in Dodecanethiolate-Protected Au Clusters. *J. Am. Chem. Soc.* **2015**, *137*, 1206-1212.

74.   Yang, H.; Wang, Y.; Huang, H.; Gell, L.; Lehtovaara, L.; Malola, S.; Häkkinen, H.; Zheng, N., All-Thiol-Stabilized Ag_{44} and $Au_{12}Ag_{32}$ Nanoparticles with Single-Crystal Structures. *Nat. Commun.* **2013**, *4*, 2422.

75.   Marques, M. A. L.; Castro, A.; Bertsch, G. F.; Rubio, A., Octopus: A First-Principles Tool for Excited Electron–Ion Dynamics. *Comput. Phys. Commun.* **2003**, *151*, 60-78.

76.   Castro, A.; Marques, M. A. L.; Rubio, A., Propagators for the Time-Dependent Kohn–Sham Equations. *J. Chem. Phys.* **2004**, *121*, 3425-3433.

77.   te Velde, G.; Bickelhaupt, F. M.; Baerends, E. J.; Fonseca Guerra, C.; van Gisbergen, S. J. A.; Snijders, J. G.; Ziegler, T., Chemistry with ADF. *J. Comput. Chem.* **2001**, *22*, 931-967.

78.   Lenthe, E. v.; Baerends, E. J.; Snijders, J. G., Relativistic Regular Two‐Component Hamiltonians. *J. Chem. Phys.* **1993**, *99*, 4597-4610.

79.   Bae, G.-T.; Aikens, C. M., TDDFT and CIS Studies of Optical Properties of Dimers of Silver Tetrahedra. *J. Phys. Chem. A* **2012**, *116*, 8260-8269.

80.   Provorse, M. R.; Habenicht, B. F.; Isborn, C. M., Peak-Shifting in Real-Time Time-Dependent Density Functional Theory. *J. Chem. Theory Comput.* **2015**, *11*, 4791-4802.

81.   Provorse, M. R.; Isborn, C. M., Electron Dynamics with Real-Time Time-Dependent Density Functional Theory. *Int. J. Quantum Chem.* **2016**, *116*, 739-749.

82.   Zhao; Jensen, L.; Schatz, G. C., Pyridine−Ag_{20} Cluster: A Model System for Studying Surface-Enhanced Raman Scattering. *J. Am. Chem. Soc.* **2006**, *128*, 2911-2919.

Chapter 8 - Conclusions

Ligand protected gold and silver nanoclusters with a core diameter less than 2 nm possess remarkable optical and luminescence properties. Despite extensive experimental investigations, the origin of these properties is still unknown. Theoretical calculations can provide useful electronic level details of these systems. While luminescent metal nanoclusters have emerged as a new class of metal nanostructures with enhanced quantum yields, their underlying photoluminescence mechanisms still remain unclear. We performed DFT and TDDFT calculations on selected thiolate-protected gold and silver nanoclusters to provide insights into the origin of their photoluminescence.

$Au_{25}(SR)_{18}{}^-$ is one of the earliest crystallographically-resolved thiolate-protected gold nanoclusters. Its photoemission has been found to span the energy region of 1.1 to 1.8 eV and the observed emission has alternately been attributed to intraband or interband transitions, charge-transfer states, and semiring or ligand-based states. Our calculations on $Au_{25}(SR)_{18}{}^-$ (R=H, CH_3, C_2H_5, C_3H_7) nanoclusters showed an excellent agreement between the calculated states and experimental emission energies, when the typical underestimation of GGA calculations was considered. We concluded that several excited states are involved in photoemission from $Au_{25}(SR)_{18}{}^-$ nanoclusters and that core-based excitations arising from superatom P orbitals into the lowest two superatom D orbitals are responsible for all of these states. Larger Stokes shifts were observed for longer ligands. However, ligands appeared to primarily affect luminescence via their interactions with the gold nanoparticle core.

We studied photoluminescence properties of the well-characterized $Au_{38}(SR)_{24}$ cluster and the highly luminescent $Au_{22}(SR)_{18}$ cluster as well. The calculated emission energies for the lowest energy E and A_2 states of $Au_{38}(SH)_{24}$ were in good agreement with the lowest two of four experimental emission bands, which predominantly arise due to a HOMO→LUMO transition that involves core-based orbitals. Minor geometric relaxations were observed in the Au_{23} core compared to relaxations of up to 0.25 Å in the $Au_{25}(SH)_{18}{}^-$ nanocluster. These small geometrical changes lead to slight electronic structure changes and relatively small Stokes shifts in comparison to a Stokes shift of 0.49 eV for the $Au_{25}(SH)_{18}{}^-$ nanoparticle. The fluorescence and phosphorescence energies were calculated to be 1.32 and 1.23 eV for the $Au_{22}(SH)_{18}$ nanoparticle, which correspond to a HOMO→LUMO transition. The large calculated Stokes

shift of 0.47 eV and microsecond scale (or longer) lifetimes agreed well with the experimental results. A larger degree of structural flexibility in the Au_7 core that leads to significant electronic structure modifications upon photoexcitation were observed for the $Au_{22}(SH)_{18}$ nanoparticle. However, this structural flexibility may imply that the theoretically predicted structure of this system is not optimal.

Photoluminescence studies on the "golden" silver nanoparticle, $Ag_{25}(SR)_{18}^-$ (R=H, PhMe$_2$), showed similar results to its gold analog. Photoemission that arises due to HOMO-LUMO transitions involved excitations from core-based superatomic P into D orbitals. Aromatic ligands and heteroatom doping did not affect the origin of photoluminescence of this system. However, the emission energies, Stokes shifts and radiative lifetimes were slightly affected.

The recent crystal structure determination of the $Au_{20}(TBBT)_{16}$ (TBBT = SPh-t-Bu) nanocluster raised the question whether $Au_{20}(SR)_{16}$ adopts the same structure when R is an aliphatic ligand. To this end, we optimized a methylthiolate version of the new crystal structure geometry of $Au_{20}(TBBT)_{16}$ and compared the stability and optical properties with the three lowest energy isomers of $Au_8[Au_3(SCH_3)_4]_4$ structures predicted previously. Our results proposed that the new geometry of the $Au_{20}(SCH_3)_{16}$ nanocluster with an Au_7 core protected by an unusual $Au_8(SR)_8$ ring motif, one trimeric and two monomeric staple motifs is more stable than the previous isomers and that the ligand effect on optical properties of $Au_{20}(SR)_{16}$ is relatively small.

The real-time TDDFT approach is gaining ground as an effective method to calculate optical properties of molecular systems. We performed a benchmark study to demonstrate the consistency of LR and RT methods for calculating the optical absorption spectra of distinct noble metal nanoclusters. The RT absorption spectra obtained using a grid-based basis set with pseudopotentials achieved results in good agreement with the LR spectrum obtained with large QZ4P atom-centered basis sets. The real-time variation of the electron density was visualized to show the collective oscillation of electron density at the longitudinal plasmon mode of the Ag_6 nanowire.

Appendix A - Supporting information for "Theoretical Insights into Origin of Photoluminescence of $Au_{25}(SR)_{18}^-$ Nanoparticles"

Table A1. Summary of experimental photoluminescence properties of thiolate protected Au_{25} nanocluster.

| Experimental Group	Structural Formula	Photoluminescence Data
Link *et al.*[1]	$Au_{25}(SG)_{18}$ SG = glutathione	two bands with maxima around 1.5 and 1.15 eV
Murray and Coworkers[2]	$Au_{25}(SR)_{18}$ R = CH_2CH_2Ph	two emission peaks at 1.38 and 1.2 eV
Pradeep and coworkers[3, 4]	$Au_{25}(SG)_{18}$ (also acetyl- and formyl-glutathione)	peak around 700 nm (~1.7-1.8 eV)
	$Au_{25}(SG')_{18}$ G' = 3-mercapto-2-butanol-glutathione	peak around 680 nm
Wu and Jin[5]	$[Au_{25}(SR)_{18}]^q$ R = CH_2CH_2Ph, $C_{12}H_{25}$, C_6H_{13} (q = -1, 0, +1, +2)	peak around 725 – 775 nm
Ramakrishna, Goodson, and coworkers[6-8]	$Au_{25}(SG)_{18}$	low quantum yield photoluminescence ~500 nm and another peak ~710 nm
	$Au_{25}(SR)_{18}$ R = C_6H_{13}	low quantum yield photoluminescence ~500 nm and another peak ~830 nm
Knappenberger and coworkers[9]	$Au_{25}(SR)_{18}$ R = CH_2CH_2Ph	Broad near-infrared photoluminescence with several peaks at 1.72, 1.57, and 1.51 eV
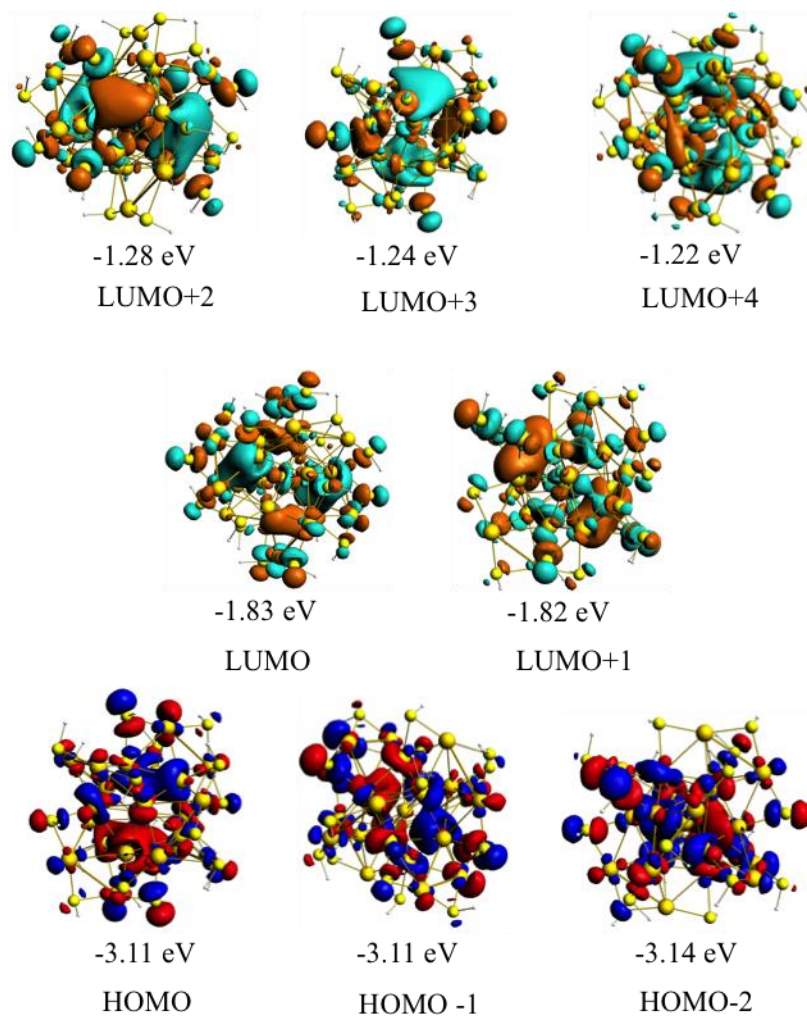
Figure A1. BP86/DZ Kohn-Sham orbitals and orbital energies for ground state of Au$_{25}$(SH)$_{18}^{-}$. |Isovalue| = 0.02

Table A2. Comparison of Au$_{shell}$–Au$_{shell}$ bond lengths in relaxed geometries of the ground state (S$_0$) and the first excited state (S$_1$) of the Au$_{25}$(SH)$_{18}^-$ nanocluster. Atoms in the Au$_{13}$ icosahedral core with elongated bonds in S$_1$ with respect to S$_0$ are highlighted in green.
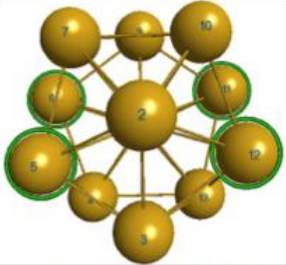
Bond	Bond Length (Å)	
	S$_0$	S$_1$
5 – 6	3.053	3.303
11 – 12	3.053	3.303
4 – 5	2.998	3.101
10 – 11	2.998	3.109
5 – 7	3.006	3.110
11 – 13	3.006	3.110
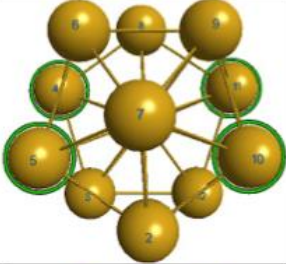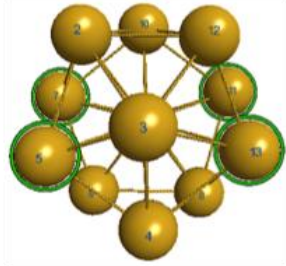
Table A3. Comparison of ground state electronic structures of Au$_{25}$(SR)$_{18}^-$ nanoclusters.

	Energy (eV)			
	Au$_{25}$(SH)$_{18}^-$	**Au$_{25}$(SCH$_3$)$_{18}^-$**	**Au$_{25}$(SCH$_2$CH$_3$)$_{18}^-$**	**Au$_{25}$(SCH$_2$CH$_2$CH$_3$)$_{18}^-$**
HOMO-2	-3.14	-2.59	-2.55	-2.53
HOMO-1	-3.11	-2.55	-2.52	-2.48
HOMO	-3.11	-2.53	-2.50	-2.46
LUMO	-1.83	-1.35	-1.31	-1.33
LUMO+1	-1.82	-1.29	-1.26	-1.26
LUMO+2	-1.28	-0.78	-0.72	-0.72
LUMO+3	-1.24	-0.74	-0.68	-0.65
LUMO+4	-1.22	-0.71	-0.65	-0.62
HOMO-LUMO gap	1.27	1.19	1.20	1.13

Table A4. Excited state energies and oscillator strengths for Au$_{25}$(SR)$_{18}^-$ at the ground state geometry.

State	**Au$_{25}$(SCH$_3$)$_{18}^-$**		**Au$_{25}$(SCH$_2$CH$_3$)$_{18}^-$**		**Au$_{25}$(SCH$_2$CH$_2$CH$_3$)$_{18}^-$**	
	Energy (eV)	Oscillator Strengh (au)	Energy (eV)	Oscillator Strengh (au)	Energy (eV)	Oscillator Strengh (au)
S$_1$	1.234	2.507×10^{-3}	1.255	2.890×10^{-3}	1.187	4.288×10^{-3}
S$_2$	1.262	6.204×10^{-4}	1.261	4.322×10^{-4}	1.219	2.129×10^{-4}
S$_3$	1.290	2.419×10^{-3}	1.295	2.410×10^{-3}	1.240	2.757×10^{-3}
S$_4$	1.327	1.907×10^{-2}	1.331	2.096×10^{-2}	1.279	1.902×10^{-2}
S$_5$	1.360	1.914×10^{-2}	1.359	2.062×10^{-2}	1.318	2.257×10^{-2}
S$_6$	1.393	1.947×10^{-2}	1.393	2.220×10^{-2}	1.378	2.338×10^{-2}

Table A5. The change in energy levels of the frontier orbitals of Au₂₅(SR)₁₈⁻ clusters in S₁ state geometry with respect to their S₀ state geometry.

	Energy Change (eV)		
	$Au_{25}(SCH_3)_{18}^-$	$Au_{25}(SCH_2CH_3)_{18}^-$	$Au_{25}(SCH_2CH_2CH_3)_{18}^-$
HOMO-2	-0.02	-0.03	-0.05
HOMO-1	0.019	0.01	0.01
HOMO	0.33	0.28	0.34
LUMO	-0.25	-0.27	-0.34
LUMO+1	-0.07	-0.08	-0.13
LUMO+2	0.03	0.01	-0.01
LUMO+3	0.05	0.04	0.00
LUMO+4	0.07	0.03	0.01

*A negative energy change indicates the amount of stabilization of that orbital whereas a positive value indicates the destabilization of a particular orbital with respect to the ground state relaxed geometry.

References

1.   Link, S.; Beeby, A.; FitzGerald, S.; El-Sayed, M. A.; Schaaff, T. G.; Whetten, R. L., Visible to Infrared Luminescence from a 28-Atom Gold Cluster. *J. Phys. Chem. B* **2002**, *106*, 3410-3415.

2.   Lee, D.; Donkers, R. L.; Wang, G.; Harper, A. S.; Murray, R. W., Electrochemistry and Optical Absorbance and Luminescence of Molecule-like Au₃₈ Nanoparticles. *J. Am. Chem. Soc.* **2004**, *126*, 6193-6199.

3.   Shibu, E. S.; Muhammed, M. A. H.; Tsukuda, T.; Pradeep, T., Ligand Exchange of Au₂₅SG₁₈ Leading to Functionalized Gold Clusters: Spectroscopy, Kinetics, and Luminescence. *J. Phys. Chem. C* **2008**, *112*, 12168-12176.

4.   Shibu, E. S.; Pradeep, T., Photoluminescence and Temperature-Dependent Emission Studies of Au₂₅ Clusters in the Solid State. *Int. J. Nanosci.* **2009**, *08*, 223-226.

5.   Wu, Z.; Jin, R., On the Ligand's Role in the Fluorescence of Gold Nanoclusters. *Nano Lett.* **2010**, *10*, 2568-2573.

6.   Devadas, M. S.; Kim, J.; Sinn, E.; Lee, D.; Goodson, T.; Ramakrishna, G., Unique Ultrafast Visible Luminescence in Monolayer-Protected Au₂₅ Clusters. *J. Phys. Chem. C* **2010**, *114*, 22417-22423.

7.   Ramakrishna, G.; Varnavski, O.; Kim, J.; Lee, D.; Goodson, T., Quantum-Sized Gold Clusters as Efficient Two-Photon Absorbers. *J. Am. Chem. Soc.* **2008**, *130*, 5032-5033.

8.   Yau, S. H.; Varnavski, O.; Gilbertson, J. D.; Chandler, B.; Ramakrishna, G.; Goodson, T., Ultrafast Optical Study of Small Gold Monolayer Protected Clusters: A Closer Look at Emission. *J. Phys. Chem. C* **2010**, *114*, 15979-15985.

9.   Green, T. D.; Yi, C.; Zeng, C.; Jin, R.; McGill, S.; Knappenberger, K. L., Temperature-Dependent Photoluminescence of Structurally-Precise Quantum-Confined $Au_{25}(SC_8H_9)_{18}$ and $Au_{38}(SC_{12}H_{25})_{24}$ Metal Nanoparticles. *J. Phys. Chem. A* **2014**, *118*, 10611-10621.

Figure B1. BP86/DZ Kohn-Sham orbitals and orbital energies at the ground state (S$_0$) of Ag$_{25}$(SH)$_{18}^-$. |Isovalue| = 0.025

Table B1. Comparison of Ag_shell–Ag_shell bond lengths in relaxed geometries of the ground state (S$_0$) and the first excited state (S$_1$) of the Ag$_{25}$(SH)$_{18}^-$ nanocluster. Atoms in the Ag$_{13}$ icosahedral core with elongated bonds in S$_1$ with respect to S$_0$ are highlighted in green.

	Bond	Bond Length (Å)	
		S$_0$	S$_1$
	9 – 12	2.928	3.029
	10 – 13	3.021	3.190
	5 – 12	2.990	3.125
	11 – 13	2.998	3.109
	6 – 12	2.882	2.795
	3 – 13	2.908	2.812
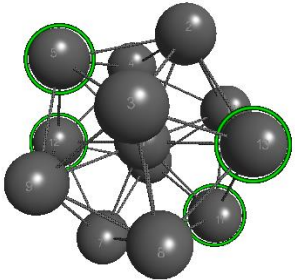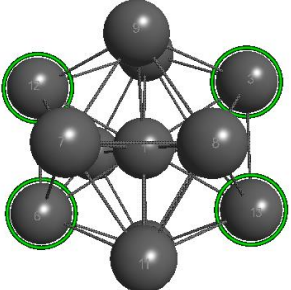
Table B2. Geometrical parameters of the ground state (S_0) and first singlet excited state (S_1) structures of $[Ag_{25}(SPhMe_2)_{18}]^-$ at the BP86/DZ level of theory.

Bond	Average Bond Length (Å)	
	Ground State (S_0)	Excited State (S_1)
Ag_{center}–Ag_{shell}	2.799 ± 0.013	2.805 ± 0.020
Ag_{shell}–Ag_{shell}	2.943 ± 0.082	2.950 ± 0.085
Ag_{shell}–$S_{terminal}$	2.565 ± 0.009	2.568 ± 0.015
Ag_{staple}–$S_{terminal}$	2.523 ± 0.005	2.524 ± 0.022
Ag_{staple}–$S_{central}$	2.509 ± 0.005	2.527 ± 0.015

Table B3. Comparison of Ag_{shell}–Ag_{shell} bond lengths in relaxed geometries of the ground state (S_0) and the first excited state (S_1) of the $[Ag_{25}(SPhMe_2)_{18}]^-$ nanocluster. Atoms in the Ag_{13} icosahedral core with elongated bonds in S_1 with respect to S_0 are highlighted in green..
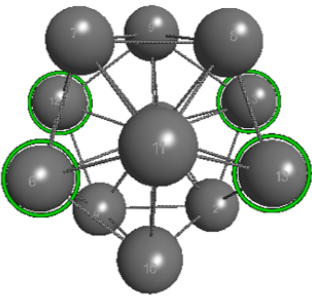
Bond	Bond Length (Å)	
	S_0	S_1
6 – 12	2.968	2.841
3 – 13	2.986	2.881
9 – 12	2.853	2.923
10 – 13	3.037	3.167
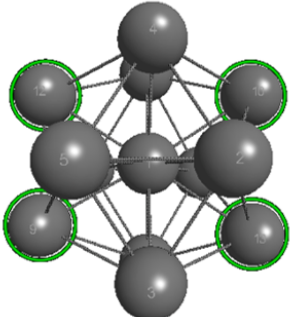
Table B4. Comparison of Ag_{shell}–Ag_{shell} bond lengths in relaxed geometries of the ground state (S_0) and the first excited state (S_1) of the $Ag_{24}Au(SH)_{18}^-$ nanocluster. Atoms in the $AuAg_{12}$ icosahedral core with elongated bonds in S_1 with respect to S_0 are highlighted in green.
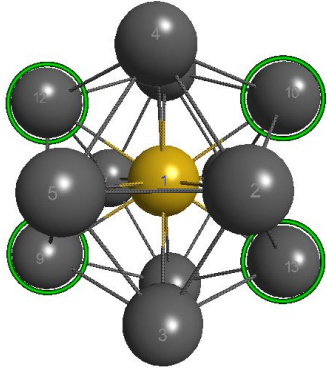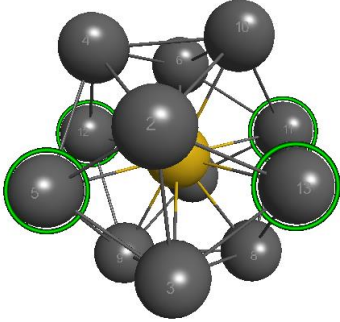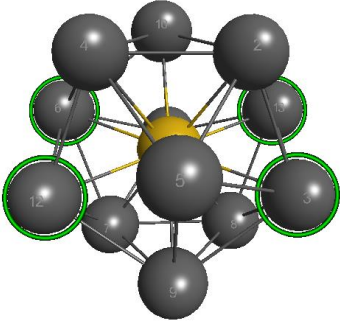
Bond	Bond Length (Å)	
	S_0	S_1
9 – 12	2.943	3.042
10 – 13	3.012	3.177
5 – 12	2.995	3.123
11 – 13	2.924	2.995
6 – 12	2.896	2.802
3 – 13	2.926	2.824